Universität Basel

Philosophisch-Naturwissenschaftliche Fakultät

Color-tuning and Stability Enhancement of Cyclometallated Iridium(III) Complexes in Light-emitting Electrochemical Cells

Inauguraldissertation

zur

Erlangung der Würde eines Doktors der Philosophie

vorgelegt der

Philosophisch-Naturwissenschaftlichen Fakultät

der Universität Basel

von

Andreas Matthias Bünzli

aus Maur ZH und Rüeggisberg BE

Basel, 2015

Genehmigt von der Philosophisch-Naturwissenschaftlichen Fakultät
auf Antrag von

Prof. Dr. Edwin C. Constable und Prof. Dr. Oliver S. Wenger

Basel, den 21.04.2015

Prof. Dr. Jörg Schibler

Dekan

Namensnennung-Keine kommerzielle Nutzung-Keine Bearbeitung 3.0 Schweiz
(CC BY-NC-ND 3.0 CH)

Sie dürfen: **Teilen** — den Inhalt kopieren, verbreiten und zugänglich machen

Unter den folgenden Bedingungen:

Namensnennung — Sie müssen den Namen des Autors/Rechteinhabers in der von ihm festgelegten Weise nennen.

Keine kommerzielle Nutzung — Sie dürfen diesen Inhalt nicht für kommerzielle Zwecke nutzen.

Keine Bearbeitung erlaubt — Sie dürfen diesen Inhalt nicht bearbeiten, abwandeln oder in anderer Weise verändern.

Wobei gilt:

- **Verzichtserklärung** — Jede der vorgenannten Bedingungen kann **aufgehoben** werden, sofern Sie die ausdrückliche Einwilligung des Rechteinhabers dazu erhalten.
- **Public Domain (gemeinfreie oder nicht-schützbare Inhalte)** — Soweit das Werk, der Inhalt oder irgendein Teil davon zur Public Domain der jeweiligen Rechtsordnung gehört, wird dieser Status von der Lizenz in keiner Weise berührt.
- **Sonstige Rechte** — Die Lizenz hat keinerlei Einfluss auf die folgenden Rechte:
    - Die Rechte, die jedermann wegen der Schranken des Urheberrechts oder aufgrund gesetzlicher Erlaubnisse zustehen (in einigen Ländern als grundsätzliche Doktrin des **fair use** bekannt);
    - Die **Persönlichkeitsrechte** des Urhebers;
    - Rechte anderer Personen, entweder am Lizenzgegenstand selber oder bezüglich seiner Verwendung, zum Beispiel für **Werbung** oder Privatsphärenschutz.
- **Hinweis** — Bei jeder Nutzung oder Verbreitung müssen Sie anderen alle Lizenzbedingungen mitteilen, die für diesen Inhalt gelten. Am einfachsten ist es, an entsprechender Stelle einen Link auf diese Seite einzubinden.

Quelle: http://creativecommons.org/licenses/by-nc-nd/3.0/ch/ Datum: 12.11.2013

Acknowledgements

First of all, I would like to thank Prof. Dr. Edwin C. Constable and Prof. Dr. Catherine E. Housecroft for giving me the opportunity to work on this project and their support during the last four years. I appreciated the possibility to work independently, realizing my own ideas with their patient and fruitful help to solve arising problems.

I would like to thank Prof. Dr. Oliver S. Wenger for being my co-examiner and co-referee.

Many thanks go to PD Dr. Daniel Häussinger and his NMR group members Dr. Heiko Gsellinger and Kaspar Zimmermann for their assistance with low temperature NMR measurements and maintaining all the NMR machines. I would like to thank all the supporting staff of the department, namely Dr. Markus Neuburger, Dr. Jennifer A. Zampese and Dr. Alessandro Prescimone for solving the crystal structures, Werner Kirsch and Sylvie Mittelheisser for providing the elemental analyses, Markus Hauri and Roy Lips for material supply and Beatrice Erismann for executing all the administrative work.

A special thank goes to Dr. Henk J. Bolink and his team in Valencia, namely Dr. Daniel Tordera, Lidón Gil-Escrig, Giulia Longo for the preparation and measurements of the LEEC devices and especially Dr. Antonio Pertegás for the additional help in analyzing their results. I would also like to thank our second collaborator in Valencia Prof. Dr. Enrique Ortí and his team, namely José M. Junquera-Hernández and Juan J. Serrano-Pérez for supporting us with theoretical calculations.

Dr. Sven Brauchli, Dr. Gabriel Schneider, Dr Collin Morris and Dr. Niamh Murray are acknowlegded for recording ESI-MS spectra and Dr. Niklaus Hostettler, Maximilian Klein and Roché Walliser for measuring low-temperature NMR spectra. Further thanks go to Prof. Dr. Catherine E. Housecroft, Dr. Collin Morris and Dr. Niklaus Hostettler for proof reading this manuscript. Many thanks go to the current and former members of the Constable/Housecroft group who shared the time and laboratories with me.

Special thanks go to Dr. Niklaus Hostettler, Dr. Jonas Schönle, Dr. Ewald Schönhofer, Dr. Sven Brauchli, Sebastian Fürer, Cathrin Ertl, Dr. Peter Kopecky, Dr. Collin Morris, Dr. Gabriel Schneider and Annika Büttner for their friendship and the great time and in and outside of the department.

Big thanks go to Matthias Wasem, Florian Weiss and Markus Gantenbein for being great flatmates and accepting the Three Kings living room becoming my home office. Annika deserves a big hug for always taking good care of us.

Finally, my parents and my sister Christa deserve a big thank you for their enthusiastic support during all my life, which was really not always the easiest thing to do. Thank you!

Abstract

In this thesis, the design and synthesis of cyclometallated iridium(III) complexes for use in light-emitting electrochemical cells (LEECs) are presented, divided into six chapters. Focus is put on the emission color-tuning of various compounds, covering almost the whole visible spectrum between blue and red including first steps towards white-light emission. Secondly, a new systematic approach for an intrinsic stability enhancement of highly pure Ir(III) complexes is investigated. The work is rounded off by the test results of all compounds for potential commercial application in LEECs.

Chapter 1 highlights the historical progress of artificial light from the incandescent light bulb towards ultrathin highly-efficient flexible LEECs and their working principle.

Chapter 2 describes the synthesis and photophysical properties of orange-emitting Ir(III) complexes supported by theoretical calculations.

Chapter 3 addresses the synthesis and characterization of green-emitting Ir(III) complexes supported by theoretical calculations.

Chapter 4 reports the design of linking a blue-emitting naphthyl group to an orange-luminescent Ir(III) complex as well as mixing experiments of a blue and orange compound towards white-light emission.

Chapter 5 comprises the effect of multiple intra-cation π-stacking interactions on the long-term stability of Ir(III) complexes in LEECs.

Chapter 6 concludes the previous chapters and gives a short outlook for future work in the field of Ir(III) based LEECs.

Parts of this work have been published

Tordera, D.; Bünzli, A. M.; Pertegás, A.; Junquera-Hernández, J. M.; Constable, E. C.; Zampese, J. A.; Housecroft, C. E.; Ortí, E.; Bolink, H. J. "Efficient Green-Light-Emitting Electrochemical Cells Based on Ionic Iridium Complexes with Sulfone-Containing Cyclometalating Ligands" *Chem. Eur. J.* **2013**, *19*, 8597.

Bünzli, A. M.; Bolink, H. J.; Constable, E. C.; Housecroft, C. E.; Junquera-Hernández, J. M.; Neuburger, M.; Ortí, E.; Pertegás, A.; Serrano-Pérez, J. J.; Tordera, D.; Zampese, J. A. "Thienylpyridine-based cyclometallated iridium(III) complexes and their use in solid state light-emitting electrochemical cells" *Dalton Trans.* **2014**, *43*, 738.

Bünzli, A. M.; Constable, E. C.; Housecroft, C. E.; Prescimone, A.; Zampese, J. A.; Longo, G.; Gil-Escrig, L.; Pertegás, A.; Ortí, E.; Bolink, H. J. "Exceptionally long-lived light-emitting electrochemical cells: multiple intra-cation π-stacking interactions in $[Ir(C\hat{}N)_2(N\hat{}N)][PF_6]$ emitters" *Chem. Sci.* **2015**, DOI: 10.1039/c4sc03942d.

List of Abbreviations

A	ampere
Å	Ångström
$AgPF_6$	silver hexafluoridophosphate
b	recombination efficiency
$[BF_4]^-$	tetrafluoridoborate
[BMIM][PF_6]	1-butyl-3-methylimidazolium hexafluoridophosphate
bpy	2,2'-bipyridine
°C	degree Celsius
$C(CH_3)_3$	*tert*-butyl
C^N	cyclometallating ligand
calc.	calculated
cd	candela
$CDCl_3$	chloroform
CF_3	trifluoromethyl
CH_2Cl_2	dichloromethane
CH_3CN	acetonitrile
CIE	Commission internationale de l'éclairage
$[ClO_4]^-$	perchlorate
cm	centimeter
COSY	correlation spectroscopy
DC	direct current
DFT	density functional theory
dm	decimeter

DMF	dimethylformamide
DMSO	dimethyl sulfoxide
dpbpy	6,6'-diphenyl-2,2'-bipyridine
E	half-cell potential or excitation energy
EL	electroluminescence
eq	equivalent
EQE	external quantum efficiency
ESI	electrospray ionization
Et_2O	diethylether
EtOH	ethanol
Fc/Fc^+	ferrocene/ferrocenium
FWHM	full width at half maximum
g	gram
GS	ground state
Gt	gigaton
h	hour
Hdfppz	1-(2,4-difluorophenyl)-1*H*-pyrazole
Hdppy	2,6-diphenylpyridine
HMBC	heteronuclear multiple bond correlation
HMQC	heteronuclear multiple quantum coherence
Hmsppz	1-[4-(methylsulfonyl)phenyl]-1*H*-pyrazole
Hnaphppy	2,7-[bis(4-phenylpyridin-2-yl)-1*H*-1,4,7-trioxaheptyl]naphthalene
HOMO	highest occupied molecular orbital
HPh_2ppy	2-(3,5-diphenyl)phenylpyridine
HPhppy	2-(3-phenyl)phenylpyridine

Hppy	2-phenylpyridine
Hthpy	2-(2'-thienyl)pyridine
Htppy	2,4,6-triphenylpyridine
Hz	hertz
IL	ionic liquid
IR	infrared, in the IR spectra weak (w), strong (s), medium (m)
irr	irreversible
iTMC	ionic transition metal complex
ITO	indium tin oxide
J	current density
J	coupling constant
K	Kelvin
K_2CO_3	potassium carbonate
L	luminance
L	liter
LC	ligand-centered
LED	light-emitting diode
LEEC	light-emitting electrochemical cell
LLCT	ligand-to-ligand charge transfer
lm	lumen
LMCT	ligand-to-metal charge transfer
LUMO	lowest unoccupied molecular orbital
m	meter
M	mol L^{-1} or parent ion
m/z	mass to charge ratio

MC	metal-centered
MeCN	acetonitrile
MeOH	methanol
mg	milligram
$MgSO_4$	magnesium sulfate
MHz	megahertz
min	minute
MLCT	metal-to-ligand charge transfer
mmol	millimol
MS	mass spectrometry
n	refractive index
[^{n}Bu$_4$N]	tetra-*n*-butyl ammonium
N^N	ancillary ligand
NaH	sodium hydride
Naphbpy	6-(2-naphthyl)-2,2'-bipyridine
NH_4OH	ammonium hydroxide
NH_4PF_6	ammonium hexafluoridophosphate
nm	nanometer
NMe_2	dimethylamino
NMR	nuclear magnetic resonance, with the signals being identified as singlet (s), doublet (d), doublet of doublet (dd), triplet (t), triplet of triplet (tt), multiplet (m), broad (br)
NOESY	nuclear overhauser enhancement spectroscopy
OHnaph	2,7-di[2-(2-hydroxyethoxy)ethoxy]naphthalene]
OLED	organic light-emitting diode
ox	oxidation
X	

pbpy	6-phenyl-2,2'-bipyridine
PEDOT:PSS	[poly(3,4-ethylendioxythiophene):polystyrenesulfonate)]
$[PF_6]^-$	hexafluoridophosphate
phen	1,10-phenanthroline
PLQY	photoluminescence quantum yield
PMMA	polymethylmethacrylate
ppm	parts per million
PWh	petawatt hour (10^{15} watt hour)
qr	quasi-reversible
red	reduction
rpm	revolutions per minute
s	second
S_0	electronic ground state
sh	shoulder
SMe	thiomethyl group
SO_2CH_3	methylsulfonyl
SSL	solid-state lighting
$t_{1/2}$	lifetime
^{t}Bu	*tert*-butyl
TD	time-dependent
T_n	triplet state
t_{on}	turn-on time
TWh	terawatt hour (10^{12} watt hour)
UV	ultraviolet
V	volt

$\tilde{\nu}$	wavenumbers in cm^{-1}
Vis	visible
W	watt
wt	weight
δ	chemical shift
ε	molar exctinction coefficient
ζ	spin-orbit coupling constant
λ_{abs}	absorption wavelength
λ_{em}	emission wavelength
λ_{ex}	excitation wavelength
ν	frequency
τ	lifetime
ϕ	fraction of excitons decaying radiatively
Φ	quantum yield

Table of Contents

Materials and Methods

^{1}H and ^{13}C NMR spectra were recorded on a Bruker Avance III-500 or III-600 NMR spectrometer referencing the chemical shifts with respect to δ(TMS) = 0 ppm. Solution electronic absorption and emission spectra were recorded on an Agilent 8453 spectrophotometer and on a Shimadzu 5301PC spectrofluorophotometer, respectively. Solution and solid-state photoluminescence quantum yields were measured using a Hamamatsu absolute PL quantum yield spectrometer C11347 Quantaurus-QY. Excited state lifetimes and emission of powdered samples were recorded on a Hamamatsu Compact Fluorescence lifetime Spectrometer C11367 Quantaurus-Tau. A Perkin Elmer Spectrum Two UATR instrument was used to measure FT-IR spectra of solid samples. Electrospray ionization mass spectra were measured using a Bruker esquire 3000^{plus} mass spectrometer. Elemental analyses were carried out on a Leco CHN-900 microanalyser. Melting points were measured by using a Krüss Optronic Melting Point Meter M5000.

Electrochemical measurements were performed using a CH Instrument 900B potentiostat or a VersaSTAT 3 potentiostat from Princeton Applied Research with a glassy carbon working electrode, a platinum-wire as auxiliary electrode and a silver-wire as pseudo-reference electrode. The redox potentials were determined by cyclic voltammetry and square wave voltammetry. Degassed HPLC grade CH_3CN or CH_2Cl_2 solutions of samples ($\approx 10^{-4}$ mol dm^{-3}) were recorded in the presence of 0.1 M [$^{n}Bu_4N$][PF_6] as supporting electrolyte at a scan rate of 0.1 V s^{-1} using ferrocene (Fc^{+}/Fc) as internal standard. A Biotage Initiator 8 reactor was used for the synthesis under microwave conditions.

Single crystal data were collected on a Bruker-Nonius KappaAPEX or a Bruker APEX-II diffractometer with data reduction, solution and refinement using the programs APEX[1] and CRYSTALS[2] or SHELX-13.[3] ORTEP-type diagrams and structure analysis used Mercury v. 3.0.1 and v. 3.3.[4],[5]

For the device preparation and characterization: glass substrates partially coated with indium-tin-oxide (ITO) (www.naranjosubstrates.com) were cleaned by 5 minute sonication in soapy water, deionized water, isopropanol and thereafter left under an UV-O_3 cleaner (Jelight 42-220) for 20 minutes. A 60 nm thick [poly(3,4-ethylendioxythiophene):polystyrenesulfonate)] PEDOT/PSS (purchased from Hereaus) film was spin coated on top of the glass substrate at 1000 rpm, and then dried at 150 ºC for 15 minutes. On top of this a blend of the iridium complex and the ionic liquid [BMIM][PF_6] (1-butyl-3-methyl-imidazolium hexafluoridophosphate) (molar ratio 4:1) was spin coated from an acetonitrile or dichloromethane solution (20 mg mL^{-1}) at 1000 rpm, leading to a 100 nm thick active layer. The thickness of the films was determined using an Ambios XP1 profilometer. After spinning the organic layers, the samples were transferred to an inert atmosphere glovebox (< 0.1 ppm O_2 and H_2O, MBraun). Finally, aluminum metal electrodes (70 nm) were thermally evaporated using a shadow mask under a vacuum (< 1 x 10^{-6} mbar) using an Edwards Auto500 evaporator integrated into

the inert atmosphere glovebox. Lifetime data were obtained by applying pulsed currents and monitoring the voltage and simultaneously the luminance by a True Colour Sensor MAZeT (MTCSICT Sensor) using a Lifetime Test System designed by BoTEST (Botest OLT OLED Lifetime-Test System).

Chapter 1

Chapter 1 Introduction

1.1 The Rise of Artificial Light

Since fire has been used by our primate ancestors sunlight-independent heat and artificial light have been integrated into human lifestyle. Nowadays, artificial light is available anytime allowing humans to be as active at night as during the day in- as well as outdoors.

Artificial light has undergone a tremendous increase in consumption and progressed in terms of efficiency since Thomas Edison patented the incandescent carbon filament lamp in 1879 (Figure 1.1). Although Edison's device converted only 0.2% of electricity into light, it was still 20 times more efficient than a candle was in converting chemical energy into useful photons.[6] In modern incandescent lamps based on a wire filament that emits light upon heating in a vacuum, 95% of the emitted energy is lost as heat. Several new technologies have been developed after Edison's first patent such as the tungsten lamp (1906), which was the dominant light source for one century, the sodium vapor lamp (1930s), nowadays used in street illumination in its modern high-pressure form, and fluorescent tubes (1940s), used for large room illumination.[7] These three designs were introduced into the halogen lamp as an advanced filament system (1960s) and the compact fluorescent lamp (1980s) appeared as a hybrid between bulbs and fluorescent tubes. The principle remains the same as for the fluorescent tube mercury vapor excited by an electrical discharge emits UV light and is then down-converted into visible light by solid or gaseous compounds.

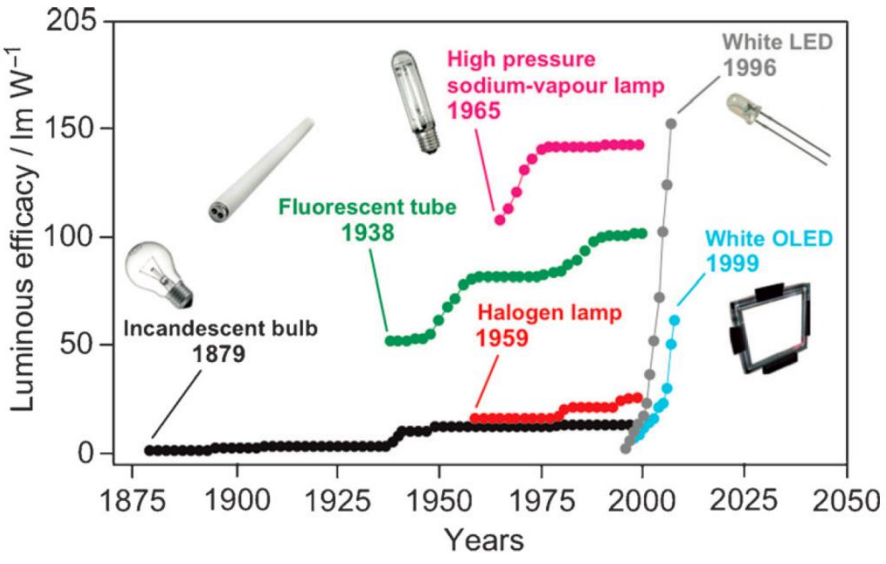

Figure 1.1 Historical trend of the luminous efficacy of the most common light sources between 1875 and 2000.[8]

The importance of, and the demand for, artificial light is such that its consumption increased by five orders of magnitude over the past three centuries in the UK. While a British person consumed 580 lumen-hours per year in 1700, a person today uses up to 46 million lumen-hours in the same period of time, whereby a lumen-hour is comparable to the light of a candle burning for an hour.[9]

Worldwide, the electricity consumption for artificial lighting consumes approximately 3 PWh, corresponding to 20% of the total power demand in the world. This results in an estimated CO_2 production of 2 Gt which equals 7% of the global emission and is equivalent to 70% of the emissions of the world's passenger transportation.[8],[10] In Switzerland, electric power consumption used for lighting in 2012 was 7.4 TWh, which is 12.9% (corresponding to ≈ 0.25% worldwide) of the overall electric power consumption for that year and is an increase of 6.9 % compared to the year 2000 (Figure 1.2).[11] The most striking fact is that 1.5 billion people in the world have no access to electric light today. This corresponds to more than one fifth of the world population and this is more than it was when Thomas Edison first popularized the incandescent light bulb in the 1880s. Alternatively, people without access to the electrical grid burn fuels to obtain illumination causing severe environmental pollution and health risks.[10]

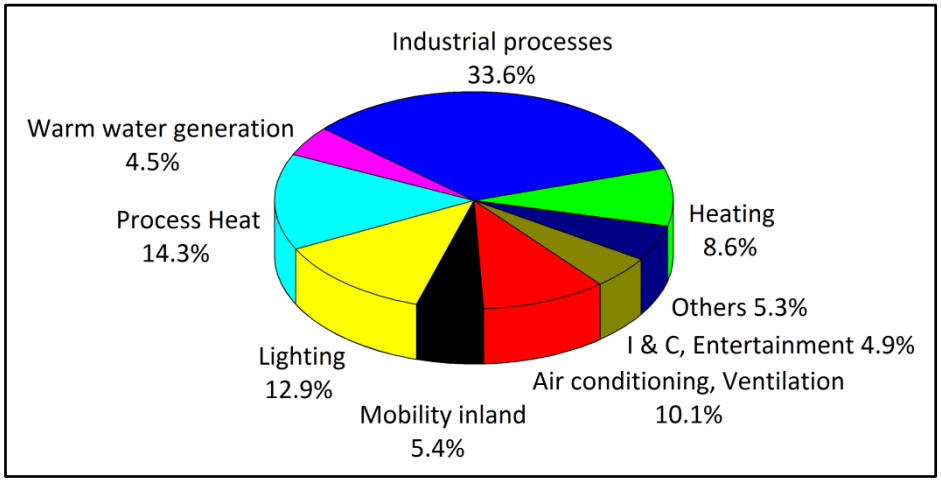

Figure 1.2 Swiss annual electric power consumption in 2012, broken down into the different consumer groups.[11]

As a result, there is obviously an urgent need to further improve and expand the use of electrical lighting because traditional lighting systems like incandescent and discharge lamps have nearly been exploited to their limits.

The huge increase in power consumption is going to be reduced by replacing these light sources with new, more efficient technologies, resulting in huge environmental and economic savings.[12] This ongoing development involves solid-state lighting (SSL) based on inorganic or organic materials that emit light in response to electric current, a process called electroluminescence. Electroluminescence occurs when charge carriers of opposite charge (electron and hole) radiatively recombine (see Figure 1.3). Prior to luminescence, non-thermal excitation is accomplished by the removal of electrons from the highest occupied molecular orbital (HOMO) and the injection of electrons to the lowest unoccupied molecular orbital (LUMO) of an active material via an external circuit.[12],[13] The opposite charges can migrate through the film and (when close enough) an exciton forms upon pairing. The decay of this exciton emits a photon following the same principle as in photoluminescence in solution and thereby the electronic ground state of the active material is recovered.

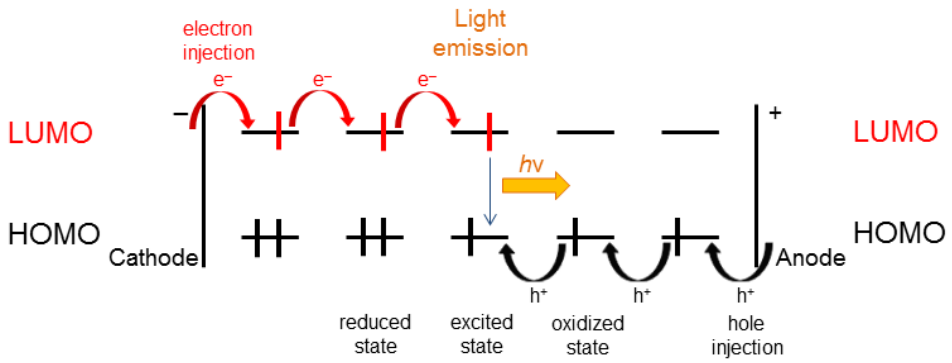

Figure 1.3 Principle of electroluminescence: Electrons are injected into the LUMO of an active material from the cathode (left hand side) and at the same time, electrons are withdrawn from (holes are injected into) the HOMO at the anode (right hand side). Both charge carriers migrate through the active material until they form an excited state when they meet and emit a photon in the case of radiative recombination.

The big advantage of SSL is that the primary product of these lighting devices is the photon itself whereas in conventional light sources, light is essentially a byproduct of other processes such as heating or discharging.[8] Therefore, SSL emits visible light with reduced heat generation or other competitive energy dissipation and its more robust solid state nature results in an increased device lifespan. The two main families of SSL devices are light-emitting diodes (LEDs)[14] and organic light-emitting diodes (OLEDs).[15],[16]

LED technology works on the basis of inorganic semiconductors consisting of several elements (e.g. In, Ga, N, P) yielding highly efficient light point sources with a broad variety of applications.[17] The importance of this invention was honored by awarding the Nobel Prize in Physics 2014 to Isamu Akasaki, Hiroshi Amano and Shuji Nakamura for their extraordinary work on efficient blue LEDs enabling bright and energy-saving white-light sources.[18]

OLEDs have become very attractive due to their potential in thin-film applications (e.g. cell phone displays and prototype TVs) where a multi-layered stack of a few hundred nanometers produces light emission through electroluminescence.[19] The light-emitting active layer is based on a luminescent material, typically a polymer,[20] a small fluorescent molecule,[21] or a phosphorescent neutral transition metal complex embedded in a charge transporting matrix.[22] State-of-the-art white-light OLEDs are multi-component systems of as many as 15 individual layers.[23] Such complex devices can only be prepared by vacuum sublimation and restricts its components to thermally stable non-ionic materials. Hence the variety of potential luminescent compounds is drastically narrowed since the vast majority of transition metal complexes are of an ionic nature.[24] The multi-layer evaporation process under inert environment, coupled with the need for rigorous encapsulation of the devices causes high manufacturing costs for OLEDs and are two of the drawbacks that prevents the wide distribution of OLED technology in the lighting market to date. Limitations in OLED technology stimulated the search for an alternative working principle for flat electroluminescent lighting devices with electrochemical light-emitting cells (LEECs) being the most popular one.

1.2 Light-emitting Electrochemical Cells

Another type of electroluminescent device that shows promising properties for highly efficient and low-cost applications in ultrathin flexible lighting is the LEEC, which consist of an ionic transition metal complex (iTMC) sandwiched between two electrodes. iTMCs support all the required processes of charge injection, charge transport, emissive recombination and can be solution-processed by spin coating or printing casts at ambient conditions. LEECs are distinguished from OLEDs by their simple architecture requiring ideally only a single active iTMC layer whereas an OLED consists of a multi-layered stack built-up under an inert environment at high temperature.

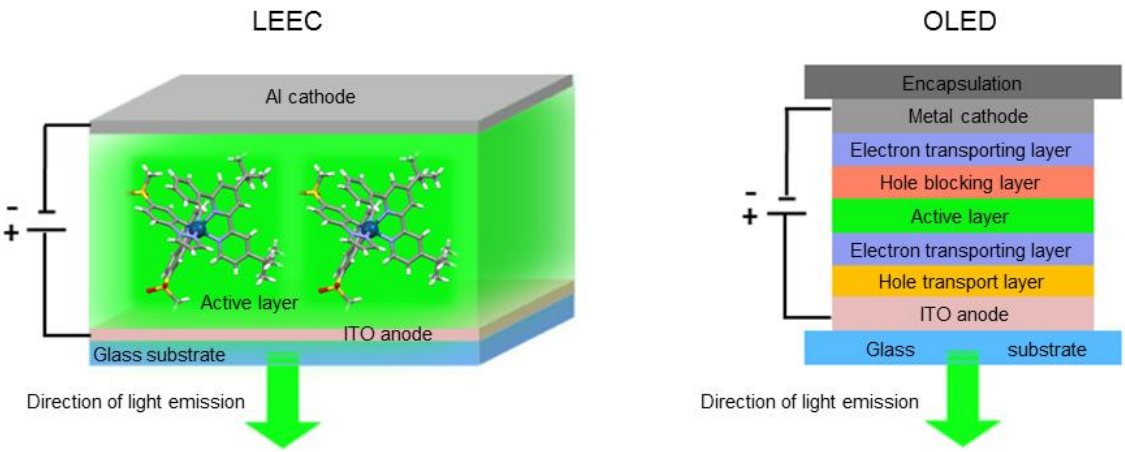

Figure 1.4 (Left) Simplistic schematics of a single-layer LEEC consisting of an iTMC (in this case: $[Ir(msppz)_2(\mathbf{4})][PF_6]$) sandwiched between two electrodes. An applied electric current between the aluminum cathode and the transparent indium tin oxide (ITO) anode induces the emission of the light in the active layer, observable through the glass. (Right) Schematics of the device architecture of an OLED containing multi-layered components.

iTMCs such as $[Ir(msppz)_2(\mathbf{4})][PF_6]$ (Hmsppz = 1-[4-(methylsulfonyl)phenyl]-1*H*-pyrazole, **4** = 6-phenyl-4,4'-di-*tert*-butyl-2,2'-bipyridine) are ionically conducting since the $[PF_6]^-$ counter-ions can rearrange under applied bias causing an excess of $[PF_6]^-$ at the anode and uncompensated $[Ir(msppz)_2(\mathbf{4})]^+$ at the cathode what assists electronic charge injection. This process makes the device independent of the work function of the electrodes and therefore air-stable metals such as gold, silver or aluminum can be used, avoiding the necessity of encapsulating and protecting the device from moisture and air. Furthermore, the Ir(III) complex cation together with its $[PF_6]^-$ counter-ion enables electron and hole transport throughout the bulk material and thanks to the intrinsic green emission of $[Ir(msppz)_2(\mathbf{4})][PF_6]$, the device is luminescent (Figure 1.4 left). Compared to OLEDs, these characteristics make LEECs suitable for low-cost and large-area illumination panels.[25],[26] Besides iTMCs, another widely used active material in LEECs are conjugated light-emitting polymers, termed polymer-LEECs (PLEECs)[27] which will not be discussed at length in this work. iTMCs based LEECs differ from PLEECs mainly in that iTMCs are intrinsically ionic and do not need additional charged species. Their phosphorescent triplet emitting properties also result in higher electroluminescence efficiencies than singlet emitters.[20]

1.3 The Uniqueness of Iridium(III) based iTMCs

Maness and co-workers reported the first iTMC-LEEC which was based on a Ru(II) complex as the single component in the active layer.[28] Further early works on iTMC-LEECs utilized ionic Ru(II) complexes such as the archetype $[Ru(bpy)_3][PF_6]_2$ (bpy = 2,2'-bipyridine) (Figure 1.5). The emission of this class of compounds is centered exclusively in the orange-red region reaching external quantum efficiencies up to 5.5%.[29],[30] These characteristics limit the use of Ru(II) complexes as chromophores and other iTMCs based on different metal centers offered a broader variety in emission color-tuning,[24] with Ir(III) being by far the most versatile metal utilized in LEECs.[31] The first LEEC based on an Ir(III)-iTMC was reported by Slinker et. al.[32] who investigated a single-layer device containing the yellow-emitting $[Ir(ppy)_2(\mathbf{3})][PF_6]$ (Hppy = 2-phenylpyridine, **3** = 4,4'-di-*tert*-butyl-2,2'-bipyridine) exhibiting a photoluminescence quantum yield (PLQY) of 23.5% in degassed CH_3CN solution (Figure 1.5).

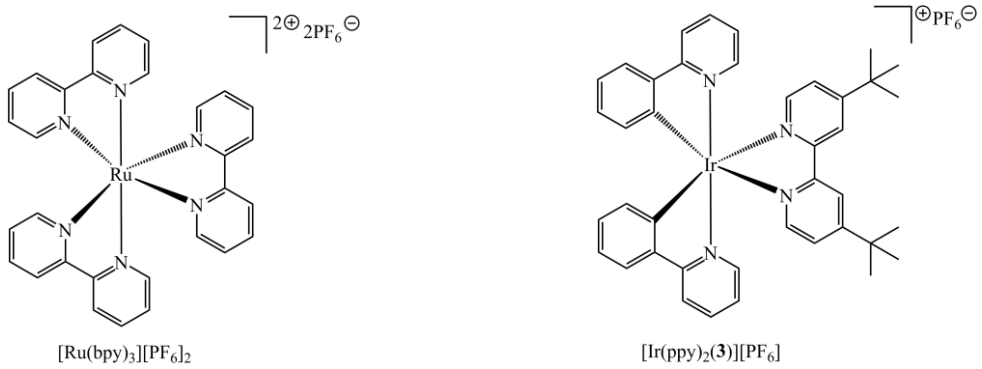

Figure 1.5 Structural formula of a Ru(II) and an Ir(III) based iTMC employed in LEEC devices: $[Ru(bpy)_3][PF_6]_2$ and $[Ir(ppy)_2(\mathbf{3})][PF_6]$.

When going from Ru (a second-row) to Ir (a third-row transition metal) the physical and chemical properties change significantly and are uniquely combined in a way such that a huge family of stable cyclometallated Ir(III) compounds can be synthesized covering the whole visible emission range from blue to red.[33]

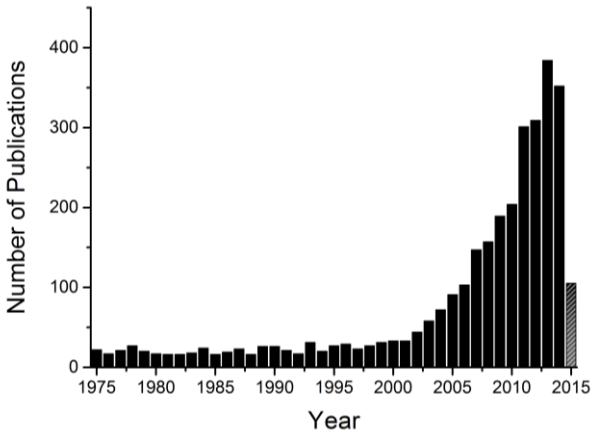

Figure 1.6 Number of publications dealing with the luminescence of iridium(III) complexes found on SciFinder® (updated March 15. 2015).

Figure 1.6 highlights the rise of iridium after 2000 where the number of publications per year rapidly increases. In this diagram, one may easily notice that over 80% of the known luminescent (mostly cyclometallating) Ir(III) complexes have been reported in the last 15 years.

1.3.1 The Ir(III) Metal Center in Octahedral Coordination

The Ir(III) metal center has a low-spin $5d^6$ electron configuration whose degenerate d orbitals split in an octahedral ligand field into three stabilized t_{2g} (d_{xy}, d_{xz}, d_{yz}) and two destabilized e_g orbitals (d_{z^2}, $d_{x^2-y^2}$) by an amount of Δ_o (Figure 1.7a). The value of Δ_o depends on 1) the oxidation state of the metal center, i.e. the greater the oxidation state the greater the splitting; 2) the orbital size: Δ_o increases on passing from 3d to 4d and 5d metals; 3) the field strength exerted by the ligands wherein a negatively charged ligand such as the cyclometallating ligand $[ppy]^-$ causes one of the strongest effects according to the spectrochemical series. In summary, the Ir(III) complexes exhibit a high Δ_o because of being high oxidation state, third-row transition metal cations coordinating very strong-field anionic cyclometallating ligands. As a consequence, the Ir(III) metal center always has a low-spin ($t_{2g}^6 e_g^0$) electron configuration. The ligand field stabilization energy is so large that Ir(III)-iTMCs are generally extraordinarily stable and nearly inert to ligand substitution reactions.

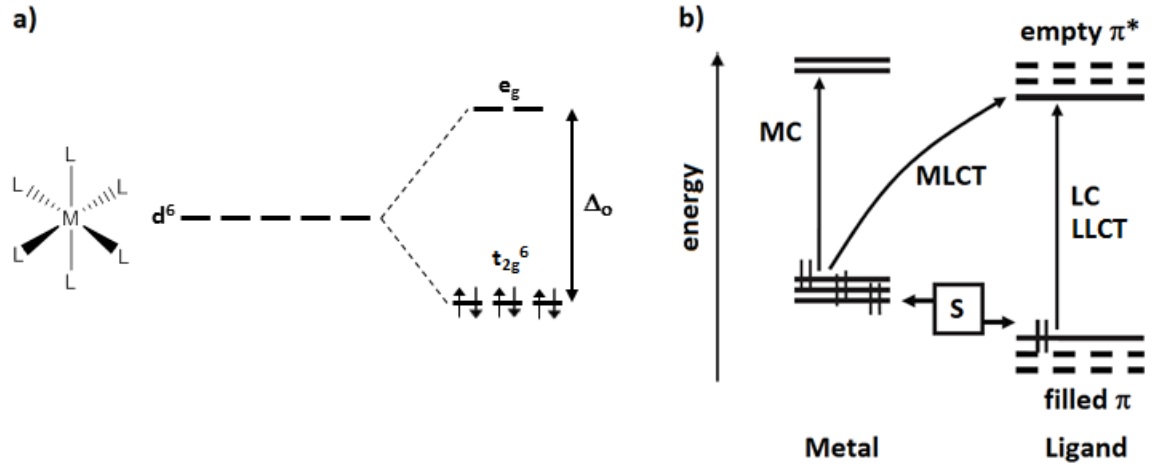

Figure 1.7 (a) Low-spin d^6 orbital configuration in an octahedral ligand field. (b) Orbital description of MC, MLCT, and LC transitions; S is a substituent group capable of exerting electron withdrawing or releasing effects (resulting in stabilization or destabilization, respectively, of the energy level of the filled d or π-orbitals).[31]

Figure 1.7b illustrates in a simple scheme the metal center and ligand orbitals between which possible electronic transitions can occur when an Ir(III)-iTMC is excited. Upon light absorption, an electron is transferred from the ground state to the excited state, mostly involving singlet metal-centered (^{1}MC), ligand-centered (^{1}LC), metal-to-ligand charge transfer (^{1}MLCT) or ligand-to-ligand charge transfer (^{1}LLCT) transitions. Furthermore, ligand-to-metal charge transfers (LMCT) can in principle also occur. Various substituent groups, attached to the ligands (indicated as S in Figure 1.7b), can either have a stabilization or destabilization effect on the energy level of the filled d or π-orbitals of the metal

and the ligands, respectively. The emission typically arises from triplet levels of ^{3}LC, ^{3}MLCT or ^{3}LLCT (not shown) nature (see Figure 1.8) as a consequence of the high spin-orbit coupling constant of iridium (ζ = 3909 cm^{-1}). This results in an efficient spin-forbidden intersystem crossing (ISC) from singlet to triplet excited states yielding a phosphorescence emission with the exception of the non-radiatively relaxing ^{3}MC states.

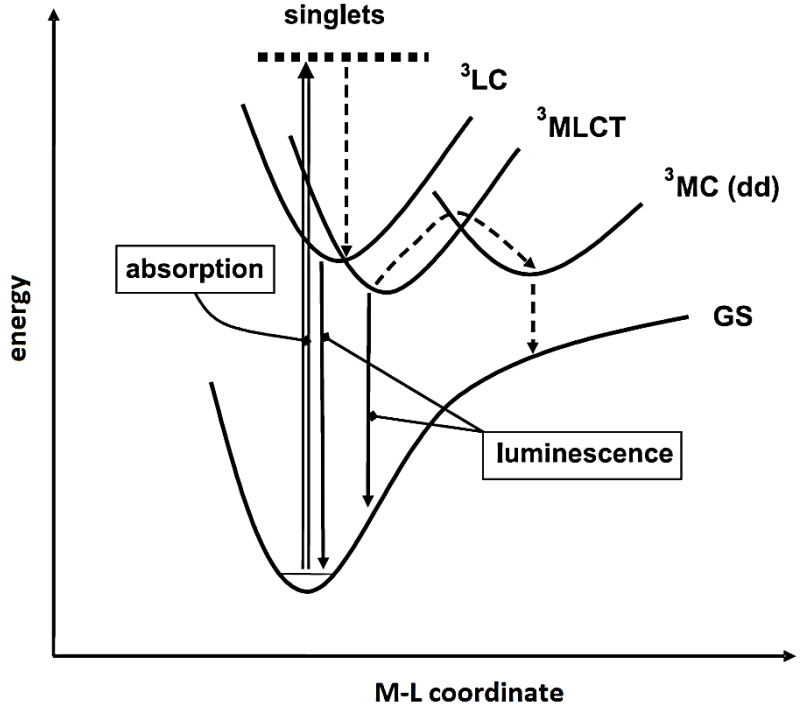

Figure 1.8 Electronic transitions upon light absorption into singlet excited states. The dashed arrows indicate non-radiative relaxations as it is observed for ^{3}MC states.[31]

There are other transition metal ions such as Os(II), Ru(II) and Fe(II) (in the presence of particular ligands) exhibiting the same low-spin d^6 electron configuration as Ir(III). However, the photophysical properties of their complexes cannot compete with the variable color-tunability, high PLQYs and photostability of Ir-iTMCs. The limitations of complexes of each of these other metals are as follows:

– Fe(II): 3d^6 configuration, the splitting of Δ_o is very small, therefore the lowest excited state is of non-emissive ^{1}MC nature.[31]

– Ru(II): 4d^6 configuration, the splitting of Δ_o is increased and the lowest excited state is an emissive ^{3}MLCT lying relatively close to the ^{3}MC level which can be thermally populated resulting in a competitive non-radiative deactivation pathway to either the GS or to degradation products. Hence the PLQYs of Ru(II) complexes increase upon cooling.[34]

– Os(II): 5d^6 configuration, the splitting of Δ_o is further increased and the ^{3}MC states are usually too high to be involved in the emission properties, but the lowered ^{3}MLCT excited state compared to Ru(II) shifts the emission bands towards the red or even infra-red region. Such emission favors non-radiative pathways yielding PLQYs typically below 1-2%.[35],[36]

1.3.2 Emission Color-tuning

Theoretical calculations reveal that the HOMO in Ir(III)-iTMCs consists mainly of a mixture of Ir dπ orbitals (t_{2g}) and phenyl π orbitals of the cyclometallating (C^N) ligands, whereas the LUMO is primarily localized on the ancillary (N^N) ligand (Figure 1.9a). The emitting T_1 triplet state is therefore usually of a mixed ^{3}MLCT/^{3}LLCT character.

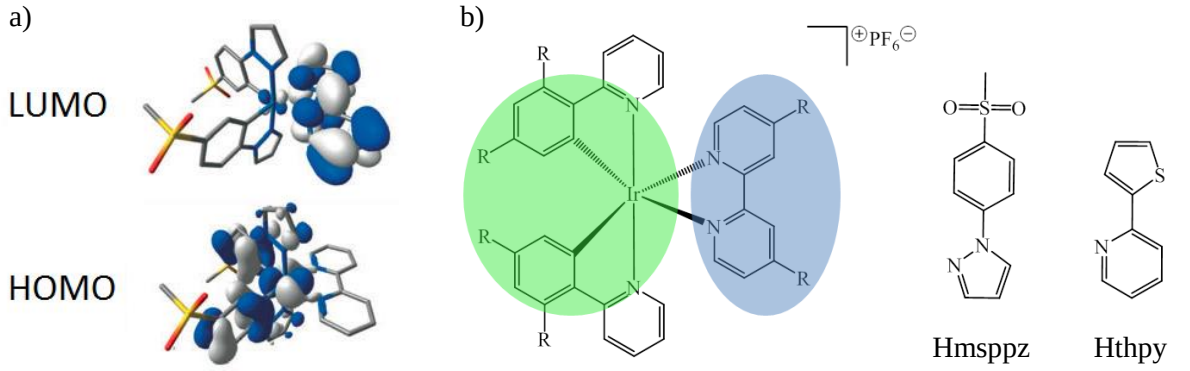

Figure 1.9 a) Schematic representation showing the electron density contours calculated for the HOMO and LUMO of $[Ir(msppz)_2(\mathbf{1})]^+$ (**1** = 2,2'-bipyridine), hydrogen atoms have been omitted.[37] b) Molecular structure of a typical Ir(III)-iTMC with the locations of the HOMO (green) and LUMO (blue) and examples of cyclometallating ligands.

The spatial separation of the HOMO and LUMO allows an almost independent color-tuning strategy. Attaching substituents onto the phenyl ring of the C^N ligand allows HOMO tuning and/or modifications on the N^N ligands enable LUMO tuning (Figure 1.9b). Thereby electron-withdrawing substituents (such as F, CF_3, SO_2CH_3) attached to the cyclometallating ligands result in a stabilization of the HOMO, whereas electron-donating substituents to the ancillary ligand (such as NMe_2, $C(CH_3)_3$) destabilize the LUMO. Consequently, the energy gap is enlarged leading to a blue-shifted emission. In addition to the archetype $[ppy]^-$ domain, other aryl compounds with a C^N coordination ability can be used as C^N ligands (e.g Hthpy or Hmsppz discussed in Chapter 2 and Chapter 3). A further strategy, which is not part of this study, is the investigation of other diimine ancillary ligands differing from the prototypical bpy unit.[8],[38]

1.4 Performance Optimization of LEEC Devices

As described in Section 1.2, a LEEC in its simplest form consists of a solution-processed single active iTMC layer sandwiched between a transparent (ITO) and an air-stable reflecting (typically Al, Au or Ag) electrode. Since the early prototype devices, several modifications were investigated leading to optimized device performances. Nowadays, most LEECs reported consist of one or two active layers but prior to it, a hole injection layer (normally PEDOT:PSS = [poly(3,4-ethylendioxythiophene) :polystyrenesulfonate)] is deposited onto the ITO anode to smoothen its surface increasing the reproducibility. Often an ionic liquid (IL) is mixed into the active layer whose effects will be

discussed in Section 1.4.2. Even with these two additives, the architecture of a LEEC remains much simpler than that of OLEDs.

1.4.1 Figures of Merit and Operation Mode

In order to characterize the device performance of a LEEC, the following figures of merit are widely applied and are important:[8]

– *Luminance* (*L*), defined as the flux of light emitted by the device, measured in candela per surface unit (cd m^{-2})

– *Current density* (*J*), given as the flux of current through the device, measured in ampere per surface unit (A m^{-2}).

– *Turn-on time* (t_{on}), taken as the time to reach the maximum luminance.

– *Lifetime* ($t_{1/2}$), set as the time to reach half of the maximum luminance.

– *Efficacy* (or current efficiency), corresponds to the emitted light per electric flux, measured in candela per ampere (cd A^{-1}), reported for the maximum observed.

– *Power efficiency*, describes the flux of light per electric input, measured in lumen per electric watt (lm W^{-1}) which is reported for the maximum value observed for a given device.

– *External quantum efficiency* (EQE), calculated as the ratio of photons emerging the device per injected electron. The EQE can also be defined through the equation EQE = $b\phi/2n^2$, where *b* is the recombination efficiency (equal to unity for two ohmic contacts[39]), ϕ is the fraction of excitons decaying radiatively and *n* is the refractive index of the glass substrate and is equal to 1.5 (the factor $1/2n^2$ accounts for the light outcoupling of the device).

Most LEECs are characterized by applying a fixed voltage while monitoring the current density and luminance over a period of time. Thereby, first a rise of the current density and the luminance is observed followed by a decay of the luminance after it has reached the maximum (within a few minutes to days). Rudmann and co-workers demonstrated the benefits of applying a pulsed voltage driving mode[40] and of exerting an initial high voltage when operating with a constant voltage.[30] Both methods were tested for Ru(II) based iTMCs. Tordera et. al.[41] combined these two techniques and adapted this finding for Ir(III)-iTMCs based LEEC devices driven with a block-wave pulsed current at a frequency of 1000 Hz and a 50% duty cycle at an averaged current density (reaching subseconds t_{on}). The latter driving scheme is also applied for all devices discussed in this work and a typical trend of the luminance, average voltage and efficacy of an operating LEEC is depicted in Figure 1.10.

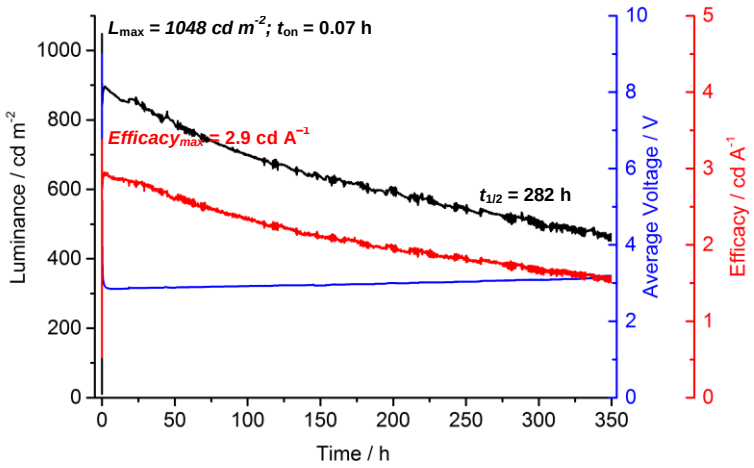

Figure 1.10 Typical trend of the luminance (black), average voltage (blue) and efficacy (red) of an Ir(III)-iTMC based LEEC driven with a block-wave pulsed driving mode.

Initially in Figure 1.10, an elevated voltage (9 V) is required to overcome the high initial barriers for the electron and hole injection to keep the applied current density constant. As soon as ionic motion is induced, the average voltage rapidly drops (to ≈ 3 V) to maintain the bulk carrier transport whereas the luminance starts to increase (in this case relatively fast) reaching a maximum of 1048 cd m^{-2} after 0.07 h = 4.2 min). As a consequence of the decreasing luminance the efficacy follows the same trend with a maximum value of 2.9 cd A^{-1}. Finally the device lifetime for this example is reached at 282 h.

1.4.2 Turn-on Time, Ionic Liquids and Device Efficiency

Besides the operating mode (discussed in Section 1.4.1) other parameters such as adding ionic liquids, chemical modifications of the iTMCs or blending with inert polymers have a significant effect on the turn-on time and the device efficiency. A key factor to reduce the turn-on time is the promotion of electronic charge injection into a LEEC. Therefore, in order to achieve applicable turn-on times, the low solid state ionic conductivity of an iTMC has to be increased. Zysman-Colman and co-workers[42] synthesized a number of Ir(III) complexes with a charged substituent (triethylammonium hexafluoridophosphate) attached to the 5-position of the N^N ligand whereby a dramatic decrease of t_{on} (from 140 to < 15 min) could be achieved. Similarly, Su et. al. obtained a reduction of t_{on} (by a factor of 2.5) by a peripherial modification of the N^N ligand which does not affect the photophysical properties of the pristine complex.[43] Further progress has been made using counter-anions smaller than $[PF_6]^-$, such as $[BF_4]^-$ or $[ClO_4]^-$.[30],[44] Also beneficial for turn-on times is the addition of an ionic liquid such as [BMIM][PF_6][45],[46] (1-butyl-3-methylimidazolium hexafluoridophosphate) which is almost uniquely reported for LEEC devices, although a huge existing market for alternative ionic liquids. Often all these advantageous conditions in terms of turn-on times, lead to a disadvantageous behavior of the device efficiency and stability.

The efficiency of a LEEC device can be analyzed by the efficacy (cd A^{-1}), the power efficiency (lm W^{-1}) or the EQE. Early studies of Ru(II)-iTMCs showed elevated EQEs when the active layer was diluted with an inert PMMA (polymethylmethacrylate) polymer preventing the concentrated solid state emitting layer from exciton hopping and hence emission quenching. This leads to reduced ionic mobility, requiring higher driving voltages, and subsequently to decreased power efficiencies. Bulky substituents such as methyl or ^{t}Bu groups on the N^N ligand,[32] on the C^N ligands[47] or intrinsic bulky diimine ligands[48] showed an increased EQE whereby non-radiative pathways are suggested to be suppressed due to reduced concentration quenching effects. This approach is limited to a certain size of the bulky groups as the driving voltage tends to increase upon the higher intermolecular separation.[49],[50],[51]

1.4.3 Stability

The stability of a LEEC device (described as $t_{1/2}$) is very important for potential applications and is related to the mobility of the charge carriers within the active layer. Another very important parameter is the intrinsic stability of an iTMC. Various investigations revealed the formation of water, moisture and solvent-induced degradation products severely limiting the robustness of the emitting compounds and acting as a photoluminescence quencher.[52],[53],[54],[55],[56] Most approaches to enhance the Ir(III)-iTMCs towards long-living LEEC devices focus on increasing the hydrophobicity of the complexes. Besides attaching hydrophobic bulky ^{t}Bu substituents, Graber et. al. first achieved $t_{1/2}$ lifetimes of thousands of hours upon the introduction of a pendant phenyl ring at the 6-position of a bpy ancillary ligand.[57] This design strategy of a hydrophobic cage formation wherein the pendant phenyl ring of the N^N ligand exhibits an intramolecular π-stacking interaction between the phenyl ring of the $[ppy]^-$ unit of the C^N ligand was adapted for various compounds.[58],[59] Extended studies attributed pyrazole-based Ir(III)-iTMCs[60] or different phenyl[61] or naphthyl[62] substituted diimine N^N ligands having comparable increasing effects on $t_{1/2}$.

Chapter 2

Chapter 2 Orange Emitters

2.1 Motivation

In the past, many cyclometallated complexes of the type $[Ir(ppy)_2(N^N)][PF_6]$ (where Hppy = 2-phenylpyridine and the N^N ligand is based on a 2,2'-bipyridine domain) have been reported by our group, all exhibiting photoluminescence maxima in the range 550–610 nm.[59],[63],[64],[65] A literature search revealed 2-(2'-thienyl)pyridine (Hthpy) to be a suitable alternative C^N ligand in cyclometallated Ir(III) complexes.[66],[67],[68],[69],[70] Furthermore, the change from C^N = $[ppy]^-$ to $[thpy]^-$ shifts the emission towards lower energy. Since the LEEC community is very interested in red-emitting complexes, $[Ir(thpy)_2(N^N)][PF_6]$ (where N^N = 6-phenyl-2,2'-bipyridine) was initially synthesized. Indeed, the photoluminescence maximum of the complex in an acetonitrile solution was remarkably red-shifted by about 50 nm (646 nm) compared to its $[ppy]^-$ analog (595 nm).[57]

A series of four new complexes of the type $[Ir(thpy)_2(N^N)][PF_6]$ (for N^N see Scheme 2.1) was synthesized. By changing the substituents attached to the ancillary ligand, the effect of (i) electron-withdrawing SMe, (ii) electron-donating ^{t}Bu and (iii) stabilizing phenyl groups on the photophysical and electrochemical behavior as well as their performances in LEEC devices were examined. The results were supported by theoretical calculations.

2.2 Synthesis and NMR Spectroscopic Characterization

The ligands 6-phenyl-2,2'-bipyridine[71] (**2**), 6-phenyl-4,4'-di-*tert*-butyl-2,2'-bipyridine[72] (**4**) and 4,4'-di(methylthio)-2,2'-bipyridine[73] (**6**) were synthesized according to the literature. The dimer $[\{Ir(thpy)_2(\mu\text{-}Cl)\}_2]$[66],[69],[74] was prepared by the general method reported by Nonoyama.[75] The complexes of the type $[Ir(thpy)_2(N^N)][PF_6]$ were synthesized according to the established literature procedure[76] by reacting the $[\{Ir(thpy)_2(\mu\text{-}Cl)\}_2]$ dimer with two equivalents of the respective N^N ligand followed by the exchange of the counter-ion with NH_4PF_6 (Scheme 2.1). After purification by chromatographic columns, yields of 64 to 84% could be achieved.

The room temperature solution ^1H and ^{13}C NMR spectroscopic assignments of this series of complexes were done by using the 2D standard methods (COSY, NOESY, HMQC and HMBC). The introduction of the pendant phenyl substituent in the N^N ligands **2** and **4** lowers the symmetry compared to the C_2-symmetric $[Ir(thpy)_2(N^N)]^+$ complexes coordinating **3** and **6**, leading to an inequivalence of the $[thpy]^-$ C^N ligands. Nevertheless, considering all four sets of signals the total assignment was achieved and a ring labelling system allowed a direct comparison of all chemical shifts (Scheme 2.1).

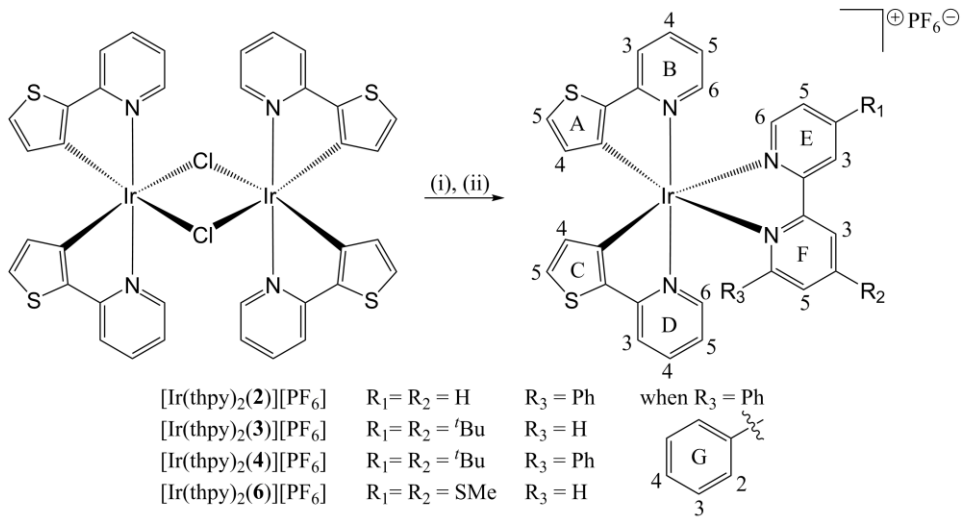

Scheme 2.1 Atom labelling for NMR spectroscopic assignments and synthetic pathway for the preparation of the complexes. Conditions: (i) **2**, **3**, **4** or **6** in MeOH, microwave reactor, 2 h, 120 °C. (ii) excess NH_4PF_6.

The aromatic regions of the ^{1}H NMR spectra of the two symmetric compounds [Ir(thpy)$_2$(**3**)][PF_6] and [Ir(thpy)$_2$(**6**)][PF_6] are depicted in Figure 2.1. A NOESY cross-peak between H^{E6} and H^{A4} allowed to distinguish the doublets of the thienyl protons H^{A4} and H^{A5}. These findings are underlined by the structural data of [Ir(thpy)$_2$(**6**)][PF_6] (Figure 2.5) where the $H^{E6}\cdots H^{A4}$ separation of 3.6 Å is significantly lower compared to 4.6 Å for $H^{E6}\cdots H^{A5}$. The change of the substituents from ^{t}Bu in [Ir(thpy)$_2$(**3**)][PF_6] to SMe in [Ir(thpy)$_2$(**6**)][PF_6] significantly shifts only the signals of the N^N ligand.

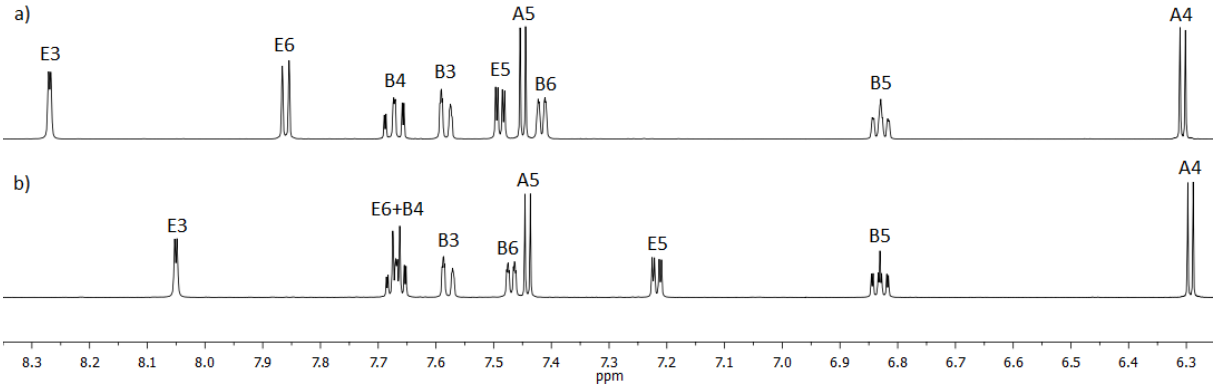

Figure 2.1 Room temperature 500 MHz ^{1}H NMR spectra of the aromatic region of a) [Ir(thpy)$_2$(**2**)][PF_6] and b) [Ir(thpy)$_2$(**6**)][PF_6] in CD_2Cl_2 solutions.

As mentioned above, the introduction of the pendant phenyl ring G desymmetrizes the spectra. The two different [thpy]$^-$ ligands in [Ir(thpy)$_2$(**2**)][PF_6] and [Ir(thpy)$_2$(**4**)][PF_6] could be distinguished starting with NOESY cross-peaks between the resonances of H^{E6} and H^{A4}, and H^{G4} and H^{C5} in order to differentiate between rings A and C. Furthermore, rings B and D could be assigned through the observation of a NOESY cross-peak between signals H^{G2} and H^{D6}. Structural data analysis of [Ir(thpy)$_2$(**2**)][PF_6] (Figure 2.7) reveals that the pendant phenyl ring G is positioned over the thienyl ring C. The centroid-to-centroid distance of 3.6 Å between rings G and C clearly shows the close through-space separation of these two aromatic systems.

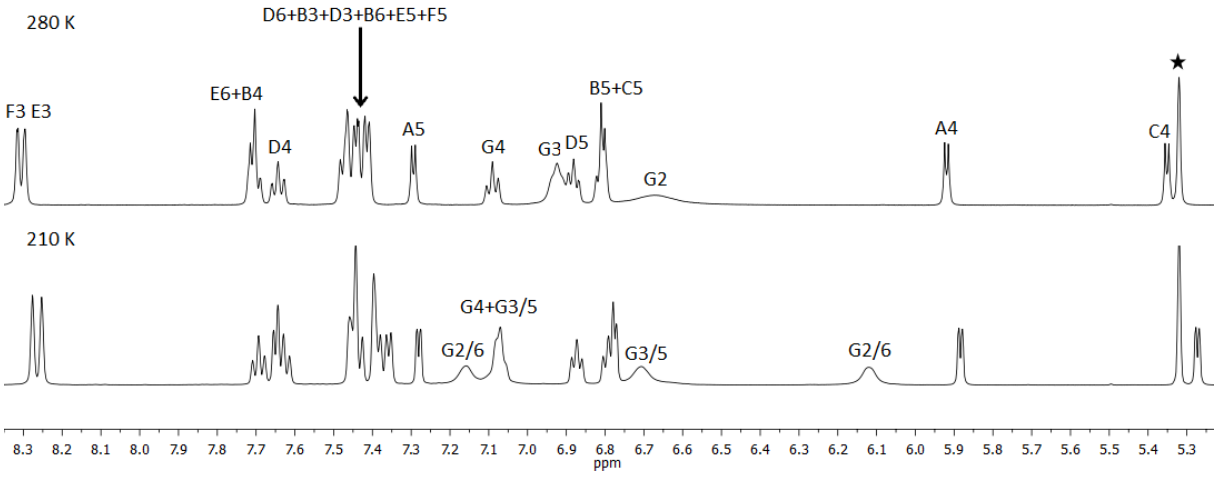

Figure 2.2 500 MHz ^{1}H NMR spectra of the aromatic region of [Ir(thpy)$_2$(**4**)][PF$_6$] in CD_2Cl_2 measured at 280 and 210 K. (* = residual solvent).

The signals H^{G2} and H^{G3} in [Ir(thpy)$_2$(**2**)][PF$_6$] at δ 6.67 and 6.92 ppm (FWHM ≈ 35 and 17 Hz, where FWHM = full width at half maximum) and in [Ir(thpy)$_2$(**4**)][PF$_6$] at δ 6.67 and 6.93 ppm (FWHM ≈ 28 and 17 Hz) are broad at room temperature due to a hindered rotation of the G ring on the NMR timescale. On cooling solutions of the compound, these broad signals start to lose intensity, collapse at 240 K and reappear split into four signals at 210 K (Figure 2.2). A COSY experiment at 210 K was needed to assign these resonances. Furthermore in a low temperature NOESY measurement, exchange cross-peaks (δ 7.16/6.12 and 7.08/6.71 ppm) in [Ir(thpy)$_2$(**4**)][PF$_6$] could be recorded, which is consistent with the phenomenon of the rotating phenyl ring G (Figure 2.3). These off-diagonal spin exchange responses refer to the slow conformational change of H^{G2} and H^{G6} as well as for H^{G3} and H^{G5} (the signal of $H^{G3/5}$ at 7.08 ppm overlaps with the resonance of H^{G4}).

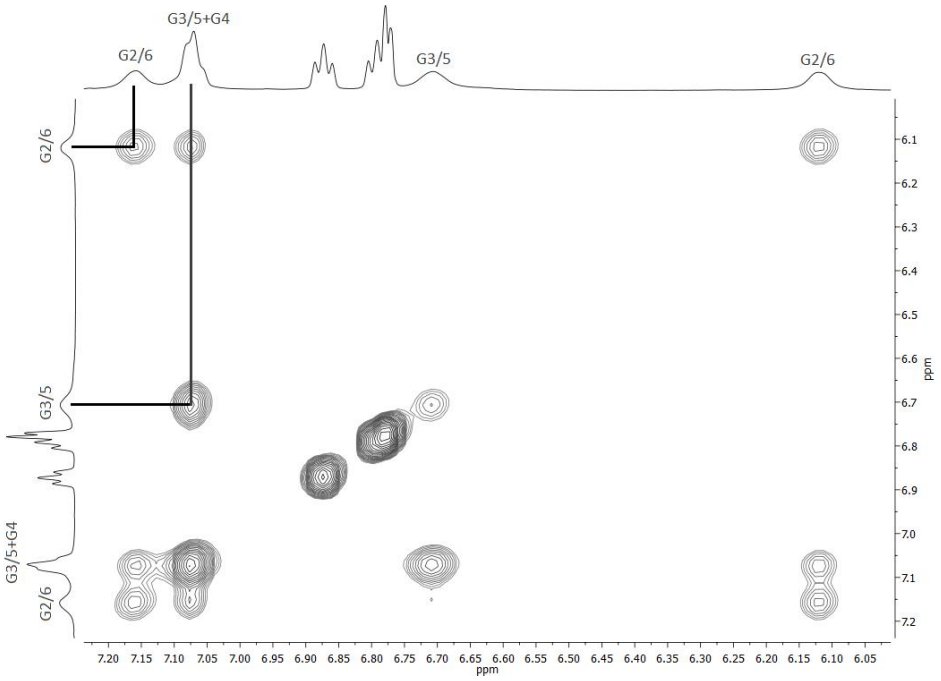

Figure 2.3 Part of the 500 MHz NOESY NMR spectrum of [Ir(thpy)$_2$(**4**)][PF$_6$] in CD_2Cl_2 at 210 K.

Contrary to the ^{1}H NMR spectra in which one can see a variation in chemical shifts for specific protons, the resonances for the specific ^{13}C nuclei have consistent trends in the ^{13}C NMR spectra throughout the [Ir(thpy)$_2$(N^N)][PF$_6$] series. Using this fact, the more complex NMR spectra of the asymmetric complexes [Ir(thpy)$_2$(**2**)][PF$_6$] and [Ir(thpy)$_2$(**4**)][PF$_6$] could be assigned with a verified accuracy.

2.3 Crystal Structures

The ancillary ligands **2**, **3**, **4** and **6** are already known in the literature (see Section 2.2) but a crystal structure of **6** was not previously reported. Crystals were grown from a $CDCl_3$ solution of **6** by slow evaporation of the solvent.

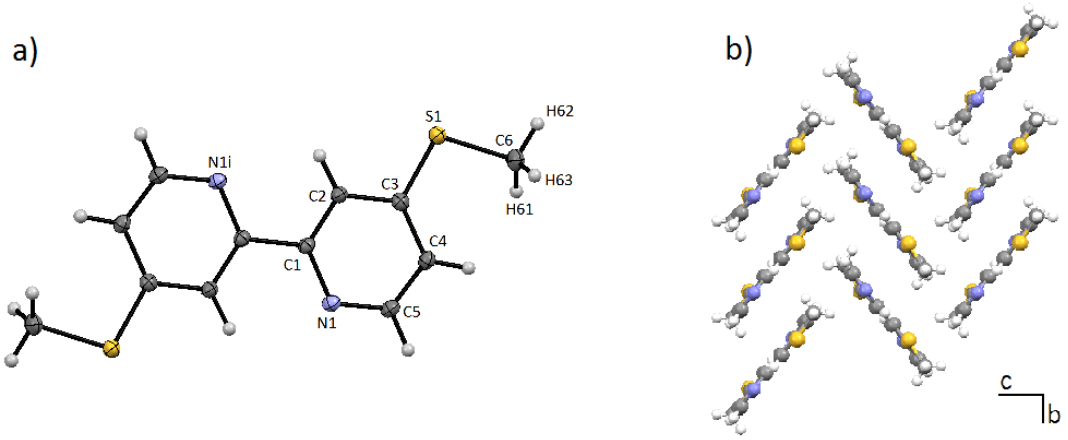

Figure 2.4 a) ORTEP representation of the crystal structure of ligand **6**, ellipsoids plotted at the 50% probability level. Symmetry code i = –x, –y, –z. Crystallographic data: $C_{12}H_{12}N_2S_2$, M = 248.37, colourless block, monoclinic, space group $P2_1/n$, a = 8.5217(8), b = 5.3745(5), c = 12.8745(10) Å, β = 105.203(4)°, U = 569.01(9) Å^3, Z = 2, D_c = 1.450 Mg m^{-3}, μ(Mo-K$_\alpha$) = 0.439 mm^{-1}, T = 123 K. Total 8091 reflections, 1891 unique, R_{int} = 0.029. Refinement of 1424 reflections (73 parameters) with $I > 2\sigma(I)$ converged at final $R1$ = 0.0294 ($R1$ all data = 0.0369), $wR2$ = 0.0401 ($wR2$ all data = 0.0580), gof = 1.0768. CCDC 949191. b) Packing of molecules of ligand **6**.

The single crystal structure is highlighted in Figure 2.4a and possesses the expected trans-conformation. The S–C$_{Me}$ bonds lie in the plane of the centrosymmetric molecule. S–C bond distances (S1–C6 = 1.7944(14), S1–C3 = 1.7490(13) Å) together with the angle C6–S1–C3 = 104.30(6)° indicate sp^3 hybridized sulfur atoms with negligible extension of the π-electron density from the pyridine ring into the S1–C3 bond. Ligands feature a packing where stacked molecule domains are related to one another in a herring-bone pattern (Figure 2.4b). These stacked molecule domains involve face-to-face π-stacking of pyridine rings[77] containing N1 and N1ii (ii = −x, 1 − y, −z) whereas the distance between the planes is 3.23 Å and 3.92 Å between the centroids. Additionally, C$_{Me}$···N, CH$_{py}$···S and CH$_{py}$···π close contacts contribute to the packing pattern.

Single crystals of 2{[Ir(thpy)$_2$(**6**)][PF$_6$]}·CH$_2$Cl$_2$ were grown by slow evaporation of a CH$_2$Cl$_2$ solution of the complex. The structure of cation [Ir(thpy)$_2$(**6**)]$^+$ is shown in Figure 2.5. Important, but unremarkable, bond lengths and angles are reported in the figure caption. Structural data reveal that the cyclometallation occurred via a C^N coordination of the [thpy]$^-$ ligand.[68] Previous studies have documented that neutral Hthpy can also bind to iridium(I) as an N^S-donor.[66],[67],[68] The cyclometallating [thpy]$^-$ ligand containing N4 and S4 is disordered and has been modelled over two sites with occupancies of 81 and 19%, respectively. Also the [PF$_6$]$^-$ counter-ion is disordered and has been modelled over two sites of occupancies of 69 and 31%. Finally, a half-occupancy CH$_2$Cl$_2$ solvent molecule is disordered across a special position.

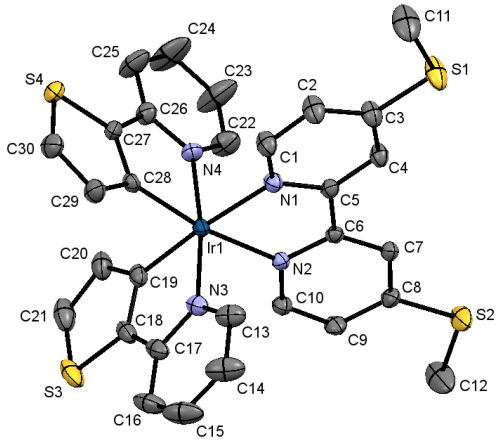

Figure 2.5 Structure of the cationic [Ir(thpy)$_2$(**6**)]$^+$ in 2{[Ir(thpy)$_2$(**6**)][PF$_6$]}·CH$_2$Cl$_2$ with ellipsoids plotted at the 40% probability level. H atoms, counter-ion and the solvent molecule are omitted for clarity and only the major occupancy for [thpy]$^-$ is shown. Summary of selected bond lengths [Å] and angles [°]: Ir1–N1 = 2.1294(15), Ir1–N2 = 2.1171(14), Ir1–N3 = 2.0601(16), Ir1–C19 = 2.0060(19), Ir1–N4 = 2.094(2), Ir1–C28 = 2.005(2), S1–C3 = 1.737(2), S1–C11 = 1.799(2), S2–C8 = 1.7421(18), S2–C12 = 1.801(3), S3–C21 = 1.709(3), S3–C18 = 1.725(2), S4–C30 = 1.719(3), S4–C27 = 1.723(2); N2–Ir1–N1 = 76.47(5), C28–Ir1–N4 = 78.84(9), C19–Ir1–N3 = 80.18(7), N3–Ir1–N4 = 171.65(8), C3–S1–C11 = 102.99(11), C8–S2–C12 = 102.16(11), C21–S3–C18 = 90.16(11), C30– S4–C27 = 90.55(12).

In Figure 2.5, only the major occupancy sites of the [Ir(thpy)$_2$(**6**)]$^+$ cation in 2{[Ir(thpy)$_2$(**6**)][PF$_6$]}·CH$_2$Cl$_2$ are shown; wherein H atoms, the [PF$_6$]$^-$ counter-ion as well as the solvent molecule are omitted for clarity. The [Ir(thpy)$_2$(**6**)]$^+$ cation features a near-octahedral geometry with a mutually trans-arrangement of the two nitrogen atoms of the C^N ligands. All three bidentate ligands are essentially planar. As already observed for ligand **6**, the S–C$_{Me}$ bonds lie in the plane of the N^N ligand with torsion angles of –4.3(2) and 1.7(2)° for C11–S1–C3–C2 and C12–S2–C8–C9, respectively. Packing interactions are dominated by primarily CH$_{py}$···S$_{thienyl}$ and CH···F contacts. Furthermore weak CH···π and SMe···π contacts also contribute to the packing but are not optimally directed. Generally it can be said that the molecular cations pack into two-dimensional sheets separated by sheets of [PF$_6$]$^-$ counter-ions. Each sheet lies in the *ab*-plane. Disordering of the solvent molecules makes it difficult to manifest their role in the packing pattern.

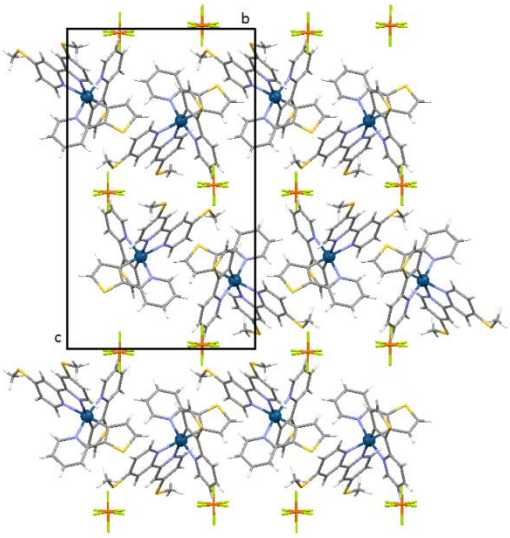

Figure 2.6 Packing in 2{[Ir(thpy)$_2$(**6**)][PF$_6$]}·CH$_2$Cl$_2$ built up of alternating cationic and anionic sheets. Solvent molecules are omitted for clarity.

By slow evaporation of a CH$_2$Cl$_2$ solution of the complex, single crystals of [Ir(thpy)$_2$(**2**)][PF$_6$] could be grown of X-ray quality. The structure of the [Ir(thpy)$_2$(**2**)]$^+$ cation and selected (unremarkable) bond lengths and angles are depicted in Figure 2.7a and its caption. As seen for [Ir(thpy)$_2$(**6**)]$^+$, the Ir1 atom is octahedrally sited with the expected trans-arrangement of the N-donors of the cyclometallating ligands, which are planar. In contrast, the pyridine units of ligand **2** are twisted by 14.1° which is most likely a consequence of the face-to-face π-stacking of the pendant 6-phenyl substituent G in **6** with the S2 atom containing thienyl unit of the C^N ligand (Figure 2.7b). The phenyl ring is twisted 70.1° with respect to the bonded pyridine ring. The centroid distance of the two π-stacking rings is 3.6 Å and the angle between the planes through the two mentioned rings is 12.1°. Such intentionally synthesized π-stacking sites were already reported in different examples by our group.[57],[58],[59],[60],[63],[78]

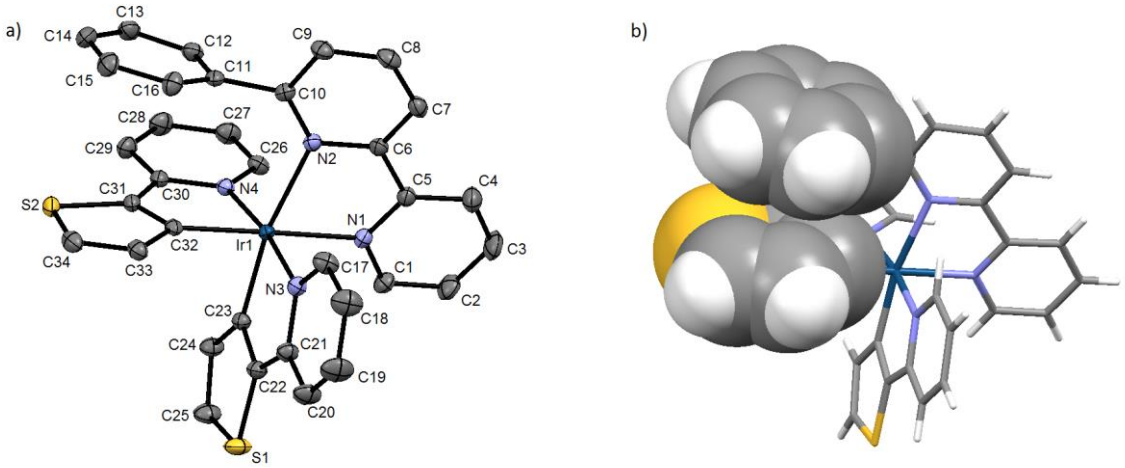

Figure 2.7 a) Crystal structure and atom labelling of the [Ir(thpy)$_2$(**2**)]$^+$ cation in [Ir(thpy)$_2$(**2**)][PF$_6$]. Ellipsoids are plotted at the 40% probability level with omitted H atoms and [PF$_6$]$^-$ anion. Selected bond lengths and angles: Ir1–C23 = 1.991(2), Ir1–C32 = 2.010(2), Ir1– N4 = 2.0430(18), Ir1–N3 = 2.0703(18), Ir1–N1 = 2.1260(18), Ir1–N2 = 2.1875(18) Å; N1–Ir1–N2 = 76.15(7), C32–Ir1–N4 = 80.11(8), C23–Ir1–N3 = 79.98(8), N4–Ir1–N3 = 172.06(7), C25–S1–C22 = 90.75(11), C34–S2–C31 = 90.45(11)°. b) Face-to-face π-stacking of the pendant phenyl ring G in ligand **2** with the thienyl unit of the C^N ligand.

The unit cell consists of a centrosymmetric pair of cations that packs with the pyridine rings containing N2 and N2i (symmetry code i = 1 − x, 1 − y, 1 – z) in a face-to-face arrangement. However, a distance between the ring planes of 4.03 Å is too large to be a significant π-stacking interaction. Main packing forces include C–H···S, C–H···F and C–H···$\pi_{pyridine}$ interactions.

Crystals were also grown of [Ir(thpy)$_2$(**4**)][PF_6] by slowly diffusing Et_2O into a CH_2Cl_2 solution of the complex. Unfortunately this gave only thin heavily twinned plates which were not of sufficient X-ray quality. The obtained data set was at least good enough to confirm the above discussed structure of a Ir(III) center with an octahedral coordination sphere consisting of two C^N cyclometallated [thpy]$^-$ in a trans arrangement with respect to the N atoms and the chelating N^N ligand **4**. Additionally, the face-to-face π-stacking of the phenyl ring of auxiliary ligand **4** with the thienyl domain of one cyclometallated ligand could be verified.

2.4 Electrochemical Properties

Cyclic voltammetric data for [Ir(thpy)$_2$(N^N)][PF_6] (N^N = **2-4**, **6**) are summarized in Table 2.1 and graphically displayed for [Ir(thpy)$_2$(**6**)][PF_6] as an example in Figure 2.8. The electrochemical processes are reversible unless otherwise stated.

Table 2.1 Cyclic voltammetric data referenced to Fc/Fc^+ include reversible processes unless otherwise stated (qr = quasi-reversible, irr = irreversible). The samples were measured in dry acetonitrile containing 0.1 M [^{n}Bu$_4$N][PF_6] as supporting electrolyte at a scan rate of 0.1 V s^{-1}.

Compound	$E_{1/2}^{ox}$ / V	$E_{1/2}^{red}$ / V	$\Delta E_{1/2}$ / V
[Ir(thpy)$_2$(**2**)][PF_6]	+0.72^{qr}, +1.21^{irr}	–1.77, –2.43^{irr}	2.49
[Ir(thpy)$_2$(**3**)][PF_6]	+0.74^{qr}, +1.26^{irr}	–1.85, –2.51^{irr}	2.59
[Ir(thpy)$_2$(**4**)][PF_6]	+0.73^{qr}, +1.28^{irr}	–1.82, –2.42^{irr}	2.55
[Ir(thpy)$_2$(**6**)][PF_6]	+0.74^{qr}, +1.28^{irr}	–1.73, –2.30^{irr}	2.47

The complexes exhibit a quasi-reversible oxidation arising from an Ir(III)-center based process with a substantial contribution from the C^N ligands followed by a second irreversible oxidation process assigned to the oxidation of the [thpy]$^-$ ligands. Therefore, all oxidation processes occur, not surprisingly, at similar potentials. The obtained values of $E_{1/2}^{ox}$ are comparable to literature data of +0.82 V for [Ir(thpy)$_2$(bpy)][PF_6] (quoted as +1.20 V vs. SCE in CH_2Cl_2, where bpy = 2,2'-bipyridine).[69] The effect of changing ancillary ligands is more distinct in the reduction processes. The first reduction process is assigned to the reversible reduction of the N^N ligands where $E_{1/2}^{red}$ shifts to more negative potentials upon the introduction of ^{t}Bu substituents whereas SMe groups lead to less negative values. As a consequence, the electrochemical gap is larger for [Ir(thpy)$_2$(N^N)][PF_6] (N^N = **3**, **4**) and slightly smaller for [Ir(thpy)$_2$(**6**)][PF_6] compared to [Ir(thpy)$_2$(**2**)][PF_6]. The second

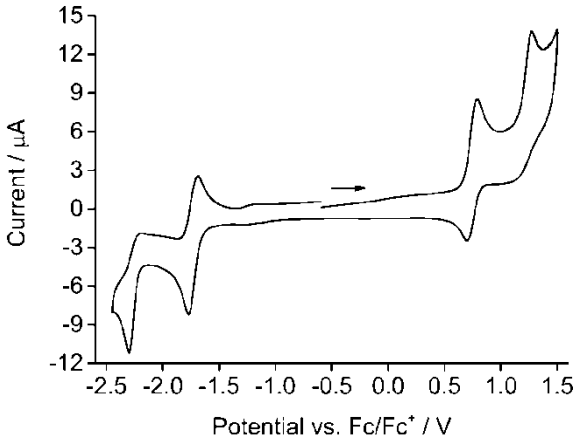

Figure 2.8 Cyclic voltammogram of [Ir(thpy)$_2$(**6**)][PF$_6$] with respect to Fc/Fc$^+$ (→ = direction of scan).

irreversible reduction process is localized on the [thpy]$^-$ ligands (see also theoretical calculations in Section 2.6).

2.5 Solution Photophysical Properties

The acetonitrile solution based UV-Vis absorption spectra of the four [Ir(thpy)$_2$(N^N)][PF$_6$] complexes are similar for all compounds and are depicted in Figure 2.9. They are dominated by intense high-energy bands between 275 to 279 nm arising from ligand-centered π* ← π and, in [Ir(thpy)$_2$(**6**)][PF$_6$], π* ← n transitions that extend into the visible region. The much stronger absorption intensity of the latter complex can be explained by the extension of the chromophoric π-system of the bpy domain due to the auxochromic SMe substituent. The less intense lower energetic absorption bands observed for each complex between 410 to 415 nm are related to MLCT transitions.

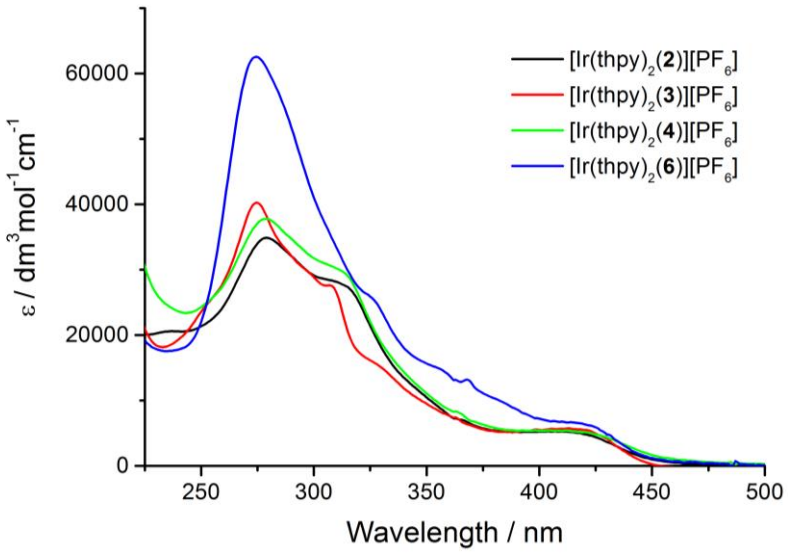

Figure 2.9 UV-Vis absorption spectra of [Ir(thpy)$_2$(N^N)][PF$_6$] (N^N = **2**-**4**, **6**) in 1.00 x 10^{-5} M CH$_3$CN solutions.

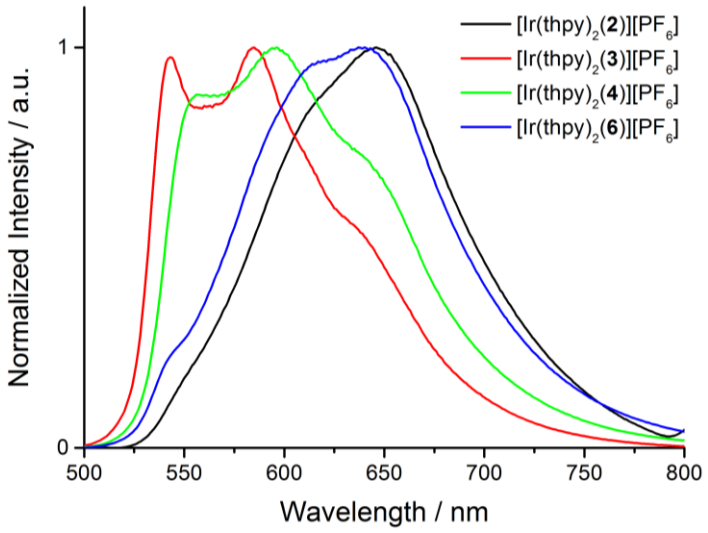

Figure 2.10 Normalized photoluminescence spectra of $[Ir(thpy)_2(N\text{^}N)][PF_6]$ (N^N = **2**-**4**, **6**) in 2.50 x 10^{-5} M CH_3CN solutions.

Figure 2.10 shows the emission spectra upon exciting into each compound's respective MLCT band. The emission maxima are listed in Table 2.2 and, as for the absorption, are comparable to the literature compound $[Ir(thpy)_2(bpy)]^+$ which has an emission maximum at 612 nm.[69] The attachment of electron-releasing ^{t}Bu substituents produces a blue-shifted emission of 543/585 nm for $[Ir(thpy)_2(\mathbf{3})][PF_6]$. Otherwise, insertion of the SMe substituent results in a red-shifted emission of 640 nm for $[Ir(thpy)_2(\mathbf{6})][PF_6]$. Comparing $[Ir(thpy)_2(\mathbf{3})][PF_6]$ and $[Ir(thpy)_2(\mathbf{4})][PF_6]$, a slight shift to lower energy (10 nm) is observed upon the additional 6-phenyl ring on ligand **3**. This is consistent with literature observations on going from $[Ir(ppy)_2(bpy)][PF_6]$ to $[Ir(ppy)_2(\mathbf{2})][PF_6]$ (ppy = 2-phenylpyridine) where the emission is red-shifted from 590 to 595 nm.[57]

The same ligand modification (i.e. the introduction of a 6-phenyl group in the N^N ligand) on going from $[Ir(thpy)_2(bpy)][PF_6]$ to $[Ir(thpy)_2(\mathbf{2})][PF_6]$ produces a more dramatic red-shift from 612 to 646 nm but the reason for this is not obvious. It is noteworthy that all complexes have a similar vibronically structured emission which is less well defined along the series starting with the complex

Table 2.2 Photophysical properties of $[Ir(thpy)_2(N\text{^}N)][PF_6]$ (N^N = **2**-**4**, **6**) in solution and diluted films (see Section 2.7).

Compound	Solution[a]				Diluted film[b]	
	λ_{ex} / nm	λ_{em}^{max} / nm	τ / ns	Φ / %	λ_{em}^{max} / nm	Φ / %
$[Ir(thpy)_2(\mathbf{2})][PF_6]$	410	646	19	≤ 1.0	553, 592	29
$[Ir(thpy)_2(\mathbf{3})][PF_6]$	415	543, 585	81	≤ 1.0	542, 585	42
$[Ir(thpy)_2(\mathbf{4})][PF_6]$	410	555, 595	64	≤ 1.0	553, 592	35
$[Ir(thpy)_2(\mathbf{6})][PF_6]$	415	640	33	≤ 1.0	542, 585	51

[a] Degassed 2.50 x 10^{-5} M CH_3CN solutions. [b] 5 wt% complex in a polymethylmethacrylate (PMMA) matrix.

coordinating N^N ligand **3** to **4**, **6** and finally **2**. Overall, the different appearance of the spectra seems to originate from the changing intensity of the respective vibronic features giving rise to the huge difference of the emission maxima. The reason for this could lie in the different rigidities of the complexes (see also theoretical calculations in Section 2.6 and low temperature emission spectra in Section 2.7). The low solution quantum yields for this set of complexes correspond to the data reported for $[Ir(thpy)_2(bpy)][PF_6]$ and $[Ir(thpyR)_2(bpy)][PF_6]$ (R = 5-Me or 5-CHO).[69]

2.6 Theoretical Calculations

More detailed insight into the electronic and photophysical properties of $[Ir(thpy)_2(N^N)][PF_6]$ (N^N = **2-4**, **6**) was provided by theoretical calculations carried out by José M. Junquera-Hernández and Juan J. Serrano-Pérez under the supervision of Enrique Ortí at the University of Valencia.[79] Combined DFT/TD-DFT theoretical calculations were performed at the B3LYP/(6-31G**+ LANL2DZ) level on the $[Ir(thpy)_2(N^N)]^+$ cations in the presence of acetonitrile solvent molecules. For additional comparison reasons, the $[Ir(thpy)_2(bpy)]^+$ cation was included into the calculation data set.

The ground electronic state (S_0) geometry of the complexes was fully optimized without imposing any symmetry constraints. In this way, the calculations correctly reproduce the near-octahedral coordination sphere of the Ir(III) metal center observed in the crystallographic studies and verify predicted geometric parameters in accordance with the experimental data. In the computational structures the $[thpy]^-$ ligands are also essentially planar and the averaged computed value for the bite angle of 79.5° is in good agreement with the X-ray data for $[Ir(thpy)_2(\mathbf{6})]^+$ (C28–Ir1–N4 = 78.8°, C19–Ir1–N3 = 80.2°; see Figure 2.5) and $[Ir(thpy)_2(\mathbf{2})]^+$ (C32–Ir1–N4 = 80.1°, C23–Ir1–N3 = 80.0°; see Figure 2.7). Planarity is also predicted for N^N ligands in $[Ir(thpy)_2(\mathbf{3})]^+$ and $[Ir(thpy)_2(\mathbf{6})]^+$ as well as the S–C_{Me} bonds to lie in the plane of the N^N ligand for the latter complex. More notably, the calculations for $[Ir(thpy)_2(\mathbf{2})]^+$ and $[Ir(thpy)_2(\mathbf{4})]^+$ suggest twisted angles between the two pyridine rings in the bpy domain of 18.4 and 20.9° being slightly larger than the 14.1° measured in the $[Ir(thpy)_2(\mathbf{2})]^+$ crystal structure. Face-to-face π-stacking of the pendant phenyl substituent with the adjacent thienyl ring of the cyclometallating ligand is verified, but the calculated centroid distances of the π-stacking rings are slightly overestimated in $[Ir(thpy)_2(\mathbf{2})]^+$ (3.77 Å) and $[Ir(thpy)_2(\mathbf{4})]^+$ (3.76 Å) compared to the crystallographic value for $Ir(thpy)_2(\mathbf{2})]^+$ (3.55 Å). The pendant phenyl ring is twisted by 61.9 and 60.4° in $[Ir(thpy)_2(\mathbf{2})]^+$ and $[Ir(thpy)_2(\mathbf{4})]^+$ deviating from the measured 70.1° in the crystal structure of $[Ir(thpy)_2(\mathbf{2})]^+$. Packing forces arising in the crystal might be the explanation for this small mismatch.

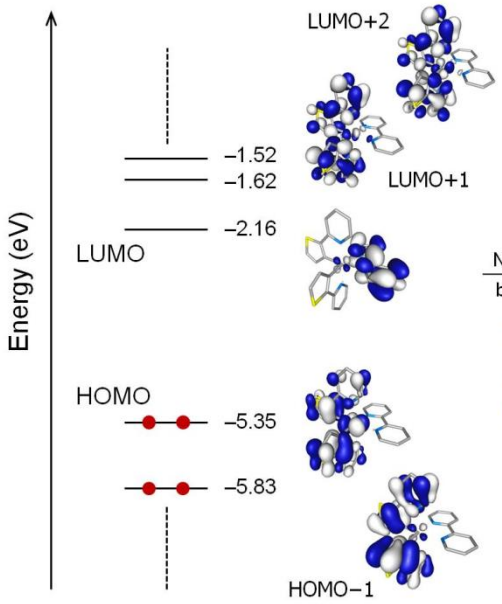

N^N	E_{HOMO} (eV)	E_{LUMO} (eV)
bpy	−5.35	−2.16
2	−5.37	−2.11
3	−5.33	−2.02
4	−5.34	−1.97
6	−5.34	−2.09

Figure 2.11 Schematic diagram showing the electron density contours (0.03 e bohr^{-3}) and energies calculated for the highest occupied and lowest unoccupied molecular orbitals of $[Ir(thpy)_2(bpy)]^+$; hydrogen atoms have been omitted. HOMO and LUMO energies for $[Ir(thpy)_2(N^N)]^+$ complexes are given in the table.[79]

The atomic orbital compositions calculated for the highest occupied (HOMO and HOMO−1) and lowest unoccupied (LUMO to LUMO+2) molecular orbitals of the $[Ir(thpy)_2(bpy)]^+$ cation are shown in Figure 2.11. All $[Ir(thpy)_2(N^N)][PF_6]$ (N^N = **2-4**, **6**) complexes possess identical distributions for these five molecular orbitals. In accordance with calculations performed for Ir(III) complexes based on $[ppy]^-$ cyclometallating ligands[8],[37],[47],[58],[80] the HOMO is comprised of Ir(III) dπ orbitals (t_{2g}), thienyl π orbitals together with some contribution from the C^N pyridine rings. The LUMO, on the other hand, corresponds to the π* orbitals of the N^N ligand. Thus, substitution on the ancillary ligand has a larger effect on the LUMO whilst the HOMO is almost unaffected. The effects of ^{t}Bu and pendant phenyl substituents on the bpy domain increases the energy level of the LUMO from −2.16 eV for $[Ir(thpy)_2(bpy)]^+$ to −2.02 eV in $[Ir(thpy)_2(\mathbf{3})]^+$ and to −1.97 eV for the combined effect in $[Ir(thpy)_2(\mathbf{4})]^+$. These effects correspond to the measured values for the first oxidation and reduction potentials in Section 2.4.

As can be seen for the representative complex cation $[Ir(thpy)_2(bpy)]^+$ in Figure 2.11, the HOMO−1 and the LUMO+1/LUMO+2 lie ~0.5 eV below and above the HOMO and LUMO, respectively, and are localized over the cyclometallating ligands. In principle, the lowest-energy triplet state can be expected to originate from the HOMO → LUMO excitation indicating an electron transfer from the Ir-thpy environment to the ancillary ligand. To further and more accurately investigate the nature of the emitting excited state, some low-lying triplet states (T_n) have been calculated using the optimized geometry of the ground state (S_0) and the time-dependent DFT (TD-DFT) approach.

Table 2.3 Summary of the three lowest triplet excited states calculated at the TD-DFT B3LYP/(6-31G**+LANL2DZ) level for complexes $[Ir(thpy)_2(N\text{^}N)]^+$ (N^N = bpy, **2-4** and **6**) in acetonitrile solution. Detailed characterization of vertical excitation energies (*E*), dominant monoexcitations with the respective contributions (within parentheses) greater than 15%, nature of the electronic transition and the description of the excited state are given.

N^N ligand	State	*E* / eV	Monoexcitations[a]	Nature[b]	Description[b]
bpy	T_1	2.37	H → L+1 (62) H–1 → L+2 (23)	$d_\pi(Ir)+ \pi_{C\text{^}N} \rightarrow \pi^*_{C\text{^}N}$ $\pi_{C\text{^}N} \rightarrow \pi^*_{C\text{^}N}$	^{3}LC/^{3}MLCT ^{3}LC
	T_2	2.41	H → L+2 (55) H–1 → L+1 (33)	$d_\pi(Ir)+ \pi_{C\text{^}N} \rightarrow \pi^*_{C\text{^}N}$ $\pi_{C\text{^}N} \rightarrow \pi^*_{C\text{^}N}$	^{3}LC/^{3}MLCT ^{3}LC
	T_3	2.51	H → L (94)	$d_\pi(Ir) + \pi_{C\text{^}N} \rightarrow \pi^*_{N\text{^}N}$	^{3}MLCT/^{3}LLCT
2	T_1	2.34	H → L+1 (50) H–1 → L+2 (19)		
	T_2	2.40	H → L+2 (42) H–1 → L+1 (35)		
	T_3	2.57	H → L (87)		
3	T_1	2.37	H → L+1 (64) H–1 → L+2 (24)		
	T_2	2.41	H → L+2 (56) H–1 → L+1 (33)		
	T_3	2.63	H → L (96)		
4	T_1	2.34	H → L+1 (49) H–1 → L+2 (20)		
	T_2	2.39	H → L+2 (43) H–1 → L+1 (34)		
	T_3	2.67	H → L (86)		
6	T_1	2.37	H → L+1 (65) H–1 → L+2 (23)		
	T_2	2.41	H → L+2 (55) H–1 → L+1 (33)		
	T_3	2.58	H → L (96)		

[a] H and L stand for HOMO and LUMO. [b] Nature and description of the monoexcitations are identical for all complexes and are only tabulated for $[Ir(thpy)_2(bpy)]^+$.

An overview of the vertical excitation energies, their nature and the detailed electronic descriptions for the three lowest triplet excited states of all complexes is given in Table 2.3. According to TD-DFT calculations, the T_1, T_2 and T_3 states are all predicted to be at similar energies between 2.34 and 2.67 eV for every complex. Surprisingly, the T_1 and T_2 states mainly originate from transitions from the HOMO−1 and HOMO to the LUMO+1 and LUMO+2 and are described as ligand-centered (^{3}LC) triplets. This follows, since primarily the $[thpy]^-$ orbitals are involved in these transitions with additional metal-to-ligand charge transfer (^{3}MLCT) character due to the participation of the Ir(III) center in the HOMO (Figure 2.11). The expected HOMO → LUMO transition with a contribution of ~90% is computed for the T_3 state lying slightly higher in energy (0.10–0.27 eV). It is composed of metal-to-ligand and ligand-to-ligand charge transfers (^{3}MLCT/^{3}LLCT).

Further optimization of the three lowest triplet state geometries using the spin-unrestricted UB3LYP approach allowed comparison of the adiabatic energy differences with respect to the ground state. Therefore the electronic energy difference between the ground and the excited state at their respective

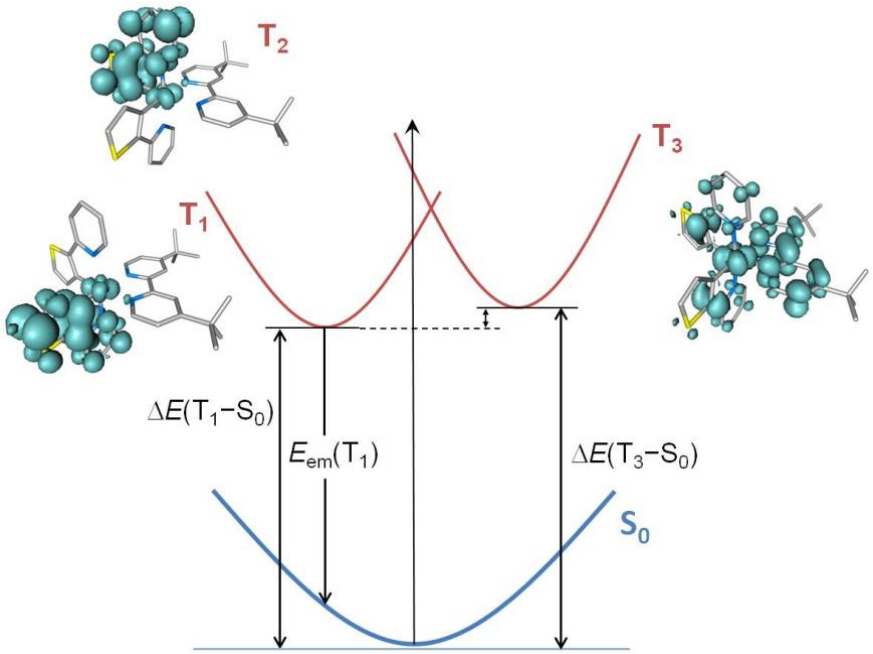

Figure 2.12 Schematic representation of the ground state (S_0) and the first triplet states (T_1–T_3, where T_2 is mainly degenerate with T_1) calculated for $[Ir(thpy)_2(\mathbf{3})]^+$ with their respective spin-density distributions (0.003 e bohr^{-3}).[79]

equilibrium geometries could be calculated and the relative energy and electronic states for $[Ir(thpy)_2(\mathbf{3})]^+$ as a representative compound are shown in Figure 2.12.

Full-geometry relaxation predicts degenerate T_1 and T_2 states (2.2379 and 2.2382 eV above S_0, respectively) and remain lower in energy than the T_3 state ($\Delta E(T_3–S_0)$ = 2.42 eV). The dominant ^{3}LC character with minor contribution of the Ir(III) metal center of state T_1 is confirmed by unpaired-electron spin-density distribution computed for the optimized geometry of T_1 in $[Ir(thpy)_2(\mathbf{3})]^+$ (Ir: 0.15e, thpy1: 1.83e, thpy2: 0.01e, **3**: 0.01e). Almost identical electronic nature could be calculated for the T_2 state just with the spin density distributed over the other $[thpy]^-$ ligand. The spin-density obtained for T_3 perfectly agrees with the HOMO → LUMO excitation underpinning the mixed ^{3}MLCT/^{3}LLCT character of this state (compare Figure 2.11 and Figure 2.12). These findings were also valid for the other three complexes with N^N ligands **2**, **4** and **6**.

Table 2.4 Comparison of the adiabatic energy differences (ΔE, in eV) and vertical emission energies (E_{em}, in nm) calculated at the TD-DFT B3LYP/(631G**+LANL2DZ) level for $[Ir(thpy)_2(N^N)]^+$ (N^N = bpy, **2**-**4** and **6**).

Compound	ΔE (T_1–S_0) / eV	ΔE (T_3–S_0) / eV	E_{em} (T_1) / nm
$[Ir(thpy)_2(bpy)]^+$	2.24	2.27	641
$[Ir(thpy)_2(\mathbf{2})]^+$	2.21	2.29	652
$[Ir(thpy)_2(\mathbf{3})]^+$	2.24	2.42	641
$[Ir(thpy)_2(\mathbf{4})]^+$	2.21	2.35	650
$[Ir(thpy)_2(\mathbf{6})]^+$	2.24	2.33	642

Geometry optimization at the TD-DFT level gave further insight into the relative ordering of the lowest-energy triplets. The ^{3}MLCT/^{3}LLCT triplet (T_3) of $[Ir(thpy)_2(\mathbf{3})]^+$ was verified to lie 0.18 eV above the ^{3}LC states T_1 and T_2, and can be explained by solvent effects stabilizing the latter two states more strongly due to their higher polarity. As an example, the ground state dipole moment of $[Ir(thpy)_2(\mathbf{3})]^+$ (12.70 D) is almost unaffected in passing to the ^{3}LC states (12.04 D) because these states imply no special charge transfer. When passing from S_0 to the ^{3}MLCT/^{3}LLCT triplet the dipole moment drastically decreases to 3.08 D because the charge transfer mostly compensates the charge separation. As a consequence, polar solvents like acetonitrile stabilize the ^{3}LC states in a larger degree compared to T_3. Therefore T_1 and T_2 become the lowest energy triplets from where the emission originates. This prediction is in good agreement with the structured emission band recorded for the room temperature solution spectra (Figure 2.10) and further explains the experimentally determined low PLQY in solution (Table 2.2).

Single-point calculations of S_0 at the optimized minimum energy of the T_1 triplet were used to compute the vertical energy difference between these two states and thus the emission energy was estimated. Similar vertical emission energies of ~1.90 eV were calculated for all complexes corresponding to 641–652 nm in Table 2.4. These values match with the experimental data obtained for $[Ir(thpy)_2(\mathbf{2})]^+$ (646 nm) and $[Ir(thpy)_2(\mathbf{6})]^+$ (640 nm) but differ remarkably from the blue-shifted emissions for complex $[Ir(thpy)_2(\mathbf{3})]^+$ and $[Ir(thpy)_2(\mathbf{4})]^+$ with maxima around 550 and 590 nm (Table 2.2). On closer inspection, all the spectral components for $[Ir(thpy)_2(\mathbf{2})]^+$ and $[Ir(thpy)_2(\mathbf{6})]^+$ are also present in the spectra of $[Ir(thpy)_2(\mathbf{3})]^+$ and $[Ir(thpy)_2(\mathbf{4})]^+$, just with different relative intensities. These findings strongly support the vibronic nature for the emission of all members of this series of complexes.

2.7 Thin-film Photophysical Properties and Device Data

Cationic Ir(III) complexes are not in solution when applied in LEECs and therefore, two different approaches to consider their photophysical properties immersed in thin films were examined. First, the $[Ir(thpy)_2(N^N)][PF_6]$ (N^N = **2-4**, **6**) complexes were analyzed as a 5 wt% dispersion in a PMMA matrix. Secondly, the complexes were diluted with an ionic liquid $[BMIM][PF_6]$ in a 4:1 molar ratio to mimic the typical film configuration of the active layer in a LEEC device.

The photoluminescence spectra of the PMMA films containing the complexes are shown in Figure 2.13 and the respective emission maxima and PLQYs are listed in Table 2.2. The different environment in PMMA films compared to CH_3CN causes a huge blue-shift for compounds $[Ir(thpy)_2(\mathbf{2})][PF_6]$ and $[Ir(thpy)_2(\mathbf{6})][PF_6]$. All complexes exhibit a very similar structured emission with maxima around 550 and 590 nm with a shoulder around 640 nm as observed for $[Ir(thpy)_2(\mathbf{3})][PF_6]$ and $[Ir(thpy)_2(\mathbf{6})][PF_6]$ in solution (Figure 2.10, Table 2.2). The environmental change on going from CH_3CN solutions to PMMA films leads to much higher PLQY values of 29–51%.

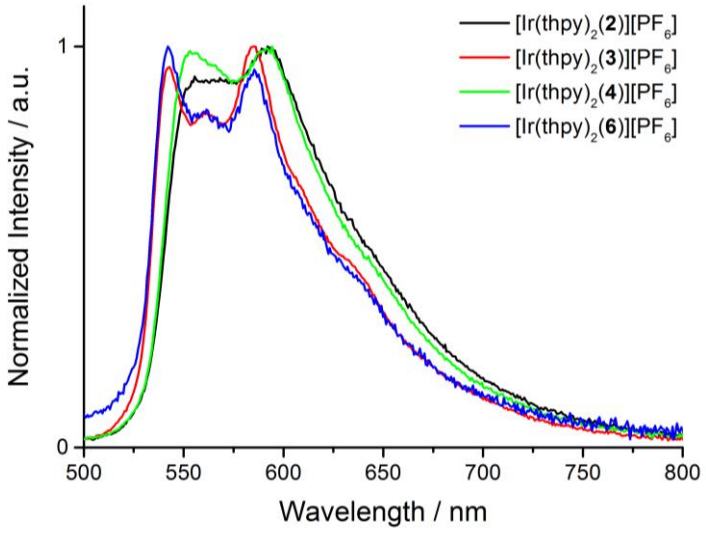

Figure 2.13 Normalized thin film emission spectra of $[Ir(thpy)_2(N^N)][PF_6]$ (N^N = **2-4**, **6**) complexes dispersed by 5 wt% in a PMMA matrix.

To try and understand the origins of this striking change in emission wavelength, low temperature photoluminescence spectra of the four complexes in CH_3CN solutions were recorded in a special cell immersed in liquid nitrogen. The CH_3CN is thereby frozen and the complexes are in a rigid solid-state environment simulating the conditions of the PMMA films. Not surprisingly, the low temperature spectra (Figure 2.14) show pronounced emissions between 540−550 nm and 585−590 as seen for the PMMA film. Even the slight red-shift of $[Ir(thpy)_2(\mathbf{2})][PF_6]$ and $[Ir(thpy)_2(\mathbf{4})][PF_6]$ with respect to the complexes with N^N ligands **3** and **6** is in accord with both measurements, which is most likely due to intra-molecular phenyl-phenyl stacking of these complexes.

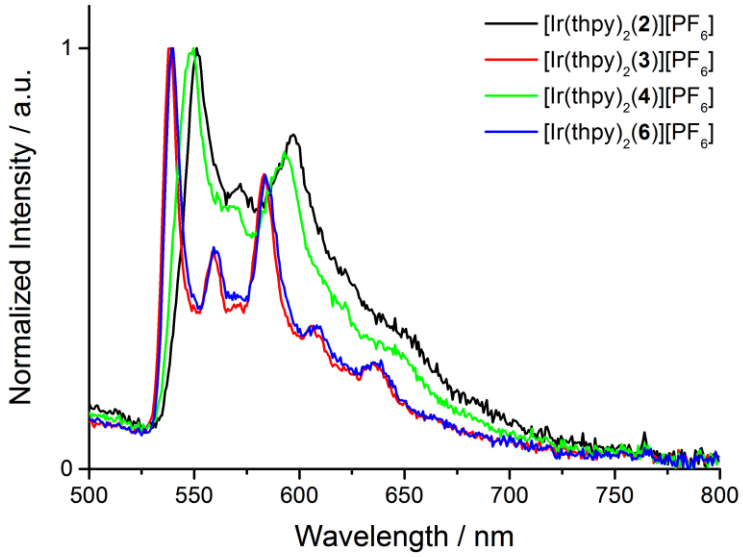

Figure 2.14 Normalized low temperature emission spectra of $[Ir(thpy)_2(N^N)][PF_6]$ (N^N = **2**-**4**, **6**) in frozen CH_3CN cooled by liquid nitrogen.

In the low temperature spectra minor emission features are also generated, e.g. the peak around 640−650 nm which corresponds to the room temperature emission maxima of $[Ir(thpy)_2(\mathbf{2})][PF_6]$ and $[Ir(thpy)_2(\mathbf{6})][PF_6]$.

These observations together with the absence of a rigidochromic shift of the emissions upon cooling leads to the following two statements: firstly, the emission occurs via a triplet state with mainly ^{3}LC character (as predicted by theoretical calculations in Section 2.6) and secondly, all four complexes possess very similar emission properties. The highly structured emission for all four complexes reveals two well-defined vibronic progressions, both about 1400 cm^{-1}. The strong red-shift of $[Ir(thpy)_2(\mathbf{2})][PF_6]$ and $[Ir(thpy)_2(\mathbf{6})][PF_6]$ in the room temperature solution emission spectra can be assigned to a different intensity distribution of the vibronic structure defining these bands. Both complexes have no ^{t}Bu substituents on the ancillary ligand. They therefore are not subject to the electron donating (blue-shifting) effect of these groups and tend to pack more closely than $[Ir(thpy)_2(\mathbf{3})][PF_6]$ and $[Ir(thpy)_2(\mathbf{4})][PF_6]$. This provides a further possible explanation for the observed emission behavior.

In the second approach where the complexes were diluted with IL, the photoluminescence was too weak to obtain good spectra and the PLQYs were too low to give measurable values. However the emission spectra looked similar to the electroluminescence of the LEECs, possessing less structured bands with maxima around 600 nm (Figure 2.15).

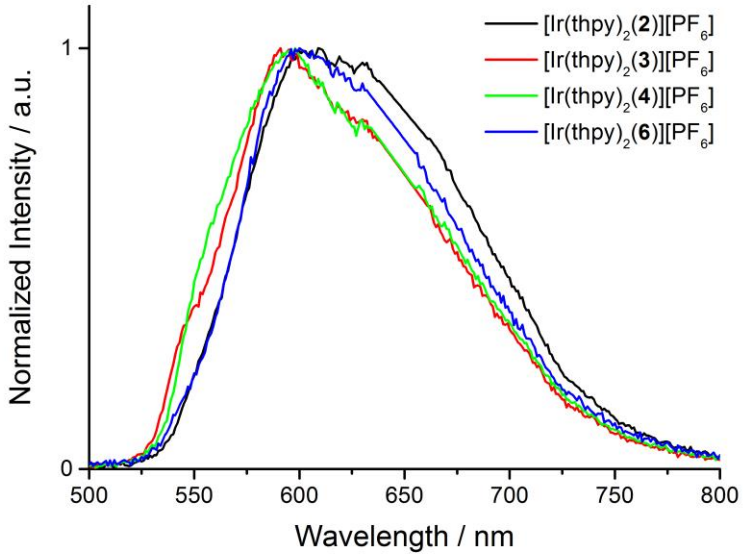

Figure 2.15 Normalized electroluminescence spectra of $[Ir(thpy)_2(N^N)][PF_6]$ (N^N = **2**-**4**, **6**) in LEECs.

Despite the low photoluminescence in the thin films, complexes with ancillary ligands **2-4** were used in devices driven using a block-wave pulsed current (J_{avg} = 100 A m^{-2}, 1000 Hz, 50% duty cycle). Complex $[Ir(thpy)_2(\mathbf{2})][PF_6]$ performed very poorly and only an electroluminescence spectrum could be obtained. An overview of the performance data of these three complexes embedded in LEECs is given in Table 2.5.

The low efficiencies arise from the poor charge transport of electrons and holes limiting the current density, as well as the luminance and most likely also the lifetime. Unfortunately, despite having good PLQY in thin PMMA films these compounds are not very highly performing compared to recently reported LEECs.

Table 2.5 Performance of ITO/PEDOT:PSS/iTMC:IL 4:1 /Al LEECs where iTMC = $[Ir(thpy)_2(N^N)][PF_6]$ (N^N = **2**-**4**) driven using a pulsed current mode (average current density 100 A m^{-2}, 1000 Hz, 50% duty cycle, block wave).

Compound	t_{on} [a] / h	L_{max} [b] / cd m^{-2}	$t_{1/2}$ [c] / h	Efficacy / cd A^{-1}	EQE [d] / %
$[Ir(thpy)_2(\mathbf{2})][PF_6]$	4.2	19	101	0.2	0.2
$[Ir(thpy)_2(\mathbf{3})][PF_6]$	Seconds	33	0.04	0.2	< 0.1
$[Ir(thpy)_2(\mathbf{4})][PF_6]$	0.4	50	9.7	0.5	0.2

[a] Time to reach the maximum luminance. [b] Maximum luminance. [c] Time to reach half of the maximum luminance. [d] External quantum efficiency.

2.8 Conclusion

A series of four new cyclometallating Ir(III) complexes of the type $[Ir(thpy)_2(N\hat{}N)][PF_6]$ (N^N = **2-4**, **6**) were successfully synthesized and fully characterized. Room temperature photoluminescence measurements of acetonitrile solutions afforded structured orange emissions in a range 543–595 nm for $[Ir(thpy)_2(\mathbf{3})][PF_6]$ and $[Ir(thpy)_2(\mathbf{4})][PF_6]$ whereas a remarkable red-shift to 646 and 640 nm was observed for $[Ir(thpy)_2(\mathbf{2})][PF_6]$ and $[Ir(thpy)_2(\mathbf{6})][PF_6]$, respectively. In thin PMMA films all complexes exhibit very similar structured emission bands with maxima between 542 and 592 nm. DFT/TD-DFT calculations of the lowest-energy triplet states attribute the origin of these emission properties to be dominantly of ^{3}LC nature involving the $[thpy]^-$ ligand with minor contributions from the Ir(III) center. These findings were supported by low temperature photoluminescence measurements in frozen acetonitrile, where no rigidochromic shift was observed compared to room temperature. The significant low-energy shift in the solution photoluminescence spectra observed for the potential red-emitting complexes $[Ir(thpy)_2(\mathbf{2})][PF_6]$ and $[Ir(thpy)_2(\mathbf{6})][PF_6]$ can simply be understood as different relative intensity distributions of the vibronic structure defining the emission band. Poor device performances (probably due to poor charge transport properties) and electroluminescence emission maxima all around 600 nm lead to the conclusion that this series of complexes is nicely emissive in the orange region of the visible spectrum with PLQY in thin PMMA films of 29–51%. However, they do not exhibit the expected red emission desired for LEECs.

2.9 Experimental

2-(2'-thienyl)pyridine and 4,4'-di-*tert*-butyl-2,2'-bipyridine (**3**) were purchased from Alfa Aesar and Sigma-Aldrich, respectively, and were used as received.

2.9.1 $[Ir(thpy)_2(\mathbf{2})][PF_6]$

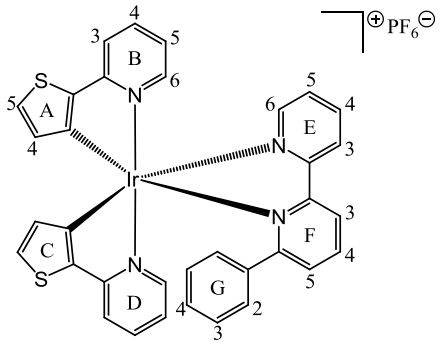

A suspension of tetrakis(2-(2'-thienyl)pyridine-*C,N*)di(μ-chloro)diiridium(III) (100 mg, 0.091 mmol, 1.00 eq) and 6-phenyl-2,2'-bipyridine (42.6 mg, 0.183 mmol, 2.01 eq) in MeOH (20 mL) was heated in a microwave reactor for 2 h at 120 °C. The orange solution was allowed to reach room temperature and an excess of NH_4PF_6 (150 mg, 0.912 mmol, 10.0 eq) was added and the reaction mixture was stirred for 30 min. Then the solution was evaporated to dryness and purified by column chromatography (Merck aluminium oxide 90 standardized; CH_2Cl_2 → CH_2Cl_2:MeOH 100:1) followed by a subsequent column chromatography (Fluka silica gel 60, 0.040–0.063 mm; CH_2Cl_2 → CH_2Cl_2:MeOH 100:1) yielding in the desired product as an orange solid (137 mg, 0.154 mmol, 84.6%).

^{1}H NMR (500 MHz, CD_2Cl_2, 295 K) δ/ppm 8.53 (overlapping m, 2H, H^{E3+F3}), 8.21 (t, J = 7.9 Hz, 1H, H^{F4}), 8.14 (td, J = 8.0, 1.6 Hz, 1H, H^{E4}), 7.84 (ddd, J = 5.4, 1.4, 0.6 Hz, 1H, H^{E6}), 7.71 (ddd, J = 8.1, 7.4, 1.5 Hz, 1H, H^{D4}), 7.64 (ddd, J = 8.1, 7.6, 1.5 Hz, 1H, H^{B4}), 7.51–7.42 (overlapping m, 6H, $H^{B3+B6+D3+D6+E5+F5}$), 7.30 (d, J = 4.8 Hz, 1H, H^{A5}), 7.10 (tt, J = 7.6, 1.2 Hz, 1H, H^{G4}), 6.93 (br t, J = 7.5 Hz, 2H, H^{G3}), 6.89 (ddd, J = 7.4, 5.9, 1.4 Hz, 1H, H^{B5}), 6.81 (overlapping m, 2H, H^{D5+C5}), 6.68 (br, 2H, H^{G2}), 5.93 (d, J = 4.8 Hz, 1H, H^{A4}), 5.38 (d, J = 4.7 Hz, 1H, H^{C4}).

^{13}C NMR (126 MHz, CD_2Cl_2, 295 K) δ/ppm 166.5 (C^{F6}), 165.4 (C^{D2}), 163.9 (C^{B2}), 157.6 (C^{E2}), 157.4 (C^{F2}), 154.2 (C^{C3}), 151.5 (C^{E6}), 150.1 (C^{B6}), 149.5 (C^{D6}), 147.5 (C^{A3}), 140.2 (C^{F4}), 140.0 (C^{E4}), 139.3 (C^{B4}), 139.0 (C^{D4}), 138.8 (C^{G1}), 136.3 (C^{A2}), 135.5 (C^{C2}), 131.7 (C^{C4}), 130.7 (C^{F5}), 130.5 (C^{A5}), 129.8 (C^{G4}), 129.6 (C^{C5}), 129.5 (C^{A4}), 128.45 (C^{G3}), 128.4 (C^{E5}), 127.7 (C^{G2}), 125.5 (C^{E3}), 124.1 (C^{F3}), 121.0 (C^{B5}), 119.8 (C^{D5}), 118.9 (C^{B3}), 118.7 (C^{D3}).

IR (solid, $\tilde{\nu}$/cm^{-1}) 3099 w, 3057 w, 2361 w, 2324 w, 1684 w, 1653 w, 1603 m, 1562 w, 1506 w, 1472 s, 1448 m, 1394 m, 1339 w, 1296 w, 1281 w, 1246 w, 1225 w, 1184 w, 1157 m, 1148 m, 1115 w, 1076 w, 1065 w, 1047 w, 1022 w, 1003 w, 989 w, 878 m, 833 s, 762 m, 716 m, 694 m, 652 w, 629 m, 555 s.

UV-Vis λ/nm (ε/dm^3 mol^{-1} cm^{-1}) (MeCN, 1.00 × 10^{-5} mol dm^{-3}) 279 (35 000), 310 sh (28 000), 410 (5000).

Emission (MeCN, 2.50 × 10^{-5} mol dm^{-3}, λ_{exc} = 410 nm) λ_{em} = 611 sh, 646 nm.

ESI-MS *m/z* 745.2 $[M - PF_6]^+$ (base peak, calc. 745.1).

Found C 45.90, H 2.77, N 6.15; $C_{34}H_{24}F_6IrN_4PS_2$ requires C 45.89, H 2.72, N 6.30%.

Crystallography $C_{34}H_{24}F_6IrN_4PS_2$, M = 889.90, orange block, triclinic, space group P–1, a = 9.6280(8), b = 12.2606(10), c = 13.9602(12) Å, α = 94.621(4), β = 103.208(4), γ = 95.953(4)°, U = 1586.4(2) Å^3, Z = 2, D_c = 1.863 Mg m^{-3}, μ(Mo-K$_\alpha$) = 4.459 mm^{-1}, T = 123 K. Total 43407 reflections, 8611 unique, R_{int} = 0.0307. Refinement of 8283 reflections (433 parameters) with $I > 2\sigma(I)$ converged at final $R1$ = 0.0183 ($R1$ all data = 0.0196), $wR2$ = 0.0473 ($wR2$ all data = 0.0498), gof = 1.095. CCDC 949190.

2.9.2 [Ir(thpy)$_2$(**3**)][PF$_6$]

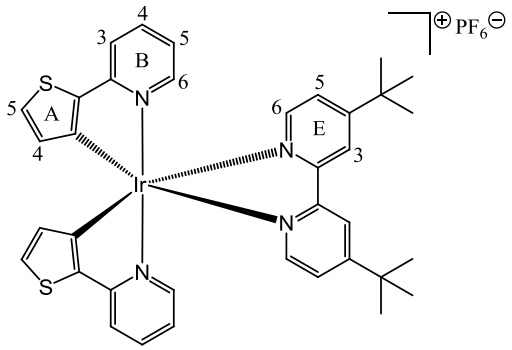

A suspension of [{Ir(thpy)$_2$(μ-Cl)}$_2$] (100 mg, 0.091 mmol, 1.00 eq) and **3** (49.2 mg, 0.183 mmol, 2.01 eq) in MeOH (20 mL) was reacted in a microwave reactor for 2 h at 120 °C. The orange solution was cooled to room temperature and an excess of NH_4PF_6 (150 mg, 0.912 mmol, 10.0 eq) was added and stirred for 30 min. Then the solution was evaporated to dryness and purified by column chromatography (Merck aluminium oxide 90 standardized; CH_2Cl_2 → CH_2Cl_2:MeOH 100:1) followed by a subsequent column chromatography (Fluka silica gel 60, 0.040–0.063 mm; CH_2Cl_2 → CH_2Cl_2:MeOH 100:1) yielding in the desired product as an orange solid (127 mg, 0.137 mmol, 75.3%).

^{1}H NMR (500 MHz, CD_2Cl_2, 295 K) δ/ppm 8.27 (d, J = 1.8 Hz, 2H, H^{E3}), 7.86 (d, J = 5.9 Hz, 2H, H^{E6}), 7.67 (ddd, J = 8.1, 7.5, 1.5 Hz, 2H, H^{B4}), 7.58 (ddd, J = 8.1, 1.3, 0.8 Hz, 2H, H^{B3}), 7.49 (dd, J = 5.9, 2.0 Hz, 2H, H^{E5}), 7.45 (d, J = 4.7 Hz, 2H, H^{A5}), 7.42 (m, 2H, H^{B6}), 6.83 (m, 2H, H^{B5}), 6.31 (d, J = 4.8 Hz, 2H, H^{A4}), 1.43 (s, 18H, H^{Me}).

^{13}C NMR (126 MHz, CD_2Cl_2, 295 K) δ/ppm 164.7 (C^{E2}), 164.6 (C^{B2}), 156.2 (C^{E4}), 153.0 (C^{A3}), 151.4 (C^{E6}), 149.5 (C^{B6}), 139.2 (C^{B4}), 137.5 (C^{A2}), 131.1 (C^{A4}), 130.9 (C^{A5}), 126.3 (C^{E5}), 121.4 (C^{E3}), 120.9 (C^{B5}), 119.0 (C^{B3}), 36.2 (C^{CMe}), 30.5 (C^{Me}).

IR (solid, $\tilde{\nu}$/cm^{-1}) 3101 m, 3051 m, 2962 m, 2876 m, 1603 m, 1558 m, 1541 m, 1472 s, 1435 m, 1414 m, 1393 m, 1364 m, 1339 m, 1302 m, 1279 m, 1248 m, 1204 m, 1157 m, 1115 m, 1074 m, 1034 m, 982 m, 955 m, 930 m, 899 m, 879 m, 829 s, 770 s, 737 m, 710 m, 656 m, 631 m, 606 m, 555 s, 527 m.

UV-Vis λ/nm (ε/dm^3 mol^{-1} cm^{-1}) (MeCN, 1.00 × 10^{-5} mol dm^{-3}) 275 (40 000), 308 sh (28 000), 330 sh (15 000), 415 (6000).

Emission (MeCN, 2.5 × 10^{-5} mol dm^{-3}, λ_{exc} = 415 nm) λ_{em} = 543, 585, 634 sh nm.

ESI-MS *m/z* 781.3 $[M - PF_6]^+$ (base peak, calc. 781.2).

Found C 46.74, H 4.02, N 5.83, $C_{36}H_{36}F_6IrN_4PS_2$ requires C 46.70, H 3.92, N 6.05%.

2.9.3 $[Ir(thpy)_2(\mathbf{4})][PF_6]$

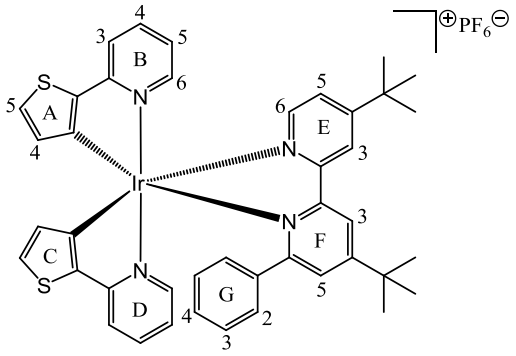

A suspension of $[\{Ir(thpy)_2(\mu\text{-}Cl)\}_2]$ (100 mg, 0.091 mmol, 1.00 eq) and **4** (62.9 mg, 0.182 mmol, 2.01 eq) in MeOH (20 mL) was reacted in a microwave reactor for 2 h at 120 °C. The orange solution was allowed to reach room temperature and NH_4PF_6 (150 mg, 0.912 mmol, 10.0 eq) was added and stirred for 30 min. Then the solution was evaporated to dryness and purified by column chromatography (Merck aluminium oxide 90 standardized; CH_2Cl_2 → CH_2Cl_2:MeOH 100:1) followed by a subsequent column chromatography (Fluka silica gel 60, 0.040–0.063 mm; CH_2Cl_2 → CH_2Cl_2:MeOH 100:1) yielding in the desired product as an orange solid (143 mg, 0.143 mmol, 78.6%).

^{1}H NMR (500 MHz, CD_2Cl_2, 295 K) δ/ppm 8.33 (d, J = 2.0 Hz, 1H, H^{F3}), 8.32 (d, J = 1.8 Hz, 1H, H^{E3}), 7.74–7.68 (overlapping m, 2H, H^{E6+B4}), 7.65 (m, 1H, H^{D4}), 7.51 (ddd, J = 5.9, 1.4, 0.8 Hz, 1H, H^{D6}), 7.48–7.41 (overlapping m, 5H, $H^{B3+D3+B6+E5+F5}$), 7.29 (d, J = 4.8 Hz, 1H, H^{A5}), 7.10 (tt, J = 7.6, 1.2 Hz, 1H, H^{G4}), 6.93 (br t, J = 7.6 Hz, 2H, H^{G3}), 6.90 (ddd, J = 7.4, 5.9, 1.4 Hz, 1H, H^{D5}), 6.85–6.79 (m, overlapping d, J = 4.7 Hz, 2H, H^{B5+C5}), 6.69 (br, 2H, H^{G2}), 5.93 (d, J = 4.8 Hz, 1H, H^{A4}), 5.37 (d, J = 4.7 Hz, 1H, H^{C4}), 1.47 (s, 9H, $H^{Me\ on\ ring\ F}$), 1.45 (s, 9H, $H^{Me\ on\ ring\ E}$).

^{13}C NMR (126 MHz, CD_2Cl_2, 295 K) δ/ppm 166.2 (C^{F6}), 165.4 (C^{D2}), 164.8 (C^{F4}), 164.5 (C^{E4}), 164.0 (C^{B2}), 157.4 (C^{E2+F2}), 154.7 (C^{C3}), 151.0 (C^{E6}), 150.1 (C^{D6}), 149.6 (C^{B6}), 148.1 (C^{A3}), 139.5 (C^{B4}), 139.1 (C^{G1}), 139.0 (C^{D4}), 136.2 (C^{A2}), 135.5 (C^{C2}), 131.7 (C^{C4}), 130.5 (C^{A5}), 129.6 (C^{G4}), 129.5 (C^{A4}), 129.49 (C^{C5}), 128.4 (C^{G3}), 127.8 (C^{G2}), 127.7 (C^{F5}), 125.9 (C^{E5}), 121.9 (C^{E3}), 120.8 (C^{D5}), 120.7 (C^{F3}), 119.7 (C^{B5}), 118.8 (C^{D3}), 118.6 (C^{B3}), 36.14 ($C^{CMe\ on\ ring\ E}$), 36.08 ($C^{CMe\ on\ ring\ F}$), 30.54 ($C^{Me\ on\ ring\ F}$), 30.52 ($C^{Me\ on\ ring\ E}$).

IR (solid, $\tilde{\nu}$/cm^{-1}) 3057 w, 2961 w, 2910 w, 2870 w, 1603 s, 1558 s, 1541m, 1472 s, 1439 m, 1420 w, 1389 w, 1366 w, 1339 w, 1300 w, 1281 w, 1248 m, 1205 w, 1148 m, 1115 w, 1072 w, 1032 w, 1001 w, 906 w, 878 m, 831 s, 768 m, 696 m, 652 m, 627 m, 555 s.

UV-Vis λ/nm (ε/dm^3 mol^{-1} cm^{-1}) (MeCN, 1.00 × 10^{-5} mol dm^{-3}) 279 (38 000), 310 sh (30 000), 410 (5000).

Emission (MeCN, 2.50×10^{-5} mol dm^{-3}, λ_{exc} = 410 nm) λ_{em} = 555 sh, 595, 638 sh nm.

ESI-MS *m/z* 857.4 $[M - PF_6]^+$ (base peak, calc. 857.2).

Found C 50.24, H 4.03, N 5.54; $C_{42}H_{40}F_6IrN_4PS_2$ requires C 50.34, H 4.02, N 5.59%.

2.9.4 [Ir(thpy)$_2$(**6**)][PF$_6$]

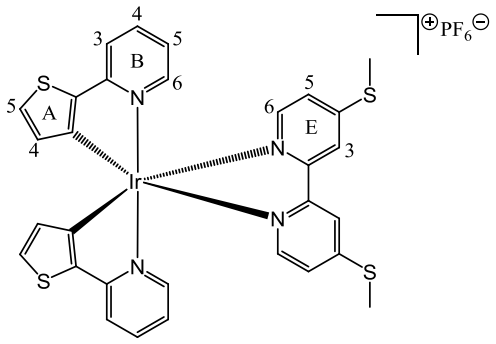

A suspension of [{Ir(thpy)$_2$(μ-Cl)}$_2$] (100 mg, 0.091 mmol, 1.00 eq) and **6** (45.5 mg, 0.183 mmol, 2.01 eq) in MeOH (20 mL) was reacted in a microwave reactor for 2 h at 120 °C. The orange solution was allowed to reach room temperature and NH_4PF_6 (149 mg, 0.912 mmol, 10.0 eq) was added and stirred for 30 min. Then the solution was evaporated to dryness and purified by column chromatography (Merck aluminium oxide 90 standardized; CH_2Cl_2 → CH_2Cl_2:MeOH 100:1) followed by a subsequent column chromatography (Fluka silica gel 60, 0.040–0.063 mm; CH_2Cl_2 → CH_2Cl_2:MeOH 100:1). Recrystallization in MeCN/diethyl ether afforded the desired product as an orange solid (105 mg, 0.116 mmol, 63.7%).

^{1}H NMR (500 MHz, CD_2Cl_2, 295 K) δ/ppm 8.05 (d, J = 1.9 Hz, 2H, H^{E3}), 7.67 (overlapping d + m, $4H^{E6+B4}$), 7.58 (ddd, J = 8.1, 1.4, 0.8 Hz, 2H, H^{B3}), 7.47 (ddd, J = 5.9, 1.5, 0.8, 2H, H^{B6}), 7.44 (d, J = 4.7 Hz, 2H, H^{A5}), 7.22 (dd, J = 6.1, 2.0 Hz, 2H, H^{E5}), 6.83 (ddd, J = 7.4, 5.9, 1.5 Hz, 2H, H^{B5}), 6.29 (d, J = 4.7 Hz, 2H, H^{A4}), 2.63 (s, 6H, H^{Me}).

^{13}C NMR (126 MHz, CD_2Cl_2, 295 K) δ/ppm 164.6 (C^{B2}), 156.8 (C^{E4}), 155.0 (C^{E2}), 152.8 (C^{A3}), 150.3 (C^{E6}), 149.5 (C^{B6}), 139.2 (C^{B4}), 137.5 (C^{A2}), 131.2 (C^{A4}), 130.9 (C^{A5}), 123.8 (C^{E5}), 120.9 (C^{B5}), 120.4 (C^{E3}), 119.0 (C^{B3}), 14.7 (C^{Me}).

IR (solid, $\tilde{\nu}$/cm^{-1}) 3101 w, 3049 w, 1599 s, 1533 w, 1475 m, 1435 w, 1393 m, 1335 w, 1283 w, 1246 w, 1161 w, 1117 m, 1080 w, 1036 w, 1016 m, 957 w, 895 m, 876 m, 831 s, 816 s, 770 s, 752 m, 710 m, 654 m, 629 m, 555 s, 532 m.

UV-Vis λ/nm (ε/dm^3 mol^{-1} cm^{-1}) (MeCN, 2.50 × 10^{-5} mol dm^{-3}) 275 (61 500), 325 sh (26 000), 362 sh (14 000), 415 (7000).

Emission (MeCN, 2.50 × 10^{-5} mol dm^{-3}, λ_{exc} = 415 nm) λ_{em} = 615 sh, 640 nm.

ESI-MS *m/z* 761.1 $[M - PF_6]^+$ (base peak, calc. 761.1).

Found C 40.41, H 3.01, N 6.86; $C_{30}H_{24}F_6IrN_4PS_4 \cdot 0.5MeCN$ requires C 40.19, H 2.77, N 6.80%.

Crystallography $C_{61}H_{50}Cl_2F_{12}Ir_2N_8P_2S_8$, M = 1896.93, orange block, monoclinic, space group $P2_1/c$, a = 9.3688(3), b = 14.4939(5), c = 24.5780(9) Å, β = 91.535(2)°, U = 3336.3(2) Å^3, Z = 2, D_c = 1.888 Mg m^{-3}, μ(Mo-K$_\alpha$) = 4.444 mm^{-1}, T = 123 K. Total 113585 reflections, 10602 unique, R_{int} = 0.0337. Refinement of 9581 reflections (578 parameters) with $I > 2\sigma(I)$ converged at final $R1$ = 0.0262 ($R1$ all data = 0.0309), $wR2$ = 0.0519 ($wR2$ all data = 0.0541), gof = 1.072. CCDC 949192.

Chapter 3

Chapter 3 Green Emitters

3.1 Motivation

In addition to the difficulty of obtaining red-emitting LEECs discussed in Chapter 2, another problem in the research field of cyclometallated Ir(III) complexes is the synthesis of stable blue-emitting compounds. Previous studies have shown that the HOMO of an $[Ir(C\hat{}N)_2(N\hat{}N)]^+$ complex is localized on the C^N ligands together with some contribution from the Ir(III) metal center, whereas the LUMO resides on the N^N ligands.[81],[82] Therefore two possible methods can be used to obtain a blue-shifted emission, either by stabilizing the HOMO or destabilizing the LUMO.[8],[26],[38] The former method mainly includes attaching electron-withdrawing fluorine substituents on the C^N ligands.[48],[83],[84] For the latter, additional electron-donating substituents have been used on the N^N ligands[45],[81] while keeping the fluorine-based substituents on the cyclometallating ligands. These strategies have something in common in order to obtain an emissive blue-shift: the use of fluorine substituents attached to the C^N ligand. The use of fluoro substituents is sometimes considered to be detrimental to the LEEC device performance. Therefore, alternative electron-withdrawing substituents were sought.

In this chapter a new series of six complexes of the type $[Ir(msppz)_2(N\hat{}N)][PF_6]$ (N^N = **1**, **3**, **4**, **6-8**; Hmsppz = 1-[4-(methylsulfonyl)phenyl]-1*H*-pyrazole based on an electron-withdrawing methyl sulfone substituent attached to the cyclometallating phenylpyrazole ligand is presented. The synthesis, NMR spectroscopic characterization, crystal structures, the electrochemical and photophysical properties in solution and thin-films are discussed in detail and supported with density functional theory calculations. Finally, their performances were tested embedded in LEEC devices.

3.2 Synthesis and NMR Spectroscopic Characterization

The synthesis of Hmsppz as the C^N ligand was adapted from a literature method for similar compounds.[85] Specifically, 4-bromophenyl methyl sulfone and pyrazole were linked together via a copper(I) catalyzed C–N coupling reaction involving L-proline in a moderate yield of 56% under basic conditions. A peak at *m/z* = 223.0 assigned to $[M + H]^+$ detected with electrospray mass spectrometry together with ^1H and ^{13}C NMR characterizations confirmed the correct structure of Hmsppz shown in Scheme 3.1. The dimer $[\{Ir(msppz)_2(\mu\text{-}Cl)\}_2]$ was prepared following the standard procedure reported by Watts and co-workers for the $[\{Ir(ppy)_2(\mu\text{-}Cl)\}_2]$ analog.[86] Since NMR spectroscopy was consistent with the correct structure for the dimer, a series of six complexes of the type $[Ir(msppz)_2(N\hat{}N)][PF_6]$ (see Scheme 3.1) was synthesized as shown for the orange emitters in Section 2.2, where also the preparations for N^N ligands **4** and **6** can be found. Ligands **7**[87] and **8**[88] were prepared following literature methods.

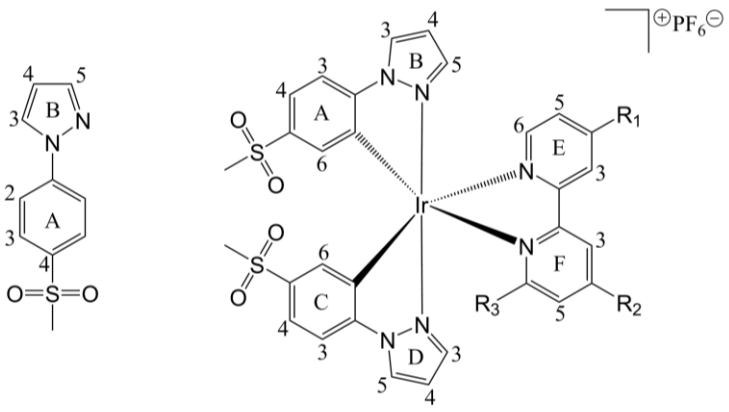

[Ir(msppz)$_2$(**1**)][PF$_6$]	$R_1 = R_2 = H$	$R_3 = H$	when R_3 = Ph
[Ir(msppz)$_2$(**3**)][PF$_6$]	$R_1 = R_2 = {}^t$Bu	$R_3 = H$	
[Ir(msppz)$_2$(**4**)][PF$_6$]	$R_1 = R_2 = {}^t$Bu	R_3 = Ph	
[Ir(msppz)$_2$(**6**)][PF$_6$]	$R_1 = R_2$ = SMe	$R_3 = H$	
[Ir(msppz)$_2$(**7**)][PF$_6$]	$R_1 = H$ R_2 = SMe	R_3 = Ph	
[Ir(msppz)$_2$(**8**)][PF$_6$]	$R_1 = H$ $R_2 = NMe_2$	$R_3 = H$	

Scheme 3.1 Structures and atom labelling of Hmsppz and the complexes used for NMR spectroscopic assignments. The ligand numbering changes when coordinated in a complex.

Standard 2D methods (COSY, NOESY, HMQC and HMBC) were used to assign the room temperature solution ^{1}H and ^{13}C NMR spectra of this series of complexes. As seen for the orange emitters (Section 2.2), complexes with N^N ligands **1**, **3**, **6** and **8** possess C_2 symmetry which is lost upon the introduction of the pendant phenyl substituent in **4** and **7**. The lowered symmetry results in an inequivalence of the [msppz]$^-$ C^N ligands and of the two pyridine rings of the N^N ligand. Following the atom and ring labelling (Scheme 3.1) a direct comparison of the NMR signals in all six complexes was possible. The C_2 symmetric complexes were assigned starting with NOESY H^{Me}/H^{A4} and H^{Me}/H^{A6} cross-peaks, continued by a COSY H^{A4}/H^{A3} cross-peak and a NOESY H^{A3}/H^{B3} cross-peak which finally allowed one to distinguish between H^{B3} and H^{B5}. For complexes [Ir(msppz)$_2$(**4**)][PF$_6$] and [Ir(msppz)$_2$(**7**)][PF$_6$], first rings E and F were assigned, and NOESY cross-peaks helped to distinguish between two sets of signals for A/C and B/D, respectively. Comparing the proton resonances to similar complexes containing [dfppz]$^-$ (Hdfppz = 1-(2,4-difluorophenyl)-1*H*-pyrazole)[80] as C^N ligand, the signal for H^{A6} appears at significantly higher frequency than the one for H^{C6}. Similarities in the chemical shifts for the ^{13}C nuclei within this series of complexes allowed the residual protons to be assigned with the help of HMQC and HMBC spectra. As observed for [Ir(thpy)$_2$(**2**)][PF$_6$] and [Ir(thpy)$_2$(**4**)][PF$_6$] of the orange emitters (Section 2.2), the pendant phenyl ring G in [Ir(msppz)$_2$(**4**)][PF$_6$] and [Ir(msppz)$_2$(**7**)][PF$_6$] undergoes hindered rotation on the NMR timescale at 295 K. The signal for H^{G4} is only slightly broadened, whereas that for H^{G3} arises as a broad signal (δ 6.83 ppm, FWHM ≈ 75 Hz for [Ir(msppz)$_2$(**4**)][PF$_6$] and δ 6.82 ppm, FWHM ≈ 70 Hz for [Ir(msppz)$_2$(**7**)][PF$_6$]). A further extremely broad resonance is observed for these two complexes (δ 6.02 ppm, FWHM ≈ 130 Hz, with N^N ligand **4** and δ 6.04 ppm, FWHM ≈ 120 Hz with N^N ligand **7**).

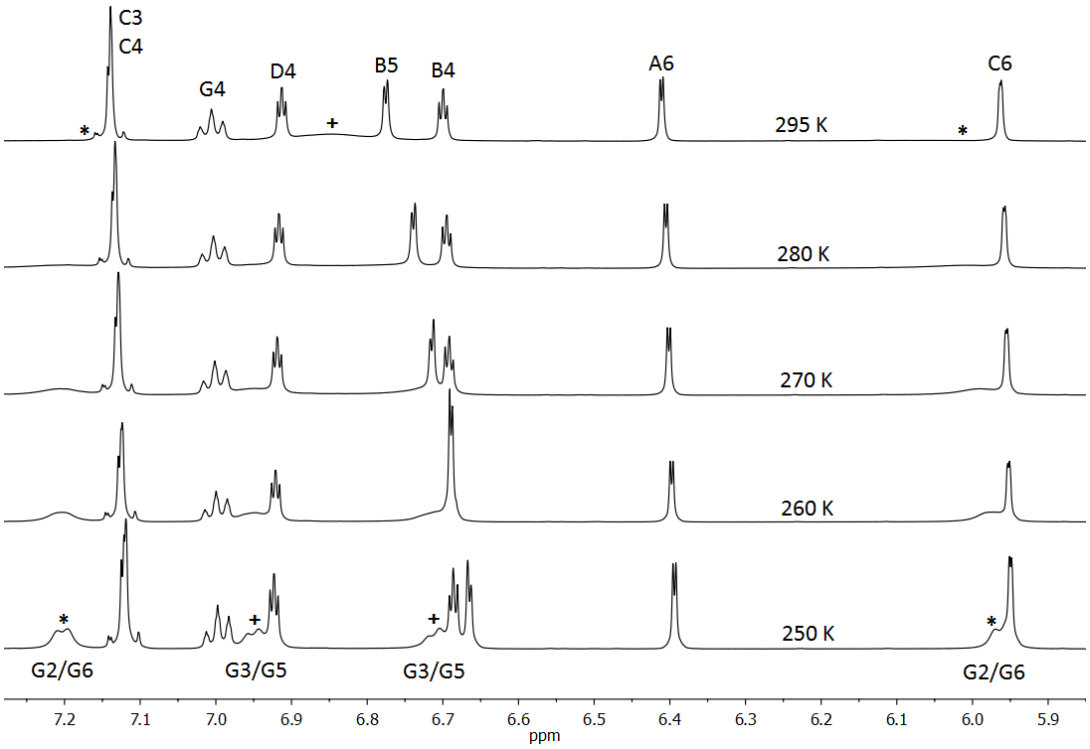

Figure 3.1 Part of the aromatic region of the 500 MHz ^{1}H NMR spectra of [Ir(msppz)$_2$(**7**)][PF$_6$] measured at variable-temperature in CD$_3$CN. See Scheme 3.1 for atom and ring labelling. The significance of the star (*) and the plus (+) is discussed in the text.

On cooling a CD$_3$CN solution of [Ir(msppz)$_2$(**7**)][PF$_6$] from 295 to 250 K, a collapse of the H^{G3} resonance at δ 6.82 ppm (marked with a + in Figure 3.1) and the reappearance split into two triplets (δ 6.94 and 6.70 ppm) was observed and the signals are assigned to H$^{G3/G5}$. Simultaneously, the very broad signal at δ 6.04 ppm (marked with a * in Figure 3.1) at 295 K sharpens to a resonance at δ 5.96 ppm (overlapping with that for H^{C6}) upon cooling, which is assigned to either H^{G2} or H^{G6}. A second signal of this pair arises as a broadened doublet at δ 7.20 ppm which was not seen at 295 K because of an overlap with the signals for H^{C3} and H^{C4}. The coalescence for exchange of H^{G2} or H^{G6} is therefore not achieved at 295 K as can be seen in Figure 3.1.

3.3 Crystal Structures

Single crystals of [Ir(msppz)$_2$(**7**)][PF$_6$]·CH$_3$CN were grown from a CH$_3$CN solution layered by Et$_2$O. Figure 3.2 depicts the structure of the [Ir(msppz)$_2$(**7**)]$^+$ cation and selected bond parameters are listed in the figure caption. The Ir(III) metal center is octahedrally sited and forms a chiral cation. The compound crystallizes in a monoclinic space group $P2_1/c$ with a racemic mixture in the unit cell. As expected, the nitrogen atoms N3 and N5 of the C^N ligands are in a mutually trans-arrangement and the presence of the sulfone substituents are confirmed by the crystal structure. Phenyl and pyrazole rings in the cyclometallating ligands are twisted about 11.4 and 8.2° and hence the [msppz]$^-$ ligands deviate slightly from planarity.

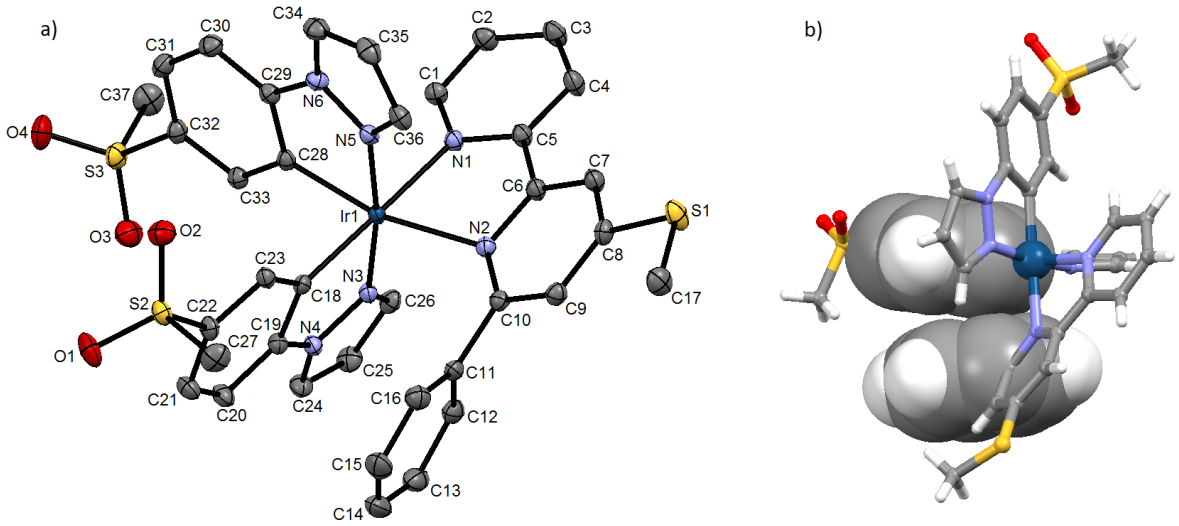

Figure 3.2 a) Crystal structure of the $[Ir(msppz)_2(\mathbf{7})]^+$ cation in $[Ir(msppz)_2(\mathbf{7})][PF_6]\cdot CH_3CN$. Ellipsoids are plotted at the 40% probability level with omitted H atoms, solvent molecules and $[PF_6]^-$ anion. Selected bond lengths and angles: Ir1–C28 = 1.9999(16), Ir1–C18 = 2.0171(16), Ir1–N3 = 2.0175(14), Ir1–N5 = 2.0182(14), Ir1–N1 = 2.1261(14), Ir1–N2 = 2.1885(14), N3–N4 = 1.3708(19), N5–N6 = 1.368(2), C8–S1 = 1.7434(17), S1–C17 = 1.7985(19), C22–S2 = 1.7630(17) O1–S2 = 1.4409(14), O2–S2 = 1.4440(14), S3–O3 = 1.4403(15), S3–O4 = 1.4418(15), S3–C37 = 1.756(2), S3–C32 = 1.7651(18) Å; N1–Ir1–N2 = 76.15(5), C18–Ir1–N3 = 79.97(6), C28–Ir1–N5 = 80.41(6), N3–Ir1–N5 = 171.43(6), C18–Ir1–N1 = 178.63(6), C28–Ir1–N2 = 166.17(6), C8–S1–C17 = 103.28(9), O1–S2–O2 = 117.45(9), O3–S3–O4 = 118.55(9)°. b) Face-to-face π-stacking of the phenyl ring G of ligand **7** with the phenyl ring of the $[msppz]^-$ ligand containing atom C19.

With a twisting angle of 15.8° between the two pyridine rings, the bpy domain is also non-planar. The pendant phenyl ring is twisted through 55.0° with respect to the pyridine ring containing N2. As shown for the $[Ir(thpy)_2(\mathbf{2})]^+$ complex cation (Figure 2.7b) the latter distortions are associated with the intra-cation face-to-face π-stacking between the phenyl ring G of ligand **7** with the phenyl ring of the $[msppz]^-$ ligand containing atom C19 (Figure 3.2). The inter-centroid separation of the two rings is 3.59 Å and the angle between their least square planes is 12.7° resulting in a moderately efficient interaction[77] very similar to the orange-emitting $[Ir(thpy)_2(\mathbf{2})][PF_6]$ (3.60 Å and 12.1°) described in Section 2.3.

Each methyl sulfone group is oriented in a way that the S–O bond is twisted towards the plane of the phenyl ring to which it is attached. Consistent with general observations for organic sulfones,[87] this arrangement forms intra-cation C–H···O hydrogen bonds. Relevant torsion angles are C21–C22–S2–O1 = –20.5(2)° and C33–C32–S3–O3 = 15.9(2)° with hydrogen bond distances of O1···H21a = 2.61 Å, and O3···H33a = 2.56 Å. The $[PF_6]^-$ counter-ion as well as the CH_3CN solvent molecule are ordered. Main packing forces include CH···N_{MeCN}, CH···F and CH···O contacts.

Unfortunately, only crystals of poor quality could be grown of $[Ir(msppz)_2(N\text{^}N)][PF_6]$ (with N^N = **1**, **3**, **6** and **8**). Nevertheless, preliminary crystallographic data for these four complexes confirmed the same fundamental structural features described for $[Ir(msppz)_2(\mathbf{7})][PF_6]$.

3.4 Electrochemical Properties

The cyclic voltammetric data of $[Ir(msppz)_2(N\hat{}N)][PF_6]$ (N^N = **1**, **3**, **4**, **6**-**8**) are given in Table 3.1. In all cases, the complexes exhibit one or two reversible or quasi-reversible oxidations arising from an Ir(III)-center based process with substantial contribution from the C^N ligand. The effect of the change in the cyclometallating ligands becomes obvious by comparing $[Ir(ppz)_2(\mathbf{1})][PF_6]$ with $[Ir(msppz)_2(\mathbf{1})][PF_6]$ where the oxidation potential shifts from +0.95 V[47] to +1.27 V, consistent with the electron-withdrawing sulfone groups attached to the C^N ligands. The N^N ligands also contribute to the oxidation processes. On going from $[Ir(msppz)_2(\mathbf{1})][PF_6]$ to $[Ir(msppz)_2(\mathbf{3})][PF_6]$ or $[Ir(msppz)_2(\mathbf{8})][PF_6]$ a small shift to less positive potentials is observed as electron-donating ^{t}Bu or NMe_2 substituents are introduced onto the ancillary ligand. The introduction of the pendant phenyl ring in $[Ir(msppz)_2(\mathbf{4})][PF_6]$ (+1.24 V) partially compensates for the effect of the ^{t}Bu substituents of $[Ir(msppz)_2(\mathbf{3})][PF_6]$ (+1.19 V). A further comparison can be made between the complex $[Ir(msppz)_2(\mathbf{4})][PF_6]$ and $[Ir(C\hat{}N)_2(\mathbf{4})][PF_6]$ (+1.21 V)[80] with C^N = $[dfppz]^-$ where the almost identical oxidation potentials indicate similar eletron-withdrawing effects of the sulfone as for the difluoro substituents on the C^N ligand.

All complexes exhibit a reversible first reduction process followed by an irreversible second reduction, except for $[Ir(msppz)_2(\mathbf{8})][PF_6]$ where only one reversible reduction process was observed. The reductions are all centered on the N^N ligand and hence the potentials are highly dependent on the substitution pattern of this ligand. Electron-donating ^{t}Bu and NMe_2 groups significantly shift the potential to more negative values on passing from $[Ir(msppz)_2(\mathbf{1})][PF_6]$ (–1.68 V) to $[Ir(msppz)_2(\mathbf{3})][PF_6]$ (–1.85 V) and $[Ir(msppz)_2(\mathbf{8})][PF_6]$ (–2.17 V) confirming the destabilizing effect on the LUMO. The SMe groups in $[Ir(msppz)_2(\mathbf{6})][PF_6]$ and $[Ir(msppz)_2(\mathbf{7})][PF_6]$ have no significant effect on the electrochemical potentials expressed by their $\Delta E_{1/2}$ of 2.93 and 2.94 V, which is almost identical to 2.95 V of $[Ir(msppz)_2(\mathbf{6})][PF_6]$. A more detailed description of the electrochemical behavior of this series of complexes is given in Section 3.6.

Table 3.1 Cyclic voltammetric data with respect to Fc/Fc^+, measured in dry CH_3CN solutions containing 0.1 M $[^n Bu_4N][PF_6]$ as supporting electrolyte at a scan rate of 0.1 V s^{-1}. All processes are reversible unless otherwise stated.

Compound	$E_{1/2}^{ox}$ / V	$E_{1/2}^{red}$ / V	$\Delta E_{1/2}$ / V
$[Ir(msppz)_2(\mathbf{1})][PF_6]$	$+1.27, +1.77^{irr}$	$-1.68, -2.37^{irr}$	2.95
$[Ir(msppz)_2(\mathbf{3})][PF_6]$	$+1.19, +1.77^{irr}$	$-1.85, -2.49^{irr}$	3.04
$[Ir(msppz)_2(\mathbf{4})][PF_6]$	+1.24	$-1.78, -2.39^{irr}$	3.02
$[Ir(msppz)_2(\mathbf{6})][PF_6]$	+1.19	$-1.74, -2.32^{irr}$	2.93
$[Ir(msppz)_2(\mathbf{7})][PF_6]$	+1.21	$-1.73, -2.32^{irr}$	2.94
$[Ir(msppz)_2(\mathbf{8})][PF_6]$	$+1.05^{qr}, +1.52^{irr}$	–2.17	3.22

3.5 Solution and Thin-film Photophysical Properties

The UV-Vis absorption spectra of $[Ir(msppz)_2(N^\wedge N)][PF_6]$ (N^N = **1**, **3**, **4**, **6-8**) in CH_3CN solutions are depicted in Figure 3.3 and absorption maxima are listed in Table 3.2. For complexes with ligands **1**, **3**, **4** and **7** the spectra are similar with intense absorption maxima in the range 252–266 nm arising from ligand-centered π* ← π transitions extending into the visible region. The other two complexes containing ligands **6** and **8** exhibit an increased intensity of the ligand-based absorption bands due to the extended π-system of the SMe and NMe_2 substituents as seen for complex $[Ir(thpy)_2(\mathbf{6})][PF_6]$ in Section 2.5.

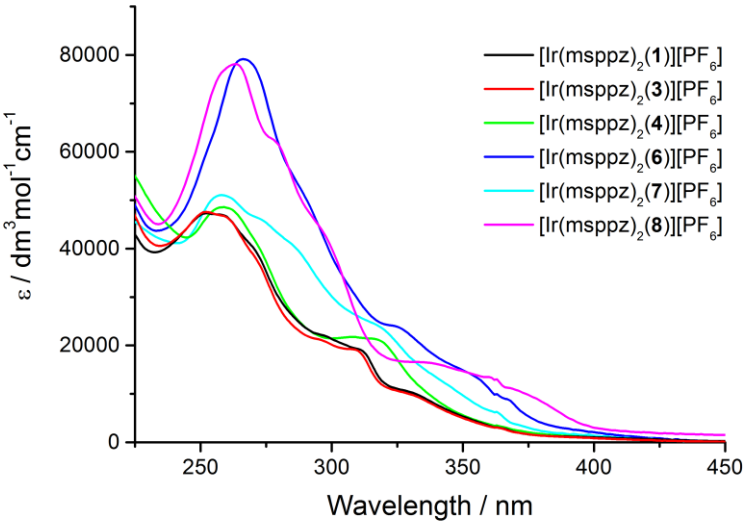

Figure 3.3 UV-Vis absorption spectra of $[Ir(msppz)_2(N^\wedge N)][PF_6]$ (N^N = **1**, **3**, **4**, **6-8**) measured in 2.50 x 10^{-5} M CH_3CN solutions.

Upon excitation into the MLCT transitions around 360 nm the complexes are emissive in CH_3CN solutions. The blue-shifting effect of the methyl sulfone substituent attached to the C^N ligand can be seen by comparing $[Ir(msppz)_2(\mathbf{1})][PF_6]$ (518 nm) to the literature value for the unsubstituted $[ppz]^-$ containing $[Ir(ppz)_2(\mathbf{1})][PF_6]$ (563 nm).[47] Table 3.2 summarizes the emission maxima and the emissive influence of the different substituents attached to the ancillary ligands are highlighted in Figure 3.4. For comparison reasons within this series of complexes, $[Ir(msppz)_2(\mathbf{1})][PF_6]$ is taken as a benchmark. In general, the photoluminescence bands are broad and unstructured but upon the introduction of NMe_2 substituents on the bpy domain the emission maxima of the complexes can be fine-tuned to the blue from 518 (N^N = **1**) to 492 nm (N^N = **8**). A small blue-shift is also observed by introducing ^{t}Bu groups in $[Ir(msppz)_2(\mathbf{3})][PF_6]$ (504 nm) and $[Ir(msppz)_2(\mathbf{4})][PF_6]$ (506 nm). As supported by the electrochemical data (see Section 3.4) the SMe substituents in ligands **6** and **7** (both 516 nm) has a neglible effect on the emission.

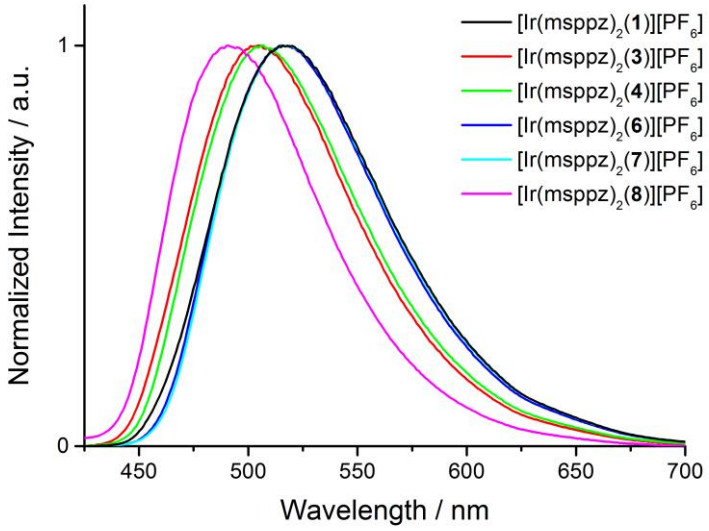

Figure 3.4 Photoluminescence spectra of $[Ir(msppz)_2(N^N)][PF_6]$ (N^N = **1**, **3**, **4**, **6**-**8**) measured for 2.50 x 10^{-5} M CH_3CN solutions.

In further accordance with the electrochemical findings is the emission maximum of $[Ir(msppz)_2(\mathbf{8})][PF_6]$ (492 nm), which essentially coincides with that of $[Ir(dfppz)_2(\mathbf{8})][PF_6]$ (493 nm),[80] strongly indicating the same electron-withdrawing ability of the $[msppz]^-$ ligand like $[dfppz]^-$.

The PLQYs of degassed CH_3CN solutions of this series of complexes are listed in Table 3.2. Complexes with ancillary ligands **4**, **7**, and **8** exhibit quantum yields of 38, 66 and 50%, respectively, and complexes with N^N = **1**, **3**, **6** have notably high PLQYs of 71, 80 and 77%, respectively. When the 15 min argon degassing process is omitted, the PLQYs drastically decrease by a factor of ten indicating a strong quenching of the phosphorescence by oxygen.

Table 3.2 Solution and thin-film photophysical properties of $[Ir(msppz)_2(N^N)][PF_6]$ (N^N = **1**, **3**, **4**, **6**-**8**).

Compound	Solution[a]				Diluted film[b]		Device configuration[c]	
	λ_{ex}^{max} / nm	λ_{em}^{max} / nm	τ / ns	Φ / %	λ_{em}^{max} / nm	Φ / %	λ_{em}^{max} / nm	Φ / %
$[Ir(msppz)_2(\mathbf{1})][PF_6]$	252	518	92	71	495	92	508	85
$[Ir(msppz)_2(\mathbf{3})][PF_6]$	252	504	85	80	487	91	497	53
$[Ir(msppz)_2(\mathbf{4})][PF_6]$	259	506	99	38	495	86	503	53
$[Ir(msppz)_2(\mathbf{6})][PF_6]$	266	516	116	77	505	94	518	60
$[Ir(msppz)_2(\mathbf{7})][PF_6]$	258	516	136	66	506	92	519	51
$[Ir(msppz)_2(\mathbf{8})][PF_6]$	262	492	76	50	493	65	510	30

[a] Degassed 2.50 x 10^{-5} M CH_3CN solutions. [b] 5 wt% complex in a PMMA matrix, λ_{ex} = 314 nm. [c] Complex mixed with the ionic liquid $[BMIM][PF_6]$ in a 4:1 molar ratio, λ_{ex} = 314 nm.

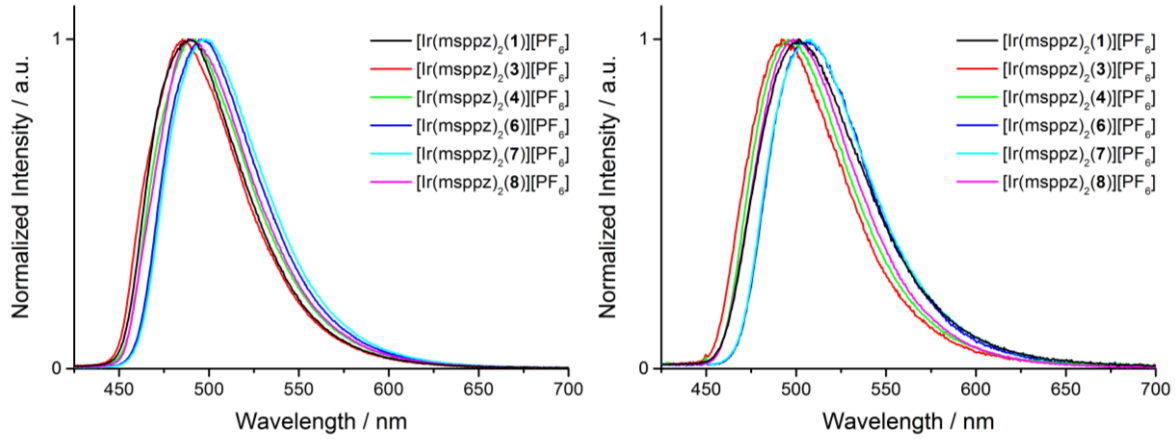

Figure 3.5 Photoluminescence spectra [Ir(msppz)$_2$(N^N)][PF$_6$] (N^N = **1**, **3**, **4**, **6-8**) in thin-films: (Left) complexes dispersed by 5 wt% in a PMMA matrix and (right) mixed with [BMIM][PF$_6$] in a molar ratio of 4:1.

Furthermore, the photophysical properties of these six complexes were examined embedded in thin solid films, either dispersed by 5 wt% in PMMA or mixed with [BMIM][PF$_6$] in a molar ratio of 4:1 corresponding to the device configuration used in LEECs. The thin-film solid-state photoluminescence spectra exhibit broad unstructured emissions (Figure 3.5) with emission maxima and PLQYs given in Table 3.2. Similar to their emission in solution, the complexes emit in the range from 493–519 nm, blue-shifting by attaching ^{t}Bu and NMe$_2$ substituents and red-shifting the emission upon introducing SMe groups to ligand **1**. The slight difference between the emission maxima measured in solution versus thin-films most likely arise from concentration effects. PLQYs of complexes diluted in a PMMA matrix reach extraordinary values of 92, 92, 86, 94, 92 and 65 % with N^N = **1**, **3**, **4**, **6-8**), respectively, and decrease to 85, 53, 53, 60, 51 and 30 % in device configuration. An increased self-quenching effect between neighboring complexes explains these decreased PLQYs in device configuration. Nevertheless, these quantum yields are amongst the highest reported for green-emitting cyclometallated Ir(III)-based complexes. Although there are no bulky substituents attached to [Ir(msppz)$_2$(**1**)][PF$_6$], its PLQY in device configuration surprisingly remains extremely high compared to the other five complexes. The reason for this observation is not totally clear and might arise from a different packing of the complexes.

3.6 Theoretical Calculations

Theoretical calculations presented in this section were performed by Enrique Ortí and his group at the University of Valencia and as in Chapter 2, support the understanding of the electrochemical and photophysical properties of this series of complexes.[37] Investigations of the molecular and electronic structures of the [Ir(msppz)$_2$(N^N)]$^+$ cations were carried out by density functional theory (DFT) calculations at the B3LYP/(6-31G**+LANL2DZ) level in the presence of CH$_3$CN solvent molecules. Electronic ground state (S$_0$) calculations correctly reproduce the near-octahedral coordination sphere of the Ir(III) metal center and predict geometric parameters in good accordance with the

crystallographic data. Taking $[Ir(msppz)_2(\mathbf{7})]^+$ as an example, the computed bite angles N1−Ir1−N2 (74.6°), N3−Ir1−C18 (79.1°) and N5−Ir1−C28 (79.4°) correspond to the experimental values of 76.2, 80.0 and 80.4°, respectively. Consistent with the X-ray structure, the methyl sulfone substituents are calculated to be orientated in a way that the methyl group is perpendicular to the plane of the phenyl ring to which they are attached (Section 3.3). The two S–O bonds form intra-cation C–H···O hydrogen bonds with average distances of 2.55 (O3···H33a) and 2.66 Å (O1···H21a) are in good agreement with the crystallographically obtained values of 2.56 and 2.61 Å, respectively. Furthermore, calculations correctly predict the intra-cation face-to-face π-stacking of the pendant phenyl ring in the ancillary ligand with the phenyl ring of the adjacent $[msppz]^-$ ligand observed for cations $[Ir(msppz)_2(\mathbf{4})]^+$ and $[Ir(msppz)_2(\mathbf{7})]^+$. The calculated inter-centroid distance of 3.80 Å for $[Ir(msppz)_2(\mathbf{7})]^+$ slightly overestimates the X-ray value of 3.59 Å. This mismatch most likely arises from packing forces acting in the crystal. The computed twisting angle of 16.6° between the two pyridine rings and the pendant phenyl ring being twisted through 58.5° (with respect to the pyridine ring containing N2) represents the experimental data (15.8 and 55.0°) in good analogy again. Whilst the N^N ligand in the complex cation $[Ir(msppz)_2(\mathbf{3})]^+$ is predicted to be close to planarity (twisting angle of (1.4°), a distortion of 16.5° is computed for $[Ir(msppz)_2(\mathbf{4})]^+$ upon introduction of the phenyl ring G. Near planarity for the ancillary ligand is also calculated for complexes with N^N = **1**, **3** and **8**.

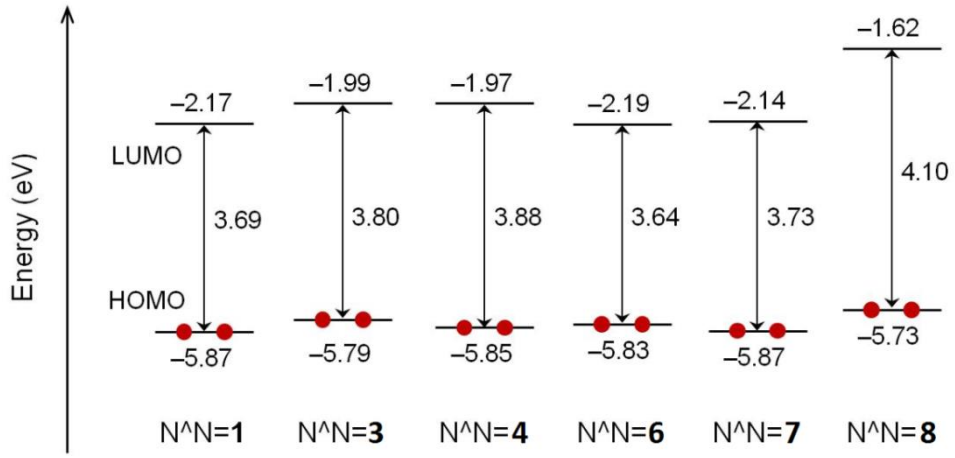

Figure 3.6 Energy diagram representing the energies in eV calculated for the HOMOs and the LUMOs of $[Ir(msppz)_2(N^N)][PF_6]$ (N^N = **1**, **3**, **4**, **6**-**8**).[37]

All calculated energies for the HOMO and LUMO levels of all complexes are depicted in Figure 3.6. In Figure 3.7 the molecular orbital distribution computed for $[Ir(msppz)_2(\mathbf{1})]^+$ and $[Ir(msppz)_2(\mathbf{8})]^+$ are shown as two representative example compounds. The substitution pattern of the N^N ligand has a large effect on the energy of the LUMO because it is fully localized on the ancillary ligand as can be seen in Figure 3.7. The electron-donating ^{t}Bu and NMe_2 substituents lead to a significant increase of the energy of the LUMO on going from $[Ir(msppz)_2(\mathbf{1})]^+$ (–2.17 eV) to $[Ir(msppz)_2(\mathbf{3})]^+$ (–1.99 eV) and especially to $[Ir(msppz)_2(\mathbf{8})]^+$ (–1.62 eV) verifying the cathodic shift measured for the first reduction potentials of the complexes N^N = **3** (–1.85 V) and N^N = **8** (–2.17 V) compared to N^N = **1** (–1.68 V) in Section 3.4.

The HOMO is mainly localized on the cyclometallating ligands and the Ir(III) center, however the substitution pattern of the N^N ligand has a measurable effect on this orbital and hence on the oxidation potential. The HOMO is slightly destabilized by the electron-donating ^{t}Bu and NMe_2 substituents in $[Ir(msppz)_2(\mathbf{3})]^+$ (–5.79 eV) and $[Ir(msppz)_2(\mathbf{8})]^+$ (–5.73 eV) compared to $[Ir(msppz)_2(\mathbf{1})]^+$ (–5.87 eV). Again, this is consistent with the electrochemical shift observed for the first oxidation potential passing from $[Ir(msppz)_2(\mathbf{1})]^+$ (+1.27 V) to $[Ir(msppz)_2(\mathbf{3})]^+$ (+1.19 V) and $[Ir(msppz)_2(\mathbf{8})]^+$ (+1.05 V) (Table 3.1). The pendant phenyl ring introduced in $[Ir(msppz)_2(\mathbf{4})]^+$ partially compensates for the effect of the ^{t}Bu substituents resulting in similar HOMO energies as for $[Ir(msppz)_2(\mathbf{1})]^+$ (–5.85 and –5.87 eV) as well as very close oxidation potentials (+1.24 and +1.27 V, respectively).

In accordance to the electrochemical observations, SMe groups have no remarkable effect on the calculated HOMO and LUMO energies resulting in a HOMO-LUMO gap for N^N = **6** (3.64 eV) and N^N = **7** (3.73 eV) being close to 3.69 eV for $[Ir(msppz)_2(\mathbf{1})]^+$. For complexes with N^N = **3** and **4** this gap increases to an intermediate value of approximately 3.85 eV and to a maximum of 4.10 eV for the complex cation containing most electron-donating NMe_2 groups, $[Ir(msppz)_2(\mathbf{8})]^+$. This trend underlines the evolution observed for the electrochemical gap which increases from approximately 2.94 V on going from complex with N^N = **1**, **6**, and **7** to approximately 3.03 V for N^N = **3** and **4,** reaching a maximum of 3.22 V for complex with ancillary ligand **8** (Table 3.1), perfectly corresponding to the blue-shifts observed in the solution photoluminescence spectra (Table 3.2).

The energies predicted for the HOMO (–5.73 eV), LUMO (–1.62 eV) and the HOMO–LUMO gap (4.11 eV) for $[Ir(msppz)_2(\mathbf{8})]^+$ are almost identical to those previously reported for $[Ir(dfppz)_2(\mathbf{8})]^+$ (–5.70, –1.33 and 4.07 eV, respectively).[80] The electrochemical potentials for these two complexes

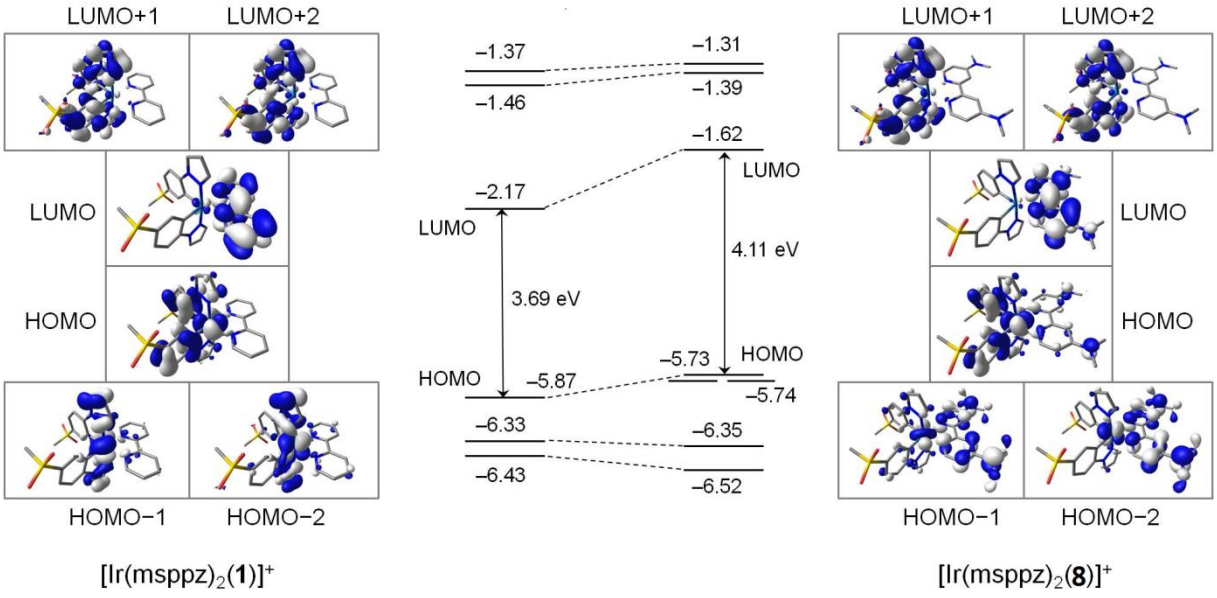

Figure 3.7 Schematic representation showing the electron density contours (0.03 e bohr^{-3}) and energies calculated for HOMO and LUMO of $[Ir(msppz)_2(\mathbf{1})]^+$ (left) and $[Ir(msppz)_2(\mathbf{8})]^+$ (right), hydrogen atoms have been omitted.[37]

correlate even better with $[Ir(msppz)_2(\mathbf{4})]^+$ ($E_{1/2}^{ox}$ = +1.05 V, $E_{1/2}^{red}$ = –2.17 V, $\Delta E_{1/2}$ = 3.22 V) and $[Ir(dfppz)_2(\mathbf{4})]^+$ ($E_{1/2}^{ox}$ = +1.04 V, $E_{1/2}^{red}$ = –2.15 V, $\Delta E_{1/2}$ = 3.19 V) demonstrating that the methyl sulfone substituent attached to the C^N ligand has a similar electron-withdrawing ability as the fluoro substituents in the $[dfppz]^-$ ligand.

The atomic orbital composition calculated for the HOMO and the LUMO predict that the lowest-energy triplet state arises from a mixed metal-to-ligand/ligand-to-ligand charge transfer (MLCT/LLCT) as already stated for analogous $[Ir(C^N)_2(N^N)]^+$ complexes.[47],[60],[74],[80],[89],[90] Nevertheless, not every complex in the series $[Ir(msppz)_2(N^N)][PF_6]$ (N^N = **1**, **3**, **4**, **6**-**8**) possesses identical molecular orbital distributions. Figure 3.7 (left) clearly shows the HOMO–1 and HOMO–2 of $[Ir(msppz)_2(\mathbf{1})]^+$ being well separated in energy from the HOMO and are localized on the Ir(III)-pyrazole environment which is also the case for complexes with N^N = **3**, **4**, **6** and **7**. In $[Ir(msppz)_2(\mathbf{8})]^+$, the HOMO–1 and HOMO–2 are almost degenerate with the HOMO, and are assigned to combinations of Ir(t_{2g}) and π orbitals of the ancillary ligand (Figure 3.7 right). The higher energy of these orbitals originates from the strongly electron-donating NMe_2 substituents and may change the nature of the emitting state.

Further investigations about the origin of the emitting excited state were performed by fully optimizing the electronic and molecular structures of the lowest triplet state (T_1) using the spin-unrestricted UB3LYP approach. After full-geometry relaxation, the T_1 state is calculated to lie in the range 2.66−2.84 eV above S_0 (see adiabatic energy differences ΔE in Figure 3.8a).

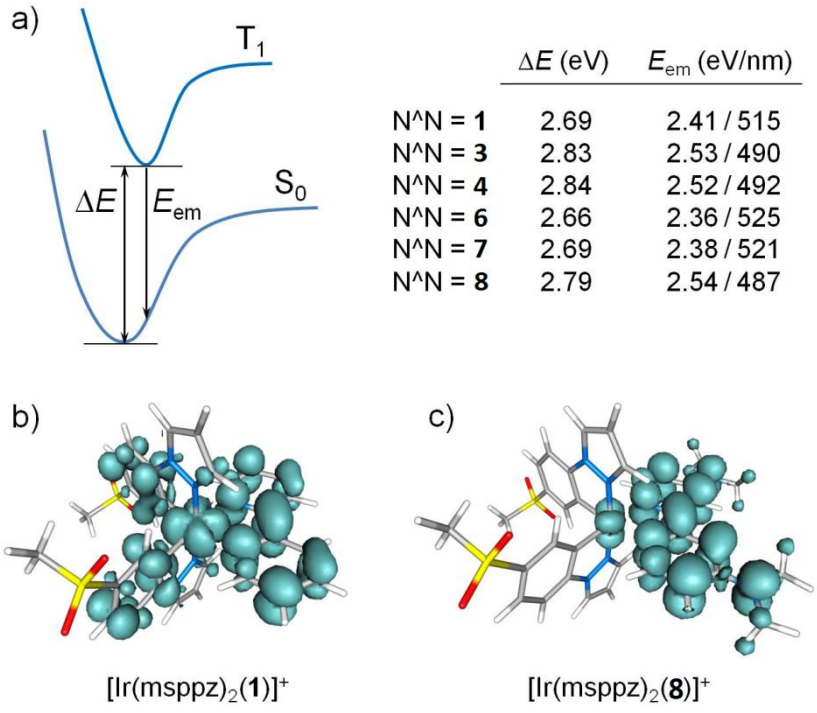

Figure 3.8 a) Schematic energy diagram of the adiabatic energy difference (ΔE) between the fully relaxed S_0 and T_1 states and the emission energy (E_{em}) computed for complexes $[Ir(msppz)_2(N^N)][PF_6]$ (N^N = **1**, **3**, **4**, **6**-**8**). Unpaired-electron spin density contours (0.003 e $bohr^{-3}$) calculated for the fully relaxed T_1 state of b) $[Ir(msppz)_2(\mathbf{1})]^+$ and c) $[Ir(msppz)_2(\mathbf{8})]^+$.[37]

These values coincide with those predicted for analogous $[Ir(dfppz)_2(N^\wedge N)]^+$ complexes (2.69–2.84 eV) and are significantly larger than computed for $[Ir(ppy)_2(\mathbf{1})]^+$ (2.40 eV).[80] The T_1 state for complexes $[Ir(msppz)_2(N^\wedge N)]^+$ with N^N = **1**, **3**, **4**, **6** and **7**, mainly arises from the HOMO → LUMO monoexcitation based on an electron transfer from the Ir-C^N environment to the N^N ligand. Computationally, this is highlighted in Figure 3.8b, wherein the spin density distribution calculated for $[Ir(msppz)_2(\mathbf{1})]^+$ (Ir: 0.48e, msppz: 0.49e, **1**: 1.03e) perfectly matches the topology of the HOMO → LUMO excitation depicted in Figure 3.7. It is noteworthy, that a small contraction of the coordination sphere of the Ir(III) center results upon the electron transfer to the T_1 state (biggest change calculated for $Ir-N_{1b}$: 2.321 Å in S_0 to 2.245 Å in T_1 for $[Ir(msppz)_2(\mathbf{4})]^+$). Furthermore, the twisting angle within the bpy unit slightly decreases in complexes with N^N = **4** and **7** (10.4° in T_1 compared to 16.6 in S_0), whereby the intra-cation π-stacking is preserved.

For complexes with ancillary ligands **1**, **3**, **4, 6** and **7** theoretical calculations predict the emitting T_1 state to possess mixed ^{3}MLCT/^{3}LLCT character, which is consistent with the broad unstructured shape of the photoluminescence emission bands (see Figure 3.4). In contradiction for $[Ir(msppz)_2(\mathbf{8})]^+$ the T_1 state converges to a π-π* ligand-centered (^{3}LC) triplet of the ligand **8** with a minor contribution from the Ir(III) metal center (Figure 3.8c). The reason for this different emission behavior lies in the HOMO–1 and HOMO–2 which are very close in energy (–5.74 eV) to the HOMO (–5.73 eV) and mainly reside on the N^N ligand (see Figure 3.7 right). As a result the HOMO–2 → LUMO and HOMO–1 → LUMO excitations belong to ^{3}LC states being lower in energy than the HOMO → LUMO excitation and therefore the emitting T_1 state is of predominantly ^{3}LC character. These findings might explain the lower PLQY measured for this compound. The vertical energy difference between T_1 and S_0 corresponding to the phosphorescence emission energy (Figure 3.8) was computed by a single-point calculation of S_0 at the optimized minimum-energy geometry of T_1. The obtained vertical emission energies shift to the blue when comparing complexes with N^N = **3** (490 nm), **4** (492 nm) and **8** (487 nm) to the complexes with N^N = **1** (515 nm), **6** (525 nm) and **7** (521 nm), verifying the trend observed for the experimentally determined emission maxima in CH_3CN (Table 3.2). It is again demonstrated that the methyl sulfone substituent in $[msppz]^-$ has an analogous effect as the fluorine atoms in $[dfppz]^-$. A perfect example is the emission energy calculated for $[Ir(msppz)_2(\mathbf{8})]^+$ (2.54 eV, 487 nm) being nearly identical to the one computed for $[Ir(dfppz)_2(\mathbf{8})]^+$ (2.53 eV, 488 nm), which are unambiguously consistent with the experimental data (492 and 493 nm, respectively).[80] These results undoubtedly support the use of electron-withdrawing sulfone substituents as an alternative method to reach similar blue-shifts as fluorine atoms.

3.7 Electroluminescence and Device Data

The electroluminescent properties of this series of complexes were tested in LEEC devices with the exception of [Ir(msppz)$_2$(**8**)][PF$_6$] whose PLQY in device configuration was too poor (Table 3.2). The electroluminescence spectra are depicted in Figure 3.9 left and are similar to those recorded by photo-excitation (Figure 3.5 right). Although the emission maxima range from 495 to 545 nm the relatively broad bands result in green emission in the CIE color space (Figure 3.9 right) for all complexes.

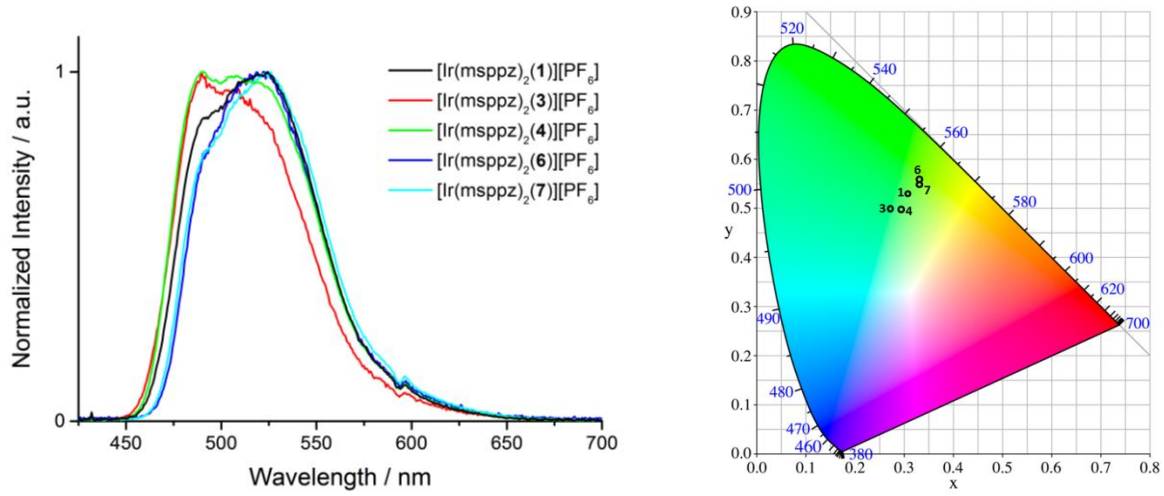

Figure 3.9 (Left) Normalized electroluminescence spectra of [Ir(msppz)$_2$(N^N)][PF$_6$] (N^N = **1**, **3**, **4**, **6**-**8**) in LEECs and (right) the respective x and y coordinates in the CIE color space.

LEEC device performances were examined by operating them under a block-wave pulsed-current driving scheme at 1000 Hz with 50% duty cycle and average (over the on- and off-pulse) current densities of 100, 50 and 25 A m^{-2}. This operation mode leads to higher stabilities and faster turn-on times than using a constant current. All complexes perform in a similar way independent of the different N^N ligands. As an example, for the best performing LEEC containing [Ir(msppz)$_2$(**1**)][PF$_6$], the luminance, voltage and efficiency versus time are shown in Figure 3.10 and the data for all compounds are listed in Table 3.3. Immediately after turning the devices on, the average applied voltage drops rapidly over the first seconds and finally remains constant for the duration of the experiment. At the beginning, high initial barriers for electron and hole injection require a higher voltage to keep the applied current density constant. Upon applying the high voltage, fast ionic motion is induced, reducing the injection barrier which leads to a gradual decrease of the operation voltage down to a value needed for the bulk carrier transport. The luminance, on the other hand, decreases with decreasing current density but this decrease is not proportional to the decrease of the current densities in all devices, leading to different power efficiencies and efficacies.

For devices containing complexes with N^N = **4**, **6** and **7**, the efficacy is independent of the current density, in contrast to LEECs based on [Ir(msppz)$_2$(**1**)][PF$_6$] and [Ir(msppz)$_2$(**3**)][PF$_6$], for which the

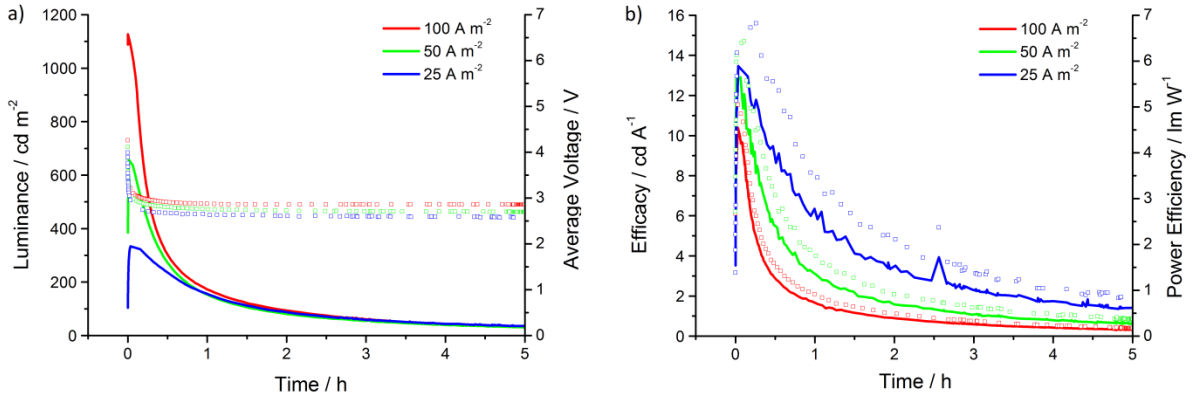

Figure 3.10 LEEC device performances of [Ir(msppz)$_2$(**1**)][PF$_6$] at different average current densities of 100, 50 and 25 A m^{-2}. a) Luminance (solid lines) and average voltage (open squares). b) Efficacy (solid lines) and power efficiency (open squares).

efficacy strongly increases when reducing the current density. It can be concluded that LEECs built of the latter two complexes are rather optimized and when reducing the current density less exciton quenching occurs and therefore higher relative luminance and efficiencies can be reached. Furthermore it appears that the efficiency of the devices based on complexes with N^N = **4**, **6** and **7** is limited by other factors explaining the lower performances obtained for these complexes.

The short turn-on time for all devices is a consequence of the pulsed-current driving mode. However, the lifetime $t_{1/2}$ of the LEEC devices is only a few minutes but lies within the time scale observed for

Table 3.3 Performances of the LEEC devices containing [Ir(msppz)$_2$(N^N)][PF$_6$] (N^N = **1**, **3**, **4**, **6** and **7**) operating with a block-wave pulsed current at a frequency of 1000 Hz and a 50% duty cycle at three different current densities.

Complex with N^N	Current Density / A m^{-2}	t_{on} [a] / s	L_{max} / cd m^{-2}	$t_{1/2}$ / min	Efficacy / cd A^{-1}	Power Efficiency / lm W^{-1}	EQE [b] / %
1	25	< 5	334	54	13.5	6.8	4.3
	50	< 5	657	23	12.8	6.4	4.1
	100	< 5	1127	14	10.4	5.0	3.3
3	25	< 5	80	0.2	2.7	0.9	0.9
	50	7	890	3.0	15.5	5.7	4.9
	100	< 5	992	3.0	9.3	3.0	2.9
4	25	< 5	238	12	9.4	4.4	2.9
	50	< 5	338	5.4	6.8	3.1	2.1
	100	< 5	853	3.3	8.1	3.2	2.5
6	25	< 5	125	7.7	5.1	2.5	1.6
	50	19	254	4.0	4.7	2.0	1.4
	100	< 5	790	1.5	7.2	2.2	2.2
7	50	350	43	35	0.8	0.4	0.2
	100	< 5	796	3.1	7.3	2.4	2.3

[a] Taken as the time needed to reach 100 cd m^{-2} and if the maximum luminance (L_{max}) is less than 100 cd m^{-2}, t_{on} is taken as the time to reach maximum luminance. [b] EQE = external quantum efficiency.

other green and green/blue-emitting LEECs. Previous studies suggested that the stability for LEECs was related to the number of fluorine atoms present in a complex by decreasing the lifetime with the increasing number of fluorine atoms.[84] However, this series of [Ir(msppz)$_2$(N^N)][PF$_6$] complexes in which no fluorine atoms are used still results in poor stabilities, and suggests that the presence of fluorines is not the only limiting factor for green and blue-emitting LEECs.

3.8 Conclusion

A series of six green-emitting cyclometallated Ir(III) complexes of the type [Ir(msppz)$_2$(N^N)][PF$_6$] (N^N = **1**, **3**, **4**, **6**-**8**) based on an electron-withdrawing methyl sulfone substituent on the C^N ligand were successfully synthesized and totally characterized. The use of methyl sulfone groups in this type of complex is a new strategy. The sulfone substituent leads to a blue-shifted emission when compared to Ir(III) complexes based on unsubstituted phenylpyrazole C^N ligands. The solution emission maxima within this series of complexes are further blue-shifted in the range from 518 nm of [Ir(msppz)$_2$(**1**)][PF$_6$] to 492 nm of [Ir(msppz)$_2$(**8**)][PF$_6$] upon introducing electron-donating ^{t}Bu and NMe$_2$ substituents on the N^N ligand. The complexes exhibit very high PLQYs when dispersed in a thin PMMA film (> 85% for N^N **1**, **3**, **4**, **6** and 65% for **8**). In device configuration, the best complex still exhibits a PLQY of 85% and is remarkably high considering the concentration in a film is over 90 wt%. This very small decrease in the quantum yield indicates a very small degree of exciton quenching between neighboring complexes. When operating in LEEC devices, the complexes exhibit green emission after a short turn-on time with good efficiencies at high luminance values. All these values are similar to analogous Ir(III) complexes based on [dfppz]$^-$ C^N ligands indicating that [msppz]$^-$ is suitable for the use as a fluorine-free cyclometallating ligand. However, despite strictly omitting fluorine atoms from the complexes, the lifetime in LEECs does not exceed several minutes. Therefore the presence of fluorine atoms is not the only reason for the low device stability of LEECs containing wide-band-gap iTMCs.

3.9 Experimental

2,2'-bipyridine (**1**) and 4,4'-di-*tert*-butyl-2,2'-bipyridine (**3**) were purchased from Sigma Aldrich and used as supplied.

3.9.1 Hmsppz

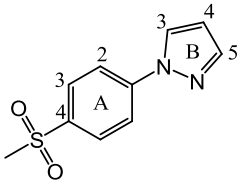

4-Bromophenyl methyl sulfone (5.00 g, 21.1 mmol, 1.00 eq), pyrazole (2.15 g, 31.6 mmol, 1.50 eq), CuI (0.401 g, 2.11 mmol, 0.100 eq) K_2CO_3 (8.73 g, 63.2 mmol, 3.00 eq) and L-proline (0.485 g, 4.21 mmol, 0.200 eq) were reacted in dry DMSO (120 mL) under inert atmosphere at 130 °C for 24 h. Aqueous NH_4OH (25%, 200 mL) and H_2O (100 mL) were added. The formed precipitate was filtered off, dissolved in CH_2Cl_2 and washed with aqueous NH_4OH (25%, 1x) and H_2O (2x), dried over $MgSO_4$ and the residual solvent was evaporated under reduced pressure. Pure product was obtained by column chromatography (Fluka silica gel 60, 0.040–0.063 mm; CH_2Cl_2:ethyl acetate 5:1) as an off-white solid (2.60 g, 0.012 mmol, 56.9%).

M.p. 138.4 °C

^{1}H NMR (500 MHz, CD_3CN, 295 K) δ/ppm 8.26 (dd, J = 2.5, 0.4 Hz, 1H, $H^{B3/B5}$), 8.01 (s, 4H, H^{A2+A3}), 7.77 (d, J = 1.6 Hz, 1H, $H^{B3/B5}$), 6.57 (dd, J = 2.6, 1.7 Hz, 1H, H^{B4}), 3.09 (s, 3H, H^{Me}).

^{13}C NMR (126 MHz, CD_3CN, 295 K) δ/ppm 144.6 (C^{A1}), 143.2 ($C^{B3/B5}$), 139.0 (C^{A4}), 130.0 ($C^{A2/A3}$), 128.8 ($C^{B3/B5}$), 119.7 ($C^{A2/A3}$), 109.7 (C^{B4}), 44.6 (C^{Me}).

ESI-MS *m/z* 223.0; $[M + H]^+$ (base peak, calc. 223.1).

Found C 53.99, H 4.53, N 12.28; $C_{10}H_{10}N_2O_2S$ requires C 54.04, H 4.54, N 12.60.

3.9.2 [{Ir(msppz)$_2$(μ-Cl)}$_2$]

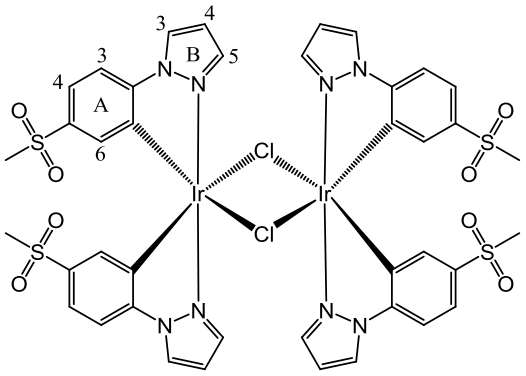

$IrCl_3.H_2O$ (1.00 g, 3.35 mmol, 1.00 eq) and Hmsppz (1.86 g, 9.37 mmol, 2.50 eq) were reacted under reflux in 2-ethoxyethanol (70 mL) and water (25 mL) for 24 h. The reaction mixture was allowed to cool down. H_2O (75 mL) was added and extracted with CH_2Cl_2 (3x). The combined organic layers were washed with H_2O (3 x 75 mL). The formed precipitate was collected by filtration and remaining CH_2Cl_2 was evaporated to dryness. The residual solid was washed with water and diethyl ether to give the pure product as pale yellow solid (1.50 g, 1.12 mmol, 66.8%). The product was used for the next steps after verification by NMR spectroscopy.

^{1}H NMR (500 MHz, [D_6]acetone, 295 K) δ/ppm 8.96 (d, J = 2.6 Hz, 1H, H^{B3}), 7.90 (d, J = 1.9 Hz,1H, H^{B5}), 7.73 (d, J = 8.3 Hz, 1H, H^{A3}), 7.42 (dd, J = 8.3, 2.0 Hz, 1H, H^{A4}), 7.05 (dd, J = 3.0, 2.0 Hz, 1H, H^{B4}), 6.54 (d, J = 2.0 Hz, 1H, H^{A6}), 2.80 (s, 3H, H^{Me}).

^{13}C NMR (126 MHz, [D_6]acetone, 295 K) δ/ppm 148.1 (C^{A2}), 142.8 (C^{B5}), 138.1 (C^{A5}), 130.9 (C^{A6}), 130.4 (C^{B3}), 128.9 (C^{A1}), 123.1 (C^{A4}), 112.3 (C^{A3}), 109.4 C^{B4}), 44.4 (C^{Me}).

3.9.3 [Ir(msppz)$_2$(**1**)][PF$_6$]

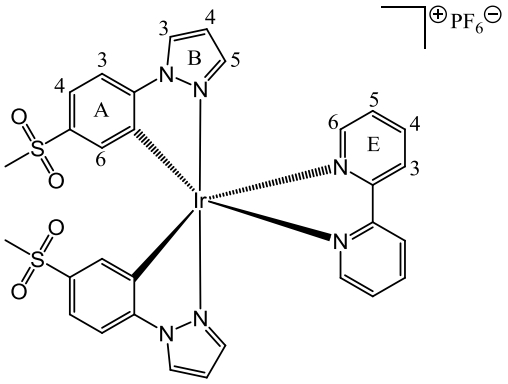

A suspension of [{Ir(msppz)$_2$(μ-Cl)}$_2$] (100 mg, 0.075 mmol, 1.00 eq) and 2,2'-bipyridine (23.4 mg, 0.150 mmol, 2.01 eq) in MeOH (20 mL) was reacted in a microwave reactor for 2 h at 120 °C. The greenish solution was allowed to reach room temperature and an excess of NH_4PF_6 (122 mg, 0.750 mmol, 10.0 eq) was added and stirred for 30 min. The product was precipitated by the addition of another 100 mg of NH_4PF_6. Recrystallization from MeOH followed by adding two equivalents of NH_4PF_6 which was washed-off with a minimum amount of cold MeOH finally afforded the pure compound as a yellow solid (75.0 mg, 0.080 mmol, 53.3%).

^{1}H NMR (500 MHz, CD_3CN) δ/ppm 8.52 (d, J = 8.2 Hz, 2H, H^{E3}), 8.50 (d, J = 3.0 Hz, 2H, H^{B3}), 8.17 (td, J = 8.0, 1.4 Hz, 2H, H^{E4}), 8.08 (d, J = 5.0 Hz, 2H, H^{E6}), 7.70–7.63 (overlapping m, 4H, H^{A3+A4}), 7.52 (ddd, J = 7.2, 5.4, 0.8 Hz, 2H, H^{E5}), 7.15 (d, J = 2.2 Hz, 2H, H^{B5}), 6.75 (d, J = 1.6 Hz, 2H, H^{A6}), 6.69 (t, J = 2.6 Hz, 2H, H^{B4}), 2.94 (s, 6H, H^{Me}).

^{13}C NMR (126 MHz, CD_3CN) δ/ppm 157.2 (C^{E2}), 152.4 (C^{E6}), 147.8 (C^{A2}), 141.4 (C^{B5}), 140.8 (C^{E4}), 139.1 (C^{A5}), 133.9 (C^{A1}), 131.77 (C^{A6}), 130.8 (C^{B3}), 129.1 (C^{E5}), 125.5 (C^{E3}), 124.4 (C^{A4}), 113.6 (C^{A3}), 110.2 (C^{B4}), 44.5 (C^{Me}).

IR (solid, $\tilde{\nu}$/cm^{-1}) 3148 (w), 2937 (w), 1628 (w), 1602 (w), 1556 (w), 1477 (m), 1471 (m), 1447 (m), 1409 (m), 1386 (m), 1344 (w), 1316 (m), 1301 (s), 1286 (s), 1273 (m), 1246 (w), 1218 (w), 1145 (s), 1120 (m), 1093 (m), 1072 (m), 1056 (m), 1046 (m), 1024 (w), 1008 (w), 956 (m), 916 (w), 832 (s), 825 (s), 789 (s), 779 (s), 761 (s), 743 (s), 731 (s), 724 (s), 668 (m), 643 (m), 609 (w), 584 (s), 548 (s).

UV-Vis λ/nm (ε/dm^3 mol^{-1} cm^{-1}) (CH_3CN, 2.50 x 10^{-5} mol L^{-1}) 252 (47 000), 272 sh (38 000), 312 (19 000), 331 (10 000), 365 sh (3 000).

Emission (CH_3CN, c = 2.50 x 10^{-5} mol L^{-1}, λ_{ex} = 366 nm): λ_{em} = 518 nm.

ESI-MS *m/z* 791.0 $[M - PF_6]^+$ (base peak, calc. 790.9).

Found C 37.95, H 3.04, N 8.71; $C_{30}H_{26}F_6IrN_6O_4PS_2$ + 1 H_2O requires C 37.77, H 2.96, N 8.81%.

3.9.4 [Ir(msppz)$_2$(**3**)][PF$_6$]

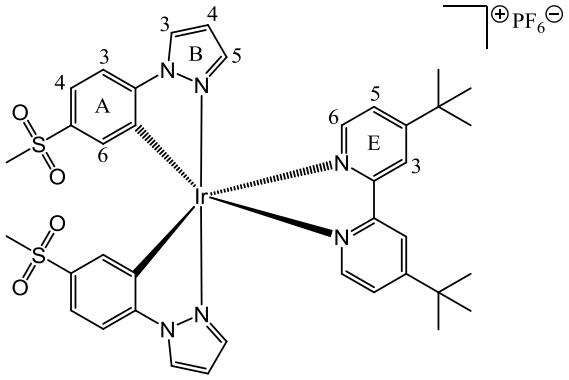

A suspension of [{Ir(msppz)$_2$(μ-Cl)}$_2$] (100 mg, 0.075 mmol, 1.00 eq) and **3** (40.2 mg, 0.150 mmol, 2.01 eq) in MeOH (20 mL) was reacted in the a microwave reactor for 2 h at 120 °C. The greenish solution was allowed to reach room temperature and an excess of NH_4PF_6 (122 mg, 0.750 mmol, 10.0 eq) was added and stirred for 30 min. Then the suspension was evaporated to dryness and purified by column chromatography (Merck aluminium oxide 90 standardized; CH_2Cl_2 → CH_2Cl_2:MeOH 100:1→ 100:5) followed by a subsequent column chromatography (Fluka silica gel 60, 0.040–0.063 mm; CH_2Cl_2 → CH_2Cl_2:MeOH 100:1 → 100:5). Recrystallization from MeCN/diethyl ether yielded the desired product as a yellow solid (55 mg, 0.053 mmol, 35.3%).

^{1}H NMR (500 MHz, CD_3CN) δ/ppm 8.50 (d, J = 3.0 Hz, 2H, H^{B3}), 8.49 (d, J = 2.0 Hz, 2H, H^{E3}), 7.95 (d, J = 5.9 Hz, 2H, H^{E6}), 7.71–7.62 (overlapping m, 4H, H^{A3+A4}), 7.51 (dd, J = 5.9, 2.0 Hz, 2H, H^{E5}), 7.11 (d, J = 2.3 Hz, 2H, H^{B5}), 6.75 (d, J = 1.8 Hz, 2H, H^{A6}), 6.70 (dd, J = 2.9, 2.4 Hz, 2H, H^{B4}), 2.94 (s, 6H, H^{Me}), 1.42 (s, 18H, H^{tBu}).

^{13}C NMR (126 MHz, CD_3CN) δ/ppm 165.6 (C^{E4}), 157.4 (C^{E2}), 151.8 (C^{E6}), 147.9 (C^{A2}), 141.1 (C^{B5}), 139.2 (C^{A5}), 134.5 (C^{A1}), 131.8 (C^{A6}), 130.8 (C^{B3}), 126.0 (C^{E5}), 124.3 (C^{A4}), 122.8 (C^{E3}), 113.6 (C^{A3}), 110.2 (C^{B4}), 44.5 (C^{Me}), 36.5 (C^{CtBu}), 30.4 (C^{tBu}).

IR (solid, $\tilde{\nu}$/cm^{-1}) 3126 (w), 2955 (w), 2874 (w), 1615 (m), 1577 (w), 1477 (m), 1411 (m), 1387 (w), 1367 (w), 1341 (w), 1315 (w), 1295 (m), 1274 (m), 1253 (m), 1145 (s), 1119 (m), 1093 (m), 1070 (m), 1057 (m), 1026 (w), 955 (m), 898 (w), 831 (s), 790 (s), 745 (s), 723 (m), 607 (m), 583 (m), 555 (s).

UV-Vis λ/nm (ε/L mol^{-1} cm^{-1}) (CH_3CN, 2.50 x 10^{-5} mol L^{-1}) 252 (48 000), 273 sh (36 000), 309 (19 000), 332 sh (10 000).

Emission (CH_3CN, c = 2.50 x 10^{-5} mol L^{-1}, λ_{ex} = 362 nm) λ_{em} = 504 nm.

ESI-MS *m/z* 903.3 $[M - PF_6]^+$ (base peak, calc. 903.2).

Found C 43.53, H 4.27, N 7.76; $C_{38}H_{42}F_6IrN_6O_4PS_2$ requires C 43.55, H 4.04, N 8.02%.

3.9.5 [Ir(msppz)$_2$(**4**)][PF$_6$]

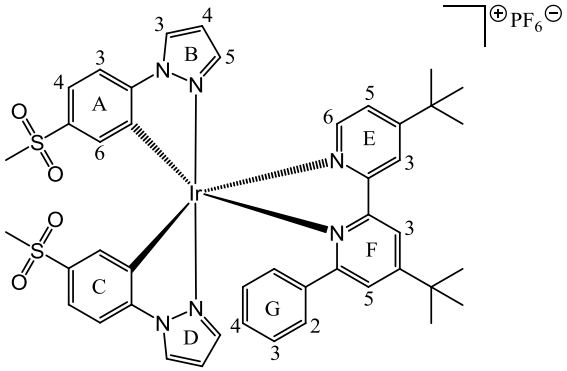

A suspension of [{Ir(msppz)$_2$(μ-Cl)}$_2$] (100 mg, 0.075 mmol, 1.00 eq) and **4** (36.3 mg, 0.150 mmol, 2.01 eq) in MeOH (20 mL) was reacted in a microwave reactor for 2 h at 120 °C. The greenish solution was allowed to reach room temperature and an excess of NH_4PF_6 (122 mg, 0.750 mmol, 10.0 eq) was added and stirred for 30 min. Then the suspension was evaporated to dryness and purified by two chromatographic columns (Merck aluminium oxide 90 standardized; CH_2Cl_2 → CH_2Cl_2:MeOH 100:1) followed by (Fluka silica gel 60, 0.040–0.063 mm; CH_2Cl_2 → CH_2Cl_2:MeOH 100:1). Recrystallization from MeCN/diethyl ether afforded the desired product as a pale yellow solid (106 mg, 0.094 mmol, 62.7%).

^{1}H NMR (500 MHz, CD_3CN) δ/ppm 8.49 (overlapping m, 2H, H^{D3+F3}), 8.45 (d, J = 1.8 Hz, 1H, H^{E3}), 8.34 (dd, J = 3.1, 0.6 Hz, 1H, H^{B3}), 8.05 (dd, J = 5.9, 0.6 Hz, 1H, H^{E6}), 7.57 (d, J = 1.9 Hz, 1H, H^{F5}), 7.54 (dd, J = 2.4, 0.6 Hz, 1H, H^{D5}), 7.53–7.49 (overlapping m, 2H, H^{A4+E5}), 7.45 (d, J = 8.4 Hz, 1H, H^{A3}), 7.14–7.10 (overlapping m, 2H, H^{C3+C4}), 6.98 (tt, J = 7.5, 1.3 Hz, 1H, H^{G4}), 6.90 (dd, J = 3.0, 2.3 Hz, 1H, H^{D4}), 6.83 (broad, H^{G3}) 6.66 (dd, J = 3.0, 2.3 Hz, 1H, H^{B4}), 6.44 (dd, J = 2.4, 0.5 Hz, 1H, H^{B5}), 6.40 (d, J = 2.0 Hz, 1H, H^{A6}), 6.02 (very broad, H^{G2}, see Section 3.2), 5.93 (dd, J = 1.6, 0.8 Hz, 1H, H^{C6}), 2.87 (s, 3H, $H^{Me\ ring\ A/C}$), 2.86 (s, 3H, $H^{Me\ ring\ A/C}$), 1.51 (s, 9H, $H^{t Bu\ ring\ F}$), 1.42 (s, 9H, $H^{t Bu\ ring\ E}$).

^{13}C NMR (126 MHz, CD_3CN) δ/ppm 165.9 (C^{F6}), 165.8 (C^{F4}), 165.5 (C^{E4}), 158.8 (C^{F2}), 158.2 (C^{E2}), 151.1 (C^{E6}), 147.3 (C^{A2}), 147.1 (C^{C2}), 141.7 (C^{D5}), 141.1 (C^{B5}), 140.1 (C^{G1}), 139.2 (C^{A5}), 137.4 (C^{C5}), 135.0 (C^{C1}), 131.4 (C^{A1}), 131.2 (C^{A6+C6}), 130.7 (C^{B3}), 130.6 (C^{D3}), 130.2 (C^{G4}), 127.1 (C^{F5}), 125.6 (C^{E5}), 124.3 (C^{A4}), 123.3 (C^{E3}), 122.4 (C^{C4}), 121.2 (C^{F3}), 113.3 (C^{A3}), 113.1 (C^{C3}), 110.4 (C^{B4}), 110.3 (C^{D4}), 44.50 ($C^{Me\ ring\ A/C}$), 44.47 ($C^{Me\ ring\ A/C}$), 36.55 ($C^{Ct Bu\ ring\ E/F}$), 36.5 ($C^{Ct Bu\ ring\ E/F}$), 30.4 ($C^{t Bu\ ring\ E/F}$), 30.3 ppm ($C^{t Bu\ ring\ E/F}$), $C^{G2/G3}$ not resolved.

IR (solid, $\tilde{\nu}$/cm^{-1}) 2961 (w), 2923 (w), 2874 (w), 1611 (w), 1579 (w), 1543 (w), 1480 (m), 1411 (w), 1388 (w), 1369 (w), 1339 (w), 1315 (w), 1294 (s), 1253 (w), 1206 (w), 1145 (s), 1121 (m), 1092 (w),

1071 (w), 1057 (w), 1028 (w), 954 (m), 915 (w), 874 (w), 831 (s), 790 (m), 744 (m), 722 (w), 700 (m), 666 (w), 653 (w), 643 (w), 582 (m), 555 (s).

UV-Vis λ/nm (ε/L mol^{-1} cm^{-1}) (CH_3CN, 2.50 x 10^{-5} mol L^{-1}) 259 (49 000), 318 (21 000).

Emission (CH_3CN, c = 2.50 x 10^{-5} mol L^{-1}, λ_{ex} = 360 nm) λ_{em} = 506 nm.

ESI-MS *m/z* 979.3 $[M - PF_6]^+$ (base peak, calc. 979.3).

Found C 46.66, H 4.20, N 7.79; $C_{44}H_{46}F_6IrN_6O_4PS_2$ requires C 47.01, H 4.12, N 7.48%.

3.9.6 [Ir(msppz)$_2$(**6**)][PF$_6$]

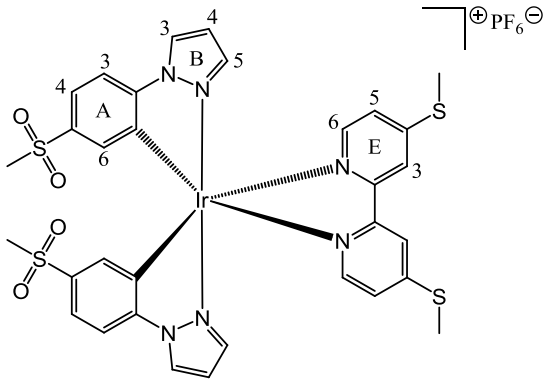

A suspension of [{Ir(msppz)$_2$(μ-Cl)}$_2$] (100 mg, 0.075 mmol, 1.00 eq) and **6** (37.2 mg, 0.15 mmol, 2.01 eq) in MeOH (20 mL) was heated in a microwave reactor for 2 h at 120 °C. The greenish solution was allowed to reach room temperature and an excess of NH_4PF_6 (122 mg, 0.750 mmol, 10.0 eq) was added and stirred for 30 min. Then the suspension was evaporated to dryness and purified by two chromatographic columns (Merck aluminium oxide 90 standardized; CH_2Cl_2 → CH_2Cl_2:MeOH 100:1→ 100:5) followed by (Fluka silica gel 60, 0.040–0.063 mm; CH_2Cl_2 → CH_2Cl_2:MeOH 100:1 → 100:5). Recrystallization from MeCN/diethyl ether yielded the desired product as a yellow solid (110 mg, 0.107 mmol, 71.3%).

^{1}H NMR (500 MHz, CD_3CN) δ/ppm 8.50 (dd, J = 3.0, 0.4 Hz, 2H, H^{B3}), 8.28 (d, J = 1.9 Hz, 2H, H^{E3}), 7.76 (d, J = 6.1 Hz, 2H, H^{E6}), 7.69–7.62 (overlapping m, 4H, H^{A3+A4}), 7.28 (dd, J = 6.1, 2.1 Hz, 2H, H^{E5}), 7.21 (dd, J = 2.2, 0.4 Hz, 2H, H^{B5}), 6.73 (dd, J = 1.9, 0.5 Hz, 2H, H^{A6}), 6.71 (dd, J = 2.9, 2.2 Hz, 2H, H^{B4}), 2.93 (s, 6H, H^{Me}), 2.62 (s, 6H, H^{SMe}).

^{13}C NMR (126 MHz, CD_3CN) δ/ppm 157.4 (C^{E4}), 155.8 (C^{E2}), 150.7 (C^{E6}), 147.9 (C^{A2}), 141.3 (C^{B5}), 139.1 (C^{A5}), 134.1 (C^{A1}), 131.8 (C^{A6}), 130.8 (C^{B3}), 124.3 (C^{A4}), 123.9 (C^{E5}), 121.5 (C^{E3}), 113.6 (C^{A3}), 110.1 (C^{B4}), 44.5 (C^{Me}), 14.4 (C^{SMe}).

IR (solid, $\tilde{\nu}$/cm^{-1}) 3136 (w), 2973 (w), 2926 (w), 2849 (w), 1599 (m), 1530 (w), 1475 (m), 1467 (m), 1415 (m), 1396 (m), 1386 (m), 1341 (w), 1313 (w), 1291 (s), 1273 (m), 1146 (s), 1119 (m), 1091 (m), 1070 (m), 1055 (m), 1021 (w), 958 (s), 917 (w), 889 (w), 877 (w), 841 (s), 827 (s), 816 (s), 794 (s), 744 (s), 709 (w), 668 (m), 653 (w), 586 (m), 564 (s), 555 (s).

UV-Vis λ/nm (ε/L mol^{-1} cm^{-1}) (CH_3CN, 1.00 x 10^{-5} mol L^{-1}) 266 (79 000), 291 sh (50 000), 325 sh (24 000), 352 sh (15 000).

Emission (CH_3CN, c = 1.00 x 10^{-5} mol L^{-1}, λ_{ex} = 366 nm) λ_{em} = 516 nm.

ESI-MS *m/z* 883.2 $[M - PF_6]^+$ (base peak, calc. 883.1).

Found C 36.87, H 3.37, N 7.77; $C_{32}H_{30}F_6IrN_6O_4PS_2$ + 1 H_2O requires C, 36.74, H 3.08, N 8.03%.

3.9.7 [Ir(msppz)$_2$(**7**)][PF$_6$]

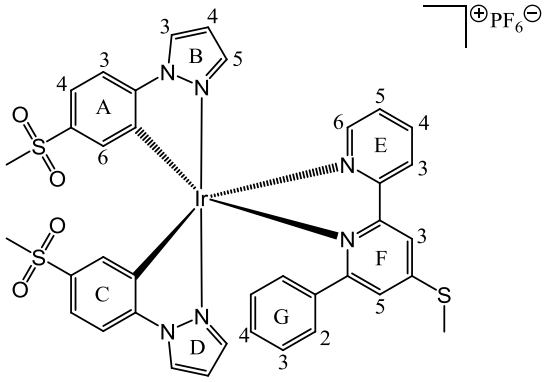

A suspension of [{Ir(msppz)$_2$(μ-Cl)}$_2$] (100 mg, 0.075 mmol, 1.00 eq) and **3** (41.7 mg, 0.150 mmol, 2.01 eq) in MeOH (20 mL) was reacted in a microwave for 2 h at 120 °C. The greenish solution was allowed to reach room temperature and an excess of NH_4PF_6 (122 mg, 0.750 mmol, 10.0 eq) was added and stirred for 30 min. Then the suspension was evaporated to dryness and purified by column chromatography (Merck aluminium oxide 90 standardized; CH_2Cl_2 → CH_2Cl_2:MeOH 100:1) followed by a subsequent column chromatography (Fluka silica gel 60, 0.040–0.063 mm; CH_2Cl_2 → CH_2Cl_2:MeOH 100:1). Recrystallization from MeCN/diethyl ether yielded in the desired product as a yellow solid (78.0 mg, 0.074 mmol, 49.3%).

^{1}H NMR (500 MHz, CD_3CN) δ/ppm 8.51 (d, J = 8.4 Hz, 1H, H^{E3}), 8.48 (d, J = 3.0 Hz, 1H, H^{D3}), 8.34 (d, J = 3.0 Hz, 1H, H^{B3}), 8.29 (d, J = 2.0 Hz, 1H, H^{F3}), 8.16 (overlapping m, 2H, H^{E4+E6}), 7.54 (d, J = 2.2 Hz, 1H, H^{D5}), 7.53–7.47 (overlapping m, 2H, H^{A4+E5}), 7.45 (d, J = 8.4 Hz, 1H, H^{A3}), 7.34 (d, J = 1.9 Hz, 1H, H^{F5}), 7.12 (overlapping m, 2H, H^{C3+C4}), 6.98 (t, J = 7.4 Hz, 1H, H^{G4}), 6.89 (t, J = 2.6 Hz, 1H, H^{D4}), 6.82 (broad, H^{G3}) 6.75 (d, J = 2.3 Hz, 1H, H^{B5}), 6.67 (t, J = 2.6 Hz, 1H, H^{B4}), 6.38 (d, J = 1.9 Hz, 1H, H^{A6}), 6.04 (very broad, H^{G2}, see Section 3.2), 5.94 (d, J = 1.4 Hz, 1H, H^{C6}), 2.86 (s, 3H, $H^{Me\ ring\ A}$), 2.84 (s, 3H, $H^{Me\ ring\ C}$), 2.69 (s, 3H, H^{SMe}).

^{13}C NMR (126 MHz, CD_3CN) δ/ppm 164.7 (C^{F6}), 157.7 (C^{F4}), 157.6 (C^{F2}), 158.2 (C^{E2}), 151.8 (C^{E6}), 147.3 (C^{A2}), 147.0 (C^{C2}), 141.9 (C^{D5}), 141.4 (C^{B5}), 140.6 (C^{E4}), 139.6 (C^{G1}), 139.1 (C^{A5}), 137.4 (C^{C5}), 134.5 (C^{C1}), 131.3 (C^{A1}), 131.2 (C^{C6}), 130.7 (C^{B3}), 130.7 (C^{A6}), 130.6 (C^{D3}), 130.3 (C^{G4}), 128.6 (C^{E5}), 125.9 (C^{E3}), 124.8 (C^{F5}), 124.4 (C^{A4}), 122.5 (C^{C4}), 119.9 (C^{F3}), 113.3 (C^{A3}), 113.1 (C^{C3}), 110.4 (C^{B4}), 110.3 (C^{D4}), 44.5 ($C^{Me\ rings\ A+C}$), 14.4 (C^{SMe}), $C^{G2/G3}$ not resolved.

IR (solid, $\tilde{\nu}$/cm^{-1}) 3128 (w), 2928 (w), 1603 (w), 1588 (m), 1528 (w), 1477 (m), 1411 (m), 1390 (w), 1341 (w), 1317 (w), 1301 (m), 1287 (m), 1274 (m), 1145 (s), 1121 (m), 1093 (m), 1071 (w), 1060 (m), 1029 (w), 1004 (w), 955 (s), 926 (w), 916 (w), 894 (w), 880 (w), 841 (s), 826 (s), 821 (s), 789 (m), 775 (m), 765 (m), 743 (s), 698 (m), 673 (w), 650 (w), 634 (w), 608 (w), 587 (s), 563 (s), 555 (s).

UV-Vis λ/nm (ε/L mol^{-1} cm^{-1}) (CH_3CN, 1.00 x 10^{-5} mol L^{-1}) 258 (51 000), 273 sh (46 000), 317 sh (24 000).

Emission (CH_3CN, c = 1.00 x 10^{-5} mol L^{-1}, λ_{ex} = 366 nm): λ_{em} = 516 nm.

ESI-MS *m/z* 913.2 $[M - PF_6]^+$ (base peak, calc. 913.1).

Found C 43.03, H 3.29, N 8.77; $C_{37}H_{32}F_6IrN_6O_4PS_3$ + 1 CH_3CN requires C 42.62 H 3.21, N 8.92%.

Crystallography $C_{39}H_{35}F_6IrN_7O_4PS_3$, M = 1099.14, yellow block, monoclinic, space group $P2_1/c$, a = 12.6915(12), b = 11.9740(11), c = 27.620(3) Å, β = 101.419(5)°, U = 4114.2(7) $Å^3$, Z = 4, D_c = 1.774 Mg m^{-3}, μ(Mo-K_α) = 3.515 mm^{-1}, T = 123 K. Total 117704 reflections, 11974 unique, R_{int} = 0.0381. Refinement of 11023 reflections (554 parameters) with $I > 2\sigma(I)$ converged at final $R1$ = 0.0185 ($R1$ all data = 0.0220), $wR2$ = 0.0413 ($wR2$ all data = 0.0429), gof = 1.028. CCDC 910854.

3.9.8 [Ir(msppz)$_2$(**8**)][PF$_6$]

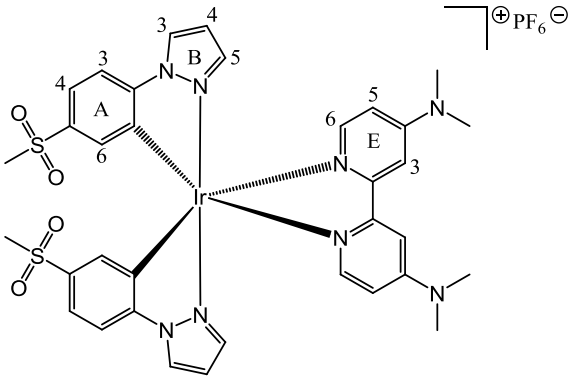

A suspension of [{Ir(msppz)$_2$(μ-Cl)}$_2$] (100 mg, 0.075 mmol, 1.00 eq) and **8** (36.3 mg, 0.150 mmol, 2.01 eq) in MeOH (20 mL) was heated in a microwave for 2 h at 120 °C. The greenish solution was allowed to reach room temperature and an excess of NH_4PF_6 (122 mg, 0.750 mmol, 10.0 eq) was added and stirred for 30 min. Then the suspension was evaporated to dryness and purified by two chromatographic columns (Fluka silica gel 60, 0.040–0.063 mm; CH_2Cl_2:acetone 4:1) followed by (Merck aluminium oxide 90 standardized; CH_2Cl_2:acetone 4:1). Recrystallization from MeCN/diethyl ether afforded the desired product as a pale yellow solid (25.0 mg, 0.025 mmol, 16.7%).

^{1}H NMR (500 MHz, CD_3CN) δ/ppm 8.48 (d, J = 2.7 Hz, 2H, H^{B3}), 7.69–7.57 (overlapping m, 4H, H^{A3+A4}), 7.51–7.39 (overlapping m, 4H, H^{E3+E6}), 7.13 (d, J = 2.0 Hz, 2H, H^{B5}), 6.76 (d, J = 1.9 Hz, 2H, H^{A6}), 6.70 (dd, J = 3.0, 2.3 Hz, 2H, H^{B4}), 6.57 (dd, J = 6.7, 2.8 Hz, 2H, H^{E5}), 3.15 (s, 12H, H^{NMe}), 2.92 (s, 6H, H^{Me}).

^{13}C NMR (126 MHz, CD_3CN) δ/ppm 157.3 (C^{E2}), 156.1 (C^{E4}), 150.1 (C^{E6}), 148.2 (C^{A2}), 140.6 (C^{B5}), 138.9 (C^{A5}), 136.2 (C^{A1}), 131.9 (C^{A6}), 130.4 (C^{B3}), 123.7 (C^{A4}), 113.3 (C^{A3}), 109.9 (C^{B4}), 109.8 (C^{E5}), 106.6 (C^{E3}), 44.5 (C^{NMe}), 40.0 (C^{Me}).

IR (solid, $\tilde{\nu}$/cm^{-1}) 3145 (w), 2935 (w), 1703 (w), 1615 (s), 1544 (w), 1522 (w), 1475 (m), 1433 (w), 1411 (m), 1381 (m), 1341 (w), 1314 (w), 1285 (s), 1225 (w), 1187 (w), 1144 (s), 1118 (m), 1092 (w), 1068 (w), 1055 (m), 1033 (m), 1016 (m), 954 (m), 916 (w), 831 (s), 825 (s), 815 (s), 790 (s), 744 (m), 723 (w), 668 (w), 587 (m), 555 (s), 55

0 (s), 519 (s).

UV-Vis λ/nm (ε/L mol^{-1} cm^{-1}) (CH_3CN, 1.00 x 10^{-5} mol L^{-1}) 262 (78 000), 279 sh (62 000), 298 sh (42 000), 334 sh (17 000), 381 sh (8 000).

Emission (CH_3CN, c = 2.50 x 10^{-5} mol L^{-1}, λ_{ex} = 366 nm) λ_{em} = 492 nm.

ESI-MS *m/z* 877.3 $[M - PF_6]^+$ (base peak, calc. 877.2).

Found C 38.77, H 3.40, N 10.60; $C_{34}H_{36}F_6IrN_8O_4PS_2$ + 2 H_2O requires C 38.60, H 3.81, N 10.59%.

Chapter 4

Chapter 4 Dual Emission – On the Way to White Light

4.1 Motivation

In Chapters 2 and 3 the aim was to synthetically color-tune cyclometallating Ir(III) complexes in a way so as to obtain red and blue emission however this resulted in orange and green emissive complexes, respectively. A third, challenging task is to reach white-light emission which can be achieved by several methods. Su et al.[91],[92] reported white-emitting LEECs by combining a blue-green with a red-emitting complex or by mixing three iTMCs of different colors (blue, red and orange).[93] Other strategies (not uniquely based on iTMCs) included multifluorophoric conjugated polymers,[94] a combined polymer-composite blue light-emitting layer with an orange ionic iridium complex[95] or employed a color conversion layer.[96] All these devices only work efficiently at low luminance values. The main reason for the small number and poor performances of white-emitting LEECs reported in the literature is largely ascribed to the lack of highly efficient and stable deep-blue-emitting complexes. However, to our knowledge, a dual-emitting iTMC in a LEEC device based on a single cyclometallating Ir(III) metal center for possible white-emission is still missing in the literature.

Herein a new approach of obtaining a dual-emitting complex for possible white-emission is presented following the principle of combining complementary colors. Therefore the synthesis of introducing a blue-emitting naphthalene unit in an orange-emitting Ir(III) complex of the type [Ir(naphppy)(N^N)][PF_6] (where Hnaphppy = 2,7-[bis(4-phenylpyridin-2-yl)-1*H*-1,4,7-trioxaheptyl] naphthalene and N^N = 4,4'-di-*tert*-butyl-6,6'-diphenyl-2,2'-bipyridine) is discussed together with NMR spectroscopic characterizations, electrochemical and photophysical properties in solution and thin-films as well as the performance in a LEEC device. Furthermore some preliminary mixing experiments of the free Hnaphppy ligand with the [Ir(naphppy)(N^N)][PF_6] complex and their photoluminescence behavior in solution and thin-films were investigated.

4.2 Synthesis and NMR Spectroscopic Characterization

The cyclometallating ligand Hnaphppy was synthesized following literature methods for similar compounds.[97],[98],[99] In the first step, 2,7-dihydroxynaphthalene was reacted with 2-(2-chloroethoxy) ethanol in DMF under basic conditions to yield the bis(alcohol)-functionalised 2,7-di[2-(2-hydroxy ethoxy)ethoxy]naphthalene] (OHnaph) which, in a second step, was converted to Hnaphppy with 2-(4-fluorophenyl)pyridine and NaH in dry DMF. The dimer [{Ir(naphppy)(μ-Cl)}$_2$] was prepared as described for [{Ir(msppz)$_2$(μ-Cl)}$_2$] (Section 3.2) but under much more dilute conditions to ensure that the two C^N coordination sites of [naphppy]$^{2-}$ coordinate to the same Ir(III) metal center.

In a new additional synthetic step, other than in the two previous chapters, the dimer was stirred in MeOH together with $AgPF_6$ to form a solvento complex of the type [Ir(naphppy)(MeOH)$_2$][PF_6]. A more detailed description for this newly introduced reaction step is given in Section 5.2. This intermediate solvento complex was used for the final reaction step without further purification. Therefore, according to an adapted procedure of Neve and co-workers,[76] [Ir(naphppy)(MeOH)$_2$][PF_6] and 4,4'-di-*tert*-butyl-6,6'-diphenyl-2,2'-bipyridine (**5**) were refluxed in MeOH to obtain complex [Ir(naphppy)(**5**)][PF_6]. Ligand **5** was synthesized according to a literature procedure.[100] Unfortunately, no crystals of X-ray quality could be grown of [Ir(naphppy)(**5**)][PF_6]. However, a peak at *m/z* = 1254.0 assigned to [M – PF_6]$^+$ detected with electrospray mass spectrometry together with an elemental analysis and full ^{1}H and ^{13}C NMR spectroscopic characterizations using standard 2D methods (COSY, NOESY, HMQC and HMBC) confirmed the correct structure shown in Scheme 4.1. For comparison reasons, [Ir(ppy)$_2$(**5**)][PF_6] was synthesized following a literature method.[76]

Complex [Ir(naphppy)(**5**)][PF_6] possesses C_2 symmetry as observed for other complexes with symmetrical N^N ligands such as [Ir(thpy)$_2$(**3**)][PF_6] or [Ir(msppz)$_2$(**6**)][PF_6] (see Sections 2.2 and 3.2). Following the atom labelling in Scheme 4.1, the ^{1}H NMR spectrum of [Ir(naphppy)(**5**)][PF_6]

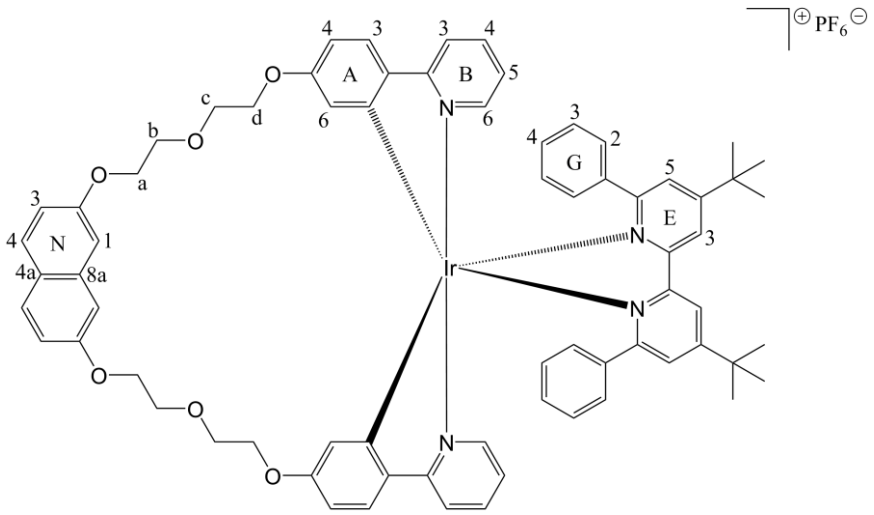

Scheme 4.1 Atom labelling for the structure of [Ir(naphppy)(**5**)][PF_6] used for the NMR spectroscopic assignment.

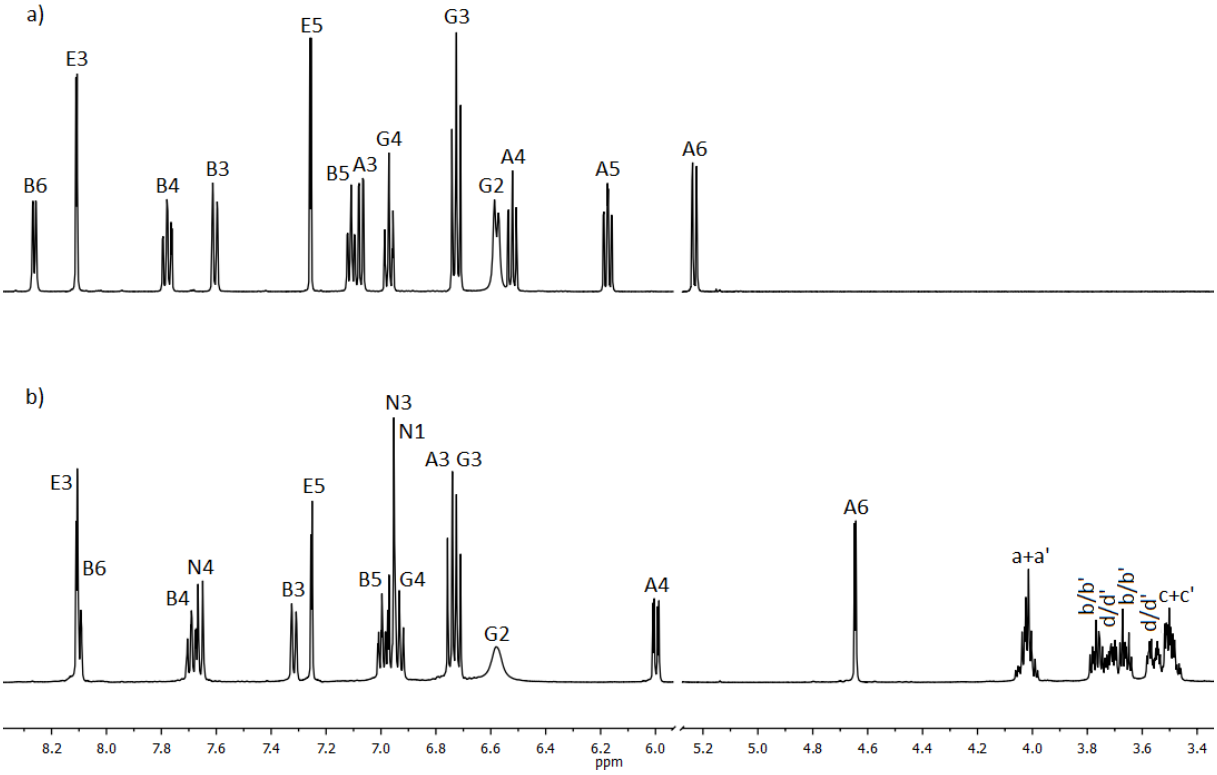

Figure 4.1 Room temperature 500 MHz ^{1}H NMR spectrum of (a) the aromatic region of [Ir(ppy)$_2$(**5**)][PF$_6$], and (b) the aromatic region and the resonances of the methylene groups of [Ir(naphppy)(**5**)][PF$_6$], each measured in CD_2Cl_2.

(Figure 4.1b) could be fully assigned starting with NOESY H^{Me}/H^{E3} and H^{Me}/H^{E5} cross-peaks, continued by a NOESY H^{E5}/H^{G2} cross-peak which allowed complete assignment of the N^N ligand. A further NOESY H^{G2}/H^{B6} cross-peak enabled one to distinguish between H^{B3} and H^{B6}. Consistent trends in the chemical shifts for the specific ^{13}C nuclei throughout the series of [Ir(naphppy)(**5**)][PF$_6$] and its precursors verified the accuracy of the assignment.

The two pendant phenyl rings G undergo hindered rotation on the NMR timescale as observed for the asymmetric complexes in Sections 2.2 and 3.2. But contrary to the asymmetric complexes in the previous chapters, only the resonance for H^{G2} (δ 6.58 ppm) appears as a broadened signal (see Figure 4.1b). It is noteworthy that the FWHM (≈ 23 Hz) of the H^{G2} signal in [Ir(naphppy)(**5**)][PF$_6$] is slightly smaller than for [Ir(thpy)$_2$(**4**)][PF$_6$] (≈ 28 Hz) but drastically different to [Ir(msppz)$_2$(**7**)][PF$_6$] (≈ 120 Hz). This observation together with the sharp signals for H^{G3} and H^{G4} indicate a faster rotation than observed in the previous complexes (e.g. in [Ir(thpy)$_2$(**4**)][PF$_6$] or [Ir(msppz)$_2$(**7**)][PF$_6$]). Also the fact that a broad H^{G2} but a sharp H^{G3} signal is observed is a consequence of the two H^{G2} signals for the static complex being at a much greater frequency difference than the two H^{G3} signals. In [Ir(ppy)$_2$(**5**)][PF$_6$], the proton signal H^{G2} (δ 6.58 ppm) appears as a slightly broadened doublet with a FWHM of ≈ 13 Hz (Figure 4.1a) which implies an even less hindered rotation of the G ring compared to [Ir(naphppy)(**5**)][PF$_6$]. This implies that the glycol chain in the latter complex sterically affects the rotation of the pendant phenyl ring G (Figure 4.2).

Table 4.1 Chemical shifts in the ^{1}H NMR spectroscopic data for protons H^{A4} and H^{A6} in [Ir(naphppy)(**5**)][PF_6] and [$Ir(ppy)_2$(**5**)][PF_6] and their respective chloride dimers.

Compound	Chemical shifts δ / ppm	
	H^{A4}	H^{A6}
[Ir(naphppy)(**5**)][PF_6]	6.00	4.65
[{Ir(naphppy)(μ-Cl)}$_2$]	6.33	5.32
[$Ir(ppy)_2$(**5**)][PF_6]	6.52	5.23
[{$Ir(ppy)_2$(μ-Cl)}$_2$]	6.61	5.87

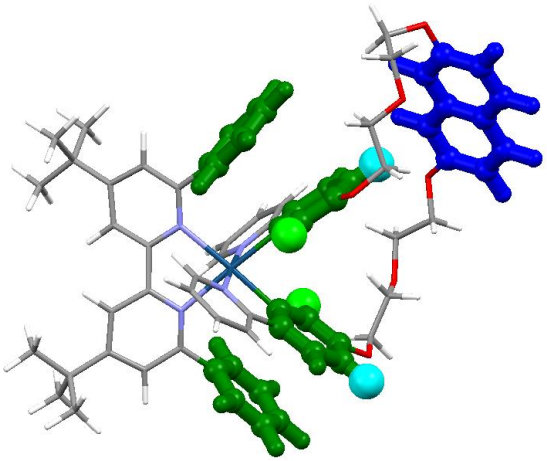

Figure 4.2 Modelled structure of [Ir(naphppy)(**5**)][PF_6] with H^{A4} highlighted in cyan (●) and H^{A6} in light green (●).

The two proton signals H^{A4} (δ 6.00 ppm) and H^{A6} (δ 4.65 ppm) of the cyclometallating phenyl ring in [Ir(naphppy)(**5**)][PF_6] are remarkably shifted to lower frequency compared to the corresponding resonances of the precursor [{Ir(naphppy)(μ-Cl)}$_2$] with chemical shifts of H^{A4} (δ 6.33 pmm) and H^{A6} (δ 5.32 ppm), measured in CD_2Cl_2 respectively (Table 4.1). Similar trends are observed for the chemical shifts on going from [$Ir(ppy)_2$(**5**)][PF_6] H^{A4} (δ 6.52 ppm) and H^{A6} (δ 5.23 ppm) to [{$Ir(ppy)_2$(μ-Cl)}$_2$] H^{A4} (δ 6.61 ppm) and H^{A6} (δ 5.87 ppm), each measured in CD_2Cl_2. Figure 4.2 depicts the highfield shifting effect for H^{A6} (●) arising from a combination of being sandwiched in a V-shaped cavity between the phenyl and pyridine ring (resulting from the double π-stacking phenyl rings, highlighted in dark green), and from the linking oxygen atom of the naphthyl glycol substituent. This can clearly be seen when the pendant phenyl rings and the naphthyl glycol substituent are omitted as in [$Ir(ppy)_2$(**3**)][PF_6], the proton resonances for H^{A4} (δ 6.94 ppm)[32] and H^{A6} (δ 6.37 ppm) appear significantly downfield compared to [$Ir(ppy)_2$(**5**)][PF_6] (δ 6.48 ppm) and H^{A6} (δ 5.29 ppm) (both measured in [D_6]-acetone). The chemical shift of the proton resonance for H^{A4} (marked with ● in Figure 4.2) is affected on the one hand by the linkage of the naphthyl glycol substituent in the 5-position of ring A, and on the other hand, by the fact that H^{A4} faces the π-cloud of the naphthyl domain. The latter possibility does not seem to have a large impact on the chemical shift since no NOESY cross-peaks are detected between the naphthyl unit and the phenyl pyridine domain of the C^N ligand nor the N^N ligand. Thus no π-stacking is expected to involve the naphthyl domain, which furthermore, has to swing back and forth on the NMR timescale from one H^{A4} to the other to keep the C_2-symmetric structure.

4.3 Electrochemical Properties

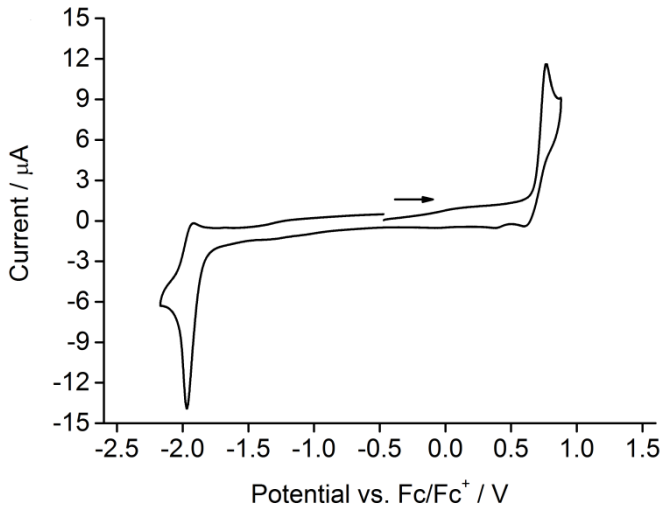

Figure 4.3 Cyclic voltammogram of [Ir(naphppy)(**5**)][PF_6] with respect to Fc/Fc^+, measured in dry CH_2Cl_2 solutions containing 0.1 M [$^nBu_4N$][PF_6] as supporting electrolyte at a scan rate of 0.1 V s^{-1}. (→ = direction of scan).

The cyclic voltammogram and redox potentials of [Ir(naphppy)(**5**)][PF_6] are shown in Figure 4.3. The complex exhibits an irreversible oxidation at +0.77 V and a quasi-reversible reduction at –1.96 V, which are comparable to the values obtained for [Ir(ppy)$_2$(**5**)][PF_6] (+0.81 and –1.94 V, respectively). This finding indicates that the naphthyl glycol linker minimally decreases $E_{1/2}^{ox}$ as a result of the electron-withdrawing oxygen atom attached on the 5-position of ring A. Furthermore, the redox behavior of complex [Ir(naphppy)(**5**)][PF_6] is not significantly influenced in the accessible solvent window (±1.8 V) resulting in similar $\Delta E_{1/2}$ of 2.73 and 2.75 V for [Ir(naphppy)(**5**)][PF_6] and [Ir(ppy)$_2$(**5**)][PF_6], respectively (Table 4.2). Therefore, the Ir (III) metal center and the phenyl ring of the C^N domain contribute to the HOMO while the LUMO fully resides on the N^N ligand corresponding to the results simulated for the related compound [Ir(ppy)$_2$(dpbpy)][PF_6] (dpbpy = 6,6'-diphenyl-2,2'-bipyridine).[78]

Table 4.2 Cyclic voltammetric data of [Ir(naphppy)(**5**)][PF_6] and [Ir(ppy)$_2$(**5**)][PF_6] with respect to Fc/Fc^+, measured in dry CH_2Cl_2 solutions containing 0.1 M [$^nBu_4N$][PF_6] as supporting electrolyte at a scan rate of 0.1 V s^{-1} (irr = irreversible, qr = quasi-reversible).

Compound	$E_{1/2}^{ox}$ / V	$E_{1/2}^{red}$ / V	$\Delta E_{1/2}$ / V
[Ir(naphppy)(**5**)][PF_6]	$+0.77^{irr}$	-1.96^{qr}	2.73
[Ir(ppy)$_2$(**5**)][PF_6]	$+0.81^{irr}$	-1.94^{irr}	2.75

4.4 Solution and Thin-film Photophysical Properties

To gain further insight into the possible dual-emitting properties of [Ir(naphppy)(**5**)][PF_6], the absorption (see Figure 4.4) and emission behavior (see Figure 4.5 and Figure 4.6) of the C^N ligand Hnaphppy, its precursor OHnaph and of N^N ligand **5** will also be discussed in this section together with the related complex [Ir(ppy)$_2$(**5**)][PF_6]. The photophysical data of these five compounds are summarized in Table 4.3 and the excited state lifetimes in Table 4.4.

The absorption spectra of Hnaphppy and OHnaph both exhibit an intense absorption band with maxima of 235 and 236 nm, respectively, (measured in CH_2Cl_2) arising from ligand-centered $\pi^* \leftarrow \pi$ transitions of the naphthalene domain. These values are very close to the solvent cutoff (230 nm for CH_2Cl_2). Absorption measurements with a maximum at 234 nm measured for Hnaphppy in a solvent with a higher energy cutoff such as CH_3CN (190 nm) verify the correctness of assignments for the CH_2Cl_2 absorption data. CH_3CN is usually avoided as a solvent for Ir(III) complexes due to the NMR spectroscopic evidence that this solvent can coordinate to Ir(III) in [Ir(C^N)$_2$(N^N)][PF_6] complexes causing ligand loss and complex decomposition. Therefore all the following photophysical measurements are performed in CH_2Cl_2 to exclude such possibilities. The maximum extinction coefficient of Hnaphppy is remarkably higher than for OHnaph indicating additional contribution from the ppy unit[101] to this band (Figure 4.4). Furthermore, the former compound possesses two additional bands at 265 and 283 nm tailing off to 335 nm while only some lower intensity ($\varepsilon < 5000$ dm^3 mol^{-1} cm^{-1}) transitions are present in OHnaph, and hence are assigned to originate mainly from the ppy ring system. N^N ligand **5** features similar absorption properties as Hnaphppy with bands at 237, 264 and 305 nm but of lower intensity, consistent with the absence of the naphthalene unit. The complex [Ir(naphppy)(**5**)][PF_6] exhibits an intense absorption band at 236 nm followed by a broad unstructured region up to 330 nm; both are assigned to ligand-centered $\pi^* \leftarrow \pi$ transitions of [naphppy]$^{2-}$ and **5**.

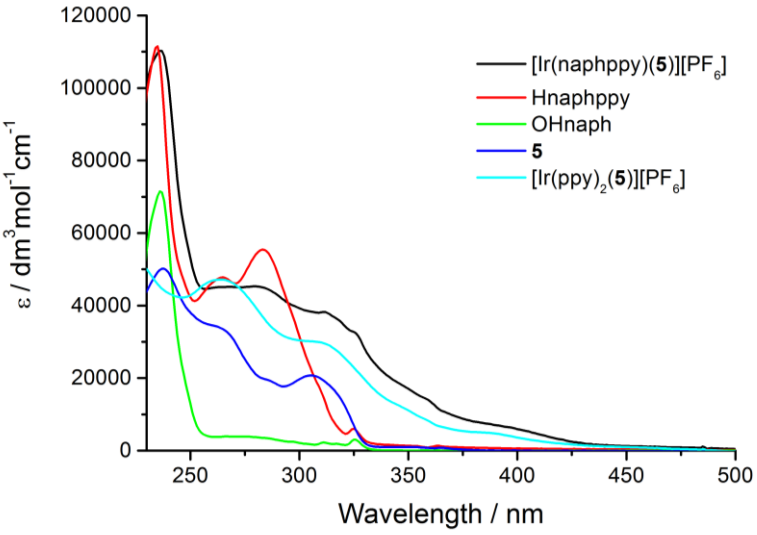

Figure 4.4 UV-Vis absorption spectra of [Ir(naphppy)(**5**)][PF_6], Hnaphppy, OHnaph, **5** and [Ir(ppy)$_2$(**5**)][PF_6] measured in 1.00 x 10^{-5} M CH_2Cl_2 solutions.

Identical extinction coefficients for the absorption maxima of Hnaphppy and [Ir(naphppy)(**5**)][PF_6] suggest this band originates mainly from the coordinated C^N ligand. Above 330 nm low intensity MLCT transitions can be observed. As expected, the absorption spectrum of [$Ir(ppy)_2$(**5**)][PF_6] features a similar shape as that of [Ir(naphppy)(**5**)][PF_6] without the intense high-energy naphthyl absorption band.

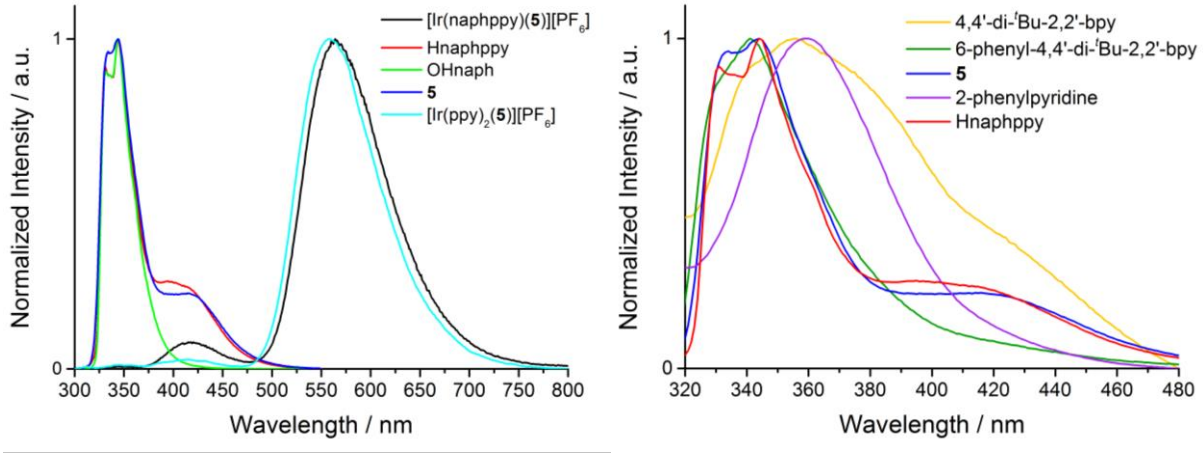

Figure 4.5 Photoluminescence spectra of (left) [Ir(naphppy)(**5**)][PF_6], Hnaphppy, OHnaph, **5** and [$Ir(ppy)_2$(**5**)][PF_6] and of (right) 4,4'-di-^{t}Bu-2,2'-bpy, 6-phenyl-4,4'-di-^{t}Bu-2,2'-bpy, **5**, 2-phenylpyridine and Hnaphppy all measured in 1.00 x 10^{-5} M CH_2Cl_2 solutions excited at 280 nm.

Upon photo-excitation at 280 nm, the emission spectra of Hnaphppy and OHnaph show identical maxima at 334 and 344 nm arising from the naphthyl unit (normalized spectra are shown in Figure 4.5). This observation is consistent with the emission maximum reported for the related compound 2,7-naphthalenediol (347 nm measured in 0.1 M H_2SO_4 solution).[102] Hnaphppy exhibits additional emission bands at 395 and 415 nm. Suspiciously, ancillary ligand **5** features an extremely similar photoluminescence spectrum as Hnaphppy. To clarify the correctness of these measurements, the photoluminescence of fresh solutions of **5** and the C^N ligands have been recorded several times and compared to the emissions of 4,4'-di-^{t}Bu-2,2'-bpy (**3**), 6-phenyl-4,4'-di-^{t}Bu-2,2'-bpy (**4**) and 2-phenylpyridine (Hppy) all measured under identical conditions (Figure 4.5 right). Each blank solution was tested for possible impurities before adding the compounds. The emission spectra were normalized to allow direct comparison since the emission of Hppy and **3** are of low intensity close to the detection limit (but **3** is consistent to reported data).[103] The latter two compounds are red-shifted and differ from the spectrum of Hnaphppy. Upon the introduction of a 6-phenyl ring in the bpy domain on going from **3** to **4,** the emission gains in intensity and adopts the peak shape of the emission band of ligand **5**. Thereby, the unexpected coincidence in the photoluminescence of **5** and Hnaphppy could be confirmed. The complex [Ir(naphppy)(**5**)][PF_6] shows two (one less intense and one predominant) clearly separated emissions at 420 and 564 nm, respectively. The latter band is described as a mixture of MLCT and LLCT due to the participation of the Ir(III) metal center and the ppy units of the C^N ligand in the HOMO whereas the LUMO resides on **5** which is consistent with the electrochemical data obtained in Section 4.3. Theoretical calculations are needed to gain a more

detailed picture of the excited-state nature of [Ir(naphppy)(**5**)][PF_6]. Nevertheless the emission maxima are in good agreement with the data reported for [Ir(ppy)$_2$(dpbpy)][PF_6] (579 nm)[78] and [Ir(ppy)$_2$(**5**)][PF_6] (555 nm)[100] which have no naphthalene-linked C^N ligand. Lepeltier and co-workers[100] have published the emission spectrum but give no data at wavelengths lower than 450 nm. The emission spectrum of [Ir(ppy)$_2$(**5**)][PF_6] was recorded below 450 nm where a second low-intensity emission band with a maximum at 415 nm is observed, similar to [Ir(naphppy)(**5**)][PF_6]. Considering these facts, the emission band at 420 nm being more pronounced in [Ir(naphppy)(**5**)][PF_6] is assumed to originate not uniquely from the naphthalene component but at least also from a contribution from ancillary ligand **5**. Since no maxima appear around 350 nm in the emission spectrum of [Ir(naphppy)(**5**)][PF_6], it can be argued that the 420 nm emission band does not arise from dissociated free ligand.

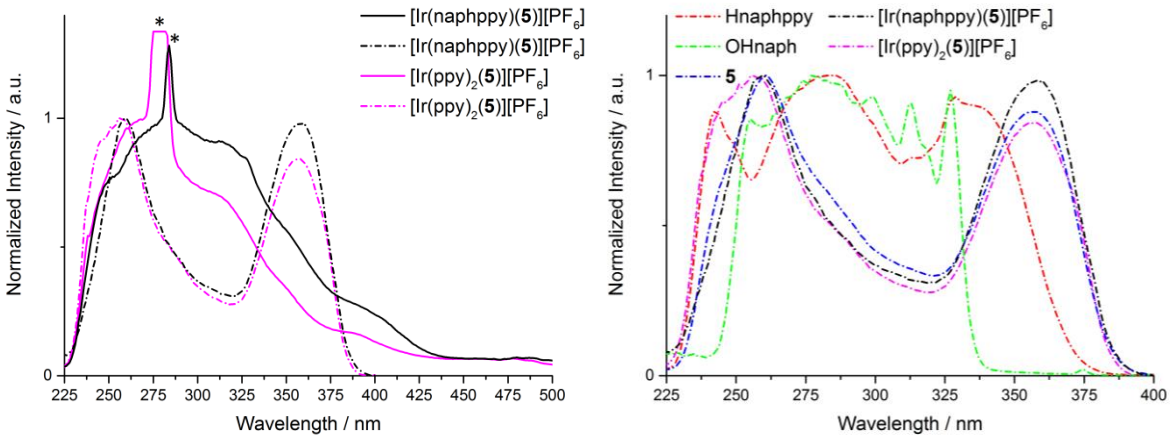

Figure 4.6 (Left) Excitation spectra measured for 1.00 x 10^{-5} M CH_2Cl_2 solutions containing [Ir(naphppy)(**5**)][PF_6] or [Ir(ppy)$_2$(**5**)][PF_6] with fixed emission wavelengths of 564 and 558 nm (solid line) and of 420 nm (dashed line), respectively (* upper harmonics of the fixed emissions at 564 and 558). (Right) Excitation spectra measured for 1.00 x 10^{-5} M CH_2Cl_2 solutions containing [Ir(naphppy)(**5**)][PF_6], [Ir(ppy)$_2$(**5**)][PF_6], Hnaphppy, OHnaph and **5** each at a fixed emission wavelength of 420 nm.

Excitation measurements of [Ir(naphppy)(**5**)][PF_6] and [Ir(ppy)$_2$(**5**)][PF_6] reveal the origins of the 564, 558 and 420 nm emissions. The low-energy MLCT emissions for both complexes arise from absorptions over the whole region from 230 to 500 nm featuring consistent shapes as in the absorption spectra (Figure 4.4) whereas the 420 nm emission results from two absorption bands at ≈ 258 and ≈ 358 nm (Figure 4.6 left). Comparing the latter excitation spectra to the ones obtained for Hnpahppy, OHnaph and **5** (Figure 4.6 right), both [Ir(naphppy)(**5**)][PF_6] and [Ir(ppy)$_2$(**5**)][PF_6] overlap with the naphthyl compounds but are nearly identical to N^N ligand **5**. This indicates that the high-energy emission arises from a fluorescent excited state of ligand **5** but it is not totally clear why the excitation spectra of [Ir(naphppy)(**5**)][PF_6] differ (in the regime < 400 nm) when looking at the different observation wavelengths. Although an extremely low concentration impurity could be responsible for such observations, the method of measuring and the reproducibility of recorded solutions of independently synthesized compounds makes it unlikely to be the case.

Even though the excited-state nature of [Ir(naphppy)(**5**)][PF_6] and [$Ir(ppy)_2$(**5**)][PF_6] is not totally understood so far, we attest the blue emission around 420 nm to be real, belonging to the two complexes. We suggest the photoluminescence properties to consist of the well-known MLCT/LLCT orange emission and a second, most likely a ligand-centered blue-fluorescent band attributed to ancillary ligand **5**. The level of the latter high-energy excited state is supposed to lie close enough to the 564 nm emission band to be thermally populated following a Boltzmann distribution. This could be proven when the emission intensity would decrease upon continuously cooling the sample down prohibiting the fluorescent excited state to be populated. Since no such measurements have been performed we cannot speak of two independent emissions which would allow to attribute [Ir(naphppy)(**5**)][PF_6] dual-emission property.

Table 4.3 Photophysical properties of Hnaphppy, OHnaph and **5** in solution and for [Ir(naphppy)(**5**)][PF_6] also as powder, diluted in a PMMA film and in device configuration.

Compound	Solution			Powder		Diluted Film[b]		Device configuration[c]	
	λ_{ex}^{max} / nm	λ_{em}^{max} / nm	Φ^a / %	λ_{em}^{max} / nm	Φ / %	λ_{em}^{max} / nm	Φ / %	λ_{em}^{max} / nm	Φ / %
[Ir(naphppy)(**5**)][PF_6]	236	420, 564	9	567	20	529	66	574	16
Hnaphppy	235	334, 344	15	–	–	342	33	–	–
OHnaph	236	334, 344	23	–	–	–	–	–	–
5	237	334, 344	–	–	–	–	–	–	–
[$Ir(ppy)_2$(**5**)][PF_6]	264	415, 558	1	–	–	–	–	–	–

[a] Degassed 1.00 x 10^{-5} M CH_2Cl_2 solutions excited at 280 nm. [b] 5 wt% complex in a PMMA matrix, λ_{ex} = 280 nm. [c] Complex mixed with the ionic liquid [BMIM][PF_6] in a 4:1 molar ratio, λ_{ex} = 331 nm.

The PLQY (Table 4.3) increases from 1 to 9% on going from [$Ir(ppy)_2$(**5**)][PF_6] to [Ir(naphppy)(**5**)][PF_6] which is not necessarily a consequence of partial energy transfer (see below) from the naphthyl unit (PLQY = 15% for Hnaphppy) onto the Ir(III) coordination sphere. Excited state lifetime measurements (Table 4.4) of [Ir(naphppy)(**5**)][PF_6] (τ_{av} = 144 ns for the 564 nm and τ_{av} = 4 ns for the 420 nm emission band) corroborate the fact that the higher-energy emission belongs to a fluorescent excited state being in the same range as for Hnaphppy and OHnaph (τ_{av} = 6 ns and τ_{av} = 8 ns for the 420 nm emission band, respectively).

Figure 4.7 left illustrates the emission spectra of [Ir(naphppy)(**5**)][PF_6] measured in CH_2Cl_2 solution compared to a 5 wt% PMMA film and a pure powder. Obviously the photoluminescence properties change when the environment changes from dilute solution to the PMMA film or the powder where no blue emission band is observed. Besides being non-radiatively deactivated via internal conversion, this may be explained by the emission band at 420 nm being quenched by intermolecular energy transfer, especially as the naphthalene does not possess bulky substituents.[89],[104] Another possibility could be a

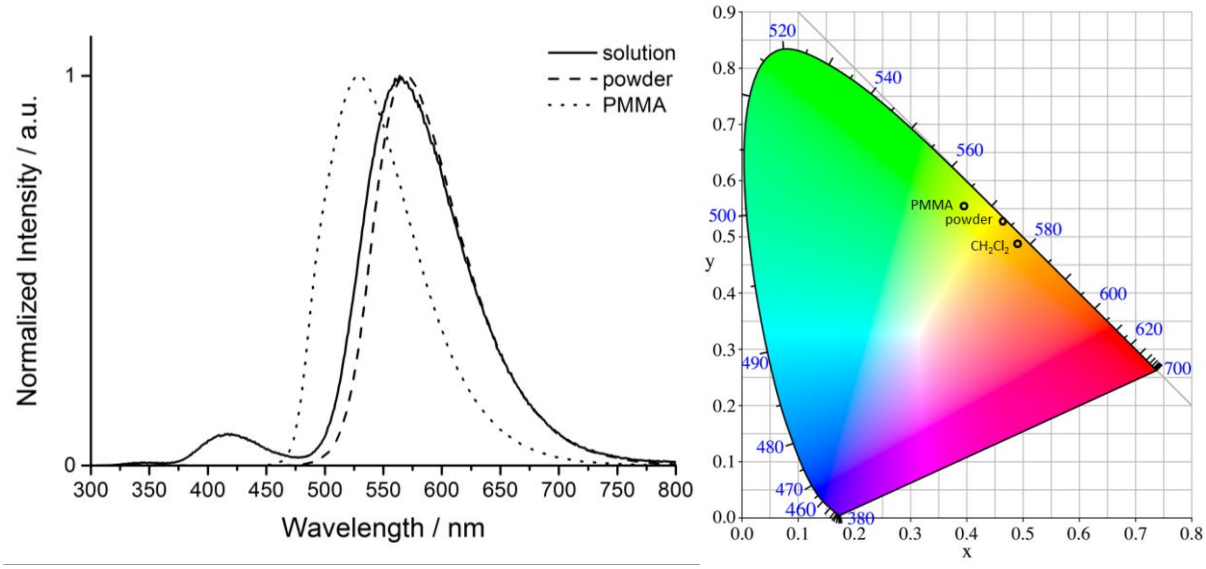

Figure 4.7 (Left) Photoluminescence spectra of [Ir(naphppy)(**5**)][PF_6] measured in a 1.00 x 10^{-5} M CH_2Cl_2 solution (—), as powder (- -) and diluted by 5 wt% in a PMMA film (····). (Right) CIE color space representing the x and y coordinates obtained for [Ir(naphppy)(**5**)][PF_6] in 1.00 x 10^{-5} M CH_2Cl_2 solution, as powder and diluted by 5 wt% in a PMMA matrix.

so-called Förster resonance energy transfer (FRET) where the energy of the naphthalene band is intramolecularly transferred to the coordination sphere of the Ir(III) center. This can occur because the 420 nm emission of [Ir(naphppy)(**5**)][PF_6] overlaps with its own MLCT absorption band above 330 nm (compare Figure 4.4 and Figure 4.5).[105],[106] The emission maximum of the powder is minimally red-shifted to 567 nm whereas a blue-shift to 529 nm is observed for the complex in a PMMA film (see Table 4.3). This is consistent with the findings for the orange (Table 2.2) and green (Table 3.2) emitters and can be related to the different packing in the respective environments. Although [Ir(naphppy)(**5**)][PF_6] possesses two emission bands in solution, it does not appear blue-shifted in the CIE color space compared to the PMMA film or powder (Figure 4.7 right).

Table 4.4 Photoluminescence lifetimes for [Ir(naphppy)(**5**)][PF_6], Hnaphppy, OHnaph and [Ir(ppy)$_2$(**5**)][PF_6] measured at different emission maxima and in varying environments.

Compound	Solution[a]			Powder			Diluted Film[b]		
	τ_{av} / ns	τ_1 / ns (A_1)	τ_2 / ns (A_2)	τ_{av} / ns	τ_1 / ns (A_1)	τ_2 / ns (A_2)	τ_{av} / ns	τ_1 / ns (A_1)	τ_2 / ns (A_2)
[Ir(naphppy)(**5**)][PF6] (λ_{em} = 564 nm)	144	135 (72891)	245 (3871)	678	569 (28144)	949 (6768)	1484	1248 (26776)	2492 (3151)
[Ir(naphppy)(**5**)][PF6] (λ_{em} = 420 nm)	4	3 (44137)	56 (27)	–	–	–	–	–	–
Hnaphppy (λ_{em} = 344 nm)	6	6 (15391)	16 (732)	–	–	–	7	4 (149106)	13 (17637)
OHnaph (λ_{em} = 344 nm)	8	8 (103181)	14 (4489)	–	–	–	–	–	–
[Ir(ppy)$_2$(**5**)][PF_6] (λ_{em} = 558 nm)	11	10 (22213)	19 (1550)	–	–	–	–	–	–

[a] Argon degassed. [b] Biexponential fit using the equation $\tau_{av} = \Sigma A_i\tau_i / \Sigma A_i$ where A_i is the pre-exponantial factor of the lifetime.

The PLQY of 9% for [Ir(naphppy)(**5**)][PF_6] in solution roughly doubles for the powder and increases to a remarkable 66% in a PMMA film. This again highlights the dependency of the emission on the environment to which the complex is exposed (see Table 4.3). Interestingly, an emission at 342 nm could be recorded for Hnaphppy in a PMMA film and additionally, the PLQY is increased from 15 to 33% on going from solution to the film. Therefore no intermolecular self-quenching is expected to happen for this compound, while for [Ir(naphppy)(**5**)][PF_6] in a PMMA film the naphthyl emission completely disappears as discussed above.

4.5 Mixing experiments

Considering the fact that [Ir(naphppy)(**5**)][PF_6] is predominately orange-emitting in solution, we considered combining the complex with the blue-emitting C^N ligand Hnaphppy to possibly obtain a white-light emissive mixture. Therefore CH_2Cl_2 solutions of [Ir(naphppy)(**5**)][PF_6] and Hnaphppy (each 1.00 x 10^{-5} M) were mixed in different ratios and then the absorption and emission spectra compared to those of the respective pure compound. Initially, addition of Hnaphppy to neat [Ir(naphppy)(**5**)][PF_6] results in a slight decrease of the characteristic features of the complex in the absorption spectrum (Figure 4.8 left). After an intermediate spectrum is reached at a ratio of 1 : 1 (complex : ligand), the shape of the spectrum resembles more and more the pure C^N ligand when further increasing the amount of Hnaphppy to 1 : 10. The photoluminescence spectra upon exciting at 250 nm are depicted in Figure 4.8 right, in which a continuous decrease of the orange compared to the enhancing blue emission (indicated by arrows in the inlet of Figure 4.8 right) can be observed by increasing the Hnaphppy concentration. The loss in intensity of the 564 nm emission upon dilution with Hnaphppy implies that no energy transfer occurs from the free C^N ligand onto the complex what would enhance its emission band. This is expected to happen at such low concentrations.

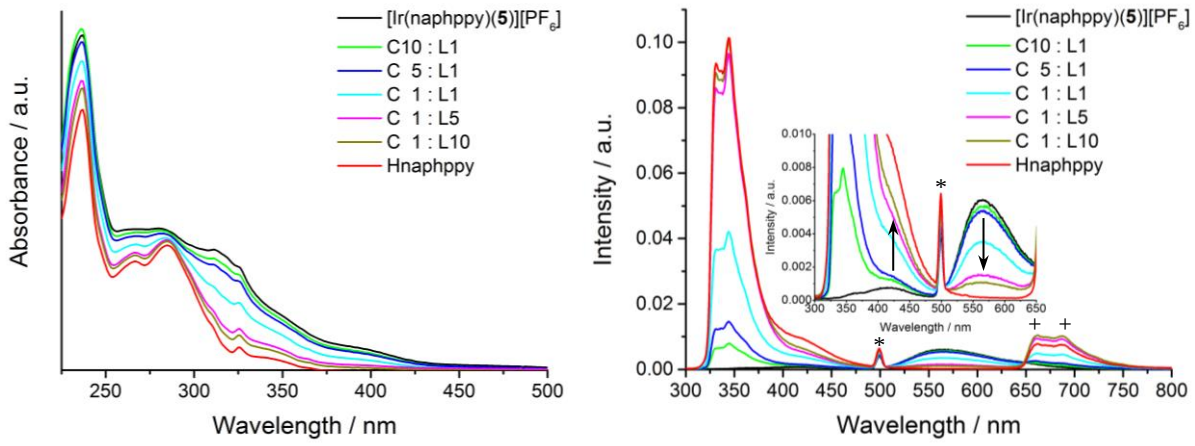

Figure 4.8 UV-Vis absorption (left) and photoluminescence (right) spectra of [Ir(naphppy)(**5**)][PF_6] and Hnaphppy in 1.00 x 10^{-5} M CH_2Cl_2 solutions and their mixtures at different ratios given in the legend (C = complex; L = ligand). The upper harmonic of the excitation wavelength and of the emission at 334 and 344 nm are indicated with a star (*) and a plus (+), respectively. The arrows (→) indicate the trends in emission upon diluting [Ir(naphppy)(**5**)][PF_6] with Hnpahppy.

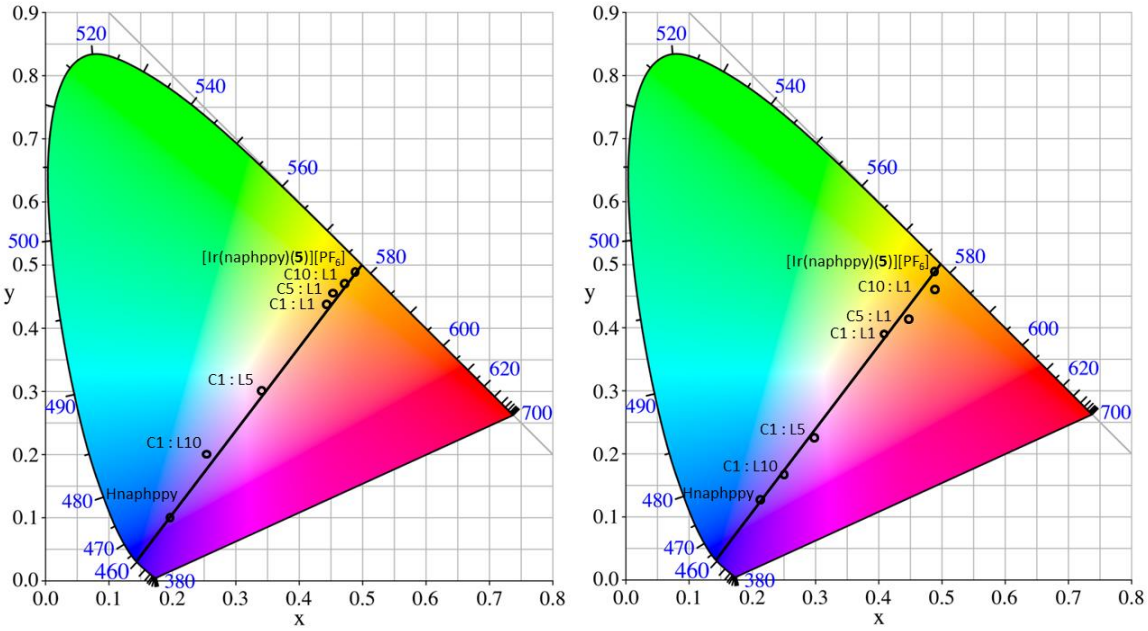

Figure 4.9 CIE color space containing the x and y coordinates obtained for non-degassed 1.00 x 10^{-5} M CH_2Cl_2 solutions of [Ir(naphppy)(**5**)][PF_6] and Hnaphppy and their mixtures at different ratios excited at (left) 280 and (right) 360 nm.

The effect on the emission by increasing the amount of Hnaphppy is more clearly shown in Figure 4.9 in which the x and y coordinates of the pure compounds and the different mixtures are represented in the CIE color space excited at 280 and 360 nm. As could be derived from the photoluminescence spectra (Figure 4.8), the different mixtures lie on a straight line drawn through the two extremes of neat [Ir(naphppy)(**5**)][PF_6] and Hnaphppy. Analogically, the CIE coordinates approach pure Hnaphppy upon increasing the amount of the C^N ligand. However, the respective CIE coordinates are sensitive to the excitation wavelength, summarized in Table 4.5. Nevertheless, this mixing experiment clearly shows that combining an orange and a blue-emitting component at different ratios enables one to tune the overall emission over a wide range straight through the CIE color space closely passing white-light emission (see Figure 4.9 and Figure 4.11).

Table 4.5 Overview of the CIE coordinates obtained for non-degassed 1.00 x 10^{-5} M CH_2Cl_2 solutions of [Ir(naphppy)(**5**)][PF_6] and Hnaphppy and their mixtures at different ratios and embedded in a PMMA film excited at 280 and 360 nm.

Compound	CIE in solution λ_{ex} = 280 nm		CIE in solution λ_{ex} = 360 nm		CIE in PMMA λ_{ex} = 280 nm		CIE in PMMA λ_{ex} = 360 nm	
	x	y	x	y	x	y	x	y
[Ir(naphppy)(**5**)][PF_6]	0.48	0.48	0.48	0.48	0.37	0.57	0.37	0.57
C10 : L1	0.47	0.47	0.48	0.47	–	–	–	–
C5 : L1	0.46	0.45	0.44	0.42	–	–	–	–
C1 : L1	0.44	0.44	0.41	0.39	0.33	0.57	0.34	0.56
C1 : L5	0.34	0.30	0.29	0.23	0.33	0.55	0.33	0.49
C1 : L10	0.26	0.20	0.25	0.17	0.32	0.52	0.31	0.47
Hnaphppy	0.19	0.10	0.22	0.13	0.29	0.29	0.28	0.32

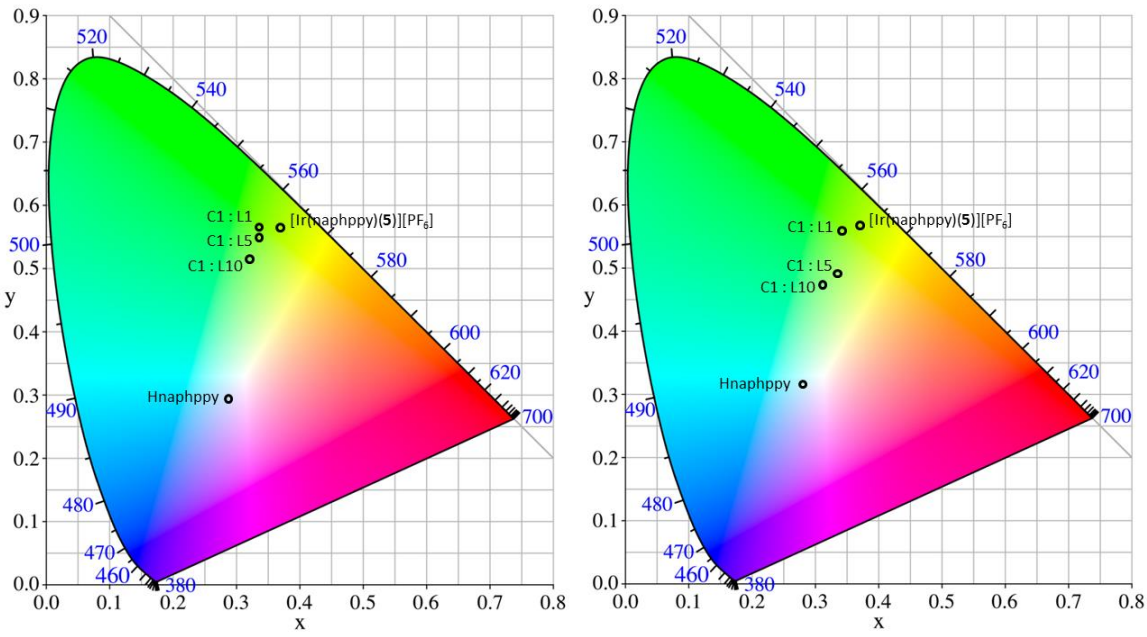

Figure 4.10 CIE color space containing the x and y coordinates obtained for [Ir(naphppy)(**5**)][PF_6] and Hnaphppy and their mixtures at different ratios and embedded in a PMMA film excited at (left) 280 and (right) 360 nm (total wt% compared to PMMA: [Ir(naphppy)(**5**)][PF_6] = 1%, C1 : L1 = 0.5%, C1 : L5 = 0.4%, C1 : L10 = 0.3%, Hnaphppy = 1%; where C = complex, L = ligand).

To imitate device configurations, these bicomponent solutions were investigated in a PMMA film. Therefore, because of the higher energy shift for the emission of the iridium complex observed in PMMA (see Figure 4.7), only ratios of [Ir(naphppy)(**5**)][PF_6] : Hnaphppy (1 : 1, 1 : 5 and 1 : 10) were compared to the respective pure compound excited at 280 and 360 nm (Figure 4.10 and Figure 4.11). Indeed, the environmental change in PMMA shifts them from the yellow-orange into the green region of the CIE color space. The three varying mixtures do not fall exactly on a straight line connecting the neat extremes which might be due to the slightly different total weight percentage of [Ir(naphppy)(**5**)][PF_6] and Hnaphppy embedded in PMMA (see caption of Figure 4.10).

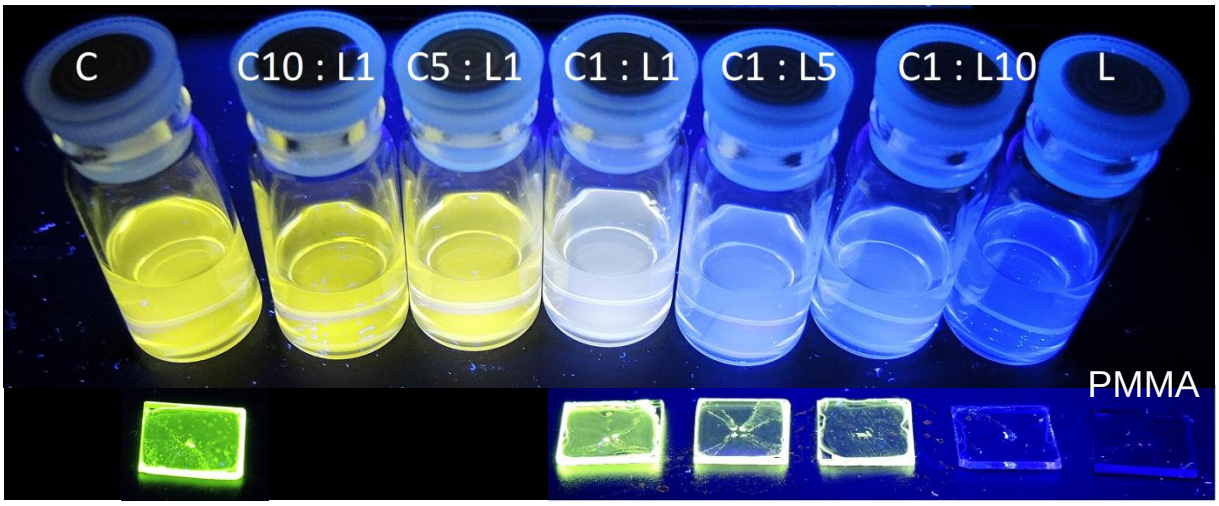

Figure 4.11 Photoluminescence of 1.00 x 10^{-5} M CH_2Cl_2 solutions of [Ir(naphppy)(**5**)][PF_6] and Hnaphppy and their mixtures at different ratios and in PMMA films irradiated at 366 nm (total wt% compared to PMMA: [Ir(naphppy)(**5**)][PF_6] = 1%, C1 : L1 = 0.5%, C1 : L5 = 0.4%, C1 : L10 = 0.3%, Hnaphppy = 1%, where C = complex, L = ligand).

The predominant nature of the emission in PMMA films arises from the Ir(III) complex, as observed for the 5 wt% film and powder in Section 4.4. Mixing [Ir(naphppy)(**5**)][PF_6] together with Hnaphppy and immersing in a PMMA film to finally obtain white-light emission requires only a small amount of the complex as the neat C^N ligand is already very close to the white CIE coordinates. More detailed studies have to be done to further understand the accurate concentration and excitation effect observed in solution as in PMMA films.

4.6 Device Data

The photoluminescence of [Ir(naphppy)(**5**)][PF_6] in device configuration has only a single slightly red-shifted emission maximum at 574 nm and a PLQY of 16% compared to solution measurements (564 nm and 9%), shown in Table 4.3. As observed for PMMA films, the emission band at 420 nm disappears in a more concentrated environment. The electroluminescence spectrum (Figure 4.12 left) of [Ir(naphppy)(**5**)][PF_6] in a LEEC exhibits a maximum at 574 nm with identical features as when photo-excited. Despite the fact that the PLQY is not remarkably enhanced and the dual-emitting properties are lost on going from solution to the device configuration, the LEEC device performance of [Ir(naphppy)(**5**)][PF_6] was tested according to standard operation schemes (see Table 4.6).

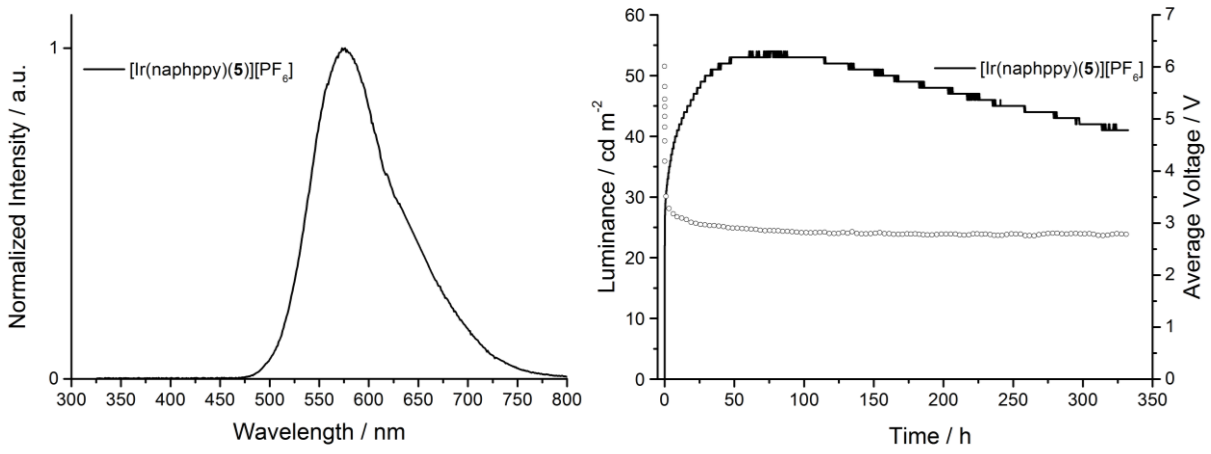

Figure 4.12 (Left) Normalized electroluminescence spectrum of [Ir(naphppy)(**5**)][PF_6] in a LEEC. (Right) LEEC device performance of [Ir(naphppy)(**5**)][PF_6] driven with a block-wave pulsed current at a frequency of 1000 Hz and a 50% duty cycle at a current density of 25 A m^{-2}. Luminance (solid line) and average voltage (open circles).

Since no device data are available for [Ir$(ppy)_2$(**5**)][PF_6], the performance of [Ir(naphppy)(**5**)][PF_6] is compared to the related reference compound [Ir$(ppy)_2$(dpbpy)][PF_6]. For the latter complex, Costa and co-workers reported a remarkable lifetime of ≈ 1300 h with a maximum luminance value of 70 cd m^{-2} when operating at a constant DC current of 3 V.[78] Running [Ir(naphppy)(**5**)][PF_6] with the same operation approach, an extremely long turn-on time around 250 h was achieved lying in the same region as reported for [Ir$(ppy)_2$(dpbpy)][PF_6] (200 h) with a very low maximum luminance of 4.5 cd m^{-2} (Table 4.6). Due to the bad resolution of the obtained data, as a consequence of these low values,

the measurement was stopped before $t_{1/2}$ was reached. Efficacy, power efficiency and the EQE could not be calculated accurately but each is significantly lower than observed for $[Ir(ppy)_2(dpbpy)][PF_6]$.

However, $[Ir(naphppy)(\mathbf{5})][PF_6]$ was tested following a second operating scheme based on a block-wave pulsed current driving at a frequency of 1000 Hz at a 50% duty cycle with a given current density, which normally leads to faster responses and more stable performances.[40],[41] For a best possible comparison $[Ir(naphppy)(\mathbf{5})][PF_6]$ was operated at 25 A m^{-2} being the current density when $[Ir(ppy)_2(dpbpy)][PF_6]$ exhibits maximum luminance.[78] Following this approach, a higher voltage (≈ 6 V) is initially required to keep the applied current density constant, and as soon as the ionic motion is induced, decreases after a few hours down to the operating voltage (≈ 2.8 V, see Figure 4.12 right), as observed for the green-emitting series in Section 3.7. The turn-on time is reduced to 74 h (Table 4.6) but since both complexes in the constant DC driving mode possess similar extremely long turn-on times above 200 h, it cannot be argued that the larger $[naphppy]^{2-}$ ligand is responsible for a lower ionic mobility and hence an increase in the turn-on time. However, the effect of the larger sized C^N ligand of $[Ir(naphppy)(\mathbf{5})][PF_6]$ induced by the new naphthyl glycol linker is sufficient to affect the LEEC performance severely, resulting in bad performances at constant DC current. The maximal luminance (54 cd m^{-2}) increases compared to the constant driving mode (4.5 cd m^{-2}), but does not reach the value observed for the reference compound (70 cd m^{-2}). Furthermore, the lifetime of $[Ir(naphppy)(\mathbf{5})][PF_6]$ is more than half of that obtained for $[Ir(ppy)_2(dpbpy)][PF_6]$ (extrapolated ≈ 575 h versus 1300 h, respectively). All residual figures of merit used to characterize the LEEC performance are also noticeably below the reference complex (see Table 4.6). A possible explanation for the worse device performances of $[Ir(naphppy)(\mathbf{5})][PF_6]$ could be an enhanced distortion of the planarity of the bpy domain affecting the π-stacking of its pendant phenyl rings with the $[ppy]^-$ units induced by the additional naphthyl glycol chain which is attached onto the C^N ligand. Such a large distortion angle (28.5° between the pyridyl rings of the bpy unit in the modelled structure of $[Ir(naphppy)(\mathbf{5})][PF_6]$, see Figure 4.2), in terms of device performance (i.e. emission loss and lower stability), was attributed to the faster nucleophilic degradation processes.[78],[107]

Table 4.6 Performances of the LEEC devices containing $[Ir(naphppy)(\mathbf{5})][PF_6]$ or $[Ir(ppy)_2(\mathbf{5})][PF_6]$ operated at different driving modes.

Compound	t_{on}[a] / h	L_{max}[b] / cd m^{-2}	$t_{1/2}$[c] / h	Efficacy / cd A^{-1}	Power Efficiency / lm W^{-1}	EQE[d] / %
$[Ir(ppy)_2(\mathbf{5})][PF_6]$[e]	200	70	1300	3.1	3.3	1.1
$[Ir(naphppy)(\mathbf{5})][PF_6]$[e]	≈ 250	4.5	–	< 1	< 1	< 1
$[Ir(naphppy)(\mathbf{5})][PF_6]$[f]	74	54	≈ 575	2.5	1.3	0.7

[a] Time to reach the maximum luminance. [b] Maximum luminance. [c] Time to reach half of the maximum luminance. [d] External quantum efficiency. [e] Operated at a constant 3 V DC current driving scheme. [f] Operated with a block-wave pulsed current at a frequency of 1000 Hz and a 50% duty cycle at a current density of 25 A m^{-2}.

4.7 Conclusion

Linking two Hppy ligands with a blue-emissive naphthyl glycol chain results in a new C^N ligand which was used to coordinate to an orange-emitting Ir(III) center with the aim of synthesizing a unique dual-emitting cyclometallated Ir(III) complex of the type [Ir(naphppy)(**5**)][PF_6]. Photoluminescence measurements in solution revealed two clearly separated emission bands centered at 420 and predominantly at 564 nm. Since the related compound [$Ir(ppy)_2$(**5**)][PF_6] used for comparison, also shows a second but less intense blue-light emission at 415 nm, the nature of this emission is possibly ligand-centered on ancillary ligand **5**. The photoluminescence property of [Ir(naphppy)(**5**)][PF_6] is therefore ascribed to consist of the well-known MLCT/LLCT orange emission at 564 nm and a second, thermally populated fluorescent excited state attributed to ligand **5**. Since no unambiguous evidence of two independent emissions could be found, no dual-emission properties were attributed to [Ir(naphppy)(**5**)][PF_6]. Variable temperature photoluminescence measurements upon cooling the sample could clarify the eventual independence of the two emission bands. In PMMA films containing [Ir(naphppy)(**5**)][PF_6] as well as for neat powder only an orange emission band at 529 and 567 nm (PLQY of 66 and 20%) could be observed displaying the strong environmental dependency of the blue emission quenching.

Mixing experiments combining the blue-emissive Hnaphppy ligand with the predominantly orange-emitting [Ir(naphppy)(**5**)][PF_6] at different ratios in solution clearly show the possibility of color-tuning the overall emission in a range between the emission of the neat components straight through the CIE color space closely passing white-light emission. The environmental change when immersing the respective mixing ratios in PMMA films leads to shifts in emission from the yellow-orange into the green region of the CIE color space. Photo- and electroluminescence spectra of [Ir(naphppy)(**5**)][PF_6] in a LEEC device configuration exhibit both a single emission with a maximum at 574 nm. Device performances of [Ir(naphppy)(**5**)][PF_6] with an optimized driving scheme cannot compete with the related compound [$Ir(ppy)_2$(dpbpy)][PF_6] and are characterized by long turn-on times at low luminance levels, but nevertheless a lifetime of ≈ 575 h can be reached.

4.8 Experimental

4.8.1 OHnaph

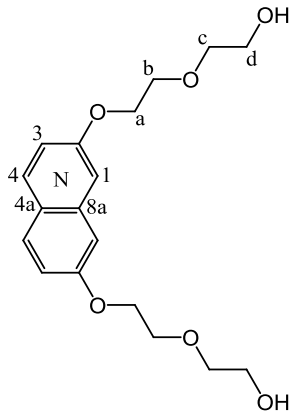

A suspension of 2,7-dihydroxynaphthalene (5.00 g, 31.2 mmol, 1.00 eq) and K_2CO_3 (25.9 g, 187 mmol, 6.00 eq) in dry N_2 degassed DMF (150 mL) was heated under rigorous stirring at 70 °C for 1 h. 2-(2-Chloroethoxy)ethanol (9.89 mL, 93.7 mmol, 3.00 eq) diluted with dry DMF (40 mL) was added dropwise and reacted at 70 °C for 5 d. The orange suspension was evaporated to dryness by the help of water and diethyl ether. The solid was extracted with CH_2Cl_2, dried over $MgSO_4$ and evaporated to dryness. Purification by column chromatography (Fluka silica gel 60, 0.040–0.063 mm; ethyl acetate:MeOH 100:3 → 100:5) afforded a brown oil. Addition of diethyl ether led to a white precipitate which was filtered off and dried to give the pure product as white solid (6.79 g, 20.2 mmol, 64.7%).

^{1}H NMR (400 MHz, $CDCl_3$) δ/ppm 7.65 (d, J = 8.6 Hz, 2H, H^{N4}), 7.06–6.98 (overlapping m, 4H, H^{N1+N3}), 4.27–4.21 (m, 4H, H^{a}), 3.96–3.89 (m, 4H, H^{b}), 3.81–3.75 (m, 4H, H^{d}), 3.72–3.68 (m, 4H, H^{c}), 2.22 (broadened s, 2H, H^{OH}).

^{13}C NMR (126 MHz, $CDCl_3$) δ/ppm 157.4 (C^{N2}), 135.8 (C^{N8a}), 129.4 (C^{N4}), 124.7 (C^{N4a}), 116.5 (C^{N3}), 106.4 (C^{N1}), 72.7 (C^{c}), 69.8 (C^{b}), 67.5 (C^{a}), 61.9 (C^{d}).

UV-Vis λ/nm (ε/L mol^{-1} cm^{-1}) (CH_2Cl_2, 1.00 x 10^{-5} mol L^{-1}) 236 (71 000), 275 (4 000), 325 (3 000).

Emission (CH_2Cl_2, c = 2.33 x 10^{-5} mol L^{-1}, λ_{ex} = 237 nm) λ_{em} = 331, 344 nm.

4.8.2 Hnaphppy

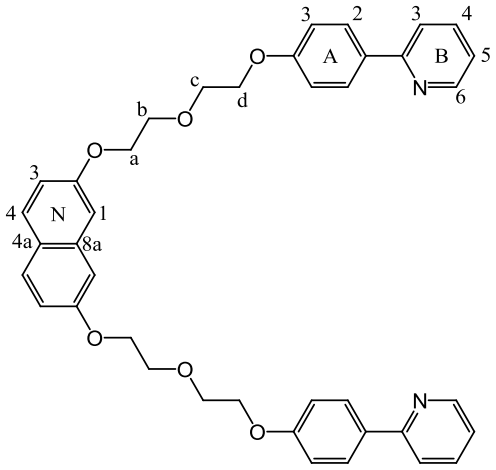

A grey suspension of NaH (232 mg, 5.80 mmol, 3.00 eq) and OHnaph (650 mg, 1.93 mmol, 1.00 eq) was rigorously stirred in dry DMF (30 mL) for 15 min before 2-(4-fluorophenyl)pyridine (1.00 g, 5.80 mmol, 3.00 eq) was added. The reaction mixture was heated under an N_2 atmosphere to 120 °C for 24 h. After cooling to room temperature the reaction mixture was poured into water whereupon a white solid precipitated which was filtered off and washed with water. The solid was boiled in 300 mL EtOH, filtered and the filtrate was evaporated to dryness to give the pure product as white solid (924 mg, 1.44 mmol, 74.6%).

M.p. 129.1 °C.

^{1}H NMR (500 MHz, $CDCl_3$) δ/ppm 8.65 (ddd, J = 4.8, 1.8, 1.0 Hz, 2H, H^{B6}), 7.95–7.90 (m, 4H, H^{A2}), 7.70 (ddd, J = 8.0, 7.4, 1.8 Hz, 2H, H^{B4}), 7.67–7.62 (overlapping m, 4H, H^{B3+N4}), 7.17 (ddd, J = 7.3, 4.8, 1.2 Hz, 2H, H^{B5}), 7.06–6.99 (overlapping m, 8H, $H^{A3+N1+N3}$), 4.28–4.21 (m, 8H, H^{a+d}), 4.02–3.96 (m, 8H, H^{b+c}).

^{13}C NMR (126 MHz, $CDCl_3$) δ/ppm 159.8 (C^{A4}), 157.4 (C^{N2}), 157.2 (C^{B2}), 149.7 (C^{B6}), 136.8 (C^{B4}), 135.9 (C^{N8a}), 132.4 (C^{A1}), 129.3 (C^{N4}), 128.3 (C^{A2}), 124.6 (C^{N4a}), 121.6 (C^{B5}), 120.0 (C^{B3}), 116.6 (C^{N3}), 115.0 (C^{A3}), 106.4 (C^{N1}), 70.1 (C^{b}), 70.1 (C^{c}), 67.7 (C^{d}), 67.6 (C^{a}).

UV-Vis λ/nm (ε/L mol^{-1} cm^{-1}) (CH_2Cl_2, 1.00 x 10^{-5} mol L^{-1}) 237 (78 000), 266 (33 000), 285 (38 000), 325 (6 000), 350 sh (2 000).

Emission (CH_2Cl_2, 9.50 x 10^{-6} mol L^{-1}, λ_{exc} = 237 nm) λ_{em} = 331, 344, 410 nm.

ESI-MS *m/z* 643.6 $[M + H]^+$ (base peak, calc. 642.7).

Found C 74.44, H 5.91, N 4.58; $C_{40}H_{38}N_2O_6$ requires C 74.75, H 5.96, N 4.36%.

4.8.3 [{Ir(naphppy)(μ-Cl)}$_2$]

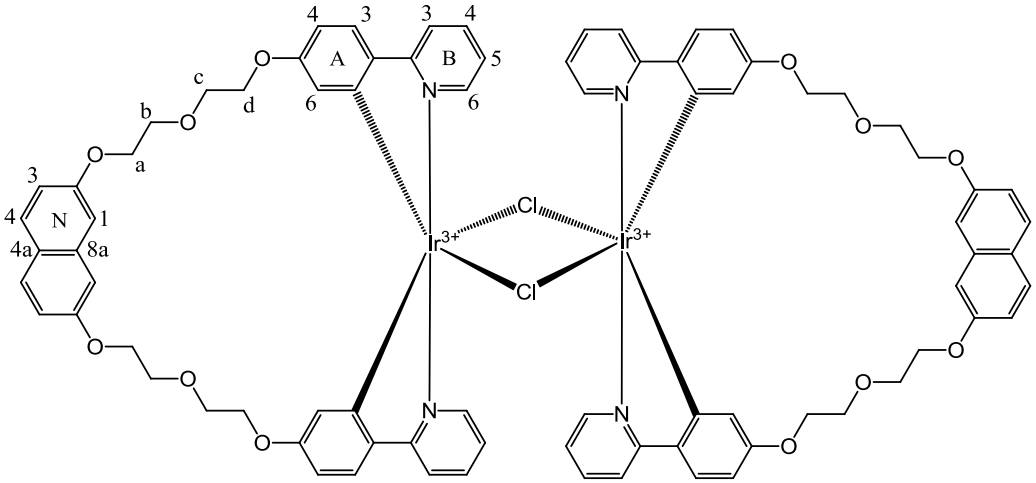

Hnaphppy (200 mg, 0.311 mmol, 1.00 eq) and $IrCl_3.H_2O$ (176 mg, 0.311 mmol, 1.00 eq) were refluxed in a solvent mixture of 2-ethoxyethanol (90 mL) and water (30 mL) at 110 °C for 24 h. The greenish suspension was allowed to reach room temperature, filtered and washed with water. The filtrate was extracted twice with little CH_2Cl_2 which was then extracted with water (3 x 100 mL). The organic phase was dried over $MgSO_4$, filtered and evaporated to dryness. Purification by a chromatographic column (Fluka silica gel 60, 0.040–0.063 mm; CH_2Cl_2 → CH_2Cl_2:MeOH 100:1) afforded the product as yellow solid (90.0 mg, 0.052 mmol, 33.4%).

^{1}H NMR (500 MHz, CD_2Cl_2) δ/ppm 9.11 (dd, J = 5.8, 0.9 Hz, 2H, H^{B6}), 7.71 – 7.63 (overlapping m, 4H, H^{B4+N4}), 7.56 (d, J = 7.9 Hz, 2H, H^{B3}), 7.20 (d, J = 8.7 Hz, 2H, H^{A3}), 6.97 (dd, J = 8.8, 2.5 Hz, 2H, H^{N3}), 6.90 (d, J = 2.4 Hz, 2H, H^{N1}), 6.71 (ddd, J = 7.3, 5.8, 1.4 Hz, 2H, H^{B5}), 6.33 (dd, J = 8.5, 2.5 Hz, 2H, H^{A4}), 5.32 (d, J = 2.6 Hz, 2H, H^{A6}), 4.04–3.94 (m, 4H, H^{a}), 3.89–3.84 (m, 2H, $H^{d/d'}$), 3.81–3.73 (m, 4H, $H^{b/b'+d/d'}$), 3.68–3.63 (m, 2H, $H^{b/b'}$), 3.61–3.57 (m, 4H, H^{c}).

^{13}C NMR (126 MHz, CD_2Cl_2) δ/ppm 168.2 (C^{B2}), 159.5 (C^{A5}), 157.7 (C^{N2}), 151.7 (C^{B6}), 147.3 (C^{A1}), 137.6 (C^{A2}), 137.0 (C^{B4}), 136.4 (C^{N8a}), 129.3 (C^{N4}), 125.5 (C^{A3}), 124.9 (C^{N4a}), 121.8 (C^{B5}), 118.4 (C^{B3}), 117.2 (C^{N3}), 116.6 (C^{A6}), 108.6 (C^{A4}), 107.5 (C^{N1}), 70.3 (C^{c}), 70.1 (C^{b}), 67.6 (C^{a}), 67.6 (C^{d}).

IR (solid, $\tilde{\nu}$/cm^{-1}) 3062 (w), 2925 (w), 2868 (w), 2030 (w), 1740 (w), 1627 (w), 1606 (w), 1582 (m), 1548 (m), 1513 (w), 1477 (w), 1462 (m), 1430 (m), 1388 (w), 1370 (w), 1316 (w), 1252 (m), 1205 (s), 1159 (m), 1118 (s), 1056 (s), 1032 (s), 936 (m), 860 (m), 833 (m), 772 (s), 752 (m), 722 (w), 681 (w), 630 (w), 470 (m).

ESI-MS *m/z* 833.5 $[C_{40}H_{36}IrN_2O_6]^+$ (base peak, calc. 832.9).

Found C 55.14, H 5.00, N 3.07; $C_{80}H_{72}Cl_2Ir_2N_4O_{12}$ + 2 $C_4H_{10}O_2$ requires C 55.13, H 4.84, N 2.92%; $C_4H_{10}O_2$ = 2-ethoxyethanol.

4.8.4 [Ir(naphppy)(MeOH)$_2$][PF$_6$]

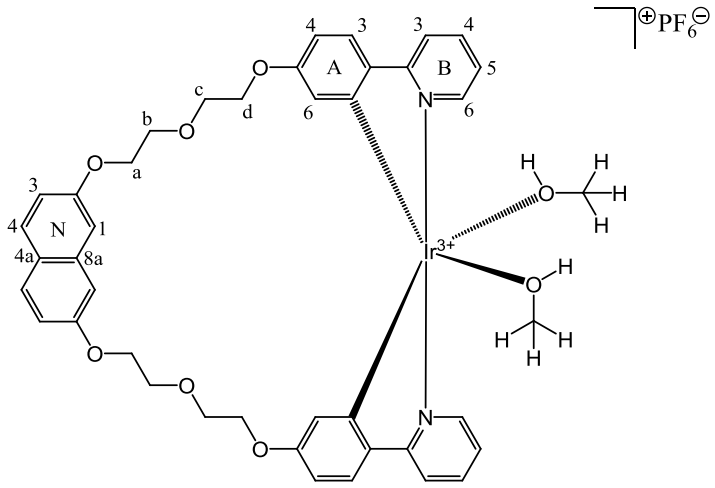

A yellow suspension of [{Ir(naphppy)(μ-Cl)}$_2$] (188 mg, 0.108 mmol, 1.00 eq) and AgPF$_6$ (59.9 mg, 0.237 mmol, 2.20 eq) in MeOH (10 mL) were stirred at room temperature for 1.5 h. The reaction mixture was filtered over celite, washed with MeOH and evaporated to dryness to give the product as yellow solid (223 mg, 0.214 mmol, 99.1%).

^{1}H NMR (500 MHz, $CDCl_3$) δ/ppm 8.75 (ddd, J = 5.8, 1.4, 0.7 Hz, 2H, H^{B6}), 7.87 (ddd, J = 8.2, 7.5, 1.5 Hz, 2H, H^{B4}), 7.70–7.63 (overlapping m,4, H^{B3+N4}), 7.37 (ddd, J = 7.3, 5.8, 1.4 Hz, 2H, H^{B5}), 7.16 (d, J = 8.6 Hz, 2H, H^{A3}), 6.97 (dd, J = 8.9, 2.5 Hz, 2H, H^{N3}), 6.89 (d, J = 2.4 Hz, 2H, H^{N1}), 6.28 (dd, J = 8.6, 2.5 Hz, 2H, H^{A4}), 5.56 (d, J = 2.5 Hz, 2H, H^{A6}), 3.98–3.91 (m, 4H, H^{a}), 3.91–3.86 (m, 2H, $H^{d/d'}$), 3.83–3.79 (m, 2H, d/d'), 3.79–3.73 (m, 2H, $H^{b/b'}$), 3.70–3.66 (m, 2H, $H^{b/b'}$), 3.66–3.60 (m, 4H, H^{c}), 3.34 (s, 6H, H^{Me}).

^{13}C NMR (126 MHz, $CDCl_3$) δ/ppm 168.9 (C^{B2}), 160.5 (C^{A5}), 158.6 (C^{N2}), 149.7 (C^{B6}), 141.0 (C^{A1}), 139.9 (C^{B4}), 139.0 (C^{A2}), 137.4 (C^{N8a}), 129.8 (C^{N4}), 126.7 (C^{A3}), 125.9 (C^{N4a}), 122.6 (C^{B5}), 120.0 (C^{A6}), 119.6 (C^{B3}), 117.7 (C^{N3}), 110.3 (C^{A4}), 108.5 (C^{N1}), 71.1 (C^{b}), 70.7 (C^{c}), 68.5 (C^{d}), 68.4 (C^{a}), 49.9 (C^{MeOH}).

IR (solid, $\tilde{\nu}$/cm^{-1}) 3165 (w), 2924 (w), 2051 (w), 1628 (w), 1608 (w), 1583 (m), 1551 (m), 1514 (w), 1479 (w), 1463 (m), 1433 (m), 1389 (w), 1316 (w), 1264 (m), 1208 (s), 1162 (m), 1127 (m), 1058 (m), 1035 (m), 957 (w), 833 (s), 774 (s), 753 (m), 740 (m), 724 (m), 629 (m), 556 (s), 471 (m).

ESI-MS *m/z* 833.6 $[C_{40}H_{36}IrN_2O_6]^+$ (base peak, calc. 832.9).

4.8.5 [Ir(naphppy)(**5**)][PF_6]

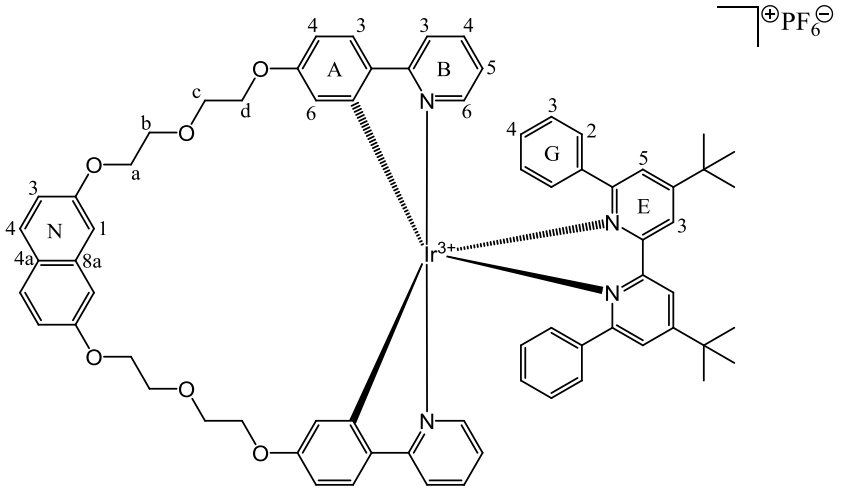

A non-emissive (under irradiation of 366 nm) suspension of [Ir(naphppy)$(MeOH)_2$][PF_6] (100 mg, 0.096 mmol, 1.00 eq), **5** (40.8 mg, 0.097 mmol, 1.01 eq) and NH_4PF_6 (156 mg, 0.960 mmol, 10.0 eq) in MeOH (20 mL) was heated to reflux for 20 h. The emissive orange suspension was filtered through a piece of cotton whereupon the filtrate was evaporated to dryness. Purification by column chromatography (Fluka silica gel 60, 0.040–0.063 mm; DCM → DCM:MeOH 100:0.5 → 100:1) and evaporation to dryness afforded the product as yellow solid (101 mg, 0.072 mmol, 75.0%).

^{1}H NMR (500 MHz, $CDCl_3$) δ/ppm 8.15–8.07 (overlapping m, 4H, H^{B6+E3}), 7.69 (ddd, J = 8.4, 7.5, 1.5 Hz, 2H, H^{B4}), 7.66 (d, J = 8.6 Hz, 2H, H^{N4}), 7.32 (d, J = 8.1 Hz, 2H, H^{B3}), 7.25 (d, J = 2.0 Hz, 2H, H^{E5}), 7.00 (ddd, J = 7.3, 5.9, 1.3 Hz, 2H, H^{B5}), 6.98–6.91 (overlapping m, 6H, $H^{G4+N1+N3}$), 6.77–6.69 (overlapping m, 6H, H^{A3+G3}), 6.58 (broadened s, 4H, H^{G2}), 6.00 (dd, J = 8.6, 2.5 Hz, 2H, H^{A4}), 4.65 (d, J = 2.5 Hz, 2H, H^{A6}), 4.08–3.96 (m, 4H, H^{a}), 3.80–3.74 (m, 2H, $H^{b/b'}$), 3.74–3.69 (m, 2H, $H^{d/d'}$), 3.69–3.63 (m, 2H, $H^{b/b'}$), 3.59–3.53 (m, 2H, $H^{d/d'}$), 3.53–3.45 (m, 4H, H^{c}), 1.40 (s, 18H, H^{tBu}).

^{13}C NMR (126 MHz, $CDCl_3$) δ/ppm 168.1 (C^{B2}), 165.3 (C^{E6}), 164.7 (C^{E4}), 160.0 (C^{E2}), 159.2 (C^{A5}), 157.9 (C^{N2}), 150.2 (C^{B6}), 149.5 (C^{A1}), 138.5 (C^{G1}), 138.2 (C^{B4}), 136.4 (C^{N8a}), 135.4 (C^{A2}), 129.3 (C^{N4}), 128.8 (C^{G4}), 128.0 (C^{G2}), 127.8 (C^{G3}), 126.8 (C^{E5}), 126.0 (C^{A3}), 124.9 (C^{N4a}), 121.6 (C^{E3}), 121.0 (C^{B5}), 118.8 (C^{B3}), 117.3 (C^{N3}), 116.2 (C^{A6}), 109.2 (C^{A4}), 107.8 (C^{N1}), 70.6 (C^{b}), 69.8 (C^{c}), 67.9 (C^{a}), 67.3 (C^{d}), 36.0 ($C^{quat\text{-}tBu\text{-}E}$), 30.5 ($C^{tBu\text{-}E}$).

IR (solid, $\tilde{\nu}$/cm^{-1}) 3058 (w), 2957 (w), 2923 (w), 2855 (w), 1629 (w), 1608 (m), 1585 (m), 1548 (m), 1514 (w), 1463 (m), 1433 (m), 1394 (w), 1369 (w), 1318 (w), 1251 (m), 1207 (s), 1161 (m), 1129 (m), 1060 (m), 1033 (w), 956 (w), 929 (w), 876 (w), 832 (s), 771 (s), 756 (m), 718 (w), 696 (s), 659 (w), 613 (w), 470 (m).

UV-Vis λ/nm (ε/L mol^{-1} cm^{-1}) (CH_2Cl_2, 1.00 x 10^{-5} mol L^{-1}) 236 (110 000), 280 (45 000), 311 (38 000), 325 (35 000), 350 sh (17 000), 395 sh (9 000).

Emission (CH_2Cl_2, 1.00 x 10^{-5} mol L^{-1}, λ_{exc} = 237 nm) λ_{em} = 420, 564 nm.

ESI-MS *m/z* 1254.0 $[M - PF_6]^+$ (base peak, calc. 1253.5).

Found C 60.49, H 5.37, N 4.16%; $C_{70}H_{68}F_6IrN_4O_6P$ requires C 60.12, H 4.90, N 4.01.

Chapter 5

Chapter 5 Multiple intra-cation π-stacking interactions

5.1 Motivation

The main drawback of the previous chapters was the limited lifetime of the complexes employed in LEEC devices. Stabilizing the complexes in the excited state thereby enhancing the device lifetimes, was achieved using iTMCs containing ligands with substituents that are capable of forming intra-cation face-to-face π-stacking interactions. Lifetimes of thousands of hours could be reached following this synthetic strategy.[57],[58],[62],[108] This groundbreaking improvement of the stability by such a synthetic modification was first observed on going from $[Ir(ppy)_2(bpy)][PF_6]$ to $[Ir(ppy)_2(pbpy)][PF_6]$ (Hppy = 2-phenylpyridine, bpy = 2,2'-bipyridine, pbpy = 6-phenyl-2,2'-bipyridine) where the additional 6-phenyl substituent in the bpy domain stacks perfectly over the phenyl ring of the cyclometallating $[ppy]^-$ unit, increasing the LEEC device lifetime by a factor of one hundred.[57] The π-stacking site is present in the ground as well as in the excited states of the complex, stabilizing it with respect to nucleophilic degradation reactions at the Ir(III) metal center caused by the attack of H_2O. Initially established for phenyl···phenyl interactions[57],[58],[59] it turned out to be effective also for other aryls such as phenyl···pyridyl,[109] or phenyl···pyrazolyl contacts.[60],[110] However, this design principle of introducing π-stacking abilities does not always work advantageously for the device stability[107] as we also observed in Sections 2.7 and 3.7 for the orange and green emitters, respectively. Interestingly, introducing a second pendant phenyl ring into the N^N domain by producing a second π-stacking site does not further improve the LEEC device lifetimes.[78],[108]

Li and co-workers have investigated the effect of attaching one pendant phenyl ring onto both cyclometallating ligands in $[Ir(ppy)_2(phen)][PF_6]$ (phen = 1,10-phenanthroline).[111] The two synthesized complexes $[Ir(dppy)_2(phen)][PF_6]$ and $[Ir(tppy)_2(phen)][PF_6]$ (Hdppy = 2,6-diphenylpyridine, Htppy = 2,4,6-triphenylpyridine) were employed in LEEC devices but no light emission could be observed although π-stacking with the N^N ligand was revealed by the X-ray structure. They argued that the double π-interactions are detrimental to the stability in the excited state, promoting the decomposition of the complexes by nucleophiles.

No example, to our knowledge, is present in the literature where it was tried to synthetically modify the C^N ligands in a way so as to obtain intra-molecular π-stacking abilities between the two cyclometallating ligands. We therefore synthesized two series of compounds of the type $[Ir(Phppy)_2(N^N)][PF_6]$ and $[Ir(Ph_2ppy)_2(N^N)][PF_6]$ (HPhppy = 2-(3-phenyl)phenylpyridine, HPh_2ppy = 2-(3,5-diphenyl)phenylpyridine). By the careful choice of the N^N ligands **1-4,** we were able to simultaneously study the systematic effect of the formation of none, one, two and up to three π-stacking interactions as well as the influence of ^{t}Bu substituents in the N^N ligand on the emission, the electrochemical behavior and the LEEC device performance. ^{1}H and ^{13}C NMR spectroscopic 2D techniques in solution at variable temperature and single crystal determinations were used to examine

the multiple π-interactions. Furthermore, the synthetic pathway to obtain the final products via an intermediate solvento precursor $[Ir(C\hat{}N)_2(MeOH)_2][PF_6]$ to circumvent the detrimental effects associated with chlorido-impurities is presented.[112]

5.2 Solvento-Precursors $[Ir(C\hat{}N)_2(MeOH)_2][PF_6]$

The conventional method of synthesizing cyclometallated Ir(III) compounds of the type $[Ir(C\hat{}N)_2(N\hat{}N)][PF_6]$ is to treat the respective chloride dimer $[Ir_2(C\hat{}N)_4Cl_2]$ with two equivalents of a N^N ancillary ligand, followed by anion exchange with NH_4PF_6.[76] (Scheme 5.1 top). This method was also used for the preparation of $[Ir(thpy)_2(N\hat{}N)][PF_6]$ (Section 2.2) and $[Ir(msppz)_2(N\hat{}N)][PF_6]$ (Section 3.2). A recent report from our group showed that even small amounts of residual chloride anion in the final complex lead to significant reductions in the performance of the iTMC in a LEEC device.[112] Since iridium is commercially obtainable mainly in the form of $IrCl_3{\cdot}xH_2O$ or $Na_3[IrCl_6]$, a complete chloride-free synthetic pathway is hard to avoid. Therefore, it is highly desirable to omit the presence of Cl^- in the final complexation reaction step. A viable alternative appeared to be using solvento-complexes of the type described by Watts et al.[113] establishing a route to $[Ir(C\hat{}N)_2(N\hat{}N)][PF_6]$ via an intermediate $[Ir(C\hat{}N)_2(MeOH)_2][PF_6]$ compound, illustrated in Scheme 5.1 (bottom) with $[Ir_2(ppy)_4Cl_2]$ as an example. In order to replace the coordinated solvent by the N^N ligand, it must be sufficiently labile. Adding $AgPF_6$, acting as a Cl^- trap, leads to the formation of insoluble AgCl. This had previously been demonstrated to be a good way to remove chloride impurities, thereby remarkably enhancing LEEC performance.[112]

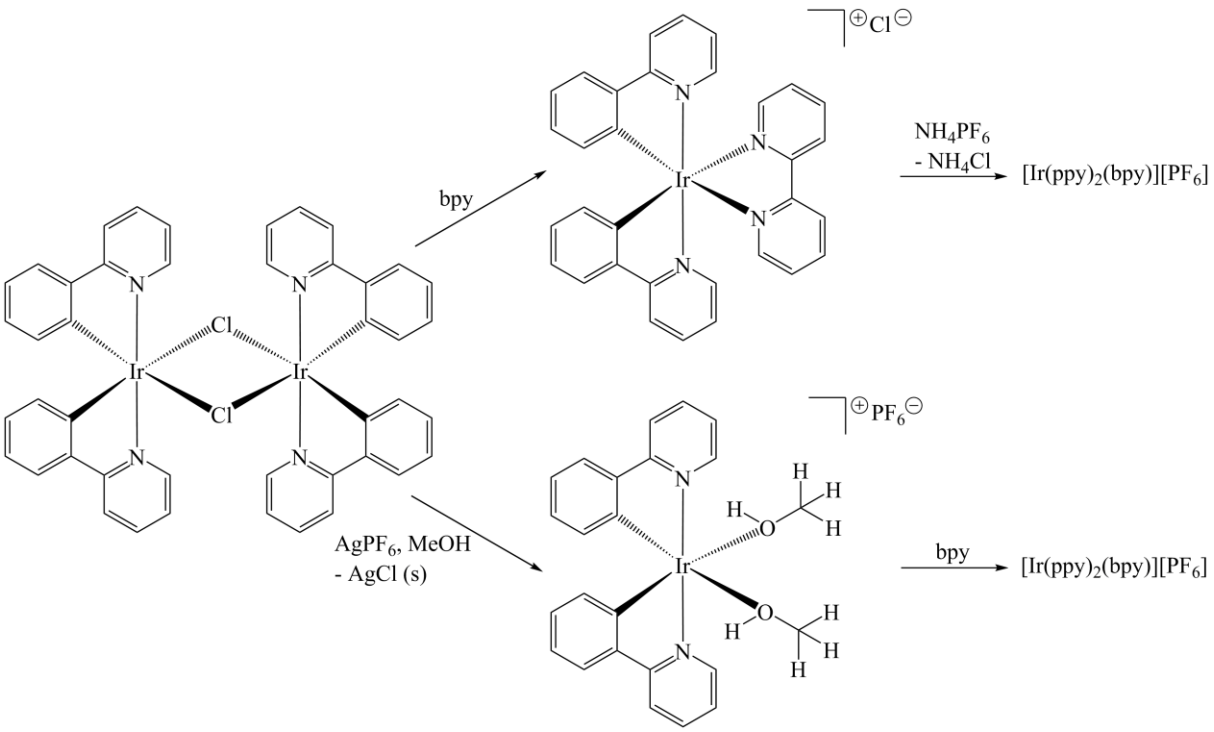

Scheme 5.1 Illustration of an alternative synthetic route from $[Ir_2(ppy)_4Cl_2]$ to $[Ir(ppy)_2(bpy)][PF_6]$.

Reacting $[Ir_2(Phppy)_4Cl_2]$ or $[Ir_2(Ph_2ppy)_4Cl_2]$ (both prepared following a standard method)[86] in the new approach with $AgPF_6$ in MeOH at room temperature quantitatively yielded intermediates $[Ir(Phppy)_2(MeOH)_2][PF_6]$ and $[Ir(Ph_2ppy)_2(MeOH)_2][PF_6]$, respectively. ^1H and ^{13}C NMR spectra reveal the expected solvento complexes in CD_3OD solutions (Figure 5.1). For each compound, an HMQC cross-peak between a singlet at δ 3.35 ppm in the ^1H NMR spectrum and a singlet at δ 49.9 ppm was assigned to the coordinated MeOH and could clearly be distinguished from the quintet arising from residual CD_2HOD. A peak envelope at *m/z* 805.5 corresponding to $[Ir(Ph_2ppy)_2]^+$ was detected by ESI mass spectrometry fitting with the calculated isotope pattern. Even the ESI conditions seem to be too harsh for the labile coordinated MeOH molecules, and hence all attempts to detect $[Ir(Phppy)_2(MeOH)_2]^+$ and $[Ir(Ph_2ppy)_2(MeOH)_2]^+$ ions failed.

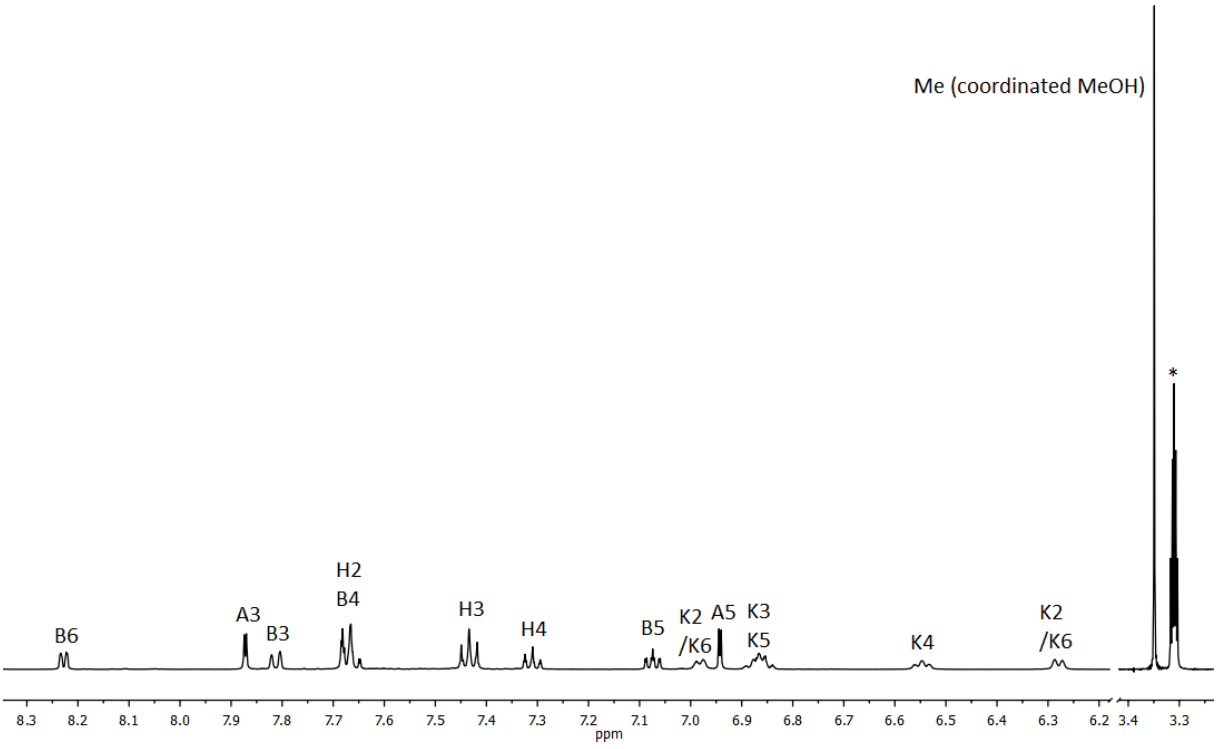

Figure 5.1 Room temperature 500 MHz ^1H NMR spectrum of $[Ir(Ph_2ppy)_2(MeOH)_2][PF_6]$ in CD_3OD (* = residual solvent peak).

5.3 Synthesis and NMR Spectroscopic Characterization

The two series of complexes $[Ir(Phppy)_2(N^\wedge N)][PF_6]$ and $[Ir(Ph_2ppy)_2(N^\wedge N)][PF_6]$ with N^N = **1-4** (see Scheme 5.2) were synthesized by reacting $[Ir(Phppy)_2(MeOH)_2][PF_6]$ or $[Ir(Ph_2ppy)_2(MeOH)_2][PF_6]$ with the respective ancillary ligand in MeOH at room temperature. Addition of NH_4PF_6 forced the product to precipitate. Crystallizations after chromatographic workup yielded the desired products in moderate to high (55–93%) yield. Base peaks assigned to $[M - PF_6]^+$ observed in the ESI mass spectra were consistent with those simulated for all compound cations.

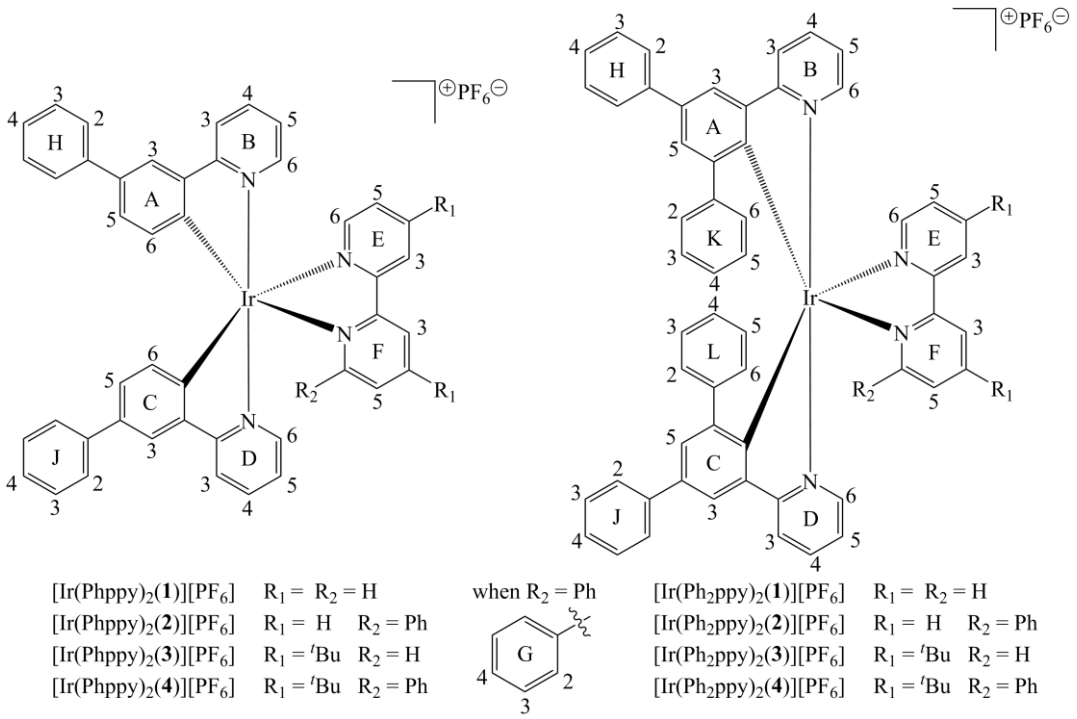

Scheme 5.2 Ring and atom labelling of the two series of $[Ir(C\hat{}N)_2(N\hat{}N)][PF_6]$ complexes based on the two C^N ligands HPhppy and HPh_2ppy and N^N ligands **1**-**4**.

^1H and ^{13}C NMR spectra of all complexes were assigned using standard 2D techniques (COSY, NOESY, HMQC and HMBC) following a consistent ring and atom labelling pattern shown in Scheme 5.2 to allow direct comparison. In complexes with ancillary ligands **1** and **3**, the cation is C_2-symmetric (ring A = C, ring B = D, etc.) whereas for N^N **3** and **4**, the introduction of the pendant phenyl ring G into the ancillary ligand desymmetrizes the structure.

Figure 5.2 illustrates this desymmetrization effect of the additional phenyl ring G when comparing the room temperature ^1H NMR spectra on going from $[Ir(Phppy)_2(\mathbf{1})][PF_6]$ to $[Ir(Phppy)_2(\mathbf{2})][PF_6]$. As described for related $[Ir(C\hat{}N)_2(N\hat{}N)][PF_6]$ compounds in Sections 2.2 and 3.2, the broad signal at δ 6.57 ppm and the broadened triplet at δ 6.76 ppm arise from hindered rotation of ring G on the NMR timescale. These broad signals collapse upon cooling from 298 K to 258 K, reappear each split into two broad doublets and two multiplets at 238 K and sharpen to two doublets (δ 5.90 and 7.06 ppm assigned to H^{G2} and H^{G6}) and two triplets (δ 6.55 and 6.85 ppm assigned to H^{G3} and H^{G5}) when further cooling to 218 K (see Figure 5.3). Pendant ring G lies over the cyclometallated phenyl ring C (Scheme 5.2) as depicted in the modelled structure of $[Ir(Phppy)_2(\mathbf{1})]^+$ (see Figure 5.4 left) based on the crystallographic data recorded for $[Ir(Phppy)_2(\mathbf{2})]^+$. Together with the signals for $H^{G2/G6}$ and $H^{G3/G5}$, as discussed above, only one other signal is considerably affected by temperature shifting from δ 6.47 ppm (at 298 K) to δ 7.18 ppm at 218 K (orange spot in Figure 5.3). An HMQC spectrum collected at 218 K revealed this signal a corresponding ^{13}C signal at 149.4 ppm. Closely, a second high-frequency signal at δ 150.0 ppm belongs to the ^1H NMR signal at δ 7.76 ppm which is not

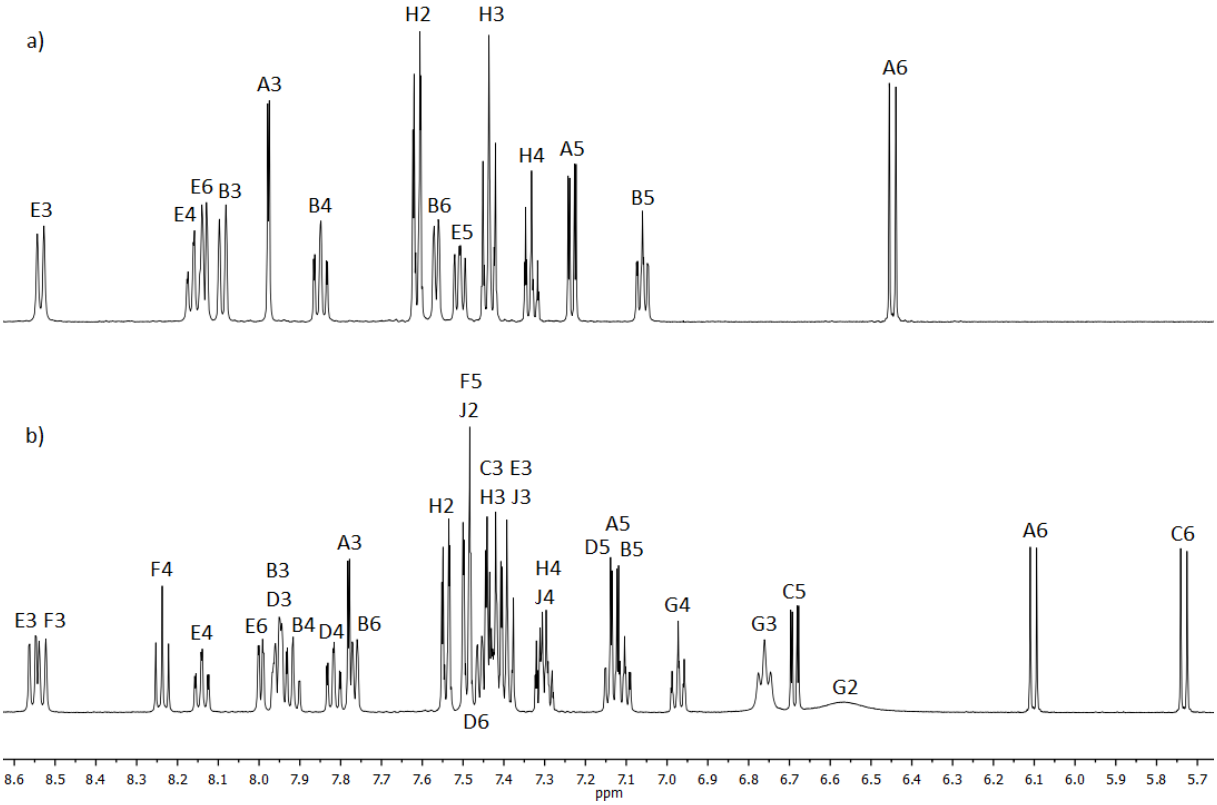

Figure 5.2 Room temperature 500 MHz ^{1}H NMR spectra of a) [Ir(Phppy)$_2$(**1**)][PF$_6$] and b) [Ir(Phppy)$_2$(**2**)][PF$_6$] measured in CD_2Cl_2.

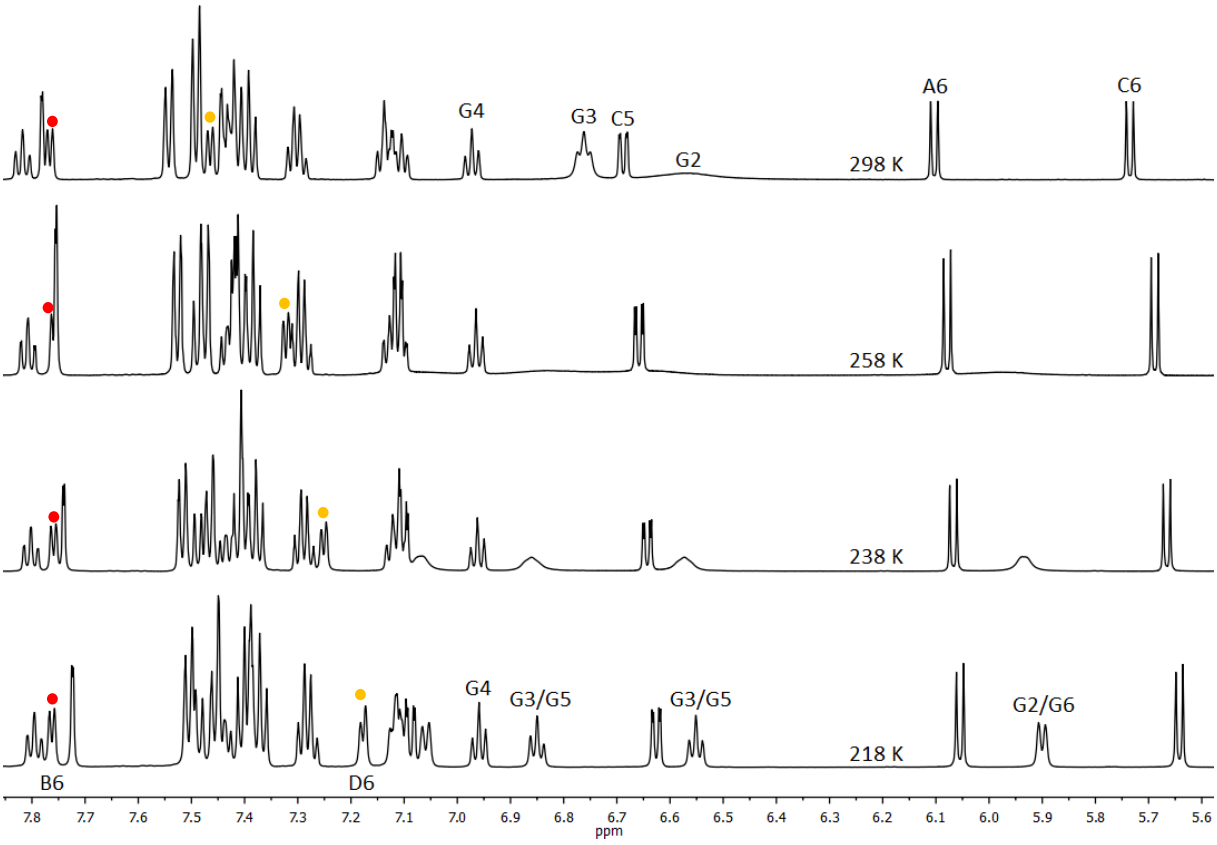

Figure 5.3 Part of the aromatic region of the 600 MHz ^{1}H spectra of [Ir(Phppy)$_2$(**2**)][PF$_6$] measured at variable temperature in CD_2Cl_2. The chemical shifts of the resonances for H^{B6} and H^{D6} are marked with a red and orange spot, respectively.

sensitive to varying temperature (red spot in Figure 5.3). Such high-frequency ^{13}C resonances are typical for pyridine C^6 nuclei and are assigned to C^{D6} and C^{B6}. NOESY spectra measured at 298 K afforded cross-peaks between H^{G3}/H^{J2} and H^{G4}/H^{J2}, and an additional one between H^{G5}/H^{J2} recorded at 218 K which allows one to distinguish between the two spin system of the two C^N ligands, since phenyl ring J is spatially closer to its analog ring H. Despite proton H^{B6} being spatially closer to ring G (highlighted in green in Figure 5.4) the freezing out of ring G has a bigger effect on the resonance of H^{D6}. A possible explanation is that the π-interactions between rings C and G increase at low-temperature, simultaneously accompanied by a deformation of the bpy unit (rings E and F) resulting in a strengthened C–H···π interaction between H^{D6} and ring E, at the end leading to low-frequency shift of H^{D6}. Similar discrepancies between the crystal structure and the twisting dynamic behavior of the bpy domain was described for $[Ir(ppy)_2(Naphbpy)]^+$ where Naphbpy = 6-(2-naphthyl)-2,2'-bipyridine.[62]

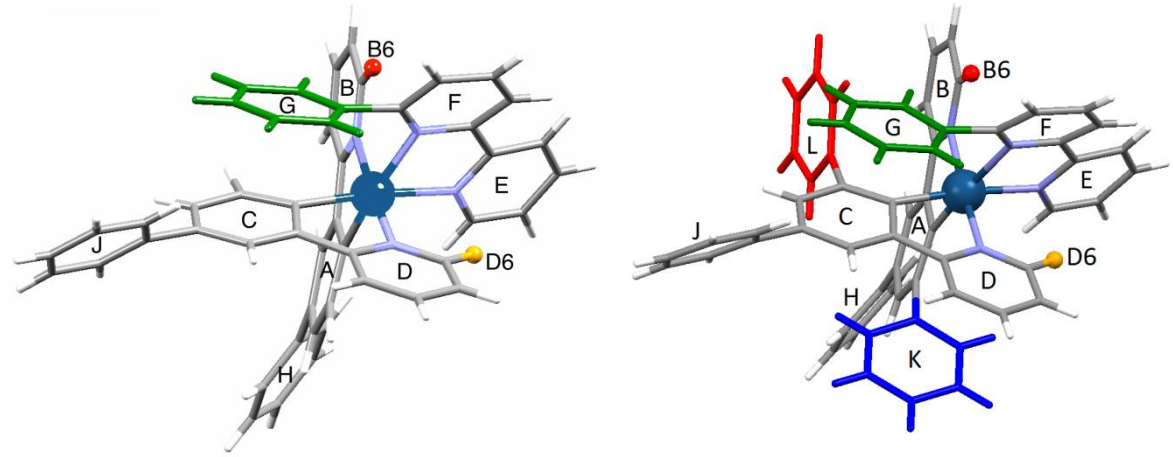

Figure 5.4 (Left) Modelled structure of $[Ir(Phppy)_2(\mathbf{2})]^+$ with highlighted ring G, H^{B6} and H^{D6}. (Right) Illustration of the crystal structure of $[Ir(Ph_2ppy)_2(\mathbf{2})]^+$ with colored ring G, L, K, H^{B6} and H^{D6}.

Table 5.1 Chemical shifts of the ^{1}H NMR spectroscopic data for ring B and K in the C_2-symmetric complexes [Ir(Phppy)$_2$(N^N)][PF$_6$] and [Ir(Ph$_2$ppy)$_2$(N^N)][PF$_6$] (N^N = **1** or **3**).

Cation	Chemical shifts δ / ppm			
	H^{B3}	H^{B4}	H^{B5}	H^{B6}
[Ir(Phppy)$_2$(**1**)]$^+$	8.09	7.85	7.06	7.56
[Ir(Phppy)$_2$(**3**)]$^+$	8.09	7.86	7.08	7.58
[Ir(Ph$_2$ppy)$_2$(**1**)]$^+$	7.53	7.31	6.48[a]	6.85
[Ir(Ph$_2$ppy)$_2$(**3**)]$^+$	7.53	7.32	6.48[a]	6.85

	H^{K2}, H^{K6}	H^{K3}+H^{K5}	H^{K4}
[Ir(Ph$_2$ppy)$_2$(**1**)]$^+$	6.95, 6.45	6.82	6.60
[Ir(Ph$_2$ppy)$_2$(**3**)]$^+$	6.99, 6.47	6.82	6.59

[a] Values obtained from HMQC spectra

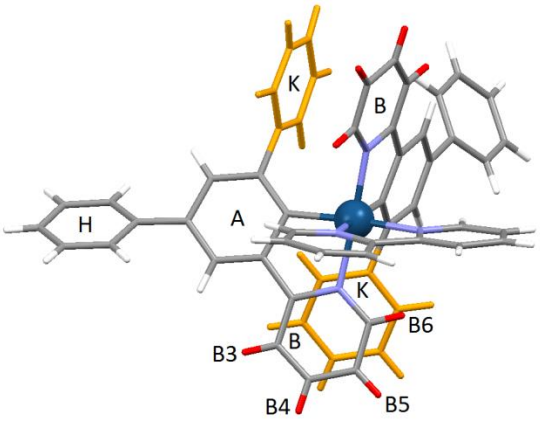

Figure 5.5 Illustration of the π-stacking of pyridine ring B and the phenyl ring K in the crystal structure of [Ir(Ph$_2$ppy)$_2$(**1**)]$^+$ being consistent with the chemical shifts in Table 5.1.

The phenyl ring H of the [Phppy]$^-$, pointing away from the Ir(III) center, is free to rotate on the NMR timescale, whereas spectroscopic data corroborate ring K in the [Ph$_2$ppy]$^-$ ligand being static at room temperature. Proton signals for the latter ring in the C_2-symmetric [Ir(Ph$_2$ppy)$_2$(**1**)][PF$_6$] and [Ir(Ph$_2$ppy)$_2$(**3**)][PF$_6$] arise at relatively low frequency (Table 5.1). Furthermore, there is a significant trend for all the ring B protons shifting to lower frequency on going from [Ir(Phppy)$_2$(**1**)][PF$_6$] to [Ir(Ph$_2$ppy)$_2$(**1**)][PF$_6$], and from [Ir(Phppy)$_2$(**3**)][PF$_6$] to [Ir(Ph$_2$ppy)$_2$(**3**)][PF$_6$]. These findings are consistent with the crystal structure of [Ir(Ph$_2$ppy)$_2$(**1**)][PF$_6$] discussed in Section 5.4, and a representation in Figure 5.5 illustrates the π-stacking of rings B and K in the solid state [Ir(Ph$_2$ppy)$_2$(**1**)]$^+$ cation. The effect on the ^{1}H NMR spectra when introducing a third phenyl moiety is shown for [Ir(Ph$_2$ppy)$_2$(**1**)][PF$_6$] (Figure 5.6a) and [Ir(Ph$_2$ppy)$_2$(**2**)][PF$_6$] (Figure 5.6b) and can be related to the comparison of [Ir(Ph$_2$ppy)$_2$(**3**)][PF$_6$] and [Ir(Ph$_2$ppy)$_2$(**4**)][PF$_6$]. 2D methods were used for the assignments, and as in [Ir(Ph$_2$ppy)$_2$(**1**)]$^+$, the pendant phenyl rings K and L in [Ir(Ph$_2$ppy)$_2$(**2**)]$^+$ are static and π-stack with the adjacent C^N ligands (Figure 5.4 right). Relatively low frequency shifts for the resonances in B, D, K and L rings in [Ir(Ph$_2$ppy)$_2$(**2**)][PF$_6$] support these observations with exceptions for the proton shifts of H^{B6} and H^{D6} which show a remarkable shift to higher frequency when passing from [Ir(Ph$_2$ppy)$_2$(**1**)][PF$_6$] (Figure 5.6a) to [Ir(Ph$_2$ppy)$_2$(**2**)][PF$_6$] (Figure 5.6b). Similarly, as described above for [Ir(Phppy)$_2$(**2**)][PF$_6$], these two protons could be distinguished in [Ir(Ph$_2$ppy)$_2$(**2**)][PF$_6$] and their chemical shifts are comparable to the former compound indicating that the introduction of the pendant phenyl ring G in the bpy unit has a dominant influence. Obviously, the signals in the room temperature ^{1}H NMR spectrum of [Ir(Ph$_2$ppy)$_2$(**2**)][PF$_6$], assigned to the bpy 6-phenyl substituent, are sharper than in the spectra of [Ir(Phppy)$_2$(**2**)][PF$_6$], although the signals overlap. The same findings when comparing [Ir(Ph$_2$ppy)$_2$(**4**)][PF$_6$] and [Ir(Phppy)$_2$(**4**)][PF$_6$] indicate a less hindered rotation of ring G in [Ir(Ph$_2$ppy)$_2$(**2**)][PF$_6$] and [Ir(Ph$_2$ppy)$_2$(**4**)][PF$_6$] than in [Ir(Phppy)$_2$(**2**)][PF$_6$] and [Ir(Phppy)$_2$(**4**)][PF$_6$]. Low temperature ^{1}H NMR measurements of [Ir(Ph$_2$ppy)$_2$(**2**)][PF$_6$] from 298 to 205 K in CD_2Cl_2 lead to the collapse of the signal at ∂ 6.84 ppm

(H^{G2}) and a broadening of the resonance at ∂ 6.92 ppm (H^{G3}). At 205 K a broad peak (FWHM ≈ 70 Hz) started to reappear at ∂ 6.33 ppm as one of the expected two signals assigned to H^{G2} or H^{G6}. Lack of available solvents limited further cooling. Nevertheless, induced distortion in the coordination sphere of the Ir(III) atom by the π-stacking rings B and L, and of D and K (supported by the crystal structure of [Ir(Ph_2ppy)$_2$(**2**)][PF_6], see Figure 5.4 right), strongly indicate to be responsible for the less hindered rotation of ring G.

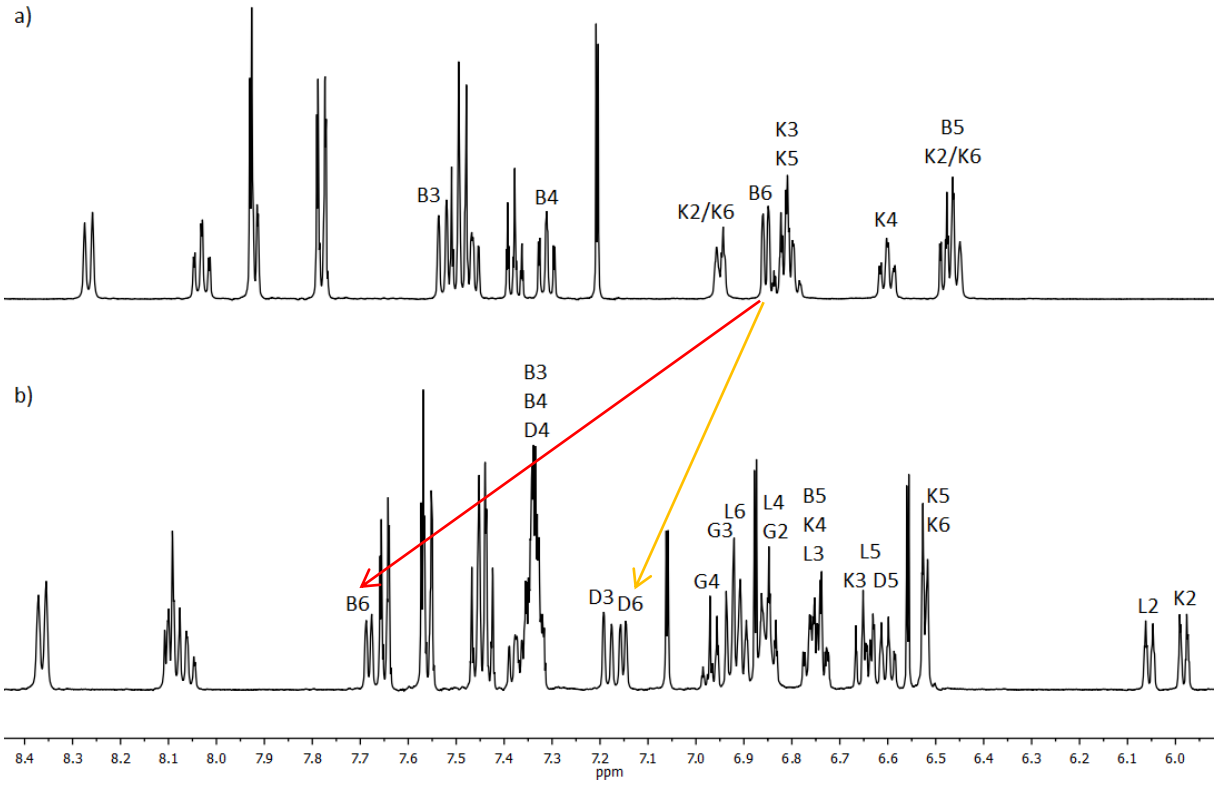

Figure 5.6 Room temperature 500 MHz ^{1}H NMR spectrum of a) [Ir(Ph_2ppy)$_2$(**1**)][PF_6] and b) [Ir(Ph_2ppy)$_2$(**2**)][PF_6], both measured in CD_2Cl_2.

5.4 Crystal Structures

The synthesis of ancillary ligand HPh_2ppy is already known in the literature but a crystal structure has not been reported. Figure 5.7 shows the crystal structure of HPh_2ppy crystallizing in the orthorhombic space group *Pna*2$_1$, (single crystals were grown from a CH_2Cl_2 solution layered with n-hexane), with important (but unremarkable) bond distances and angles given in the figure caption. As expected, rings containing N1, C12 and C18 are in a twisted arrangement with respect to the central arene ring (angles between the planes of the rings containing C6/N1, C6/C12 and C6/C18 are 32.2, 39.1 and 31.1°). The exchange of one phenyl for a 2-pyridyl group has little influence on the molecular packing, since HPh_2ppy is isostructural with 1,3,5-triphenylbenzene.[114] Replacing a second phenyl for a 2-pyridyl substituent in 1,3,5-tris(2-pyridyl)benzene[115] (which also crystallizes in the space group *Pna*2$_1$)

results in slightly decreased inter-ring twist angles (16.0 to 24.6°) compared to HPh_2ppy and 1,3,5-triphenylbenzene. However, the authors report the CH···N contacts which are suggested to be responsible for this change, to be very weak.

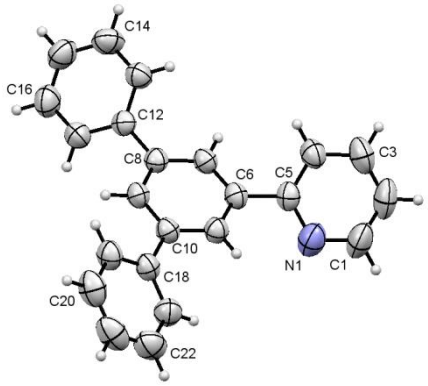

Figure 5.7 Crystal structure of HPh_2ppy with ellipsoids plotted at 50 % probability level. Selected bond lengths: N1–C5 = 1.364(3), N1–C1 = 1.366(3), C5–C6 = 1.485(3), C8–C12 = 1.489(3), C10–C18 = 1.488(3) Å. Crystallographic data: $C_{23}H_{17}N$, M = 307.38, colourless block, orthorhombic, space group $Pna2_1$, a = 7.4701(2), b = 19.7919(5), c = 11.1894(3) Å, U = 1654.32(8) Å^3, Z = 4, D_c = 1.234 Mg m^{-3}, μ(Cu-K$_\alpha$) = 0.544 mm^{-1}, T = 296 K. Total 11157 reflections, 2874 unique, R_{int} = 0.0255. Refinement of 2734 reflections (217 parameters) with $I > 2\sigma(I)$ converged at final $R1$ = 0.0343 ($R1$ all data = 0.0360), $wR2$ = 0.0966 ($wR2$ all data = 0.0986), gof = 1.052. CCDC 1019226.

Single crystals of [Ir(Phppy)$_2$(**1**)][PF_6] and [Ir(Ph$_2$ppy)$_2$(**1**)][PF_6]·EtOH were grown from a CH_2Cl_2 solution layered with Et_2O or with a mixture of EtOH : n-hexane (1 : 1), respectively. [Ir(Phppy)$_2$(**1**)][PF_6] crystallizes in the monoclinic space group $P2_1/n$ whereas [Ir(Ph$_2$ppy)$_2$(**1**)][PF_6]·EtOH crystallizes in the orthorhombic $Pna2_1$, each with one complex cation in the asymmetric unit (Figure 5.8 left and right).

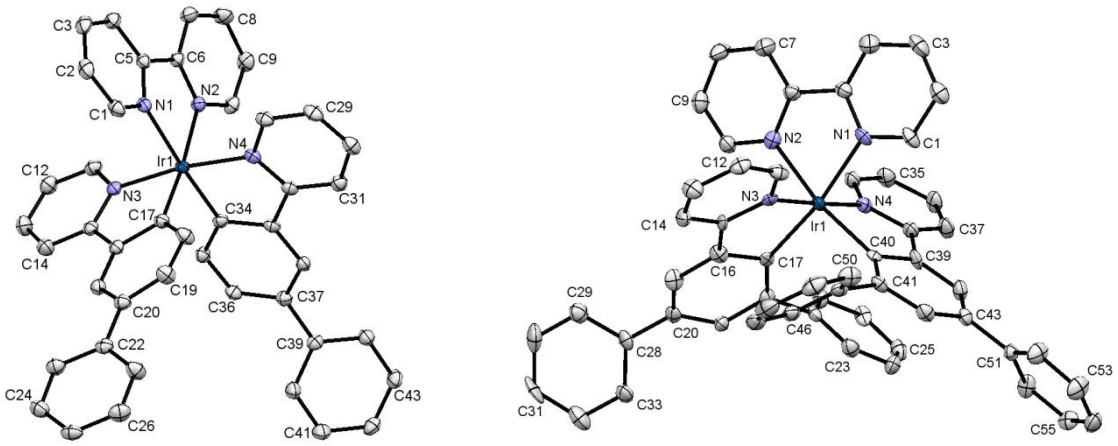

Figure 5.8 ORTEP representations of the X-ray structure of (left) the Δ-[Ir(Phppy)$_2$(**1**)]$^+$ cation in racemic [Ir(Phppy)$_2$(**1**)][PF_6] (ellipsoids plotted at 40% probability, hydrogen atoms are omitted for clarity) and of (right) Λ-[Ir(Ph$_2$ppy)$_2$(**1**)]$^+$ cation in racemic [Ir(Ph$_2$ppy)$_2$(**1**)][PF_6]·EtOH (ellipsoids plotted at 40% probability, solvent molecules and hydrogen atoms are omitted for clarity). Selected bond parameters for Δ-[Ir(Phppy)$_2$(1)]$^+$: Ir1–C17 = 2.010(2), Ir1–C34 = 2.011(2), Ir1–N4 = 2.0442(18), Ir1–N3 = 2.0517(17), Ir1–N2 = 2.1349(18), Ir1–N1 = 2.1399(18) Å; N2–Ir1–N1 = 76.56(7), C17–Ir1–N3 = 80.46(8), C34–Ir1–N4 = 80.60(8)° and for Λ-[Ir(Ph$_2$ppy)$_2$(1)]$^+$: Ir1–C17 = 2.027(9), Ir1–N3 = 2.043(9), Ir1–C40 = 2.052(9), Ir1–N4 = 2.078(8), Ir1–N1 = 2.125(8), Ir1–N2 = 2.152(7) Å; N1–Ir1–N2 = 76.7(3), C17–Ir1–N3 = 80.9(3), C40–Ir1–N4 = 81.5(3)°.

The tris-chelating octahedral Ir(III) cations are chiral and in both structures, the Λ and Δ-enantiomers exist in the lattice as a racemic mixture. Both structures exhibit the typical bond parameters within the coordination sphere of atom Ir1 and are listed in the caption to Figure 5.8. Ancillary ligand **1** is slightly twisted about 13.1° (angle between the planes of the two pyridine rings) in $[Ir(Phppy)_2(\mathbf{1})]^+$ but with 6.3° in $[Ir(Ph_2ppy)_2(\mathbf{1})]^+$ being closer to planarity. The two cyclometallating ligands in $[Ir(Phppy)_2(\mathbf{1})]^+$ have only a minor deviation from planarity (angles between the planes of rings containing N3/C17 and N4/C34 = 4.1 and 5.1°, respectively). On the other hand in $[Ir(Ph_2ppy)_2(\mathbf{1})]^+$, the corresponding angles (angles between the planes of rings containing N3/C17 and N4/C40) increase to 4.4 and 12.6°. In $[Ir(Phppy)_2(\mathbf{1})]^+$, the pendant phenyl rings (containing C22 or C39) are twisted through 17.0 and 42.4° with respect to the cyclometallated phenyl ring to which they are bonded being comparable to the related values of 46.2 and 46.8° observed in $[Ir(Ph_2ppy)_2(\mathbf{1})]^+$. In the latter complex, the larger twisting angles for the two additional phenyl rings (containing C23 and C46 Figure 5.8 right) of 75.4 and 61.8°, respectively, are closely related to the face-to-face π-stacking of these rings over the $[Ph_2ppy]^-$ pyridine rings containing N3 and N4 (see Figure 5.10 left). The π-stacking pyridine ring (containing N4) exhibits a $centroid_{(py)}\cdots plane_{(ph)}$ distance to the phenyl substituent (containing C23) of 3.27 Å, a $centroid_{(py)}\cdots centroid_{(ph)}$ separation of 3.48 Å with planes twisted about 9.9°. The corresponding π-interactions between the rings containing N3 and C46 are characterized by an angle of 18.6°, and distances of 3.37 Å and 3.51 Å. In the packing of $[Ir(Phppy)_2(\mathbf{1})][PF_6]$, the cations are in close contact through embraces of the arene units (Figure 5.9) resulting in anion-separated columns assembled along the *b*-axis. The $[PF_6]^-$ counter-ion is ordered in both $[Ir(Phppy)_2(\mathbf{1})][PF_6]$ and $[Ir(Ph_2ppy)_2(\mathbf{1})][PF_6]\cdot EtOH$, whereby the EtOH molecule is disordered for the latter structure and has been modelled over two sites, each of half occupancy.

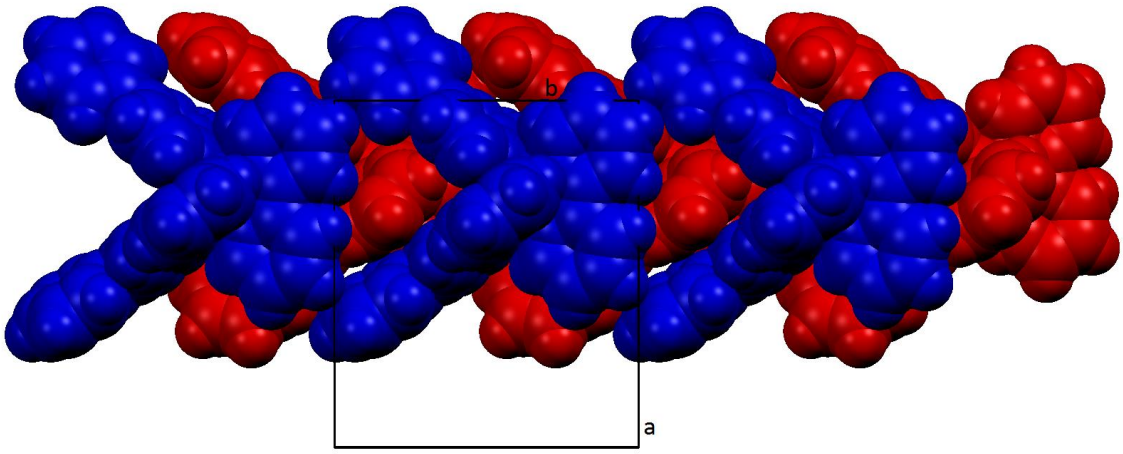

Figure 5.9 Tight embraces of arene units between the cations in $[Ir(Phppy)_2(\mathbf{1})][PF_6]$.

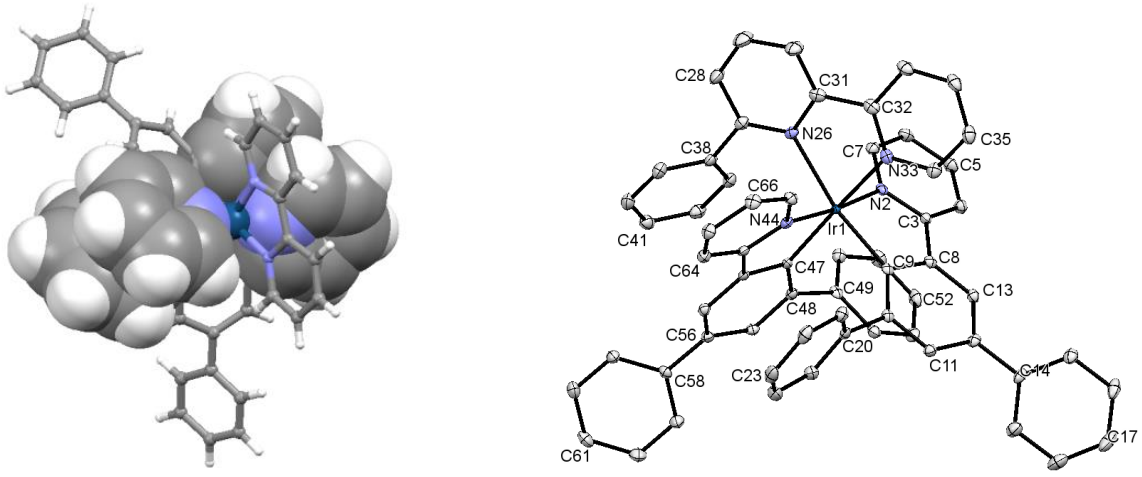

Figure 5.10 (Left) Face-to face pyridine···phenyl π-stacking interactions between rings containing N3/C46 and N4/C23 in $[Ir(Ph_2ppy)_2(\mathbf{1})]^+$. (Right) Crystal structure of the cationic Λ-enantiomer of the racemic mixture in $[Ir(Ph_2ppy)_2(\mathbf{2})][PF_6]\cdot 2C_6H_5Me$ with ellipsoids plotted at 40% probability (hydrogen atoms and solvent molecules are omitted for clarity). Selected bond parameters: Ir1–N2 = 2.0479(18), Ir1–C9 = 2.031(2), Ir1–N26 = 2.2610(18), Ir1–N33 = 2.1454(19), Ir1–N44 = 2.0549(18), Ir1–C47 = 2.047(2) Å; N26–Ir1–N33 = 76.14(7), N2–Ir1–C9 = 80.64(8), N44–Ir1–C47 = 80.11(8)°.

Crystals of X-ray quality of $[Ir(Ph_2ppy)_2(\mathbf{2})][PF_6]\cdot 2C_6H_5Me$ (grown from a CH_2Cl_2 solution layered with toluene) crystallize in the triclinic space group *P*–1. Both enantiomers of the octahedral Ir(III) cation are present in the lattice; the Λ-enantiomer is shown in Figure 5.10 right. The chelate angles of the three bidentate ligands in $[Ir(Ph_2ppy)_2(\mathbf{2})]^+$ are, as expected, similar to those in $[Ir(Phppy)_2(\mathbf{1})]^+$ and $[Ir(Ph_2ppy)_2(\mathbf{1})]^+$ (given in the captions to Figure 5.8 and Figure 5.10). However, the remaining angles in the coordination sphere of atom Ir1 possess a greater deviation (Table 5.2).

Table 5.2 Comparison of the non-chelate angles in the octahedral coordination sphere of the Ir1 atom in the complex cations $[Ir(Phppy)_2(\mathbf{1})]^+$, $[Ir(Ph_2ppy)_2(\mathbf{1})]^+$ and $[Ir(Ph_2ppy)_2(\mathbf{2})]^+$ (see Figure 5.8 and Figure 5.10).

Angles	$Ir(Phppy)_2(\mathbf{1})]^+$	$[Ir(Ph_2ppy)_2(\mathbf{1})]^+$	$[Ir(Ph_2ppy)_2(\mathbf{2})]^+$
trans-N–Ir–N	172.08(7)	175.9(3)	174.85(7)
trans-N–Ir–C	175.22(7)	170.9(4)	174.64(8)
	173.96(7)	169.6(3)	169.36(7)
cis-N–Ir–N	88.66(7)	84.3(3)	83.03(7)
	98.37(7)	95.8(3)	95.77(7)
	98.36(7)	92.0(3)	94.32(7)
	86.89(7)	84.9(3)	80.53(7)
cis-C–Ir–C	87.28(8)	94.5(3)	83.91(8)
cis-C–Ir–N	92.71(8)	94.4(3)	93.87(8)
	94.91(8)	94.5(3)	101.37(8)
	97.46(8)	97.7(3)	104.46(8)
	98.71(7)	102.4(3)	106.35(7)

The enhanced values of the *cis*-C–Ir–N angles in $[Ir(Ph_2ppy)_2(\mathbf{2})]^+$ are associated to the three intra-cation π-stacking moieties depicted in Figure 5.11. The face-to-face π-stacking interactions between pairs of pyridine and phenyl rings (containing N2/C49 and N44/C20) and between cyclometallating ring (containing C47) and pendant phenyl (ring containing C38) include ring-plane···centroid distances, centroid···centroid separations and inter-plane angles of 3.18 Å, 3.47 Å and 5.8° (between rings for rings N2/C49), 3.37 Å, 3.61 Å and 14.9° (with atoms N44/C20), and 3.24 Å, 3.42 Å and 10.9° (for rings C38/C47). The $[PF_6]^-$ counter-ion and toluene molecules are ordered in the crystal structure of $[Ir(Ph_2ppy)_2(\mathbf{2})][PF_6]\cdot 2C_6H_5Me$. Extensive CH···F contacts between cations and anions dominate the packing interactions, which further involve some edge-to-face π-contacts of one of the toluene molecules with a pendant phenyl substituent of the complex cation.

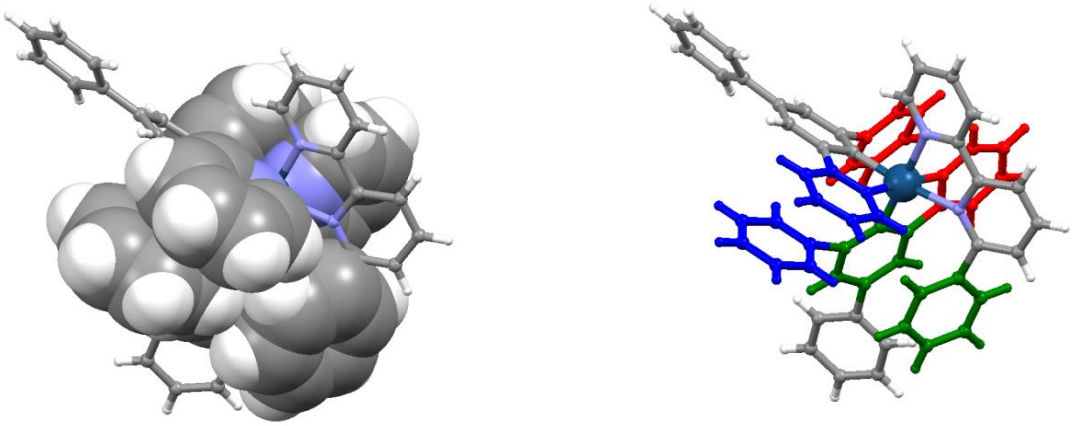

Figure 5.11 The three intra-cation face-to-face π-stacking moieties in the complex cation $[Ir(Ph_2ppy)_2(\mathbf{2})]^+$: (Left) in the space-filling representations, and (right) highlighting the two pyridyl···pendant phenyl substituent interactions in red and blue, and the cyclometallating phenyl···pendant phenyl interaction in green.

5.5 Electrochemical Properties

Cyclic voltammetric data for the complex series $[Ir(C\text{^}N)_2(N\text{^}N)][PF_6]$ (C^N = Phppy or Ph_2ppy, each with N^N = **1-4**) is summarized in Table 5.3 and graphically depicted in Figure 5.12.

Table 5.3 Cyclic voltammetric data with respect to Fc/Fc^+, measured in degassed CH_2Cl_2 solutions containing 0.1 M $[^nBu_4N][PF_6]$ as supporting electrolyte at a scan rate of 0.1 V s^{-1}. (qr = quasi-reversible)

Compound	$E^{ox}_{1/2}$ / V	$E^{red}_{1/2}$ / V	$\Delta E_{1/2}$ / V
$[Ir(Phppy)_2(\mathbf{1})][PF_6]$	+0.79	-1.84^{qr}	2.63
$[Ir(Phppy)_2(\mathbf{2})][PF_6]$	+0.74	-1.84^{qr}	2.58
$[Ir(Phppy)_2(\mathbf{3})][PF_6]$	+0.75	-1.88^{qr}	2.63
$[Ir(Phppy)_2(\mathbf{4})][PF_6]$	+0.72	-1.89^{qr}	2.61
$[Ir(Ph_2ppy)_2(\mathbf{1})][PF_6]$	+0.75	-1.82^{qr}	2.57
$[Ir(Ph_2ppy)_2(\mathbf{2})][PF_6]$	+0.72	-1.85^{qr}	2.57
$[Ir(Ph_2ppy)_2(\mathbf{3})][PF_6]$	+0.71	-1.88^{qr}	2.59
$[Ir(Ph_2ppy)_2(\mathbf{4})][PF_6]$	+0.69	-1.91^{qr}	2.60

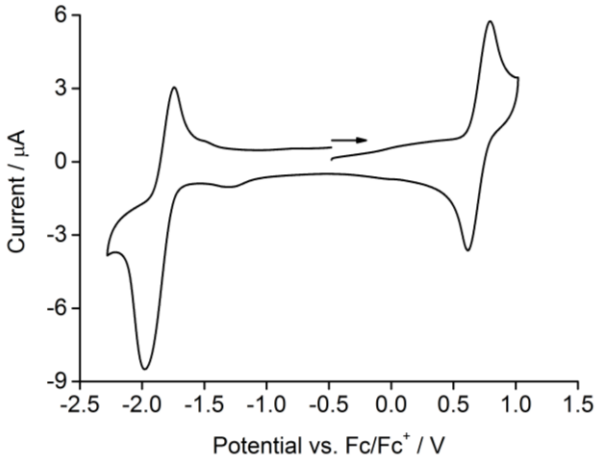

Figure 5.12 Cyclic voltammogram of $[Ir(Ph_2ppy)_2(\mathbf{2})][PF_6]$ with respect to Fc/Fc^+, measured in degassed CH_2Cl_2 solutions at a scan rate of 0.1 V s^{-1}. (→ = direction of scan).

Each complex exhibits a reversible oxidation arising from an Ir(III) metal center based process being consistent with trends in the oxidation potential upon the introduction of electron-releasing phenyl and/or ^{t}Bu groups. The related compound $[Ir(ppy)_2(\mathbf{1})][PF_6]$ shows an oxidation process at +0.84 V (versus Fc/Fc^+, in DMF)[64]. The $E^{ox}_{1/2}$ for the same process occurs at increasingly lower potential on passing from $[Ir(Phppy)_2(\mathbf{1})][PF_6]$ (+0.79 V) to $[Ir(Ph_2ppy)_2(\mathbf{1})][PF_6]$ (+0.75 V). This corresponds to the destabilization of the HOMO (localized on the Ir(III) center and the cyclometallating ligand) upon sequential introduction of electron-releasing phenyl substituents into the C^N ligands (Figure 5.13). A further lowering of $E^{ox}_{1/2}$ (destabilization of the HOMO) is observed when introducing phenyl groups into the N^N ligand on going from $[Ir(Phppy)_2(\mathbf{1})][PF_6]$ to $[Ir(Phppy)_2(\mathbf{2})][PF_6]$, and similarly, the

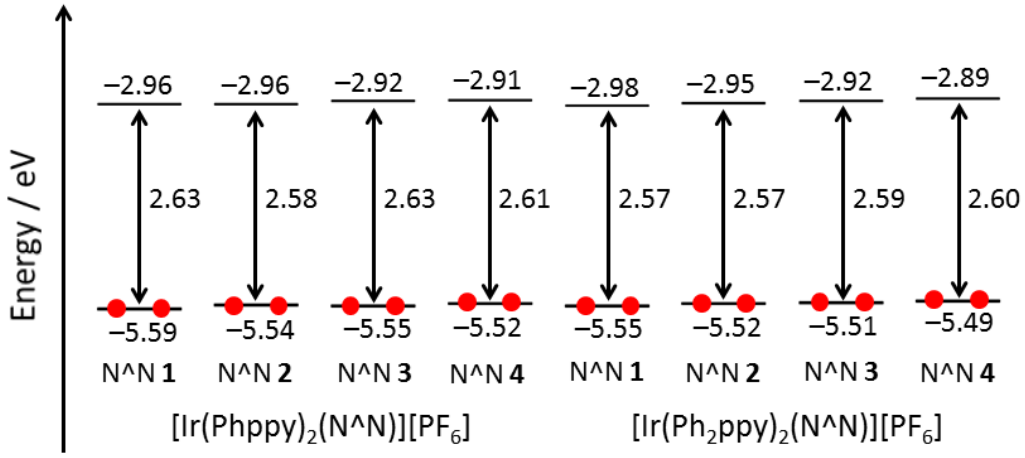

Figure 5.13 Energy diagram representing the energies in eV calculated for the HOMOs and the LUMOs of $[Ir(C\text{^}N)_2(N\text{^}N)][PF_6]$ (C^N = Phppy or Ph_2ppy, each with N^N = **1-4**).

effect of ^{t}Bu and of phenyl substituents can be observed from [Ir(Ph$_2$ppy)$_2$(**1**)][PF$_6$] to [Ir(Ph$_2$ppy)$_2$(**3**)][PF$_6$] to [Ir(Ph$_2$ppy)$_2$(**4**)][PF$_6$] (see Table 5.3 and Figure 5.13). Each complex exhibits a quasi-reversible reduction arising from the N^N ligand leading to destabilized LUMOs (located on the bpy domain) upon introducing ^{t}Bu substituents, consistent with observations for previous complex series (2.4 and 3.4).

5.6 Solution, Thin-film and Powder Photophysical Properties

The UV-Vis absorption spectra of CH_2Cl_2 solutions containing the [Ir(Phppy)$_2$(N^N)][PF$_6$] and [Ir(Ph$_2$ppy)$_2$(N^N)][PF$_6$] complexes with N^N **1-4** are depicted in Figure 5.14. The broad and intense absorption band of the [Ir(Phppy)$_2$(N^N)][PF$_6$] series with λ_{max} ranging from 276 to 278 nm arises from spin-allowed ligand-centred $\pi^* \leftarrow \pi$ transitions. In contrast, the four complexes of the [Ir(Ph$_2$ppy)$_2$(N^N)][PF$_6$] family exhibit corresponding bands which are less intense and broader featuring two or three maxima in between 250 to 300 nm. The similar absorption bands around 400 and 425 nm for both series are assigned to MLCT transitions.

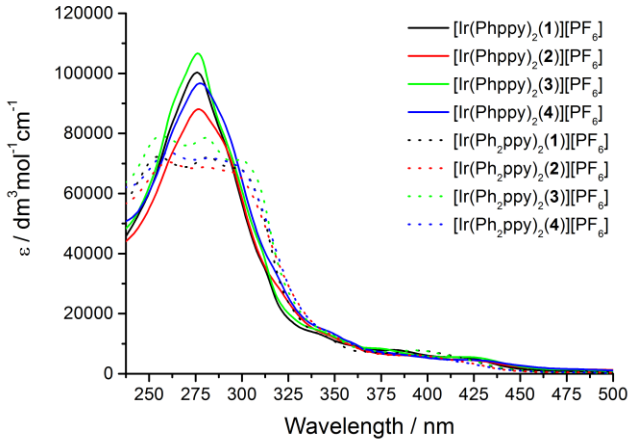

Figure 5.14 UV-Vis absorption spectra of the [Ir(Phppy)$_2$(N^N)][PF$_6$] and [Ir(Ph$_2$ppy)$_2$(N^N)][PF$_6$] complexes with N^N **1-4**, measured in 1.00 x 10^{-5} M CH_2Cl_2 solutions.

In solution, upon excitation into the latter MLCT bands, broad, unstructured emissions can be observed for [Ir(Phppy)$_2$(**1**)][PF$_6$] and [Ir(Ph$_2$ppy)$_2$(**1**)][PF$_6$] with maxima at 600 and 611 nm, respectively (Figure 5.15 left). This red-shift is consistent with the destabilization of the HOMO induced by the introduction of the electron-releasing phenyl substituent into the cyclometallating ligand [Ph$_2$ppy]$^-$. Analogously, a red-shift is recorded in passing from [Ir(Phppy)$_2$(**2**)$_2$][PF$_6$] to [Ir(Ph$_2$ppy)$_2$(**2**)$_2$][PF$_6$], from [Ir(Phppy)$_2$(**3**)$_2$][PF$_6$] to [Ir(Ph$_2$ppy)$_2$(**3**)$_2$][PF$_6$] and from Ir(Phppy)$_2$(**4**)$_2$][PF$_6$] to [Ir(Ph$_2$ppy)$_2$(**4**)$_2$][PF$_6$] (see Table 5.4). Furthermore, in both complex series, an additional red-shift is observed as the pendant phenyl ring is introduced into the ancillary ligand, whereas ^{t}Bu substituents in the 4- and 4'-positions lead to a blue-shift in the emission.

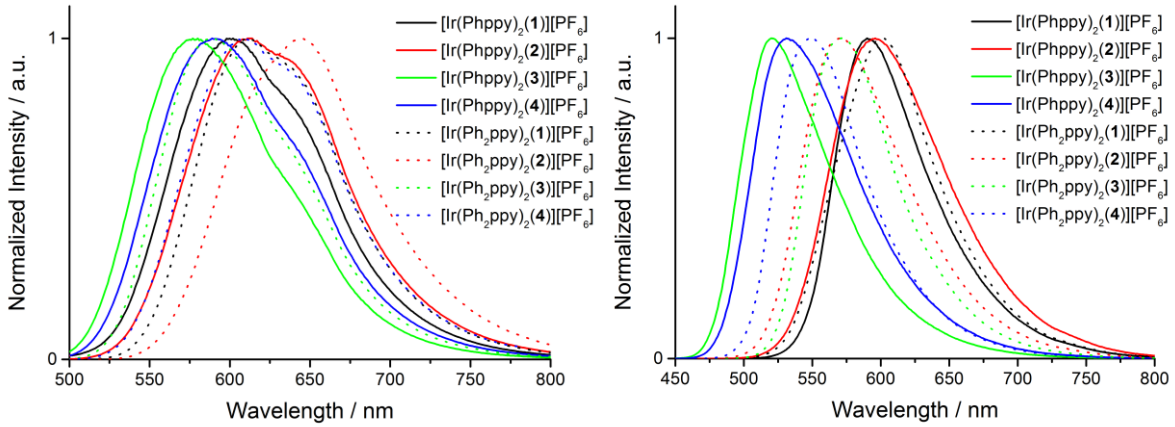

Figure 5.15 Emission spectra of $[Ir(Phppy)_2(N^\wedge N)][PF_6]$ and $[Ir(Ph_2ppy)_2(N^\wedge N)][PF_6]$ with N^N **1**-**4**, measured in (left) 1.00 x 10^{-5} M CH_2Cl_2 solutions (λ_{ex} = 420 nm, 400 nm for $[Ir(Ph_2ppy)_2(4)][PF_6]$) and (right) of the respective powder excited at 400 nm.

Compared to the spectra obtained in solution, the photoluminescence emissions of the powdered complexes show, in each case, a blue-shift (Table 5.4 and Figure 5.15 right). According to the solution measurements, a red-shift is observed due to the additional phenyl group on going from C^N ligands $[Phppy]^-$ to $[Ph_2ppy]^-$. The only exception is observed on passing from $[Ir(Phppy)_2(\mathbf{2})][PF_6]$ (596 nm) to $[Ir(Ph_2ppy)_2(\mathbf{2})][PF_6]$ (570 nm) which may be a consequence of the sterically crowded $[Ir(Ph_2ppy)_2(\mathbf{2})]^+$ cation suggested to result in packing effects. However, the electron-donating ^{t}Bu substituents attached to the N^N ligands lead to significant blue-shifts in the emission maxima in both solution and solid state (see also Figure 5.16).

Table 5.4 Photoluminescence maxima and PLQYs for $[Ir(Phppy)_2(N^\wedge N)][PF_6]$ and $[Ir(Ph_2ppy)_2(N^\wedge N)][PF_6]$ with N^N **1**-**4**.

Compound	Solution[a]		Powder[b]		Device configuration[c]	
	λ_{em}^{max} / nm	PLQY / %	λ_{em}^{max} / nm	PLQY / %	λ_{em}^{max} / nm	PLQY / %
$[Ir(Phppy)_2(\mathbf{1})][PF_6]$	600	13	590	30	599	20
$[Ir(Phppy)_2(\mathbf{2})][PF_6]$	611	4	596	11	615	11
$[Ir(Phppy)_2(\mathbf{3})][PF_6]$	577	35	520	13	592	24
$[Ir(Phppy)_2(\mathbf{4})][PF_6]$	590	13	531	13	597	15
$[Ir(Ph_2ppy)_2(\mathbf{1})][PF_6]$	611	8	600	28	614	17
$[Ir(Ph_2ppy)_2(\mathbf{2})][PF_6]$	645	2	570	26	618	7
$[Ir(Ph_2ppy)_2(\mathbf{3})][PF_6]$	588	23	571	56	596	23
$[Ir(Ph_2ppy)_2(\mathbf{4})][PF_6]$	609	4	548	56	602	14

[a] CH_2Cl_2 solutions, Argon degassed for the PLQY measurements, λ_{ex} = 420 nm, 400 nm for $[Ir(Ph_2ppy)_2(\mathbf{4})][PF_6]$. [b] λ_{ex} = 400 nm. [c] Complexes mixed with the ionic liquid $[BMIM][PF_6]$ in a 4:1 molar ratio.

Thin film photoluminescence data of each complex mixed with the ionic liquid $[BMIM][PF_6]$ in a 4:1 molar ratio, as used in device configuration, is shown in Table 5.4. Consistent to the solution data, the emission maxima for films of the $[Ir(Ph_2ppy)_2(N^\wedge N)][PF_6]$ compounds are slightly red-shifted

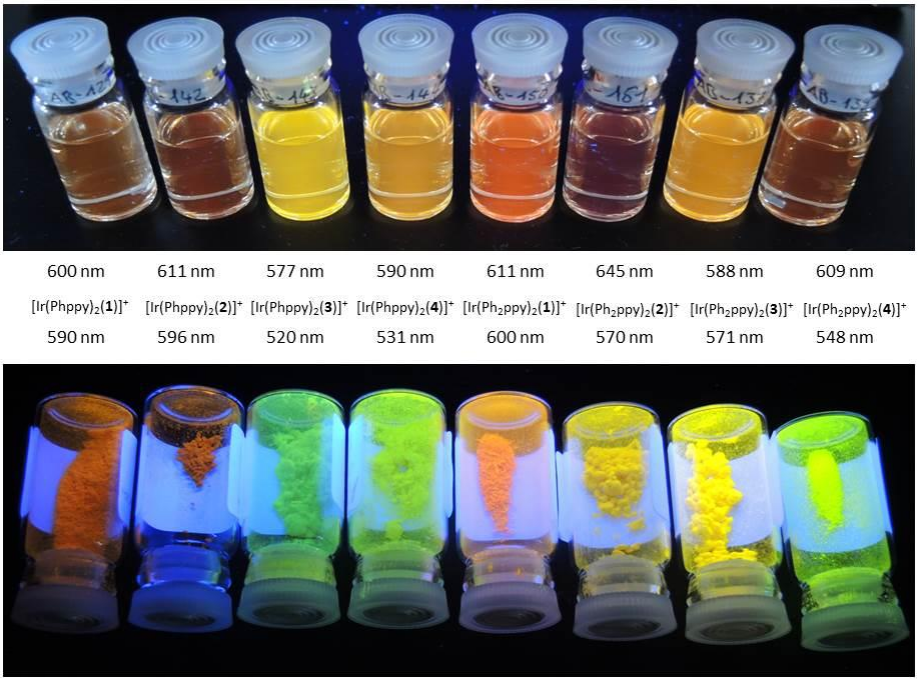

Figure 5.16 Photoluminescent emission behavior upon excitation at 365 nm of the $[Ir(Phppy)_2(N^\wedge N)][PF_6]$ and $[Ir(Ph_2ppy)_2(N^\wedge N)][PF_6]$ series with N^N **1**-**4** in (top) solution and (bottom) solid state.

compared to the $[Ir(Phppy)_2(N^\wedge N)][PF_6]$ series. In each case, the introduction of ^{t}Bu substituents on the N^N ligand leads to a blue-shifted emission maximum. The similar emission maxima observed for films and in solution stand in contradiction to the data obtained for the solid state. Since the complexes in thin films are present in low concentrations compared to solution, packing effects may be causing the sometimes unexpected large blue-shifted emission maxima in the solid state.

Table 5.5 Photoluminescence lifetimes for $[Ir(Phppy)_2(N^\wedge N)][PF_6]$ and $[Ir(Ph_2ppy)_2(N^\wedge N)][PF_6]$ with N^N **1**-**4** in solution and solid state.

Compound	Solution[a]			Powder		
	τ_{av}[b] / ns	τ_1 / ns (A_1)	τ_2 / ns (A_2)	τ_{av} / ns	τ_1 / ns (A_1)	τ_2 / ns (A_2)
$[Ir(Phppy)_2(\mathbf{1})][PF_6]$	260	257 (54164)	658 (346)	464	457 (80530)	1011 (1068)
$[Ir(Phppy)_2(\mathbf{2})][PF_6]$	101	99 (40267)	208 (657)	309	305 (59393)	1207 (252)
$[Ir(Phppy)_2(\mathbf{3})][PF_6]$	522	472 (35392	573 (34561)	364	331 (25592)	1109 (1144)
$[Ir(Phppy)_2(\mathbf{4})][PF_6]$	266	265 (46403)	740 (130)	383	368 (28153)	1118 (570)
$[Ir(Ph_2ppy)_2(\mathbf{1})][PF_6]$	166	164 (44021)	314 (711)	591	584 (1329)	1329 (514)
$[Ir(Ph_2ppy)_2(\mathbf{2})][PF_6]$	36	28 (6400)	39 (18317)	617	611 (44188)	2204 (162)
$[Ir(Ph_2ppy)_2(\mathbf{3})][PF_6]$	322	368 (35110)	189 (12273)	806	791 (71945)	3088 (480)
$[Ir(Ph_2ppy)_2(\mathbf{4})][PF_6]$	88	87 (41551)	373 (80)	1148	1105 (61273)	1761 (4344)

[a] Argon degassed CH_2Cl_2. [b] Biexponential fit using the equation $\tau_{av} = \Sigma A_i\tau_i / \Sigma A_i$ where A_i is the pre-exponantial factor of the lifetime.

In general, the PLQYs are enhanced passing from solution to thin film to solid state with $[Ir(Ph_2ppy)_2(N\hat{}N)][PF_6]$ (N^N **3** or **4**) exhibiting by far the highest PLQY values of 56 % (Table 5.4). The photoluminescence lifetimes of each complex in solution and solid state are collected in Table 5.5. On going from solution to the powdered compounds, the emission lifetime generally increases, especially for the most sterically crowded complex cations $[Ir(Ph_2ppy)_2(\mathbf{2})]^+$ and $[Ir(Ph_2ppy)_2(\mathbf{4})]^+$ which reaches averaged lifetimes of 617 and 1158 ns in the solid state compared to 36 and 88 ns when dissolved in argon-degassed CH_2Cl_2, respectively.

5.7 Electroluminescence and Device Data

Dr. Henk J. Bolink and his team in Valencia tested all eight iTMCs in the classical ITO/PEDOT:PSS/iTMC:IL 4:1 /Al LEEC device configuration driven with a block-wave pulsed current at a frequency of 1000 Hz and a 50% duty cycle at different current densities of 50, 100 and 300 A m^{-2}. Figure 5.17 left depicts the electroluminescence spectra with emission maxima ranging from 585–599 nm which are slightly blue-shifted compared to the photoluminescence maxima of the complexes in thin films as reported in Table 5.4. The performance data of each iTMC at an applied current density of 300 A m^{-2} is summarized in Table 5.6. The turn-on time for the LEEC devices varies significantly from relatively short (29 sec) for [Ir(Ph_2ppy)$_2$(**4**)][PF_6] to (> 1 h) for devices based on [Ir(Phppy)$_2$(**4**)][PF_6] or [Ir(Ph_2ppy)$_2$(**1**)][PF_6]. Starting at a high potential (9 V), rapidly reducing the value down to ≈ 2.8 V, the voltage follows a behavior, typically observed for LEECs, when the formation of the electric double layer reduces the initially high injection barriers (see Figure 5.17 right).[116]

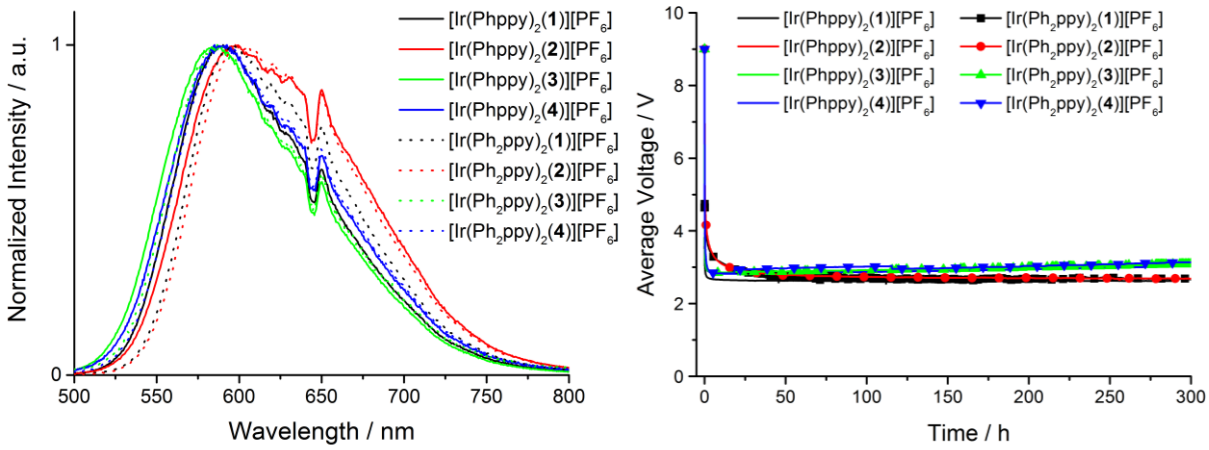

Figure 5.17 (Left) Normalized electroluminescence spectra of iTMCs [Ir(Phppy)$_2$(N^N)][PF_6] and [Ir(Ph_2ppy)$_2$(N^N)][PF_6] with N^N **1-4** in ITO/PEDOT:PSS/iTMC:IL 4:1 /Al LEEC devices and (right) their voltage vs. time curves at 300 A m^{-2} at a frequency of 1000 Hz and duty cycles of 50%.

As mentioned above, the different devices were tested at 50, 100 and 300 A m^{-2} with the luminance versus time curves presented in Figure 5.18. No decay over time is observed for the luminance of certain devices when running them at 50 and 100 A m^{-2}. This actually good and highly desired property makes it impossible to evaluate and directly compare these eight iTMCs. Therefore, to investigate the different performances, all LEEC devices were operated at 300 A m^{-2}, which is a much higher current density than normally used, allowing an accelerated degradation of the devices induced by the harsher conditions. As a result, the luminance increases with higher current density, but due to a reduction in the device efficiency caused by charge induced carrier quenching, this process is not linear.[117],[118]

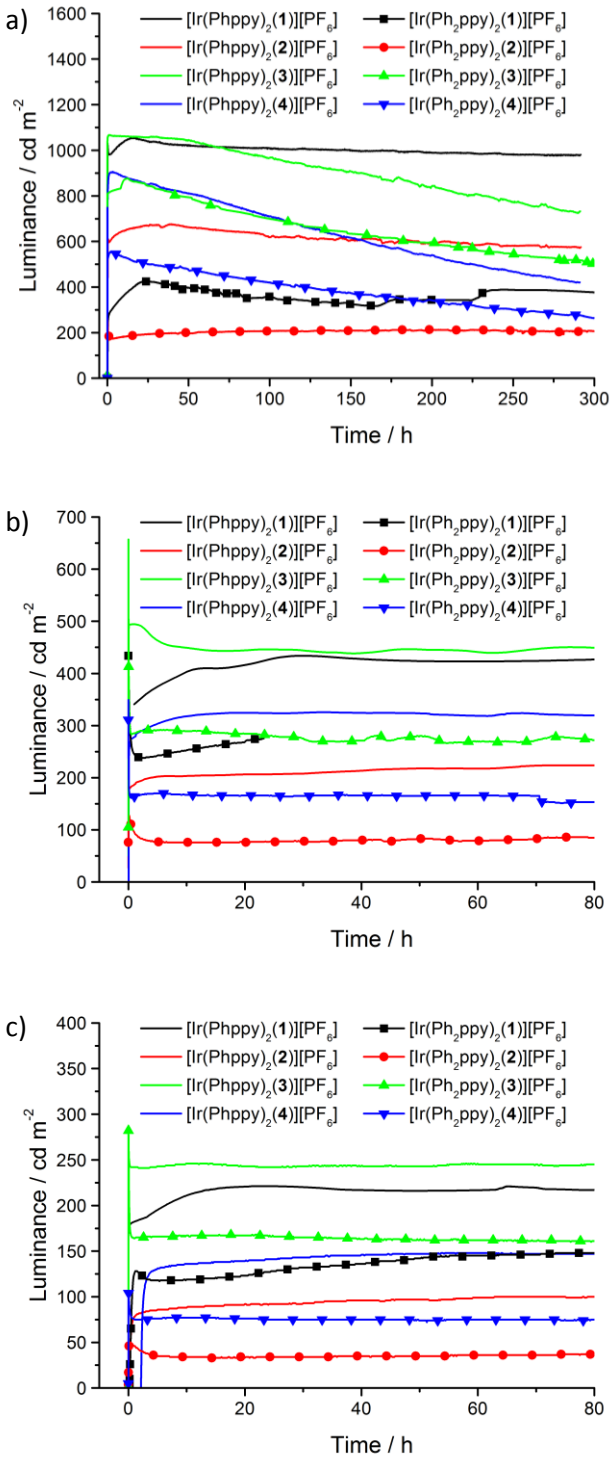

Figure 5.18 Luminance vs. time for the LEEC devices ITO/PEDOT:PSS/iTMC:IL 4:1 /Al based on iTMCs $[Ir(Phppy)_2(N^N)][PF_6]$ and $[Ir(Ph_2ppy)_2(N^N)][PF_6]$ with N^N **1-4** using pulsed current driving modes at (a) 300 A m^{-2}, (b) 100 A m^{-2} and (c) at 50 A m^{-2} current densities at a frequency of 1000 Hz and duty cycles of 50%.

Generally, devices based on $[Ir(Ph_2ppy)_2(N^N)][PF_6]$ reach slightly lower luminance values than with complexes containing the $[Phppy]^-$ C^N ligand. The efficiency scales directly to the luminance using pulsed current conditions, and hence, the $[Ir(Ph_2ppy)_2(N^N)][PF_6]$ series exhibits also lower efficiencies. Therefore, introducing π-stacking sites on the cyclometallating ligands does not have the expected advantageous effect in terms of device performance. Contrary to previous results, no

enhancement in the luminance nor the efficiency could be achieved upon attaching ^{t}Bu groups, acting as bulky substituents, onto the N^N ligand.[58] A plausible explanation could be that the $[Phppy]^-$ as well as the $[Ph_2ppy]^-$ ligands are so sterically demanding, leading to reduced close packing in the film offering enhanced non-radiative decay pathways. For LEEC devices containing the ancillary ligands **2** or **4** (additional π-stacking phenyl ring in the 6-position of the bpy domain), the efficiency is not improved compared to symmetric bpy ligands, a phenomena which was also reported by Zhang and co-workers.[107] The same trends can be observed for the PLQY.

Comparing the trends in the lifetime of LEEC devices, on going from $[Ir(Phppy)_2(N^N)][PF_6]$ to $[Ir(Ph_2ppy)_2(N^N)][PF_6]$, the $t_{1/2}$ is lowered despite the two π-stacking sites enabled by the two phenyl rings K and L (see Scheme 5.2). Likewise, the introduction of a further intra-cation π-stacking ability in the N^N ligand **2** and **4** leads to a faster decay of luminance. However, the only exception is observed for the device based on $[Ir(Ph_2ppy)_2(\mathbf{2})][PF_6]$ which, although exhibiting the lowest luminance (200 cd m^{-2}) of all compounds, remains constant over a period of more than 300 hours at a current density of 300 A m^{-2} (Figure 5.18).

Nevertheless, all compounds tested in this study possess exceptional stabilities in LEECs. The best performance is observed for devices based on iTMC $[Ir(Phppy)_2(\mathbf{1})][PF_6]$ with a maximum luminance of 1024 cd m^{-2}, an efficiency of 3.5 cd A^{-1} (recorded under enhanced measurement conditions, i.e. at an average current density of 300 A m^{-2}) and an extrapolated lifetime exceeding 2800 hours. Interestingly, $[Ir(Phppy)_2(\mathbf{1})][PF_6]$ possesses neither intra-cation π-stacking sites nor bulky side groups attached to the N^N ligand which are two widely used synthetic strategies reported to be advantageous for LEEC performances.[8],[57],[59] Therefore, these are not general design principles to obtain improved data[78],[80], as corroborated by $[Ir(Phppy)_2(\mathbf{1})][PF_6]$.

Table 5.6 Performance data of the LEEC devices containing $[Ir(Phppy)_2(N^N)][PF_6]$ and $[Ir(Ph_2ppy)_2(N^N)][PF_6]$ complexes with N^N **1**-**4** operated at a pulsed current density of 300 A m^{-2}, at a frequency of 1000 Hz and a 50% duty cycle.

Compound	$Luminance_{max}$ / cd m^{-2}	$Efficacy_{max}$ / cd A^{-1}	t_{on} / h	$t_{1/2}$ / h
$[Ir(Phppy)_2(\mathbf{1})][PF_6]$	1024	3.5	0.14	2800
$[Ir(Phppy)_2(\mathbf{2})][PF_6]$	676	2.2	0.42	1204
$[Ir(Phppy)_2(\mathbf{3})][PF_6]$	1090	3.5	0.03	437
$[Ir(Phppy)_2(\mathbf{4})][PF_6]$	910	2.9	1.11	260
$[Ir(Ph_2ppy)_2(\mathbf{1})][PF_6]$	425	1.4	1.21	360
$[Ir(Ph_2ppy)_2(\mathbf{2})][PF_6]$	261	0.7	0.05	>2800
$[Ir(Ph_2ppy)_2(\mathbf{3})][PF_6]$	1048	2.9	0.07	282
$[Ir(Ph_2ppy)_2(\mathbf{4})][PF_6]$	748	1.8	0.01	147

5.8 Conclusion

Two new series of cyclometallated Ir(III) complexes of the type $[Ir(Phppy)_2(N^N)][PF_6]$ and $[Ir(Ph_2ppy)_2(N^N)][PF_6]$ with N^N **1-4** were successfully synthesized to investigate the effects of multiple π-stacking interactions within the coordination sphere of the Ir(III) metal center. An additional solvento-precursor $[Ir(C^N)_2(MeOH)_2][PF_6]$ was introduced in the classical synthetic route to prevent the final complexes from detrimental chloride-impurities. Extended variable temperature solution ^1H NMR spectroscopic measurements and single crystal structure determinations ascribed these series of complexes the ability of forming up to three π-stacking interactions. Thereby, the cyclometallating $[Ph_2ppy]^-$ ligands in this work were synthetically modified in a way so as to enable face-to-face intramolecular π-stacking sites between the two C^N ligands which is, to our knowledge, the first class of compounds, reported until now. The eight iTMCs show excellent luminescent properties exhibiting orange emissions centered between 592–618 nm and PLQYs up to 24% in solid thin films. Employing these complexes in LEEC devices leads to exceptional stable luminance output over time even when operated at elevated current densities of 300 A m^{-2}. The best performance is observed for devices based on iTMC $[Ir(Phppy)_2(\mathbf{1})][PF_6]$ with a maximum luminance of 1024 cd m^{-2}, an efficiency of 3.5 cd A^{-1} and an extrapolated lifetime exceeding 2800 hours even under accelerated measuring conditions. Interestingly, these remarkable lifetimes were reached by devices based on complexes with and without the π-stacking ability corroborating that multiple face-to-face π-stacking sites are not necessarily a general design principle to achieve good LEEC device performances.

5.9 Experimental

Ligands 2,2'-bipyridine (**1**) and 4,4'-di-*tert*-butyl-2,2'-bipyridine (**3**) were purchased from Sigma Aldrich and used as supplied. 6-phenyl-2,2'-bipyridine[71] (**2**) and 6-phenyl-4,4'-di-*tert*-butyl-2,2'-bipyridine[72] (**4**) were synthesized according to literature procedures.

5.9.1 $[Ir_2(Phppy)_4Cl_2]$

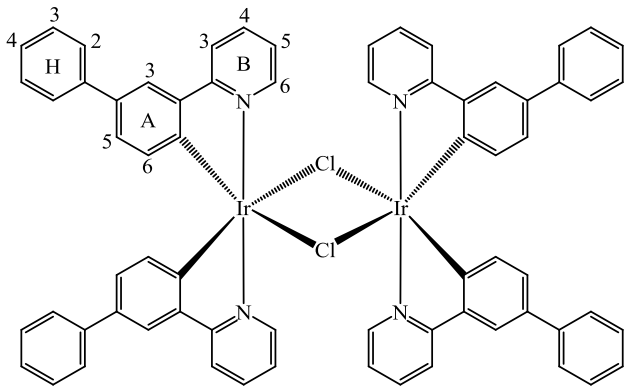

A mixture of H_2O (8 mL) and 2-ethoxyethanol (25 mL) containing HPhppy (0.600 g, 2.59 mmol, 2.30 eq) and $IrCl_3.H_2O$ (0.638 g 1.13 mmol, 1.00 eq) was heated at 115 °C for 20 h. The reaction mixture was allowed to reach room temperature, and then the yellow precipitate was filtered off, washed with H_2O and n-hexane and finally redissolved in acetone to be purified by column chromatography (Fluka silica gel 60, 0.040–0.063 mm; CH_2Cl_2:iPrOH 100:1) to give a yellow solid (0.362 g, 0.263 mmol, 46.5%).

^{1}H NMR (500 MHz, acetone-d_6) δ/ppm 9.34 (ddd, J = 5.8, 1.5, 0.7 Hz, 4H, H^{B6}), 8.41 (d, J = 8.0 Hz, 4H, H^{B3}), 8.06 (ddd, J = 8.1, 7.6, 1.6 Hz, 4H, H^{B4}), 7.97 (d, J = 2.0 Hz, 4H, H^{A3}), 7.58 – 7.52 (m, 8H, H^{H2}), 7.36 – 7.31 (m, 8H, H^{H3}), 7.24 – 7.20 (m, 4H, H^{H4}), 7.14 – 7.09 (m, 4H, H^{B5}), 6.86 (dd, J = 8.1, 2.0 Hz, 4H, H^{A5}), 6.03 (d, J = 8.1 Hz, 4H, H^{A6}).

^{13}C NMR (126 MHz, acetone-d_6) δ/ppm 168.9 (C^{B2}), 152.3 (C^{B6}), 146.0 (C^{A2}), 145.8 (C^{A1}), 142.3 (C^{H1}), 138.3 (C^{B4}), 135.1 (C^{A4}), 131.8 (C^{A6}), 129.5 (C^{H3}), 128.3 (C^{A5}), 127.2 (C^{H4}), 127.1 (C^{H2}), 124.1 (C^{B5}), 123.0 (C^{A3}), 120.2 (C^{B3}).

5.9.2 $[Ir_2(Ph_2ppy)_4Cl_2]$

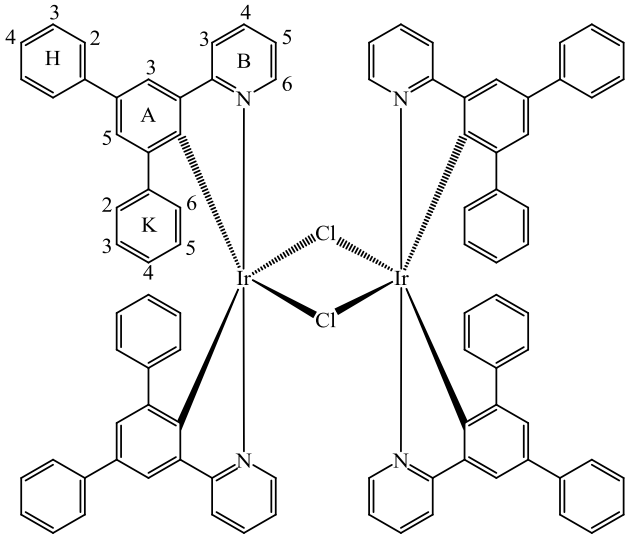

A mixture of H_2O (5 mL) and 2-ethoxyethanol (15 mL) containing HPh_2ppy (0.500 g, 1.63 mmol, 2.30 eq) and $IrCl_3.H_2O$ (0.400 g, 0.707 mmol, 1.00 eq) was heated at 110 °C for 20 h under an inert atmosphere. The reaction mixture was allowed to reach room temperature, and then the yellow precipitate was filtered off, washed with H_2O and diethyl ether and finally redissolved in dichloromethane to be purified by column chromatography (Fluka silica gel 60, 0.040–0.063 mm; $CH_2Cl_2 \rightarrow CH_2Cl_2$:MeOH 100:3) to give a yellow solid (0.342 g, 0.203 mmol, 57.4%).

^{1}H NMR (500 MHz, acetone-d_6) δ/ppm 8.05 – 8.00 (m, 4H, H^{B6}), 7.66 (d, J = 2.0 Hz, 4H, H^{A3}), 7.60 (dt, J = 8.0, 1.6 Hz, 8H, H^{H2}), 7.40 – 7.35 (m, 8H, H^{H3}), 7.34 (d, J = 8.1 Hz, 4H, H^{B3}), 7.29 – 7.24 (m, 4H, H^{H4}), 7.10 (td, J = 8.2, 1.5 Hz, 4H, H^{B4}), 7.08 – 7.03 (m, 4H, $H^{K2/K6}$), 6.89 (d, J = 2.1 Hz, 4H, H^{A5}), 6.84 (t, J = 6.8 Hz, 4H, $H^{K3/K5}$), 6.67 (tt, J = 7.3, 1.3 Hz, 4H, H^{K4}), 6.27 – 6.15 (m, 8H, $H^{K2/K6+K3/K5}$), 5.86 (ddd, J = 7.2, 5.8, 1.3 Hz, 4H, H^{B5}).

^{13}C NMR (126 MHz, acetone-d_6) δ/ppm 167.2 (C^{B2}), 151.3 (C^{B6}), 148.7 (C^{A2}), 148.4 (C^{A6}), 145.0 (C^{K1}), 142.7 (C^{A1}), 141.4 (C^{H1}), 135.6 (C^{B4}), 134.7 (C^{A4}), 130.7 (C^{A5}), 128.7 (C^{H3}), 128.4 ($C^{K2/K6}$), 126.8 ($C^{K3/K5}$), 126.6 (C^{H2}), 125.2 (C^{H4}), 121.9 (C^{B5}), 120.9 (C^{A3}), 118.6 (C^{B3}).

5.9.3 $[Ir(Phppy)_2(MeOH)_2][PF_6]$

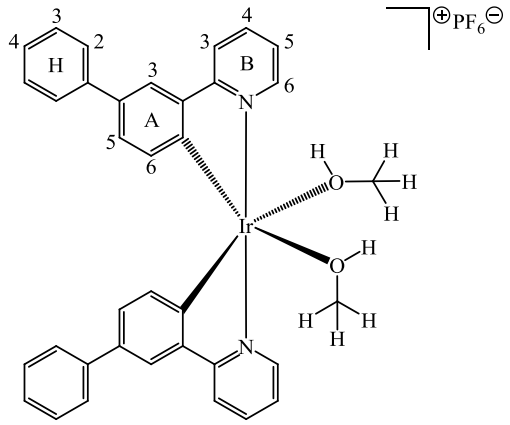

A suspension of $[Ir_2(Phppy)_4Cl_2]$ (1.15 g, 0.838 mmol, 1.00 eq) and $AgPF_6$ (0.464 g, 1.84 mmol, 2.19 eq) in MeOH (70 mL) was stirred at room temperature for 2 h. The precipitated AgCl was removed by filtrating over celite. Evaporation of the yellow filtrate under reduced pressure afforded the product as yellow solid (1.43 g, 1.66 mmol, 99.0%).

^{1}H NMR (500 MHz, CD_3OD) δ/ppm 8.92 (d, J = 5.0 Hz, 2H, H^{B6}), 8.28 (d, J = 8.1 Hz, 2H, H^{B3}), 8.07 (t, J = 7.4 Hz, 2H, H^{B4}), 7.93 (d, 2H, H^{A3}), 7.59 – 7.46 (m, 6H, H^{B5+H2}), 7.35 (t, J = 7.7 Hz, 4H, H^{H3}), 7.24 (t, J = 7.4 Hz, 2H, H^{H4}), 6.96 (dd, J = 8.0, 1.9 Hz, 2H, H^{A5}), 6.18 (d, J = 7.9 Hz, 2H, H^{A6}), 3.35 (s, 6H, H^{Methyl}).

^{13}C NMR (126 MHz, CD_3OD) δ/ppm 169.5 (C^{B2}), 150.2 (C^{B6}), 146.7 (C^{A2}), 142.4 (C^{H1}), 140.4 (C^{B4}), 138.2 (C^{A1}), 137.1 (C^{A4}), 134.5 (C^{A6}), 129.8 (C^{H3}), 129.4 (C^{A5}), 127.8 (C^{H4}), 127.6 (C^{H2}), 124.2 (C^{B5}), 123.8 (C^{A3}), 120.8 (C^{B3}), 49.9 (C^{Methyl}).

5.9.4 $[Ir(Ph_2ppy)_2(MeOH)_2][PF_6]$

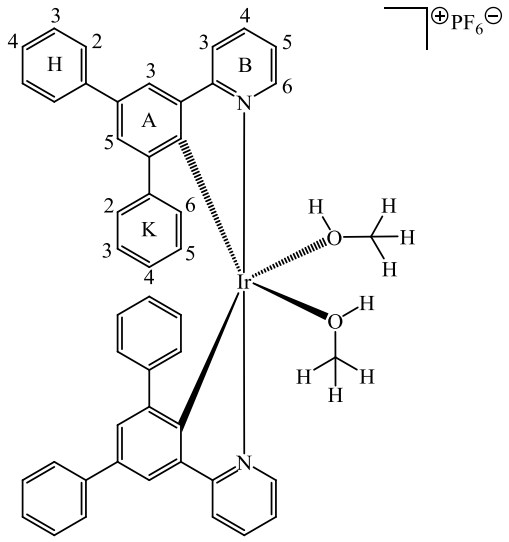

A suspension of 298 mg (0.177 mmol, 1.000 eq) $[Ir_2(Ph_2ppy)_4Cl_2]$ and 98.2 mg (0.388 mmol, 2.19 eq) $AgPF_6$ was stirred in MeOH at room temperature for 2 h. The yellow suspension was filtered over celite where upon the filtrate was evaporated to dryness to give a yellow greenish solid (358 mg, 0.353 mmol, 99.7%).

^{1}H NMR (500 MHz, CD_3OD) δ/ppm 8.23 (ddd, J = 5.9, 1.4, 0.6 Hz, 2H, H^{B6}), 7.87 (d, J = 2.1 Hz, 2H, H^{A3}), 7.81 (d, J = 8.2 Hz, 2H, H^{B3}), 7.70 – 7.64 (m, 6H, H^{H2+B4}), 7.47 – 7.40 (m, 4H, H^{H3}), 7.31 (tt, J = 7.0, 1.2 Hz, 2H, H^{H4}), 7.07 (ddd, J = 7.3, 5.8, 1.3 Hz, 2H, H^{B5}), 6.98 (d, J = 6.8 Hz, 2H, $H^{K2/K6}$), 6.94 (d, J = 2.1 Hz, 2H, H^{A5}), 6.91 – 6.82 (m, 4H, H^{K3+K5}), 6.55 (t, J = 6.8 Hz, 2H, H^{K4}), 6.28 (d, J = 7.5 Hz, 2H, $H^{K2/K6}$), 3.35 (s, 6H, H^{Methyl}).

^{13}C NMR (126 MHz, CD_3OD) δ/ppm 168.6 (C^{B2}), 153.4 (C^{A6}), 151.0 (C^{B6}), 150.3 (C^{A2}), 146.3 (C^{K1}), 141.9 (C^{H1}), 139.4 (C^{B4}), 137.0 (C^{A4}), 132.0 (C^{A1}), 131.0 (C^{A5}), 130.0 ($C^{K2/K6}$), 130.0 (C^{H3}), 129.6 ($C^{K2/K6}$), 128.2 ($C^{K3/K5}$), 128.1 (C^{H4}), 127.7 (C^{K4}), 127.5 (C^{H2}), 127.1 ($C^{K3/K5}$), 122.8 (C^{B5}), 122.7 (C^{A3}), 120.8 (C^{B3}), 49.9 (C^{Methyl}).

5.9.5 [Ir(Phppy)$_2$(**1**)][PF$_6$]

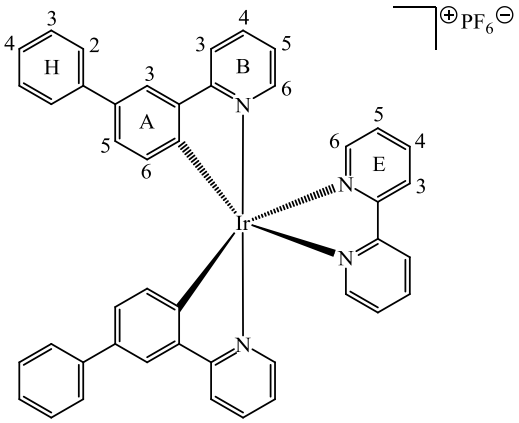

A suspension of [Ir$_2$(Phppy)$_2$(MeOH)$_2$][PF$_6$] (150 mg, 0.174 mmol, 1.00 eq) and **1** (27.5 mg, 0.176 mmol, 1.01 eq) in MeOH (15 mL) was sonicated until all the solid had dissolved. An excess of NH_4PF_6 (10.0 eq) was added to the solution which was stirred for 1 h at room temperature. The yellow precipitate was filtered off, washed with MeOH and diethyl ether and then purified by column chromatography (Fluka silica gel 60, 0.040–0.063 mm; CH_2Cl_2 → CH_2Cl_2:MeOH 100:0.5). The pure product was obtained by crystallization in CH_2Cl_2 overlaid with EtOH:n-hexane 2:1 as orange solid (154 mg 0.161 mmol, 92.5%).

^{1}H NMR (500 MHz, CD_2Cl_2) δ/ppm 8.54 (d, J = 8.1 Hz, 2H, H^{E3}), 8.19 – 8.11 (m, 4H, H^{E4+E6}), 8.19 (m, 2H, H^{B3}), 7.98 (d, J = 2.0 Hz, 2H, H^{A3}), 7.85 (m, 2H, H^{B4}), 7.61 (m, 4H, H^{H2}), 7.56 (m, 2H, H^{B6}), 7.51 (ddd, J = 7.5, 5.4, 0.9 Hz, 2H, H^{E5}), 7.43 (m, 4H, H^{H3}), 7.33 (m, 2H, H^{H4}), 7.23 (dd, J = 7.9, 1.9 Hz, 2H, H^{A5}), 7.06 (ddd, J = 7.3, 5.8, 1.4 Hz, 2H, H^{B5}), 6.45 (d, J = 7.9 Hz, 2H, H^{A6}).

^{13}C NMR (126 MHz, CD_2Cl_2) δ/ppm 168.1 (C^{B2}), 156.2 (C^{E2}), 151.4 (C^{E6}), 149.6 (C^{A1}), 149.2 (C^{B6}), 144.9 (C^{A2}), 141.6 (C^{H1}), 140.1 (C^{E4}), 138.9 (C^{B4}), 136.5 (C^{A4}), 132.7 (C^{A6}), 130.2 (C^{A5}), 129.4 (C^{H3}), 129.0 (C^{E5}), 127.5 (C^{H4}), 127.1 (C^{H2}), 125.2 (C^{E3}), 124.2 (C^{B5}), 124.0 (C^{A3}), 120.6 (C^{B3}).

IR (solid, $\tilde{\nu}$/cm^{-1}) 3028 (w), 1600 (w), 1563 (w), 1534 (w), 1479 (m), 1461 (w), 1447 (w), 1428 (m), 1313 (w), 1262 (w), 1165 (w), 1073 (w), 1027 (w), 878 (w), 837 (s), 826 (s), 773 (s), 760 (s), 744 (s), 734 (m), 720 (m), 705 (m), 693 (m), 637 (m), 608 (w), 556 (s), 518 (w), 489 (w), 475 (w).

UV-Vis λ/nm (ε/L mol^{-1} cm^{-1}) (CH_2Cl_2, 1.00 × 10^{-5} mol dm^{-3}) 276 (100 000), 295 sh (69 000), 315 sh (32 000), 345 (13 000), 380 (8 000), 420 (5 000).

Emission (CH_2Cl_2, c = 1.00 × 10^{-5} mol dm^{-3}, λ_{ex} = 420 nm) λ_{em} = 600, 639 sh nm.

ESI-MS *m/z* 809.6 [M – PF$_6$]$^+$ (base peak, calc. 809.0).

Found C 54.71, H 3.57, N 5.93; $C_{44}H_{32}F_6IrN_4P{\cdot}0.5\ H_2O$ requires C 54.88, H 3.45, N 5.82%.

Crystallography $C_{44}H_{32}F_6IrN_4P$, M = 953.93, orange block, monoclinic, space group $P2_1/n$, a = 15.0877(10), b = 13.1747(9), c = 18.0930(12) Å, β = 96.094(2)°, U = 3576.1(4) Å^3, Z = 4, D_c = 1.772 Mg m^{-3}, μ(Cu-K$_\alpha$) = 8.270 mm^{-1}, T = 123 K. Total 63369 reflections, 6470 unique, R_{int} = 0.0329. Refinement of 6256 reflections (505 parameters) with $I > 2\sigma(I)$ converged at final $R1$ = 0.0192 ($R1$ all data = 0.0199), $wR2$ = 0.0487 ($wR2$ all data = 0.0492), gof = 1.054. CCDC 1019228.

5.9.6 [Ir(Phppy)$_2$(**2**)][PF$_6$]

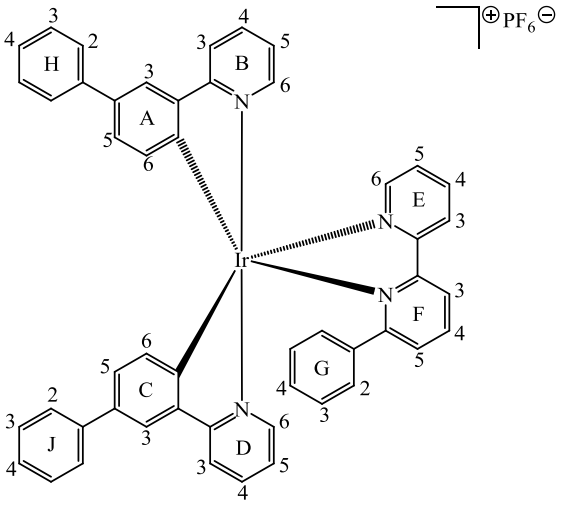

A suspension of [Ir(Phppy)$_2$(MeOH)$_2$][PF$_6$] (150 mg, 0.174 mmol, 1.00 eq) and **2** (40.8 mg, 0.176 mmol, 1.01 eq) in MeOH (15 mL) was sonicated until all the solid had dissolved. An excess of NH_4PF_6 (10.0 eq) was added to the solution which was stirred for 1 h at room temperature. The yellow precipitate was filtered off, washed with MeOH and diethyl ether and then purified by column chromatography (Fluka silica gel 60, 0.040–0.063 mm; CH_2Cl_2 → CH_2Cl_2:MeOH 100:0.5). The pure product was obtained by crystallization in CH_2Cl_2 overlaid with EtOH:n-hexane 2:1 as orange solid (105 mg 0.102 mmol, 58.6%).

^{1}H NMR (500 MHz, CD_2Cl_2) δ/ppm 8.56 (dd, J = 8.1, 1.1 Hz, 1H, H^{F3}), 8.53 (d, J = 8.2 Hz, 1H, H^{E3}), 8.24 (t, J = 7.9 Hz, 1H, H^{F4}), 8.14 (td, J = 8.0, 1.5 Hz, 1H, H^{E4}), 8.00 (dd, J = 5.5, 1.1 Hz, 1H, H^{E6}), 7.96 (m, 2H, H^{B3+D3}), 7.92 (m, 1H, H^{B4}), 7.82 (m, 1H, H^{D4}), 7.78 (d, J = 2.0 Hz, 1H, H^{A3}), 7.75 (m, 1H, H^{B6}), 7.55 (m, 2H, H^{H2}), 7.50 (m, 3H, H^{J2+F5}), 7.46 (m, 1H, H^{D6}), 7.45–7.36 (m, 6H, $H^{C3+E5+H3+J3}$), 7.33–7.25 (m, 2H, H^{H4+J4}), 7.17–7.07 (m, 3H, $H^{A5+B5+D5}$), 6.97 (tt, J = 7.5, 1.2 Hz, 1H, H^{G4}), 6.76 (broadened t, 2H, H^{G3}), 6.69 (dd, J = 7.9, 1.9 Hz, 1H, H^{C5}), 6.57 (br, H^{G2}), 6.10 (d, J = 8.0 Hz, 1H, H^{A6}), 5.73 (d, J = 7.9 Hz, 1H, H^{C6}).

^{13}C NMR (126 MHz, CD_2Cl_2) δ/ppm 169.2 (C^{B2}), 167.5 (C^{D2}), 166.4 (C^{F6}), 157.5 (C^{E2}), 157.3 (C^{F2}), 150.9 (C^{E6}), 150.6 (C^{C1}), 149.5 (C^{B6}), 149.5 (C^{D6}), 146.1 (C^{A1}), 144.2 (C^{A2}), 144.0 (C^{C2}), 142.2 (C^{J1}), 141.2 (C^{H1}), 140.3 (C^{F4}), 139.9 (C^{E4}), 138.9 (C^{D4}), 138.8 (C^{B4}), 138.5 (C^{G1}), 136.5 (C^{A4}), 134.3 (C^{C4}), 132.5 (C^{C6}), 131.3 (C^{A6}), 130.7 (C^{F5}), 130.2 (C^{A5}), 129.4 ($C^{H3/J3}$), 129.3 ($C^{H3/J3}$), 129.2 (C^{C5}), 129.0 (C^{G4}), 128.5 (C^{G3}), 128.4 (C^{E5}), 128.1 (C^{G2}), 127.6 (C^{H4}), 127.1 (C^{J4}), 127.0 (C^{H2}), 126.9 (C^{J2}), 125.6 (C^{E3}), 124.3 (C^{D5}), 124.2 (C^{F3}), 123.8 (C^{C3}), 123.7 (C^{A3}), 123.3 (C^{B5}), 120.7 (C^{B3}), 120.5 (C^{D3}).

IR (solid, $\tilde{\nu}$/cm^{-1}) 3027 (w), 1599 (m), 1562 (w), 1535 (w), 1478 (m), 1449 (m), 1428 (m), 1326 (w), 1296 (w), 1253 (w), 1224 (w), 1165 (w), 1113 (w), 1072 (w), 1031 (w), 877 (w), 835 (s), 781 (m), 760 (s), 718 (m), 696 (s), 639 (m), 624 (w), 608 (w), 556 (s), 487 (w).

UV-Vis λ/nm (ε/L mol^{-1} cm^{-1}) (CH_2Cl_2, 1.00 × 10^{-5} mol dm^{-3}) 277 (88 000), 295 sh, (69 000), 315 sh (33 000), 345 (13 000), 380 (6 000), 420 (5 000).

Emission (CH_2Cl_2, c = 1.00 × 10^{-5} mol dm^{-3}, λ_{ex} = 420 nm) λ_{em} = 611, 639 sh nm.

ESI-MS *m/z* 885.7 $[M - PF_6]^+$ (base peak, calc. 885.1).

Found C 58.00, H 3.90, N 5.37; $C_{50}H_{36}F_6IrN_4P$ requires C 58.30, H 3.52, N 5.44%.

5.9.7 [Ir(Phppy)$_2$(**3**)][PF$_6$]

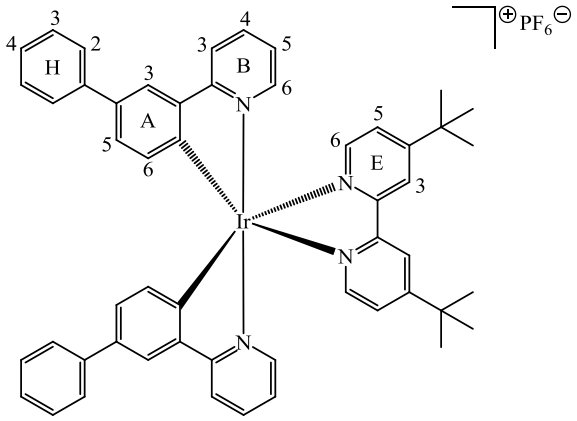

A suspension of [Ir(Phppy)$_2$(MeOH)$_2$][PF$_6$] (150 mg, 0.174 mmol, 1.00 eq) and **3** (47.2 mg, 0.176 mmol, 1.01 eq) in MeOH (15 mL) was sonicated until all the solid had dissolved. An excess of NH_4PF_6 (10.0 eq) was added to the solution which was stirred for 1 h at room temperature. The yellow precipitate was filtered off, washed with MeOH and diethyl ether and then purified by column chromatography (Fluka silica gel 60, 0.040–0.063 mm; CH_2Cl_2 → CH_2Cl_2:MeOH 100:0.5). The pure product was obtained by crystallization in CH_2Cl_2 overlaid with EtOH:n-hexane 2:1 as yellow solid (148 mg 0.139 mmol, 79.9%).

^{1}H NMR (500 MHz, CD_2Cl_2) δ/ppm 8.31 (d, J = 1.7 Hz, 2H, H^{E3}), 8.09 (d, J = 8.0 Hz, 2H, H^{B3}), 8.02 (d, J = 5.8 Hz, 2H, H^{E6}), 7.97 (d, J = 1.9 Hz, 2H, H^{A3}), 7.86 (ddd, J = 8.3, 7.6, 1.5 Hz, 2H, H^{B4}), 7.61 (m, 4H, H^{H2}), 7.58 (m, 2H, H^{B6}), 7.48 (dd, J = 5.9, 1.9 Hz, 2H, H^{E5}), 7.44 (m, 4H, H^{H3}), 7.33 (m, 2H, H^{H4}), 7.22 (dd, J = 7.9, 2.0 Hz, 2H, H^{A5}), 7.08 (ddd, J = 7.3, 5.9, 1.3 Hz, 2H, H^{B5}), 6.44 (d, J = 7.9 Hz, 2H, H^{A6}), 1.44 (s, 18H, H^{tBu}).

^{13}C NMR (126 MHz, CD_2Cl_2) δ/ppm 168.2 (C^{B2}), 164.7 (C^{E4}), 156.1 (C^{E2}), 151.0 (C^{E6}), 150.1 (C^{A1}), 149.3 (C^{B6}), 144.9 (C^{A2}), 141.7 (C^{H1}), 138.8 (C^{B4}), 136.3 (C^{A4}), 132.6 (C^{A6}), 130.1 (C^{A5}), 129.4 (C^{H3}), 127.5 (C^{H4}), 127.1 (C^{H2}), 126.3 (C^{E5}), 124.0 (C^{B5}), 123.9 (C^{A3}), 121.5 (C^{E3}), 120.5 (C^{B3}), 36.2 ($C^{quat\text{-}tBu}$), 30.6 (C^{tBu}).

IR (solid, $\tilde{\nu}$/cm^{-1}) 2958 (w), 1610 (w), 1563 (w), 1478 (m), 1429 (w), 1415 (w), 1368 (w), 1253 (w), 1224 (w), 1166 (w), 1070 (w), 1030 (w), 914 (w), 895 (w), 877 (w), 832 (s), 824 (s), 784 (m), 761 (s), 741 (m), 720 (w), 698 (m), 639 (w), 607 (m), 556 (s), 483 (w).

UV-Vis λ/nm (ε/L mol^{-1} cm^{-1}) (CH_2Cl_2, 1.00 × 10^{-5} mol dm^{-3}) 276 (107 000), 295 sh (73 000), 310 sh (41 000), 345 (14 000), 375 (8 000), 420 (5 000).

Emission (CH_2Cl_2, c = 1.00 × 10^{-5} mol dm^{-3}, λ_{ex} = 420 nm) λ_{em} = 577, 639 sh nm.

ESI-MS *m/z* 921.8 $[M - PF_6]^+$ (base peak, calc. 921.2).

Found C 58.32, H 4.88, N 5.42; $C_{52}H_{48}F_6IrN_4P$ requires C 58.58, H 4.54, N 5.26%.

5.9.8 [Ir(Phppy)$_2$(**4**)][PF$_6$]

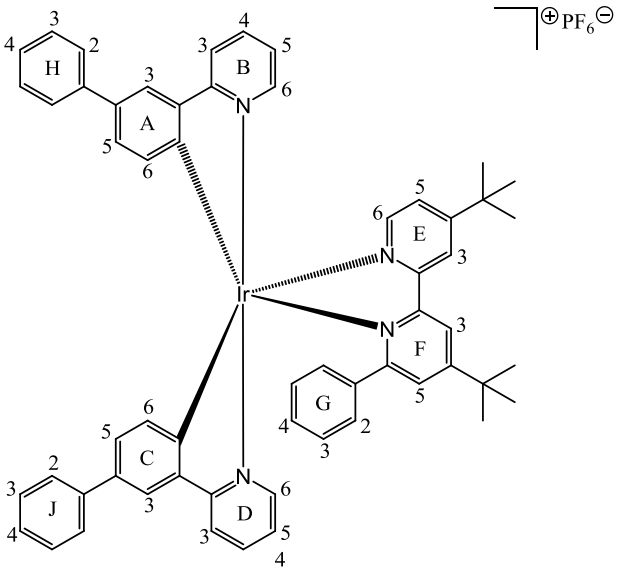

A suspension of [Ir(Phppy)$_2$(MeOH)$_2$][PF$_6$] (150 mg, 0.174 mmol, 1.00 eq) and **4** (60.6 mg, 0.176 mmol, 1.01 eq) in MeOH (15 mL) was sonicated until all the solid had dissolved. An excess of NH_4PF_6 (10.0 eq) was added to the solution which was stirred for 1 h at room temperature. The yellow precipitate was filtered off, washed with MeOH and diethyl ether and then purified by column chromatography (Fluka silica gel 60, 0.040–0.063 mm; CH_2Cl_2 → CH_2Cl_2:MeOH 100:0.5). The pure product was obtained by crystallization in CH_2Cl_2 overlaid with EtOH:n-hexane 2:1 as yellow solid (145 mg 0.127 mmol, 73.0%).

^{1}H NMR (500 MHz, CD_2Cl_2) δ/ppm 8.35 (d, J = 2.0 Hz, 1H, H^{F3}), 8.32 (d, J = 1.9 Hz, 1H, H^{E3}), 7.96 (d, J = 8.1 Hz, 2H, H^{D3+B3}), 7.92 (m, 1H, H^{B4}), 7.88 (d, J = 5.9 Hz, 1H, H^{E6}), 7.83 (ddd, J = 8.2, 7.6, 1.5 Hz, 1H, H^{D4}), 7.78 (d, J = 2.0 Hz, 1H, H^{A3}), 7.75 (d, J = 5.7 Hz, 1H, H^{B6}), 7.54 (m, 2H, H^{H2}), 7.50 (m, 2H, H^{J2+J6}), 7.47–7.37 (m, 8H, $H^{C3+D6+E5+F5+H3+J3}$), 7.33–7.27 (m, 2H, H^{H4+J4}), 7.15–7.09 (m, 3H, $H^{A5+B5+D5}$), 6.97 (tt, J = 7.6, 1.2 Hz, 1H, H^{G4}), 6.76 (broadened t, 2H, H^{G3}), 6.68 (dd, J = 8.0, 1.9 Hz, 1H, H^{C5}), 6.58 (br, 2H, H^{G2}), 6.11 (d, J = 8.0 Hz, 1H, H^{A6}), 5.72 (d, J = 7.9 Hz, 1H, H^{C6}), 1.49 (s, 9H, H^{tBu-F}), 1.44 (s, 9H, H^{tBu-E}).

^{13}C NMR (126 MHz, CD_2Cl_2) δ/ppm 169.2 (C^{B2}), 167.7 (C^{D2}), 166.1 (C^{F6}), 164.9 (C^{F4}), 164.5 (C^{E4}), 157.4 (C^{F2}), 157.3 (C^{E2}), 151.0 (C^{C1}), 150.4 (C^{E6}), 149.6 (C^{D6}), 149.5 (C^{B6}), 146.6 (C^{A1}), 144.2 (C^{A2}), 144.0 (C^{C2}), 142.2 (C^{J1}), 141.3 (C^{H1}), 138.9 (C^{G1}), 138.8 (C^{D4}), 138.7 (C^{B4}), 136.3 (C^{A4}), 134.2 (C^{C4}), 132.5 (C^{C6}), 131.4 (C^{A6}), 130.2 (C^{A5}), 129.4 (C^{H3}), 129.3 (C^{J3+J5}), 129.1 (C^{C5}), 128.9 (C^{G4}), 128.4 (C^{G3}), 128.2 (C^{G2}), 127.6 (C^{F5}), 127.5 (C^{H4}), 127.0 (C^{H2}), 126.9 (C^{J2+J6}), 125.8 (C^{E5}), 124.1 (C^{D5}), 123.7 (C^{C3}), 123.6 (C^{A3}), 123.2 (C^{B5}), 122.0 (C^{E3}), 120.8 (C^{F3}), 120.6 ($C^{B3/D3}$), 120.5 ($C^{B3/D3}$), 36.2 ($C^{quat\text{-}tBu\text{-}E/F}$), 36.1 ($C^{quat\text{-}tBu\text{-}E/F}$), 30.6 ($C^{tBu-F}$), 30.5 ($C^{tBu-E}$).

IR (solid, $\tilde{\nu}$/cm^{-1}) 2959 (w), 1610 (m), 1600 (m), 1563 (w), 1544 (w), 1477 (m), 1427 (m), 1387 (w), 1369 (w), 1252 (w), 1224 (w), 1166 (w), 1068 (w), 1030 (w), 908 (w), 876 (w), 840 (s), 824 (s), 785 (m), 758 (s), 718 (w), 696 (s), 638 (w), 609 (w), 598 (w), 584 (w), 557 (s), 523 (w), 484 (w).

UV-Vis λ/nm (ε/L mol^{-1} cm^{-1}) (CH_2Cl_2, 1.00 × 10^{-5} mol dm^{-3}) 278 (97 000), 295 sh (71 000), 315 sh (37 000), 345 (15 000), 375 (7 000), 420 (5 000).

Emission (CH_2Cl_2, c = 1.00 × 10^{-5} mol dm^{-3}, λ_{ex} = 420 nm) λ_{em} = 590, 639 sh nm.

ESI-MS *m/z* 997.9 $[M - PF_6]^+$ (base peak, calc. 997.3).

Found C 60.61, H 4.94, N 4.95; $C_{58}H_{52}F_6IrN_4P$ requires C 60.99, H 4.59, N 4.90%.

5.9.9 [Ir(Ph$_2$ppy)$_2$(**1**)][PF$_6$]

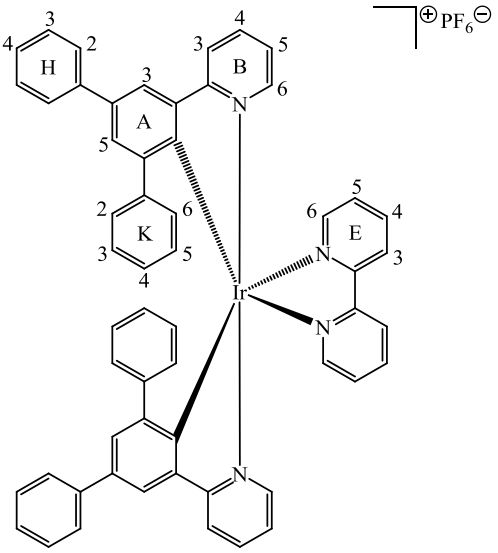

A mixture of [{Ir(Ph$_2$ppy)$_2$(μ-Cl)}$_2$] (200 mg, 0.197 mmol, 1.00 eq) and **1** (31.1 mg, 0.199 mmol, 1.01 eq) was dissolved in MeOH (30 mL). An excess of NH_4PF_6 (10.0 eq) was added and the reaction mixture was stirred for 1 h at room temperature. The yellow precipitate was filtered off, washed with MeOH and diethyl ether and then purified by column chromatography (Fluka silica gel 60, 0.040–0.063 mm; CH_2Cl_2 → CH_2Cl_2:MeOH 100:0.5). The pure product was obtained by crystallization in CH_2Cl_2 overlaid with EtOH:n-hexane 2:1 as orange solid (142 mg 0.128 mmol, 65.0%).

^{1}H NMR (500 MHz, CD_2Cl_2) δ/ppm 8.27 (d, J = 8.1 Hz, 2H, H^{E3}), 8.03 (td, J = 7.9, 1.6 Hz, 2H, H^{E4}), 7.95-7.90 (m, 4H, H^{A3+E6}), 7.78 (m, 4H, H^{H2}), 7.53 (d, J = 8.3 Hz, 2H, H^{B3}), 7.51–7.45 (m, 6H^{H3+E5}), 7.38 (m, 2H, H^{H4}), 7.31 (m, 2H, H^{B4}), 7.21 (d, J = 2.1 Hz, 2H, H^{A5}), 6.95 (m, 2H, $H^{K2/K6}$), 6.85 (m, 2H, H^{B6}), 6.84-6.78 (m, 4H, H^{K3+K5}), 6.60 (m, 2H, H^{K4}), 6.50-6.44 (m, 4H, $H^{B5+K2/K6}$).

^{13}C NMR (126 MHz, CD_2Cl_2) δ/ppm 167.2 (C^{B2}), 156.0 (C^{E2}), 152.0 (C^{A6}), 150.2 (C^{E6}), 148.9 (C^{B6}), 147.7 (C^{A2}), 145.5 (C^{K1}), 144.3 (C^{A1}), 141.2 (C^{H1}), 140.3 (C^{E4}), 137.8 (C^{B4}), 135.9 (C^{A4}), 132.0 (C^{A5}), 129.5 (C^{H3}), 129.4 ($C^{K2/K6}$), 129.2 ($C^{K2/K6}$), 129.0 (C^{E5}), 127.7 (C^{H4}), 127.6 ($C^{K3/K5}$), 127.3 (C^{K4}), 127.1 (C^{H2}), 126.6 ($C^{K3/K5}$), 125.0 (C^{E3}), 122.9 (C^{A3}), 122.8 (C^{B5}), 120.5 (C^{B3}).

IR (solid, $\tilde{\nu}$/cm^{-1}) 3044 (w), 1600 (m), 1565 (w), 1480 (m), 1445 (w), 1408 (w), 1381 (w), 1345 (w), 1313 (w), 1295 (w), 1243 (w), 1177 (w), 1165 (w), 1103 (w), 1072 (w), 1031 (w), 1020 (w), 908 (w), 880 (w), 834 (s), 774 (m), 760 (s), 716 (m), 699 (s), 636 (m), 612 (w), 600 (m), 557 (s), 525 (m), 495 (w).

UV-Vis λ/nm (ε/L mol^{-1} cm^{-1}) (CH_2Cl_2, 1.00 × 10^{-5} mol dm^{-3}) 255 (72 000), 282 (72 000), 299 (68 000), 325 sh (23 000), 345 (12 000), 400 (8 000), 420 sh (5 000).

Emission (CH_2Cl_2, c = 1.00 × 10^{-5} mol dm^{-3}, λ_{ex} = 420 nm) λ_{em} = 611, 638 sh nm.

ESI-MS *m/z* 961.8 $[M - PF_6]^+$ (base peak, calc. 961.2).

Found C 60.50, H 3.88, N 5.17; $C_{56}H_{40}F_6IrN_4P$ requires C 60.81, H 3.64, N 5.07%.

Crystallography $C_{58}H_{46}F_6IrN_4OP$, M = 1152.18, orange block, orthorhombic, space group $Pna2_1$, a = 13.1280(6), b = 37.8916(17), c = 10.2900(5) Å, U = 5118.7(4) $Å^3$, Z = 4, D_c = 1.495 Mg m^{-3}, μ(Cu-K_α) = 5.901 mm^{-1}, T = 123 K. Total 48035 reflections, 9189 unique, R_{int} = 0.0435. Refinement of 8655 reflections (670 parameters) with $I > 2\sigma(I)$ converged at final $R1$ = 0.0467 ($R1$ all data = 0.0493), $wR2$ = 0.1210 ($wR2$ all data = 0.1228), gof = 1.117. CCDC 1019227.

5.9.10 [Ir(Ph$_2$ppy)$_2$(**2**)][PF$_6$]

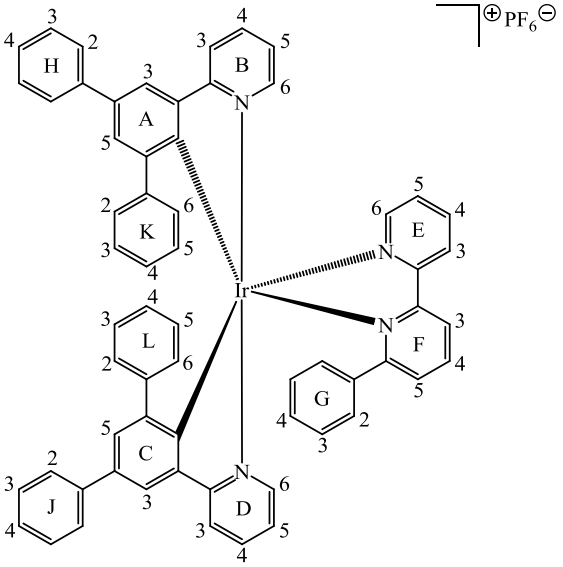

A mixture of [{Ir(Ph$_2$ppy)$_2$(μ-Cl)}$_2$] (200 mg, 0.197 mmol, 1.00 eq) and **2** (46.3 mg, 0.199 mmol, 1.01 eq) was dissolved in MeOH (30 mL). An excess of NH_4PF_6 (10.0 eq) was added and the reaction mixture was stirred for 1 h at room temperature. The yellow precipitate was filtered off, washed with MeOH and diethyl ether and then purified by column chromatography (Fluka silica gel 60, 0.040–0.063 mm; CH_2Cl_2 → CH_2Cl_2:MeOH 100:0.5). The pure product was obtained by crystallization in CH_2Cl_2 overlaid with EtOH:n-hexane 2:1 as orange solid (152 mg 0.129 mmol, 65.5%).

^{1}H NMR (500 MHz, CD_2Cl_2) δ/ppm 8.36 (m, 2H, H^{E3+F3}), 8.12–8.03 (overlapping m, 3H, $H^{E4+F4+E6}$), 7.68 (d, J = 5.7 Hz, 1H, H^{B6}), 7.65 (m, 2H, H^{H2}), 7.57 (m, 3H, H^{A3+J2}), 7.45 (m, 4H, H^{H3+J3}), 7.40–7.31 (overlapping m, 7H, $H^{B3+B4+D4+E5+F5+H4+J4}$), 7.18 (d, J = 8.1 Hz, 1H, H^{D3}), 7.15 (dd, J = 5.9, 0.7 Hz, 1H, H^{D6}), 7.06 (d, J = 2.1 Hz, 1H, H^{C3}), 6.98 (m, 1H, H^{G4}), 6.92 (m, 3H, H^{G3+L6}), 6.88 (d, J = 2.1 Hz, 1H, H^{A5}), 6.84 (m, 3H, H^{G2+L4}), 6.79–6.71 (overlapping m, 3H, $H^{B5+K4+L3}$), 6.67–6.58 (overlapping m, 3H, $H^{D5+K3+L5}$), 6.56 (d, J = 2.1 Hz, 1H, H^{C5}), 6.52 (m, 2H, H^{K5+K6}), 6.05 (dt, J = 7.5, 1.3 Hz, 1H, H^{L2}), 5.98 (m, 1H, H^{K2}).

^{13}C NMR (126 MHz, CD_2Cl_2) δ/ppm 169.3 (C^{D2}), 166.7 (C^{B2}), 165.2 (C^{F6}), 157.8 (C^{E2}), 157.1 (C^{F2}), 151.2 (C^{A6}), 150.5 (C^{C6}), 149.9 (C^{E4}), 149.5 (C^{B6}), 148.3 (C^{D6}), 147.7 (C^{C2}), 147.3 (C^{A2}), 146.0 (C^{L1}), 144.4 (C^{K1}), 141.9 (C^{J1}), 141.4 (C^{C1}), 140.9 (C^{H1}), 140.3 (C^{F4}), 140.1 (C^{E6}), 137.9 (C^{B4}), 137.6 (C^{G1}), 137.5 (C^{D4}), 135.7 (C^{A4}), 134.4 (C^{A1}), 134.1 (C^{C4}), 132.4 (C^{A5}), 131.7 (C^{C5}), 131.2 (C^{F5}), 130.6 (C^{L2}), 129.7 (C^{K6}), 129.5 (C^{K2}), 129.5 (C^{G4}), 129.4 ($C^{H3/J3}$), 129.3 ($C^{H3/J3}$), 129.0 (C^{G2}), 128.3 (C^{L6}), 128.3 (C^{E5}), 128.3 (C^{G3}), 127.7 (C^{H4}), 127.2 (C^{J4}), 127.0 ($C^{H2/J2}$), 127.0 ($C^{H2/J2}$), 127.0 (C^{K3+L3}), 126.5 (C^{K4}), 126.5 (C^{K5}), 126.4 (C^{L5}), 126.1 (C^{L4}), 125.8 (C^{E3}), 125.0 (C^{F3}), 123.6 (C^{C3}), 123.2 (C^{B5}), 122.9 (C^{A3}), 122.1 (C^{D5}), 120.8 (C^{D3}), 120.7 (C^{B3}).

IR (solid, $\tilde{\nu}$/cm^{-1}) 3031 (w), 1598 (m), 1563 (w), 1481 (m), 1444 (m), 1411 (w), 1379 (w), 1346 (w), 1294 (w), 1233 (w), 1170 (w), 1071 (w), 1026 (w), 996 (w), 905 (w), 887 (w), 834 (s), 787 (m), 757 (s), 717 (w), 702 (s), 693 (s), 630 (m), 599 (m), 555 (s), 526 (m), 506 (w), 488 (w).

UV-Vis λ/nm (ε/L mol^{-1} cm^{-1}) (CH_2Cl_2, 1.00 × 10^{-5} mol dm^{-3}) 261 (70 000), 280 (69 000), 294 (67 000), 325 sh (23 000), 345 (14 000), 400 (6 000), 420 sh (4 000).

Emission (CH_2Cl_2, c = 1.00 × 10^{-5} mol dm^{-3}, λ_{ex} = 420 nm) λ_{em} = 615 sh, 645 nm.

ESI-MS *m/z* 1037.8 $[M - PF_6]^+$ (base peak, calc. 1037.3).

Found C 61.92, H 4.02, N 4.75; $C_{62}H_{44}F_6IrN_4P{\cdot}H_2O$ requires C 62.04, H 3.86, N 4.67%.

Crystallography $C_{76}H_{60}F_6IrN_4P$, M = 1366.52, yellow block, triclinic, space group P–1, a = 10.8073(6), b = 13.5065(8), c = 20.8777(12) Å, α = 80.953(3), β = 86.577(3), γ = 78.797(3)°, U = 2950.90(17) Å^3, Z = 2, D_c = 1.538 Mg m^{-3}, μ(Cu-K$_\alpha$) = 5.207 mm^{-1}, T = 123 K. Total 50598 reflections, 10694 unique, R_{int} = 0.037. Refinement of 10647 reflections (793 parameters) with I >2σ (I) converged at final R1 = 0.0204 (R1 all data = 0.0243), wR2 = 0.0474 (wR2 all data = 0.0492), gof = 0.9016. CCDC 1019229.

5.9.11 [Ir(Ph$_2$ppy)$_2$(**3**)][PF$_6$]

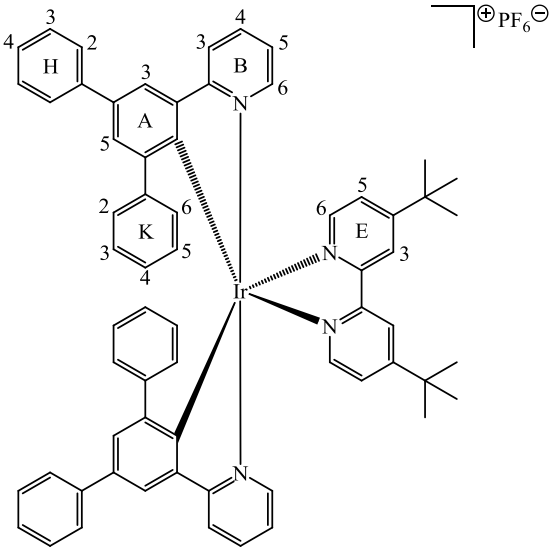

A mixture of [{Ir(Ph$_2$ppy)$_2$(μ-Cl)}$_2$] (200 mg, 0.197 mmol, 1.00 eq) and **3** (53.5 mg, 0.199 mmol, 1.01 eq) was dissolved in MeOH (10 mL). An excess of NH_4PF_6 (10.0 eq) was added and the reaction mixture was stirred for 1 h at room temperature. The yellow precipitate was filtered off, washed with MeOH and diethyl ether and then purified by column chromatography (Fluka silica gel 60, 0.040–0.063 mm; CH_2Cl_2 → CH_2Cl_2:MeOH 100:0.5). The pure product was obtained by crystallization in DCM overlaid with EtOH:n-hexane 2:1 as orange solid (131 mg 0.108 mmol, 54.8%).

^{1}H NMR (500 MHz, CD_2Cl_2) δ/ppm 8.01 (d, J = 1.9 Hz, 2H, H^{E3}), 7.94 (d, J = 2.1 Hz, 2H, H^{A3}), 7.82–7.74 (m, 6H, H^{H2+E6}), 7.53 (d, J = 8.3 Hz, 2H, H^{B3}), 7.50 (m, 4H, H^{H3}), 7.44 (dd, J = 6.0, 1.9 Hz, 2H, H^{E5}), 7.39 (m, 2H, H^{H4}), 7.32 (ddd, J = 8.4, 7.4, 1.5 Hz, 2H, H^{B4}), 7.22 (d, J = 2.1 Hz, 2H, H^{A5}), 6.99 (m, 2H, $H^{K2/K6}$), 6.85 (ddd, J = 5.9, 1.4, 0.7 Hz, 2H, H^{B6}), 6.82 (m, 4H, H^{K3+K5}), 6.59 (m, 2H, H^{K4}), 6.50–6.45 (m, 4H, $H^{B5+K2/K6}$), 1.34 (s, 18H, H^{tBu}).

^{13}C NMR (126 MHz, CD_2Cl_2) δ/ppm 167.3 (C^{B2}), 164.9 (C^{E4}), 155.8 (C^{E2}), 152.0 (C^{A6}), 149.8 (C^{E6}) , 149.0 (C^{B6}), 147.7 (C^{A2}), 145.6 (C^{K1}), 145.0 (C^{A1}), 141.2 (C^{H1}), 137.7 (C^{B4}), 135.8 (C^{A4}), 132.0 (C^{A5}), 129.5 (C^{H3}), 129.4 ($C^{K2/K6}$), 129.1 ($C^{K2/K6}$), 127.7 ($C^{H4+K3/K5}$), 127.4 (C^{K4}), 127.1 (C^{H2}), 126.5 ($C^{K3/K5}$), 126.2 (C^{E5}), 122.8 (C^{A3}), 122.6 (C^{B5}), 121.2 (C^{E3}), 120.4 (C^{B3}), 36.1 ($C^{quat\text{-}tBu}$), 30.5 (C^{tBu}).

IR (solid, $\tilde{\nu}$/cm^{-1}) 2965 (w), 1609 (w), 1567 (w), 1541 (w), 1481 (m), 1411 (m), 1382 (w), 1296 (w), 1246 (w), 1169 (w), 1155 (w), 1070 (w), 1019 (w), 895 (w), 878 (w), 835 (s), 782 (m), 772 (m), 758 (s), 737 (w), 704 (s), 637 (w), 610 (w), 599 (w), 556 (s), 525 (w), 498 (w).

UV-Vis λ/nm (ε/L mol^{-1} cm^{-1}) (CH_2Cl_2, 1.00 × 10^{-5} mol dm^{-3}) 256 (79 000), 280 (79 000), 300 (71 000), 325 sh (27 000), 345 (14 000), 400 (8 000), 420 sh (5 000).

Emission (CH_2Cl_2, c = 1.00 × 10^{-5} mol dm^{-3}, λ_{ex} = 420 nm) λ_{em} = 588, 639 sh nm.

ESI-MS *m/z* 1073.9 $[M - PF_6]^+$ (base peak, calc. 1073.4).

Found C 62.96, H 4.80, N 4.88; $C_{64}H_{56}F_6IrN_4P$ requires C 63.09, H 4.63, N 4.60%.

5.9.12 [Ir(Ph$_2$ppy)$_2$(**4**)][PF$_6$]

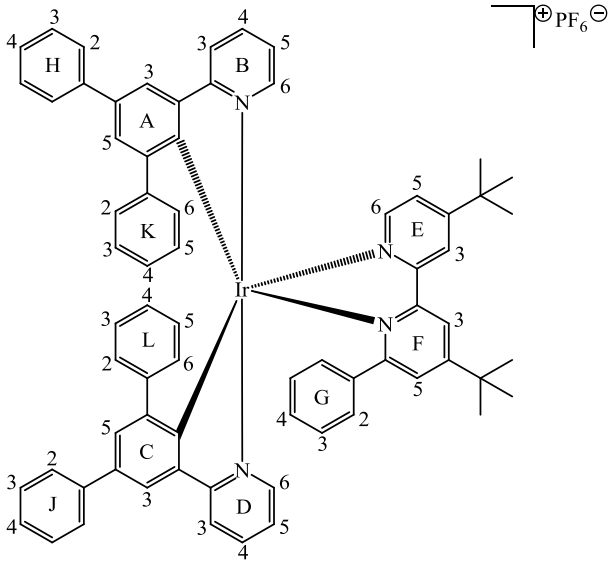

A mixture of [{Ir(Ph$_2$ppy)$_2$(μ-Cl)}$_2$] (150 mg, 0.148 mmol, 1.00 eq) and **4** (51.5 mg, 0.149 mmol, 1.01 eq) was dissolved in MeOH (30 mL). An excess of NH_4PF_6 (10.0 eq) was added and the reaction mixture was stirred for 1 h at room temperature. The yellow precipitate was filtered off, washed with MeOH and diethyl ether and then purified by column chromatography (Fluka silica gel 60, 0.040–0.063 mm; CH_2Cl_2 → CH_2Cl_2:MeOH 100:0.5). The pure product was obtained by crystallization in CH_2Cl_2 overlaid with EtOH:n-hexane 2:1 as yellow solid (106 mg 0.082 mmol, 54.1%).

^{1}H NMR (500 MHz, CD_2Cl_2) δ/ppm 8.12 (d, J = 1.8 Hz, 1H, H^{E3}), 8.11 (d, J = 2.0 Hz, 1H, H^{F3}), 7.96 (d, J = 6.0 Hz, 1H, H^{E6}), 7.67–7.62 (m, 3H, H^{B6+H2}), 7.58 (d, J = 2.1 Hz, 1H, H^{A3}), 7.58–7.55 (m, 2H, H^{J2}), 7.44 (m, 4H, H^{H3+J3}), 7.38–7.31 (overlapping m, 6H, $H^{B3+B4+D4+E5+H4+J4}$), 7.28 (d, J = 2.0 Hz, 1H, H^{F5}), 7.19 (d, J = 8.1 Hz, 1H, H^{D3}), 7.14 (dd, J = 5.9, 0.7 Hz, 1H, H^{D6}), 7.07 (d, J = 2.1 Hz, 1H, H^{C3}), 6.98 (m, 1H, H^{G4}), 6.93 (m, 2H, H^{G3}), 6.89 (m, 1H, H^{L6}), 6.87 (d, J = 2.1 Hz, 1H, H^{A5}), 6.84 (m, 3H, H^{G2+L4}), 6.78–6.71 (overlapping m, 3H, $H^{B5+K4+L3}$), 6.67–6.58 (overlapping m, 3H, $H^{D5+K3+L5}$), 6.55 (d, J = 2.1 Hz, 1H, H^{C5}), 6.53 (m, 2H, H^{K5+K6}), 6.05 (dt, J = 7.5, 1.3 Hz, 1H, H^{L2}), 5.98 (m, 1H, H^{K2}), 1.39 (s, 9H, $H^{t\text{Bu-F}}$), 1.37 (s, 9H, $H^{t\text{Bu-E}}$).

^{13}C NMR (126 MHz, CD_2Cl_2) δ/ppm 169.4 (C^{D2}), 166.8 (C^{B2}), 165.1 (C^{F6}), 164.8 (C^{E4+F4}), 157.7 (C^{E2}), 157.3 (C^{F2}), 151.3 (C^{A6}), 150.5 (C^{C6}), 149.5 (C^{E6}), 149.5 (C^{B6}), 148.4 (C^{D6}), 147.7 (C^{C2}), 147.3 (C^{A2}), 146.0 (C^{L1}), 144.4 (C^{K1}), 141.9 (C^{J1}), 141.7 (C^{C1}), 141.0 (C^{H1}), 138.0 (C^{G1}), 137.7 (C^{B4}), 137.4 (C^{D4}), 135.6 (C^{A4}), 134.9 (C^{A1}), 134.0 (C^{C4}), 132.3 (C^{A5}), 131.6 (C^{C5}), 130.6 (C^{L2}), 129.6 (C^{K6}), 129.5 (C^{K2}), 129.4 (C^{H3}), 129.4 (C^{G4}), 129.3 (C^{J3}), 129.0 (C^{G2}), 128.4 (C^{L6}), 128.3 (C^{G3}), 128.1 (C^{F5}), 127.7 (C^{H4}), 127.1 (C^{J4}), 127.0 (C^{H2+J2}), 127.0 (C^{K3}), 126.9 (C^{L3}), 126.5 (C^{K5}), 126.4 (C^{K4}), 126.4 (C^{L5}), 126.1 (C^{L4}), 125.6 (C^{E5}), 123.5 (C^{C3}), 123.0 (C^{B5}), 122.8 (C^{A3}), 122.0 (C^{E3}), 121.9 (C^{D5}), 121.7 (C^{F3}), 120.8 (C^{D3}), 120.7 (C^{B3}), 36.1 ($C^{\text{quat-tBu-E}}$), 36.0 ($C^{\text{quat-tBu-F}}$), 30.5 ($C^{t\text{Bu-F}}$), 30.4 ($C^{t\text{Bu-E}}$).

IR (solid, $\tilde{\nu}$/cm^{-1}) 3596 (w), 3031 (w), 1598 (m), 1563 (w), 1481 (m), 1444 (m), 1411 (w), 1379 (w), 1346 (w), 1294 (w), 1233 (w), 1170 (w), 1071 (w), 1026 (w), 996 (w), 905 (w), 887 (w), 834 (s), 787 (m), 757 (s), 717 (w), 702 (s), 693 (s), 630 (m), 599 (m), 555 (s), 526 (m), 506 (w), 488 (w).

UV-Vis λ/nm (ε/L mol^{-1} cm^{-1}) (CH_2Cl_2, 1.00 × 10^{-5} mol dm^{-3}) 261 (74 000), 280 (72 000), 298 (69 000), 325 sh (29 000), 345 (14 000), 400 (6 000), 420 (4 000).

Emission (CH_2Cl_2, c = 1.00 × 10^{-5} mol dm^{-3}, λ_{ex} = 420 nm) λ_{em} = 609, 636 sh nm.

ESI-MS *m/z* 1149.9 $[M - PF_6]^+$ (base peak, calc. 1149.5).

Found C 64.54, H 4.88, N 4.61; $C_{70}H_{60}F_6IrN_4P{\cdot}0.5H_2O$ requires C 64.50, H 4.72, N 4.30%.

Chapter 6

Chapter 6 Conclusions and Outlook

In this thesis, various series of cyclometallated Ir(III) complexes were successfully synthesized, characterized and tested for use in LEECs. It was demonstrated that upon careful consideration of combining the C^N and N^N ligands, the emission color could be tuned in a way so as to cover almost the entire range of the visible spectrum between blue and red (Figure 6.1).

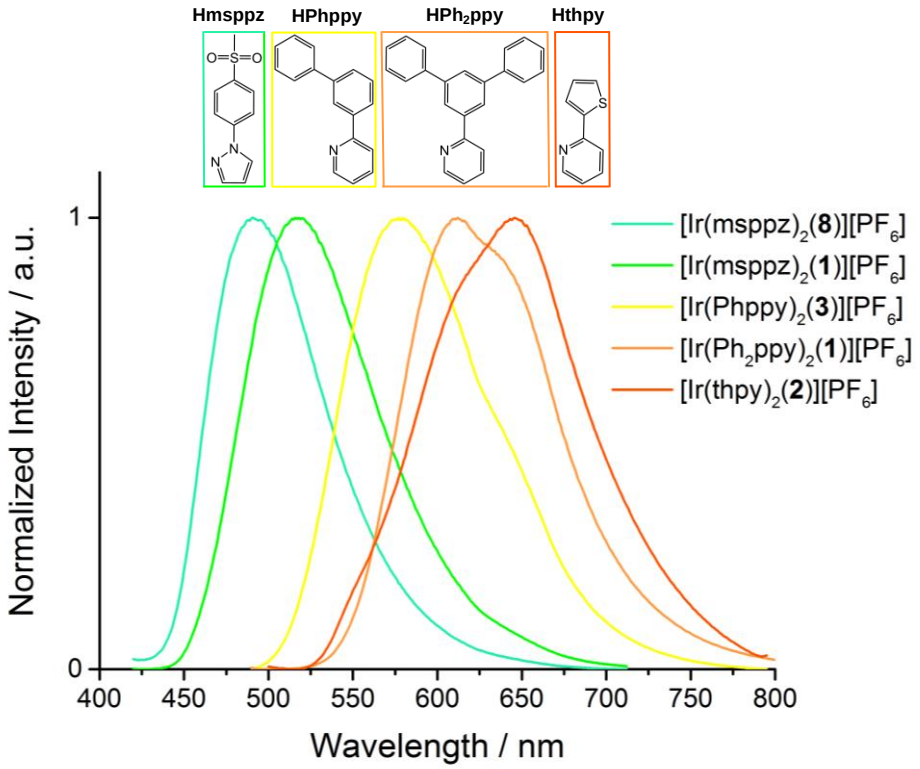

Figure 6.1 Normalized photoluminescence spectra of selected cyclometallated Ir(III) complexes based on different C^N and N^N ligands, measured in CH_2Cl_2 solutions (**1** = 2,2'-bipyridine; **2** = 6-phenyl-2,2'-bipyridine; **3** = 4,4'-di-*tert*-butyl-2,2'-bipyridine; **8** = 4,4'-bis(methylamino)-2,2'-bipyridine).

Based on a $[thpy]^-$ C^N ligand, a series of four Ir(III) complexes was synthesized exhibiting orange to red emission with maxima ranging from 543–646 nm in CH_3CN solution (see $[Ir(thpy)_2(\mathbf{2})][PF_6]$ in Figure 6.1). In PMMA films, the emission maxima window is narrowed to 542–592 nm whereby all complexes possess very similar structured emission. DFT/TD-DFT calculations of lowest-energy triplet states attribute the origin of these emission properties to be dominantly of ^{3}LC nature involving the $[thpy]^-$ ligand with minor contributions from the Ir(III) center. Since no ridigochromic shift was observed for the complexes in frozen CH_3CN, the potential red emission in solution can be understood as different relative intensity distributions of the vibronic structure defining the emission band. Therefore, their orange-emitting solid state behavior together with the poor performance in LEEC devices (suggested to arise from poor charge transport properties) makes this $[Ir(thpy)_2(N^N)][PF_6]$ series not a good candidate for red-emitting iTMCs in LEECs. To achieve deeply red-emitting complexes the search for alternative C^N ligands is necessary.

Depicted in the high-energy part of Figure 6.1, it was tried to obtain blue-emitting complexes based on $[msppz]^-$ cyclometallating ligand. The series of six highly luminescent complexes covered a green emission range from 492–518 nm. The best complex still exhibits a remarkably high PLQY of 85% in LEEC device configuration. Also when operating in LEEC devices this series of complexs stands out with short turn-on times (< 5 s), good efficiencies and high luminace values. However, the short lifetime in devices, which does not exceed several minutes, limits their use in LEECs. Nevertheless, initial experiments revealed that the emission could be blue-shifted upon introduction of a second methyl sulfone group on the 2-position of the Hmsppz ligand. Whether this substitution is also beneficial for the device lifetime remains to be tested.

The focus of the yellow/orange-emitting $[Ir(Phppy)_2(N\text{^}N)][PF_6]$ and $[Ir(Ph_2ppy)_2(N\text{^}N)][PF_6]$ complex series (see Figure 6.1), was mainly to understand how the intrinsic stability of an Ir(III) complex can be enhanced rather than the color-tuning. Therefore, the systematic effect of up to three intra-cation π-stacking interactions forming a hydrophobic cage around the Ir(III) metal center was investigated. Thereby, the cyclometallating $[Ph_2ppy]^-$ ligands were synthetically modified in a way so as to enable face-to-face intramolecular π-stacking sites between the two C^N ligands which is, to our knowledge, the first class of compounds to do so. Additionally, a solvento-precursor $[Ir(C\text{^}N)_2(MeOH)_2][PF_6]$ was introduced in the classical synthetic route to prevent the final complexes from detrimental chloride-impurities. The best performance is observed for devices based on iTMC $[Ir(Phppy)_2(\mathbf{1})][PF_6]$ with a maximum luminance of 1024 cd m^{-2}, an efficiency of 3.5 cd A^{-1} and an extrapolated lifetime exceeding 2800 hours even under accelerated measuring conditions. Interestingly, these remarkable lifetimes were reached by devices based on complexes with and without the π-stacking ability corroborating the fact that multiple face-to-face π-stacking sites is not necessarily a general design principle to achieve good LEEC device performances. Still an open question is whether the new synthetic route via the solvento-precursor has a significant effect on the device performance. Further experiments of reported Ir(III) complexes which were resynthesized following this synthetic procedure should clarify the necessity of the solvento-precursor route becoming a standard preparation method for chloride-free cyclometallated Ir(III) compounds.

Finally, by linking two Hppy ligands with a blue-emissive naphthyl glycol chain resulted in a new C^N ligand which was used to coordinate to an orange-emitting Ir(III) center with the aim of synthesizing a unique dual-emitting cyclometallated Ir(III) complex of the type $[Ir(naphppy)(\mathbf{5})][PF_6]$ (Figure 6.2). The photoluminescence property of $[Ir(naphppy)(\mathbf{5})][PF_6]$ in solution is ascribed to consist of the well-known MLCT/LLCT predominantly orange emission at 564 nm and a second, thermally populated fluorescent excited state (420 nm) attributed to ligand **5**. PMMA films containing $[Ir(naphppy)(\mathbf{5})][PF_6]$ and neat powders only exhibited an orange emission band at 529 and 567 nm (PLQY of 66 and 20%) displaying the strong environmental dependency of the blue emission quenching. Since no unambiguous evidence of two independent emissions could be found, no dual-

emission properties were attributed to [Ir(naphppy)(**5**)][PF_6]. Variable temperature photoluminescence measurements upon cooling the sample down could clarify the eventual independence of the two emission bands in solution. Furthermore, it would be of significant interest to investigate the photophysical properties of a series of [Ir(naphppy)(N^N)][PF_6] complexes with N^N such as 4,4'-di-*tert*-butyl-2,2'-bipyridine or 6-phenyl-4,4'-di-*tert*-butyl-2,2'-bipyridine, thereby examining the eventual existence of dual-emission. Alternatively, the effect of expanding the naphthyl to an anthracene unit of the linked C^N ligand should be tested.

White-light emission could be generated upon mixing a solution containing the yellow-emissive [Ir(naphppy)(**5**)][PF_6] complex with a blue-emitting solution of Hnaphppy in a 1 : 1 ratio (Figure 6.2). Embedding this mixture in a PMMA film leads to a green-shifted emission due to the environmental changes between the two states.. Nevertheless, this experiment clearly shows that mixing of two ideally complementary-emitting compounds opens the door to achieve white-light emission. In future works this approach should be investigated in more detail, especially how to conserve the white-light emission in the LEEC device.

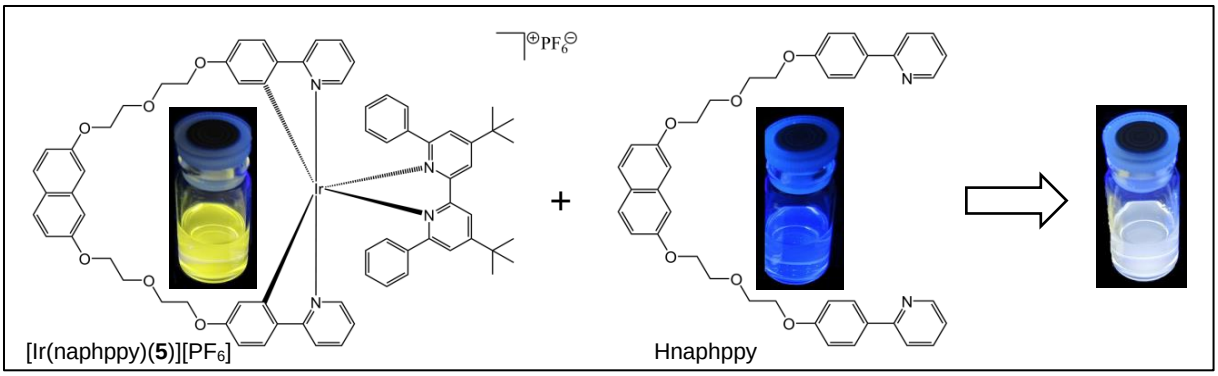

Figure 6.2 White-light emission, obtained upon mixing a yellow-emissive 1.00 x 10^{-5} M CH_2Cl_2 solution of [Ir(naphppy)(**5**)][PF_6] with a blue-emitting 1.00 x 10^{-5} M CH_2Cl_2 solution containing Hnaphppy in a 1 : 1 ratio.

References

[1] Bruker Analytical X-ray Systems, Inc., 2006, APEX2, version 2 User Manual, M86-E01078, Madison, WI.

[2] Betteridge, P. W.; Carruthers, J. R.; Cooper, R. I.; Prout, K.; Watkin, D. J. *J. Appl. Cryst.* **2003**, *36*, 1487.

[3] Sheldrick, G. M. *Acta Crystallogr. Sect. A* **2008**, *64*, 112.

[4] Bruno, I. J.; Cole, J. C.; Edgington, P. R.; Kessler, M.; Macrae, C. F.; McCabe, P.; Pearson, J.; Taylor, R. *Acta Crystallogr. Sect. B* **2002**, *58*, 389.

[5] Macrae, C. F.; Bruno, I. J.; Chisholm, J. A.; Edgington, P. R.; McCabe, P.; Pidcock, E.; Rodriguez-Monge, L.; Taylor, R.; Van De Streek, J.; Wood, P. A. *J. Appl. Cryst.* **2008**, *41*, 466.

[6] Smil, V. *Creating the Twentieth Century: Technical Innovations of 1867 – 1914 and Their Lasting Impact*; Oxford University Press, Oxford, 2005.

[7] Brox, J. *Brilliant: The Evolution of Artificial Light*; Houghton Mifflin Harcourt, New York, 2010.

[8] Costa, R. D.; Ortí, E.; Bolink, H. J.; Monti, F.; Accorsi, G.; Armaroli, N. *Angew. Chem. Int. Ed.* **2012**, *51*, 8178.

[9] Tsao, J. Y.; Saunders, H. D.; Creighton, J. R.; Coltrin, M. E.; Simmons, J. A. *J. Phys. D. Appl. Phys.* **2010**, *43*, 354001.

[10] International Energy Agency. *Light's Labour's Lost—Policies for Energy-Efficient Lighting*; http://www.iea.org/, 2006.

[11] Ley, A.; Kemmler, A.; Piégsa, A. *Analyse des schweizerischen Energieverbrauchs 2000 - 2012 nach Verwendungszwecken*; 2013.

[12] Mitschke, U.; Bäuerle, P. *J. Mater. Chem.* **2000**, *10*, 1471.

[13] Dini, D. *Chem. Mater.* **2005**, *17*, 1933.

[14] Crawford, M. H. *IEEE J. Sel. Top. Quantum Electron.* **2009**, *15*, 1028.

[15] Tang, C. W.; Vanslyke, S. A. *Appl. Phys. Lett.* **1987**, *51*, 913.

[16] Ota, K.; Matsui, M.; Milford, E. L.; Mackin, G. A.; Weiner, H. L.; Hafler, D. A. *Nature* **1990**, *346*, 183.

[17] Humphreys, C. J. *MRS Bull.* **2008**, *33*, 459.

[18] *The Nobel Prize in Physics 2014*; The Royal Swedish Academy of Sciences, Press release http://www.nobelprize.org/nobel_prizes/physics/laureates/2014/press.pdf 2014.

[19] Holder, E.; Langeveld, B. M. W.; Schubert, U. S. *Adv. Mater.* **2005**, *17*, 1109.

[20] Friend, R. H.; Gymer, R. W.; Holmes, A. B.; Burroughes, J. H.; Marks, R. N.; Taliani, C.; Bradley, D. D. C.; Dos Santos, D. A.; Brédas, J. L.; Lögdlund, M.; Salaneck, W. R. *Nature* **1999**, *397*, 121.

[21] Thirion, D.; Romain, M.; Rault-Berthelot, J.; Poriel, C. *J. Mater. Chem.* **2012**, *22*, 7149.

[22] Lamansky, S.; Djurovich, P.; Murphy, D.; Abdel-Razzaq, F.; Lee, H.-E. E.; Adachi, C.; Burrows, P. E.; Forrest, S. R.; Thompson, M. E. *J. Am. Chem. Soc.* **2001**, *123*, 4304.

[23] Reineke, S.; Lindner, F.; Schwartz, G.; Seidler, N.; Walzer, K.; Lüssem, B.; Leo, K. *Nature* **2009**, *459*, 234.

[24] Evans, R. C.; Douglas, P.; Winscom, C. J. *Coord. Chem. Rev.* **2006**, *250*, 2093.

[25] Bernards, D. A.; Slinker, J. D.; Malliaras, G. G.; Flores-Torres, S.; Abruña, H. D. *Appl. Phys. Lett.* **2004**, *84*, 4980.

[26] Slinker, J. D.; Rivnay, J.; Moskowitz, J. S.; Parker, J. B.; Bernhard, S.; Abruña, H. D.; Malliaras, G. G. *J. Mater. Chem.* **2007**, *17*, 2976.

[27] Pei, Q.; Yu, G.; Zhang, C.; Yang, Y.; Heeger, A. J. *Science* **1995**, *269*, 1086.

[28] Maness, K. M.; Terrill, R. H.; Meyer, T. J.; Murray, R. W.; Wightman, R. M. *J. Am. Chem. Soc.* **1996**, *118*, 10609.

[29] Elliott, C. M.; Pichot, F.; Bloom, C. J.; Rider, L. S. *J. Am. Chem. Soc.* **1998**, *120*, 6781.

[30] Rudmann, H.; Shimada, S.; Rubner, M. F. *J. Am. Chem. Soc.* **2002**, *124*, 4918.

[31] Flamigni, L.; Barbieri, A.; Sabatini, C.; Ventura, B.; Barigelletti, F. *Top Curr Chem* **2007**, *281*, 143.

[32] Slinker, J. D.; Gorodetsky, A. A.; Lowry, M. S.; Wang, J.; Parker, S.; Rohl, R.; Bernhard, S.; Malliaras, G. G. *J. Am. Chem. Soc.* **2004**, *126*, 2763.

[33] Lowry, M. S.; Bernhard, S. *Chem. Eur. J.* **2006**, *12*, 7970.

[34] Juris, A.; Balzani, V.; Barigelletti, F.; Campagna, S.; Belser, P.; von Zelewsky, A. *Coord. Chem. Rev.* **1988**, *84*, 85.

[35] Kober, E. M.; Caspar, J. V; Sullivan, B. P.; Meyer, T. J. *Inorg. Chem.* **1988**, *27*, 4587.

[36] Kumaresan, D.; Shankar, K.; Vaidya, S.; Schmehl, R. H. *Top. Curr. Chem.* **2007**, *281*, 101.

[37] Tordera, D.; Bünzli, A. M.; Pertegás, A.; Junquera-Hernández, J. M.; Constable, E. C.; Zampese, J. A.; Housecroft, C. E.; Ortí, E.; Bolink, H. J. *Chem. Eur. J.* **2013**, *19*, 8597.

[38] Hu, T.; He, L.; Duan, L.; Qiu, Y. *J. Mater. Chem.* **2012**, *22*, 4206.

[39] Malliaras, G. G.; Scott, J. C. *J. Appl. Phys.* **1998**, *83*, 5399.

[40] Rudmann, H.; Rubner, M. F. *J. Appl. Phys.* **2001**, *90*, 4338.

[41] Tordera, D.; Meier, S.; Lenes, M.; Costa, R. D.; Ortí, E.; Sarfert, W.; Bolink, H. J. *Adv. Mater.* **2012**, *24*, 897.

[42] Zysman-Colman, E.; Slinker, J. D.; Parker, J. B.; Malharas, G. G.; Bernhard, S. *Chem. Mater.* **2008**, *20*, 388.

[43] Su, H. C.; Chen, H. F.; Wu, C. C.; Wong, K. T. *Chem. Asian J.* **2008**, *3*, 1922.

[44] Buda, M.; Kalyuzhny, G.; Bard, A. J. *J. Am. Chem. Soc.* **2002**, *124*, 6090.

[45] Slinker, J. D.; Koh, C. Y.; Malliaras, G. G.; Lowry, M. S.; Bernhard, S. *Appl. Phys. Lett.* **2005**, *86*, 173506.

[46] Parker, S. T.; Slinker, J. D.; Lowry, M. S.; Cox, M. P.; Bernhard, S.; Malliaras, G. G. *Chem. Mater.* **2005**, *17*, 3187.

[47] Tamayo, A. B.; Garon, S.; Sajoto, T.; Djurovich, P. I.; Tsyba, I. M.; Bau, R.; Thompson, M. E. *Inorg. Chem.* **2005**, *44*, 8723.

[48] Su, H.-C.; Fang, F.-C.; Hwu, T.-Y.; Hsieh, H.-H.; Chen, H.-F.; Lee, G.-H.; Peng, S.-M.; Wong, K.-T.; Wu, C.-C. *Adv. Funct. Mater.* **2007**, *17*, 1019.

[49] Zeng, X.; Rothe, C.; Chiang, C. J.; Jankus, V.; Abdullah, K.; Jitchati, R.; Batsanov, A. S.; Bryce, M. R.; Monkman, A. P. *Adv. Funct. Mater.* **2009**, *19*, 2038.

[50] Zeng, X.; Tavasli, M.; Perepichka, I. F.; Batsanov, A. S.; Bryce, M. R.; Chiang, C. J.; Rothe, C.; Monkman, A. P. *Chem. Eur. J.* **2008**, *14*, 933.

[51] Xu, W.-J.; Liu, S.-J.; Ma, T.-C.; Zhao, Q.; Pertegás, A.; Tordera, D.; Bolink, H. J.; Ye, S.-H.; Liu, X.-M.; Sun, S.; Huang, W. *J. Mater. Chem.* **2011**, *21*, 13999.

[52] Kalyuzhny, G.; Buda, M.; McNeill, J.; Barbara, P.; Bard, A. J. *J. Am. Chem. Soc.* **2003**, *125*, 6272.

[53] Pile, D. L.; Bard, A. J. *Chem. Mater.* **2005**, *17*, 4212.

[54] Slinker, J. D.; Kim, J.-S.; Flores-Torres, S.; Delcamp, J. H.; Abruña, H. D.; Friend, R. H.; Malliaras, G. G. *J. Mater. Chem.* **2007**, *17*, 76.

[55] Soltzberg, L. J.; Slinker, J. D.; Flores-Torres, S.; Bernards, D. a.; Malliaras, G. G.; Abruña, H. D.; Kim, J. S.; Friend, R. H.; Kaplan, M. D.; Goldberg, V. *J. Am. Chem. Soc.* **2006**, *128*, 7761.

[56] Zhao, W.; Liu, C. Y.; Wang, Q.; White, J. M.; Bard, A. J. *Chem. Mater.* **2005**, *17*, 6403.

[57] Bolink, H. J.; Coronado, E.; Costa, R. D.; Ortí, E.; Sessolo, M.; Graber, S.; Doyle, K.; Neuburger, M.; Housecroft, C. E.; Constable, E. C. *Adv. Mater.* **2008**, *20*, 3910.

[58] Costa, R. D.; Ortí, E.; Bolink, H. J.; Graber, S.; Housecroft, C. E.; Constable, E. C. *Adv. Funct. Mater.* **2010**, *20*, 1511.

[59] Graber, S.; Doyle, K.; Neuburger, M.; Housecroft, C. E.; Constable, E. C.; Costa, R. D.; Ortí, E.; Repetto, D.; Bolink, H. J. *J. Am. Chem. Soc.* **2008**, *130*, 14944.

[60] Costa, R. D.; Ortí, E.; Bolink, H. J.; Graber, S.; Housecroft, C. E.; Constable, E. C. *J. Am. Chem. Soc.* **2010**, *132*, 5978.

[61] Costa, R. D.; Ortí, E.; Bolink, H. J.; Graber, S.; Housecroft, C. E.; Constable, E. C. *Chem. Commun.* **2011**, *47*, 3207.

[62] Schneider, G. E.; Pertegás, A.; Constable, E. C.; Housecroft, C. E.; Hostettler, N.; Morris, C. D.; Zampese, J. A.; Bolink, H. J.; Junquera-Hernández, J. M.; Ortí, E.; Sessolo, M. *J. Mater. Chem. C* **2014**, *2*, 7047.

[63] Bünzli, A. M.; Bolink, H. J.; Constable, E. C.; Housecroft, C. E.; Neuburger, M.; Ortí, E.; Pertegás, A.; Zampese, J. A. *Eur. J. Inorg. Chem.* **2012**, 3780.

[64] Costa, R. D.; Ortí, E.; Tordera, D.; Pertegás, A.; Bolink, H. J.; Graber, S.; Housecroft, C. E.; Sachno, L.; Neuburger, M.; Constable, E. C. *Adv. Energy Mater.* **2011**, *1*, 282.

[65] Constable, E. C.; Housecroft, C. E.; Kopecky, P.; Martin, C. J.; Wright, I. A.; Zampese, J. A.; Bolink, H. J.; Pertegás, A. *Dalton Trans.* **2013**, *42*, 8086.

[66] McGee, K. A.; Mann, K. R. *Inorg. Chem.* **2007**, *46*, 7800.

[67] Colombo, M. G.; Brunold, T. C.; Riedener, T.; Guedel, H. U.; Fortsch, M.; Buergi, H.-B. *Inorg. Chem.* **1994**, *33*, 545.

[68] Neve, F.; Ghedini, M.; Crispini, A. *J. Organomet. Chem.* **1994**, *466*, 259.

[69] Bandini, M.; Bianchi, M.; Valenti, G.; Piccinelli, F.; Paolucci, F.; Monari, M.; Umani-Ronchi, A.; Marcaccio, M. *Inorg. Chem.* **2010**, *49*, 1439.

[70] Tsuboyama, A.; Iwawaki, H.; Furugori, M.; Mukaide, T.; Kamatani, J.; Igawa, S.; Moriyama, T.; Miura, S.; Takiguchi, T.; Okada, S.; Hoshino, M.; Ueno, K. *J. Am. Chem. Soc.* **2003**, *125*, 12971.

[71] Kauffmann, T.; Koenig, J.; Woltermann, A. *Chem. Ber.* **1976**, *109*, 3864.

[72] Lu, W.; Mi, B.-X.; Chan, M. C. W.; Hui, Z.; Che, C.-M.; Zhu, N.; Lee, S.-T. *J. Am. Chem. Soc.* **2004**, *126*, 4958.

[73] Ten Brink, G.-J.; Arends, I. W. C. E.; Hoogenraad, M.; Verspui, G.; Sheldon, R. A. *Adv. Synth. Catal.* **2003**, *345*, 497.

[74] Lowry, M. S.; Hudson, W. R.; Pascal, R. A.; Bernhard, S. *J. Am. Chem. Soc.* **2004**, *126*, 14129.

[75] Nonoyama, M. *Bull. Chem. Soc. Jpn.* **1979**, *52*, 3749.

[76] Neve, F.; Crispini, A.; Campagna, S.; Serroni, S. *Inorg. Chem.* **1999**, *38*, 2250.

[77] Janiak, C. *J. Chem. Soc., Dalt. Trans.* **2000**, 3885.

[78] Costa, R. D.; Ortí, E.; Bolink, H. J.; Graber, S.; Housecroft, C. E.; Neuburger, M.; Schaffner, S.; Constable, E. C. *Chem. Commun.* **2009**, 2029.

[79] Bünzli, A. M.; Bolink, H. J.; Constable, E. C.; Housecroft, C. E.; Junquera-Hernández, J. M.; Neuburger, M.; Ortí, E.; Pertegás, A.; Serrano-Pérez, J. J.; Tordera, D.; Zampese, J. A. *Dalton Trans.* **2014**, *43*, 738.

[80] Baranoff, E.; Bolink, H. J.; Constable, E. C.; Delgado, M.; Häussinger, D.; Housecroft, C. E.; Nazeeruddin, M. K.; Neuburger, M.; Ortí, E.; Schneider, G. E.; Tordera, D.; Walliser, R. M.; Zampese, J. A. *Dalton Trans.* **2013**, *42*, 1073.

[81] Lowry, M. S.; Goldsmith, J. I.; Slinker, J. D.; Rohl, R.; Pascal, R. A.; Malliaras, G. G.; Bernhard, S. *Chem. Mater.* **2005**, *17*, 5712.

[82] Terki, R.; Simoneau, L.-P.; Rochefort, A. *J. Phys. Chem. A* **2009**, *113*, 534.

[83] Bolink, H. J.; Coronado, E.; Costa, R. D.; Lardiés, N.; Ortí, E. *Inorg. Chem.* **2008**, *47*, 9149.

[84] Tordera, D.; Delgado, M.; Ortí, E.; Bolink, H. J.; Frey, J.; Nazeeruddin, M. K.; Baranoff, E. *Chem. Mater.* **2012**, *24*, 1896.

[85] He, L.; Duan, L.; Qiao, J.; Wang, R.; Wei, P.; Wang, L.; Qiu, Y. *Adv. Funct. Mater.* **2008**, *18*, 2123.

[86] Sprouse, S.; King, K. A.; Spellane, P. J.; Watts, R. J. *J. Am. Chem. Soc.* **1984**, *106*, 6647.

[87] Bouamaied, I.; Constable, E. C.; Housecroft, C. E.; Neuburger, M.; Zampese, J. A. *Dalton Trans.* **2012**, *41*, 10276.

[88] Zhang, D.; Telo, J. P.; Liao, C.; Hightower, S. E.; Clennan, E. L. *J. Phys. Chem. A* **2007**, *111*, 13567.

[89] Costa, R. D.; Ortí, E.; Bolink, H. J.; Graber, S.; Schaffner, S.; Neuburger, M.; Housecroft, C. E.; Constable, E. C. *Adv. Funct. Mater.* **2009**, *19*, 3456.

[90] Bolink, H. J.; Cappelli, L.; Cheylan, S.; Coronado, E.; Costa, R. D.; Lardiés, N.; Nazeeruddin, M. K.; Ortí, E. *J. Mater. Chem.* **2007**, *17*, 5032.

[91] He, L.; Qiao, J.; Duan, L.; Dong, G.; Zhang, D.; Wang, L.; Qiu, Y. *Adv. Funct. Mater.* **2009**, *19*, 2950.

[92] Su, H.-C.; Chen, H.-F.; Fang, F.-C.; Liu, C.-C.; Wu, C.-C.; Wong, K.-T.; Liu, Y.-H.; Peng, S.-M. *J. Am. Chem. Soc.* **2008**, *130*, 3413.

[93] Su, H.-C.; Chen, H.-F.; Shen, Y.-C.; Liao, C.-T.; Wong, K.-T. *J. Mater. Chem.* **2011**, *21*, 9653.

[94] Tang, S.; Pan, J.; Buchholz, H. A.; Edman, L. *J. Am. Chem. Soc.* **2013**, *135*, 3647.

[95] Akatsuka, T.; Roldán-Carmona, C.; Ortí, E.; Bolink, H. J. *Adv. Mater.* **2014**, *26*, 770.

[96] Wu, H. B.; Chen, H. F.; Liao, C. T.; Su, H. C.; Wong, K. T. *Org. Electron. Physics, Mater. Appl.* **2012**, *13*, 483.

[97] Asakawa, M.; Ashton, P. R.; Boyd, S. E.; Brown, C. L.; Gillard, R. E.; Kocian, O.; Raymo, F. M.; Stoddart, J. F.; Tolley, M. S.; White, A. J. P.; Williams, D. J. *J. Org. Chem.* **1997**, *62*, 26.

[98] Chow, H. S.; Constable, E. C.; Housecroft, C. E.; Neuburger, M. *Dalt. Trans.* **2003**, 4568.

[99] Chow, H. S.; Constable, E. C.; Housecroft, C. E.; Neuburger, M.; Schaffner, S. *Polyhedron* **2006**, *25*, 1831.

[100] Lepeltier, M.; Kwok-Ming Lee, T.; Kam-Wing Lo, K.; Toupet, L.; Le Bozec, H.; Guerchais, V. *Eur. J. Inorg. Chem.* **2005**, 110.

[101] Maestri, M.; Sandrini, D.; Balzani, V.; von Zelewsky, A.; Deuschel-Cornioley, C.; Jolliet, P. *Helv. Chim. Acta* **1988**, *71*, 1053.

[102] Hercules, D. M.; Rogers, L. B. *Spectrochim. Acta* **1959**, *15*, 393.

[103] Abedi, A.; Amani, V. *Synth. React. Inorganic, Met. Nano-Metal Chem.* **2014**, *44*, 1326.

[104] Sun, L.; Galan, A.; Ladouceur, S.; Slinker, J. D.; Zysman-Colman, E. *J. Mater. Chem.* **2011**, *21*, 18083.

[105] Wasserberg, D.; Meskers, S. C. J.; Janssen, R. A. J. *J. Phys. Chem. A* **2007**, *111*, 1381.

[106] Sandroni, M.; Zysman-Colman, E. *Dalton Trans.* **2014**, *43*, 3676.

[107] Zhang, F.; Duan, L.; Qiao, J.; Dong, G.; Wang, L.; Qiu, Y. *Org. Electron.* **2012**, *13*, 2442.

[108] Chen, H.-F.; Hung, W.-Y.; Chen, S.-W.; Wang, T.-C.; Lin, S.-W.; Chou, S.-H.; Liao, C.-T.; Su, H.-C.; Pan, H.-A.; Chou, P.-T.; Liu, Y.-H.; Wong, K.-T. *Inorg. Chem.* **2012**, *51*, 12114.

[109] Constable, E. C.; Housecroft, C. E.; Schneider, G. E.; Zampese, J. A.; Bolink, H. J.; Pertegás, A.; Roldan-Carmona, C. *Dalton Trans.* **2014**, *43*, 4653.

[110] He, L.; Duan, L.; Qiao, J.; Zhang, D.; Wang, L.; Qiu, Y. *Chem. Commun. (Camb).* **2011**, *47*, 6467.

[111] Li, P.; Shan, G. G.; Cao, H. T.; Zhu, D. X.; Su, Z. M.; Jitchati, R.; Bryce, M. R. *Eur. J. Inorg. Chem.* **2014**, 2376.

[112] Schneider, G. E.; Bolink, H. J.; Constable, E. C.; Ertl, C. D.; Housecroft, C. E.; Pertegàs, A.; Zampese, J. a; Kanitz, A.; Kessler, F.; Meier, S. B. *Dalton Trans.* **2014**, *43*, 1961.

[113] Schmid, B.; Garces, F. O.; Watts, R. J. *Inorg. Chem.* **1994**, *33*, 9.

[114] Prasad, D.; Preetam, A.; Nath, M. *Comptes Rendus Chim.* **2013**, *16*, 252.

[115] Farley, S. J.; Rochester, D. L.; Thompson, A. L.; Howard, J. A. K.; Williams, J. A. G. **2005**, *44*.

[116] Van Reenen, S.; Matyba, P.; Dzwilewski, A.; Janssen, R. A. J.; Edman, L.; Kemerink, M. *J. Am. Chem. Soc.* **2010**, *132*, 13776.

[117] Meier, S. B.; Hartmann, D.; Tordera, D.; Bolink, H. J.; Winnacker, A.; Sarfert, W. *Phys. Chem. Chem. Phys.* **2012**, *14*, 10886.

[118] Tordera, D.; Frey, J.; Vonlanthen, D.; Constable, E.; Pertegás, A.; Ortí, E.; Bolink, H. J.; Baranoff, E.; Nazeeruddin, M. K. *Adv. Energy Mater.* **2013**, *3*, 1338.